Electronic Type Separation of Single-Walled Carbon Nanotubes by Weak Field Centrifugation

TECHNISCHE UNIVERSITÄT DARMSTADT

Zur Erlangung des Grades Doktor - Rer. Nat.

vom Fachbereich Material- und Geowissenschaften

der Technischen Universität Darmstadt (D17)

genehmigte

Dissertation

von

Wieland Gabriel Reis (M. Sc.)

aus Köln

Referent: Prof. Dr. Ralph Krupke

Korreferent: Prof. Dr. Thomas Weitz

Prüfer: Prof. Dr. Jörg Schneider

Prüfer: Prof. Dr. Robert Stark

Darmstadt, 2017

Tag der Einreichung: 12.12.2016

Tag der Prüfung: 23.02.2017

Abstract:

The potential of semiconducting single–walled carbon nanotubes (SWCNTs) to outperform silicon in electronic application was finally realized in terms of on-state current density in September of 2016. High purity semiconducting SWCNT arrays were necessary to exceed the performance of silicon. But the desired semiconducting nanotubes cannot be grown exclusively without their metallic counterparts. Since electronic application requires predictable and uniform performance, strategies are sought for effective post synthesis separation of SWCNTs.
The identification of scalable processes that transfer random mixtures of SWCNTs into fractions featuring a high content of semiconducting species is therefore crucial for future application of SWCNTs in high-performance electronics.
Established separation methods employ SWCNT dispersions with polymeric dispersants and typically provide high semiconducting purity samples with narrow diameter distribution, i.e. almost single chiralities. But for a wide range of applications high purity mixtures of small and large diameters are sufficient or even required. The requirement of large quantities of organic solvents additionally hampers the scaling of these methods.
Herein a highly efficient and simple separation method is demonstrated that relies on selective interactions between tailor-made amphiphilic polymers and semiconducting SWCNTs in the presence of low viscosity separation media. The separation method relies on weak field centrifugation (WFC), i.e. <10,000 x *g*, of a SWCNT dispersion with a polymeric dispersant. In this work non-selective and strong adsorption of polymeric polyarylether dispersants on nanostructured carbon surfaces is demonstrated, which enables simple separation of diverse raw materials with different SWCNT diameter.
High purity individualized semiconducting SWCNTs or even self-organized semiconducting sheets are separated from an as-produced SWCNT dispersion via a single WFC run. Absorption and Raman spectroscopy are applied to verify the high purity of the obtained SWCNTs.
In addition and for the first time, increased temperatures were demonstrated to enable higher purity separation. Additionally it is shown that the mode of action behind this electronic enrichment is unique, i.e. strongly connected to both colloidal stability and protonation.
Furthermore SWCNT - network field-effect transistors (FETs) were fabricated, which exhibit high ON/OFF ratios (10^5) and field-effect mobilities (17 cm^2/Vs). In addition to demonstrating the feasibility of high purity separation by a novel low complexity process, the WFC method can be readily transferred to large scale production and provide economical relevance to SWCNTs of any diameter.

Abstrakt:

Das Potential halbleitender, einwandiger Kohlenstoffnanoröhren (EWKNRs) Silizium als Halbleiter in elektronischer Anwendung zu übertreffen wurde letztendlich im September 2016 realisiert mit Hinsicht auf die Stromdichte im An-Zustand. Hochreine halbleitende EWKNR Anordnungen waren notwendig um die Leistung von Silizium zu überschreiten. Aber die gewünschten halbleitenden Nanoröhren können nicht ausschließlich erzeugt werden ohne ihre metallischen Gegenstücke. Weil elektronische Anwendung vorhersehbare und gleichbleibende Leistung erfordert, werden Strategien zur effektiven post-Synthese Separation von EWKNRs gesucht.
Die Identifikation von skalierbaren Prozessen die zufällige Mixturen von EWKNRs in Fraktionen überführen mit einem hohen Gehalt an halbleitenden EWKNRs ist daher entscheidend für die zukünftige Anwendung von EWKNRs in Hochleistungselektronik.
Etablierte Separationsmethoden wenden EWKNR Dispersionen mit polymerischen Dispergiermitteln an und liefern typischerweise hohe halbleitende Reinheit bei schmaler Durchmesserverteilung, d.h. fast einzelne Chiralitäten. Aber für eine große Breite von Anwendungen reichen hochreine Mixturen großer und kleiner Durchmesser aus oder sind sogar erforderlich. Die Erforderlichkeit von großen Mengen von organischen Lösemitteln hindert zusätzlich das Aufskalieren dieser Methoden.
Hier wird ein hocheffizientes und einfaches Trennverfahren gezeigt, das auf selektiver Wechselwirkungen zwischen maßgeschneiderten amphiphilen Polymeren und halbleitenden SWCNTs in Gegenwart von niedrigviskosen Trennmedien beruht. Das Trennverfahren beruht auf einer Schwachfeldzentrifugation (SFZ), d.h. <10.000 x g, einer SWCNT-Dispersion mit einem polymerischen Dispergiermittel. In dieser Arbeit wird eine nichtselektive und starke Adsorption von polymerischen Polyarylether-Dispergiermitteln auf nanostrukturierten Kohlenstoffoberflächen demonstriert, was eine einfache Trennung verschiedener Rohmaterialien mit unterschiedlichem SWCNT-Durchmesser ermöglicht.
Hochreine individualisierte halbleitende SWCNTs oder sogar selbstorganisierte halbleitende Blätter werden von einer so produzierten SWCNT-Dispersion über einen einzigen SFZ-Lauf getrennt. Absorption und Raman-Spektroskopie werden angewendet, um die hohe Reinheit der erhaltenen SWCNTs zu verifizieren.
Zusätzlich und zum ersten Mal wurde gezeigt, dass erhöhte Temperaturen eine Trennung höherer Reinheit ermöglichen. Zusätzlich wird gezeigt, dass die Wirkungsweise hinter dieser elektronischen Anreicherung einzigartig ist, d.h. stark mit der kolloidalen Stabilität und der Protonierung verbunden ist.
Weiterhin wurden SWCNT-Netzwerk-Feldeffekttransistoren (FETs) hergestellt, die hohe AN / AUS-Verhältnisse (10^5) und Feldeffektmobilitäten (17 cm^2 / Vs) aufweisen. Außer der Demonstration der Durchführbarkeit einer hochreinen Trennung durch ein neuartiges Verfahren mit geringer Komplexität, kann das WFC-Verfahren leicht in die Großmengenproduktion überführt werden und bietet eine wirtschaftliche Relevanz für SWCNTs mit beliebigem Durchmesser.

Declaration

I declare that this thesis submitted to the Technische Universität Darmstadt for the award of the doctoral degree in natural sciences has not yet been submitted anywhere else at the Technische Universität Darmstadt or any other university for the award of any degree. Excerpt where indicated in the text, this is my own work. Collaborations with or with assistance of others is indicated as such. I did not use any other sources or tools besides those cited, mentioned and acknowledged. All citations are listed in the references chapter.

Date, Location

Signature

Contents

1. Introduction and Motivation

Ever since demonstrating the first application of semiconductors in electronic circuits dating back to 1947 [1], mankind has made faster and faster progress throughout all sciences leveraging the ability of computational power. May that progress be calculating larger and larger prime numbers in mathematics, simulating neuron interactions resulting in ever growing understanding of the human brain to the practical engineering part where people have been to the moon, sent a Rover to Mars and are discussing manned Mars missions already. In the current era, companies and governments use very large computational power to collect and process so called "Big Data". As one result, navigation systems that access live traffic data can help to relieve traffic hubs by directing a proper amount of cars via alternative routes to their respective destinations. The future might even bring communicating devices that use this processed data from multiple sources as collective intelligence that could be called a first generation of artificial intelligence.

The impact computers are having each day in every person's life is tremendous, although one barely notices them anymore. The best example is that life in the last couple of years has been largely influenced by the invention of smartphones. These hand sized computers can be used for a variety of operations. Sliding one finger across the screen commands tiny switches within the smartphone to operate according to the prevailing demand. These tiny switches are called transistors and work by opening and closing channels for electric currents. This operation can be understood as the zeroes and ones in the binary code that enables functionality of each and every computer or related device.

The number of connected transistors and intrinsic properties like switching time and operation voltage of the transistors actually determine how fast a phone, notebook, tablet, or any other kind of computer can operate and how much energy it consumes. Today's transistors usually consist of silicon as active semiconducting material, which over the past decades allowed constant reduction in size, resulting in exponentially increasing computing speed. However, silicon sets a natural boundary to this size reduction process, where channel lengths around 5 nm are cost piling to make because the architecture has to prevent quantum tunneling from obliterating silicon's semiconductor properties [2].

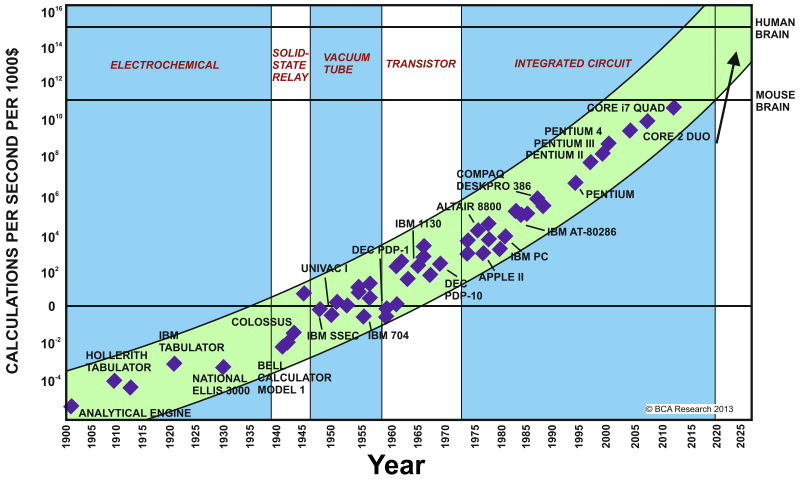

Figure 1.1. Moore's law. The logic operations per second per $1000 in logarithmic scale put in reference to the year the corresponding device hit the market to show Moore's law from an economic point of view. Reproduced from [3].

Therefore, strong efforts are made by scientists around the globe to find alternatives to silicon. These alternatives must enable smaller and faster transistors, which ideally also use less power, staying again with the smartphone example, making the battery last longer. When moving away from silicon the new material not only has to outperform silicon but finally must deliver better performance based on the cost (see Figure 1.1) to be relevant. This step is the crucial point as silicon is the second most abundant element in the earth's crust. Scientists have experimented a lot with carbon structures, which led to the discovery of fullerenes [4]. They observed nanoscale tube-like carbon structures already as early as 1953 [5]. Especially since Iijima's description of multi-walled carbon nanotubes (MWCNTs) in 1991 [6] and single-walled carbon nanotubes (SWCNTs) in 1993 [7], these carbon structures have attracted tremendous interest from research facilities of all disciplines. Over time, research has established synthesis methods [8] to provide SWCNTs and revealed their outstanding electronic properties. Thus carbon nanotubes became a very prominent candidate to eventually replace silicon for integrated circuit applications. Actually, SWCNTs bear the potential for transistors that work a hundred to a thousand [9] times faster than today's silicon transistors with respect to their electron mobility [10]. This feature comes along with the possibility of further downscaling these nanotube based transistors beyond the scales of today's silicon based counterparts [11], so that silicon could be outperformed and ultimately replaced by SWCNTs in modern computers.

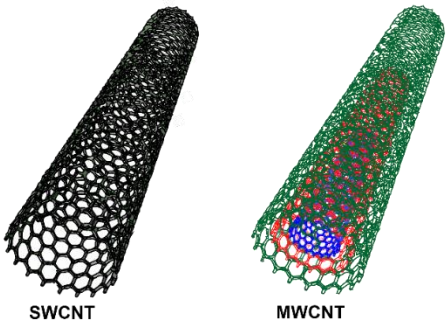

Figure 1.2. A single-wall carbon nanotube (SWCNT) and a multi-wall carbon nanotube (MWCNT) are depicted.

In graphene, carbon atoms are ordered in a two dimensional sheet of a hexagonal lattice structure, where multiple layers of these sheets form natural graphite. SWCNTs can be visualized as single layer graphene sheets rolled up into hollow seamless cylinders of typically 1 - 2 nm in diameter. Any nanotube can be completely characterized by a pair of integers (n, m), also called the chiral index, describing the way the graphene sheet is rolled up to form the SWCNT. The electronic properties of a certain SWCNT are depending on its specific chirality, which can cause either metallic or semiconducting behavior [12]. By nature, a random sample of SWCNTs contains 33% of metallic and 67% of semiconducting nanotubes. However, electronic applications such as Field-Effect Transistors (FETs) are short-wired by metallic SWCNTs and can only work if pure semiconducting SWCNTs are employed. Nowadays, it is not possible to economically grow SWCNTs in solely a desired semiconducting structure but only into multiple chiralities of close diameter range using typical fabrication processes [13]. The work in this thesis deals with SWCNTs produced via the so called High Pressure Carbon monoxide (HiPco) process, via the

arc discharge (AD) synthesis route and via plasma torch (PT) production. The basic chemistry behind each of those processes involves evaporation of carbon from a carbon source and the subsequent condensation of carbon as SWCNT on a catalyst material. In the HiPco process for example, carbon is obtained by the disproportionation of carbon monoxide via the Boudouard reaction $CO + CO \rightleftharpoons CO_2 + C_{(SWCNT)}$ [14]. The HiPco process continuously produces small diameter (0.7 - 1.2 nm) SWCNTs at relatively low costs compared to other processes of SWCNT production [15]. The advantage of the continuously synthesized PT or the batch processed AD SWCNTs, however, is that they contain fewer structural defects [16, 17] . Following the synthesis protocol for AD and PT SWCNTs, the diameter range is additionally shifted towards larger diameter SWCNTs (1.0 - 1.8 nm).

The huge potential for SWCNT transistors replacing silicon and the limitation of being grown electronically unsorted, leads to the need for an effective way of separating SWCNTs after production. A separation process resulting in electronic type enrichment could be the basis for large scale usage of SWCNTs in integrated electronics. Semiconductor applications such as backplanes for cell phone display configurations require nanotube samples of less semiconducting purity as compared to logic applications in integrated circuits and could therefore enable the near future breakthrough of the nanotube technology [18, 19]. Before trying to separate SWCNT material, safe handling of the highly toxic [20] SWCNTs must be assured and was achieved by dispersing them in solvents [21-23]. This prevents the formation of SWCNT aerosols. However, dispersing SWCNTs requires the addition of dispersants to functionalize the highly hydrophobic surfaces of SWCNTs [24]. Furthermore being able to disperse SWCNTs allowed the development of several separation techniques.

A multitude of separation techniques has evolved varying from dielectrophoresis [25] over gel chromatography [26-28], selective solubilization [29, 30], selective reaction [31, 32] to density gradient ultracentrifugation (DGU) [33-35] and spontaneous phase separation [36-39], to name the most common ones. Before those methods can be employed, in each method a prerequisite for separating SWCNTs is the removal of non-nanotube material from the as-synthesized material. Therefore centrifugation typically is an additional first step used to prepare the SWCNT dispersion by removing the amorphous carbon and catalyst particles for those methods. This hints that a great advantage, centrifugation techniques hold, is a potential one-step separation, where amorphous carbon and catalyst particles are excluded at the same time as the electronic sorting is executed.

Centrifugation of nm-sized objects was first used in the beginning of the last century, when colloid research created a connection between preparative chemistry and theoretical physics [40]. It was Einstein himself, who related the Brownian motion to the diffusional coefficient, a connection which was later used by Perrin to calculate Avogadro's constant, for example [41]. The connection between both research fields is also demonstrated by the Nobel Prizes in physics and chemistry in 1926, when Perrin was awarded the prize in physics for his discovery of the sedimentation equilibrium in ultracentrifuges, while Theodor Svedberg, the inventor of the

ultracentrifuge, was awarded for his use of the technique in chemistry [42, 43]. Svedberg originally used his invention to characterize nanoparticles according to their size [44] and was able to determine the size distribution of very small gold colloid particles by exposing them to a density gradient. From there the ultracentrifuge evolved as a powerful tool and was consequently also recognized as option for the separation of SWCNTs after their discovery. Modern ultracentrifuges enable strong centrifugal fields up to 500,000 x *g*. The density gradient method uses the high centrifugal acceleration to form a gradient in density by depletion and accumulation of dissolved heavy materials (Figure 1.3). Density gradients force particles with the smallest differences in density to accumulate in their respective density zone of the gradient. Density differences are present in dispersed SWCNTs due to their different chiralities and resulting surfactant encapsulation. This method can therefore be used to purify and extract pristine samples of semiconducting SWCNTs for high performance electronic devices. This was first shown by Arnold and coworkers in 2005 [34]. Here, the achievable purity is the most important advantage. A great challenge in DGU is the very limited yield of the method. On the one hand it is restricted due to small loading amounts of material into the very high centrifugal fields, on the other hand, the very fine bands of separated nanotubes are connected with high complexity extraction processes. For example, after separation in DGU, the SWCNTs form bands of equal density that are only separated on a millimeter scale. Additionally, during extraction a loss of purity occurs as a result of the high viscosity originating from sugar based density media (see Figure 1.3).

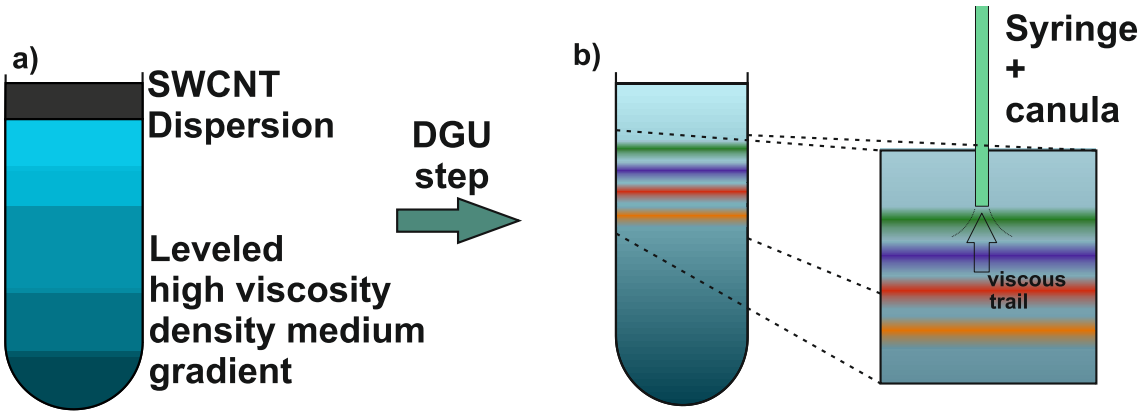

Figure 1.3. A DGU process is shown for SWCNTs. In a) a dispersion of SWCNTs is loaded onto a leveled sugar based density gradient and centrifuged so that a density gradient forms. In b) the SWCNTs have separated and split into distinct bands of their respective density. They are extracted by a syringe through a canula. This leads to the formation of a viscous trail.

In other words a tradeoff exists between yield and purity. DGU, although giving access to high purity SWCNT fractions, is therefore not the answer to provide separated semiconducting SWCNTs for more than research application. Thus the search for a highly efficient and reliable separation method for SWCNTs is still ongoing. To impact the electronics industry, the separation method must produce on a scale that can matter economically while maintaining high enough purity for logic operation of SWCNT transistors. Experimental FETs made from SWCNTs have already been reduced to sizes below 10 nm [45], while also first flexible or even

moldable transistors have been realized from SWCNTs [46]. These results indicate the great advances, which could be made in the future.

The first aim of this work is the separation of samples highly enriched with semiconducting SWCNTs using only weak-field centrifugation. To offer a scalable method, the centrifugal field has to be kept to small dimensions. G-forces that are enabled by standard large volume centrifuges reach 15,000 x *g*. Thus the samples are going to be evaluated after weak field centrifugation (WFC) using mostly the randomly grown HiPco SWCNTs but also AD and PT SWCNTs.

To develop the WFC separation method various parameters such as density media, dispersants, centrifugation time and speed were varied, but also pH-values and temperature were investigated during centrifugation experiments. To give the weak centrifugal fields an access point to electronic type separation of carbon nanotubes, stable surfactants are sought throughout all parameter variations. Here BASF's chemistry offers enormous opportunities providing stable dispersing agents for SWCNTs [47]. In fact, polymeric dispersants from BASF have been investigated in combination with SWCNTs by research groups around the world [48, 49]. Specific polymers even showed potential for electronic type separation [50-52]. Lastly, decisive for large scale production of pristine semiconducting SWCNTs would be the high yield dispersing of carbon nanotubes and subsequent avoiding of ultracentrifuges in the entire process.

Following this **introduction, chapter 2** provides the theoretical background of the methods used in the thesis in order to support the understanding of SWCNT separation via standard centrifugation in a density medium. The individual sections also focus on explaining the prevailing theoretical considerations of the structure and properties of SWCNTs, the interaction between dispersants and SWCNTs, and how SWCNTs' optical features differ from those of graphene.

Chapters 3 & **4** deal with the introduction of the materials and methods used for the experimental work of this thesis. Materials employed include different SWCNT materials, different dispersants and density media for centrifugation as well as further chemicals specifically used in certain experiments. The methods chapter details how the respective experiments were performed and which equipment was used.

In the ensuing **chapters 5** & **6,** the experimental details of preparing aqueous polymer/SWCNT dispersions and using them for separating SWCNTs to a high degree considering yield and purity by electronic character in a centrifugal field are shown. The focus lies on detailing the effects leading to the observation of a paramount semiconducting sample that was separated by WFC under specific conditions using BASF's tailored polymeric dispersants [53].

The analysis after separation of all isolated and extracted SWCNTs bands is described in **chapter 7** according to their chiralities and concomitant electronic character by optical absorbance as well

as Raman spectroscopy. These optical techniques are the methods of choice for SWCNTs as they rely on characteristic energy transitions that can be induced in isolated SWCNTs [54-56].

The optical analysis revealed samples that are of enriched semiconducting character. In **chapter 8** these samples are embedded in SWCNT networks on silicon wafers covered with dielectrics to build thin-film FETs. The morphology of the SWCNT films is imaged using atomic force microscopy. The transistor performance is explored in relation to the progress of SWCNT extraction and preparation of SWCNT inks.

Lastly, in **chapter 9** this work is summarized and an outlook is given towards future research activities that could follow in order to show how it can be classified in the context of nanotube research across the globe.

2. Theoretical Background

The following sections cover the established theoretical aspects of this thesis starting with the structure and properties of SWCNTs followed by the fundamentals of the experimental techniques used throughout this work. Also in focus is the physics behind the crucial analytical methods to support a sound understanding of the carried out experiments, observations and the critical interpretation of the collected data.

2.1. Introduction of Carbon Nanotubes

In natural resources carbon is generally found in form of three allotropes, which include amorphous carbon, graphite and diamonds [57]. These carbon allotropes differ by their respective configuration of the carbon atom bonds. While for amorphous carbon no homogeneous binding structure can be observed, diamonds are comprised of carbon atoms in sp^3-hybridization. Graphite is comprised of multiple layers of carbon in sp^2-hybridization called graphene, which are bound to one another by weak van-der-Waals interactions.

The sp^2-hybridization of the carbon atoms within each graphene layer results in a hexagonal lattice. If such a single graphene layer is hypothetically rolled into a seamless cylinder, the arising structure is called a SWCNT (Figure 2.1). Since the symmetry of graphene does not allow formation of arbitrary seamless cylinders, the carbon nanotube structure generally exhibits a spiral conformation, which is called the chirality of the nanotube [57]. Following this approach the structural and electronic properties of SWCNTs will be revealed in the following (sub)sections.

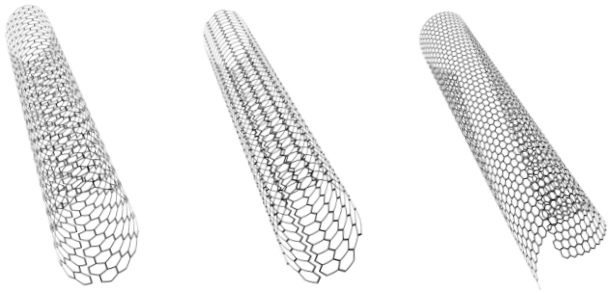

Figure 2.1. Illustration of the differently named carbon nanotubes. The hypothetical graphene sheet is rolled up into a seamless cylinder in a) along the zig-zag symmetry of the graphene lattice in b) along the armchair symmetry and in c) not along a high symmetry path. Note that the carbon atoms along the hypothetical seem of zig-zag tubes form an armchair pattern and vice versa a result of the 6-fold symmetry of graphene.

2.2. Synthesis of Carbon Nanotubes

The purchased SWCNTs in this thesis were synthesized by three different methods. As discussed in the introduction, these processes all include the release of carbon atoms from a carbon source. However, besides depending on the configuration of the oven, they also differ in the temperature

ranges used to obtain carbon as well as the pressure conditions and the catalyst material applied to the free carbon so that SWCNTs are formed [57]. More popular are the low temperature methods [58] as they allow a better control of the critical SWCNT parameters including length and diameter and foremost for economic reasons as they offer scalability.

Arc Discharge

The first single-wall carbon nanotubes observed by Iijima [59] were produced by arc discharge of two opposing graphite electrodes [60]. During this procedure both electrodes are enclosed in a sealed chamber under an atmosphere of argon or helium. High temperatures (>1700°C) arise from the electrical discharge, a temperature high enough for sublimation of carbon atoms out of the solid electrode material [16]. The nanotubes form at the cathode, where addition of catalyst particles from transition metals lead to the mere formation of single-walled carbon nanotubes [61].

Plasma Torch

The plasma torch method is comparable to the arc discharge synthesis. The first similarity is the high temperature that can be achieved in the plasma jet (15,000°C). Secondly the resulting nanotubes contain only few structural defects [62]. However, the arc discharge method cannot produce continuously due to the consumption of the electrode material, here the plasma torch method allows more efficient SWCNT production by the use of gaseous [63] or carbon black as source material [62]. The plasma jet is operated by direct current to dismantle gaseous carbon sources like CO and catalyst precursors like $Fe(CO)_5$ [63]. This process was developed into a highly efficient, meaning economically relevant, process and delivers SWCNTs with diameters in the range of 1.2 - 1.6 nm on a 100 g/h scale [64].

Chemical Vapor Deposition (CVD)

In 1992 a low temperature [65] method for multi-walled carbon nanotube synthesis based on chemical vapor deposition (CVD) was introduced [66]. Gaseous carbon sources such as methane or acetylene are mixed with noble gases or hydrogen. At temperatures of about 1000°C carbon nanotubes form by the use of suitable catalyst material (Fe, Co, Ni) in the reaction chamber [67]. The process can be modified by use of plasma irradiation, which leads to lower defect rates in the formed carbon nanotubes [68].

High Pressure Carbon Monoxide (HiPco)

One of the many CVD methods that synthesize carbon structures is the so called HiPco process developed in 1999 [69]. The HiPco method involves a continuous flow of Carbon Monoxide as carbon source, while $Fe(CO)_5$ (iron pentacarbonyl) serves as catalyst precursor. The temperature ranges from 800 - 1200°C to grow the SWCNTs. The architecture of the reaction chamber has

an influence on the yield while the pressure roughly controls the diameter distribution of the nanotubes. This way the HiPco process can deliver thin SWCNTs of diameters between 0.7 - 1.2 nm.

However, the problem with the introduced methods remains the production of a mixture of semiconducting (2/3) and metallic (1/3) SWCNTs and the necessity for post synthesis separation.

2.3. Structure of Single-Walled Carbon Nanotubes

By studying the intimate relation between SWCNTs and graphene, the structure and properties of SWCNTs can be deduced. SWCNTs can be fully described as graphene sheets rolled into a seamless cylinder so that the emerging structure is a one-dimensional (with respect to λ_{Fermi}) tube with axial symmetry. Here, the phrase "one dimensional" means that the diameter is orders of magnitude smaller (roughly 1 nm) than the length (around 1 µm) of the tube. A graphene sheet shows a honeycomb like structure and can be described with the parameters shown in Figure 2.2.

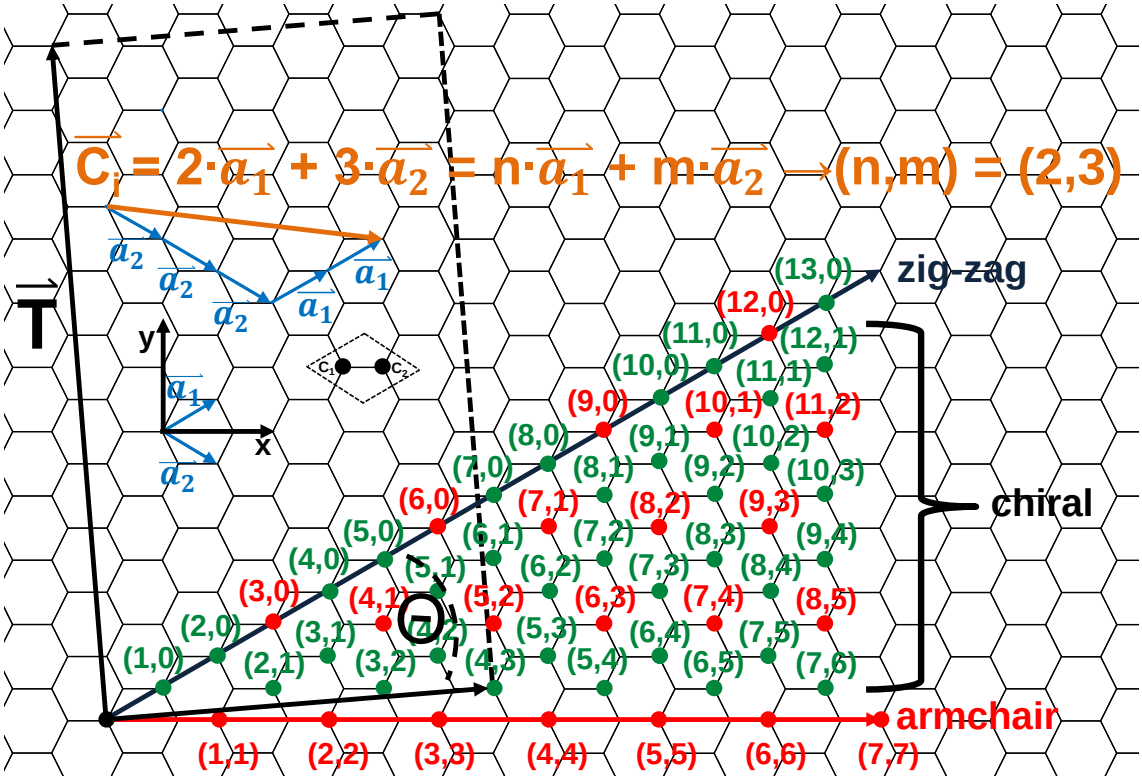

Figure 2.2. The hexagonal lattice of a graphene sheet is shown with all basic parameters that are used to describe SWCNTs. The basic vectors of the graphene lattice are shown in blue next to x- and y-axes and the two atom base of the graphene lattice (dotted black). The orange vector shows an example of how the chiral index is calculated for an arbitrary chiral vector. The possible ways to roll up the graphene sheet into a seamless nanotube are indicated by their (n,m) pair. The semiconducting SWCNTs are marked green, while metallic tubes are marked red. The nomenclature of the nanotubes according to (n,m) and their classification into armchair, zigzag or chiral species is presented. For the hypothetical (4,3)-SWCNT the chiral angle as well as the translational vector $\vec{T}$ are indicated in black.

In detail the graphene sheet possesses a hexagonal lattice with a two atom base forming the honeycomb structure. The unit vectors $\overrightarrow{a_1}$ and $\overrightarrow{a_2}$ are shown in Figure 2.2 with $|\overrightarrow{a_1}| = |\overrightarrow{a_2}| = a_0$ = 2.461 Å. Here a_0 is $\sqrt{3} \cdot a_{C-C} \approx \sqrt{3} \cdot 1.42$ Å with a_{C-C} being the distance between two neighboring carbon atoms as described in [70].The SWCNTs can be characterized by only one vector describing the path, along the circumference of the nanotube

$$\overrightarrow{C_h} = n \cdot \overrightarrow{a_1} + m \cdot \overrightarrow{a_2} \qquad with\, m, n \in Z\,. \tag{2.1}$$

This so called chiral vector $\overrightarrow{C_h}$ connects two equivalent positions within the graphene lattice, which lie on top of each other after the graphene sheet is rolled up into a SWCNT. Thus $\overrightarrow{C_h}$ is always positioned perpendicular to the tube axis and its absolute value directly gives the circumference of the SWCNT as defined. The nanotube diameter d_t is therefore also directly defined by the chiral vector $\overrightarrow{C_h}$ and the lattice constant a_0.

$$d_t = \frac{U}{\pi} = \frac{|\overrightarrow{C_h}|}{\pi} = \frac{a_0\sqrt{(m^2 + m \cdot n + n^2)}}{\pi} \tag{2.2}$$

Typical diameters of SWCNTs lie in the range of 0.7 nm up to about 2 nm depending on the production process [71].

$\overrightarrow{C_h}$ forms the unit cell of the nanotube together with the translational vector $\vec{T}$ [12, 57]. Here, $\vec{T}$ is the smallest lattice vector connecting two equivalent positions in the lattice perpendicular to $\overrightarrow{C_h}$

$$\vec{T} = \frac{((2m+n) \cdot \overrightarrow{a_1} - (2n+m) \cdot \overrightarrow{a_2})}{g} \qquad \text{and} \qquad |\vec{T}| = t, \tag{2.3}$$

where g is the greatest common divisor $(2m + n)$ and $(2n + m)$ [12] and the length of $\vec{T}$ is called the translational period t. In Figure 2.2 one can check that the translational period t of armchair and zig-zag nanotubes is $t = a_0$ and $t = \sqrt{3} \cdot a_0$, respectively [72].
When facing the hexagonal symmetry of the graphene lattice it is evident that the angle between the chiral vector $\overrightarrow{C_h}$ and $\overrightarrow{a_1}$ defines another characteristic parameter called chiral angle

$$\cos(\Theta) = \frac{\overrightarrow{C_h} \cdot \overrightarrow{a_1}}{|\overrightarrow{C_h}| \cdot |\overrightarrow{a_1}|} = \frac{2n + m}{2\sqrt{(n^2 + nm + m^2)}}. \tag{2.4}$$

The six-fold symmetry of the graphene lattice restricts theoretical considerations for Θ to values between 0° and 30° limiting n and m in the chiral index to values greater or equal to zero. The hexagonal structure although highly symmetric still allows many different ways of forming a cylinder in the diameter ranges of any of the nanotube production processes. Special names are given to SWCNTs of high symmetry as those with $(n, m = 0)$, $(\Theta = 0°)$ and with $(n, m = n)$, $(\Theta = 30°)$, which are called zig-zag or armchair tubes, respectively (see Figure 2.1 & 2.2). The names zig-zag and armchair can be visualized looking at the way the carbon atoms align along the

circumference of the SWCNT. All other existing SWCNTs with (n = arbitrary, $m \neq n \neq 0$) are called chiral.

2.4. Electronic Structure of Graphene

Following the approach of deducing the structure of SWCNTs from graphene sheets also gives access to their electronic properties. The weak van-der-Waals interactions between single graphene layers in graphite are formed by delocalized π-bonds [73]. Since these π-bonds are delocalized, they decisively determine the electronic properties of single graphene sheets. The band structure of graphene can be calculated from a tight binding approximation using the reciprocal lattice (Figure 2.3a & b) [73]. This band structure is shown in Figure 2.4 for the π-bands that match the last valence band and the first conduction band cross at the Fermi level $E_F = 0$ at six K-points of high symmetry in the lattice. This means that graphene exhibits the band structure of a metal, but it is called a semimetal [74], because the Fermi surface is limited to only six points, of which only two are inequivalent (see Figure 2.4) [73].

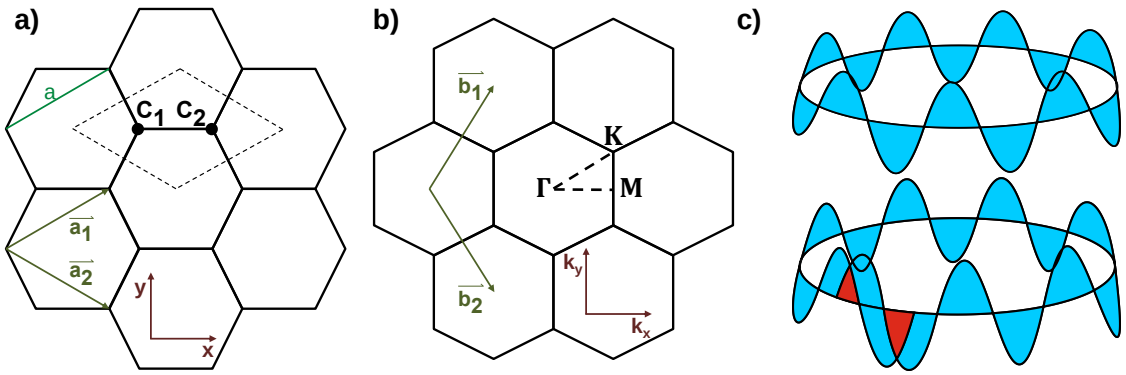

Figure 2.3. Lattice, reciprocal lattice and a scheme of waves along a circle are shown. In a) an excerpt of a SWCNT lattice is shown with its basic vectors $\overrightarrow{a_1}$ and $\overrightarrow{a_2}$ as well as a unit cell indicated by dashed lines containing two carbon atoms C_1 and C_2 . In b) the corresponding reciprocal lattice of the SWCNT is shown with its basic vectors $\overrightarrow{k_1}$ and $\overrightarrow{k_2}$. In reciprocal space the hexagons are rotated compared to normal space. For the k-space lattice also points of high symmetry are shown, namely Γ, M and K. In c) waves along a circle are shown for visualization of the periodic boundary conditions.

2.5. Zone-Folding-Method and Electronic Structure of SWCNTs

In this approach SWCNTs cannot be considered to be infinitely large spread as graphene sheets usually are in theoretical considerations. Therefore quantum mechanical restrictions for the wave functions perpendicular to the tube axis have to be regarded. Meaning periodic boundary conditions have to be matched for the Bloch waves in nanotubes

$$exp\left(i \cdot \overrightarrow{k_\perp} \cdot \vec{r}\right) = exp\left(i \cdot \overrightarrow{k_\perp}\left(\vec{r} + \overrightarrow{C_h}\right)\right), \tag{2.5}$$

which lead to

$$\overrightarrow{k_\perp} \cdot \overrightarrow{C_h} = 2 \cdot \pi \cdot q \qquad where\ q \in \mathbb{Z}. \tag{2.6}$$

Only in this form a wave can develop without cancelling itself by destructive interference (Figure 2.3c). Combining this and the relation between the circumference of the tube and $\overrightarrow{C_h}$, this leads to the expression

$$q \cdot \lambda = \left|\overrightarrow{C_h}\right| = \pi \cdot d_t \Leftrightarrow \left|\overrightarrow{k_\perp}\right| = \frac{2\pi}{\lambda} = \frac{2}{d_t} \cdot q. \tag{2.7}$$

The factor q is defined by the number of atoms N_c in the unit cell as it gives the maximum number of hubs in the non-cancelling wave. A maximum number of $\frac{N_c}{2} = N$ allowed states can be obtained by noting there are two hubs per wavelength. Therefore q is restricted as in $1 - \frac{N}{2} \leq q \leq \frac{N}{2}$ [74]. The Brillouin zone of the reciprocal lattice must be known to finally derive the electronic properties of SWCNTs. The reciprocal lattice vectors are obtained via

$$\begin{aligned} \overrightarrow{k_1} \cdot \overrightarrow{a_1} &= 2 \cdot \pi & \overrightarrow{k_1} \cdot \overrightarrow{a_2} &= 0 \\ \overrightarrow{k_2} \cdot \overrightarrow{a_1} &= 0 & \overrightarrow{k_2} \cdot \overrightarrow{a_2} &= 2 \cdot \pi. \end{aligned} \tag{2.8}$$

The vector equivalents in reciprocal space to $\overrightarrow{C_h}$ and $\overrightarrow{T}$ span each (n, m) tube's unique Brillouin zone. They are the reciprocal vectors $\overrightarrow{k_z}$ along the tube axis and $\overrightarrow{k_\perp}$ along its circumference

$$\begin{aligned} \overrightarrow{k_\perp} \cdot \overrightarrow{C_h} &= 2 \cdot \pi & \overrightarrow{k_\perp} \cdot \overrightarrow{T_z} &= 0 \\ \overrightarrow{k_z} \cdot \vec{T} &= 2 \cdot \pi & \overrightarrow{k_z} \cdot \overrightarrow{C_h} &= 0. \end{aligned} \tag{2.9}$$

Following a nanotube's axis, the one dimensionality of the carbon nanotubes allows to approximate it as infinitely long and therefore the wave vector $\overrightarrow{k_z}$ can adopt continuous values [73], whereas $\overrightarrow{k_\perp}$ is quantized as in equation (2.6). The first Brillouin zone extends from $-\frac{\pi}{t} \leq \left|\overrightarrow{k_z}\right| \leq \frac{\pi}{t}$ in z-direction and consists of q lines of allowed k-states parallel to the z-axis separated by $\left|\overrightarrow{k_\perp}\right| = \frac{2}{d}$.

In the zone folding approximation it is decisive for the electronic character of the carbon nanotube, whether one of graphene's six K-points is in contact with allowed $\overrightarrow{k_\perp}$-values. If the allowed k-values comprise the K-point as for example in the (9,0) nanotube (see Figure 2.5) the tube exhibits a metallic behavior, since contact between the valence band and the conduction band is still established after applying the quantum mechanical constraints. For an overall statistical consideration whether a nanotube is metallic or semiconducting the conditions under which the K-points of graphene fall onto allowed $\overrightarrow{k_\perp}$-values can be evaluated. The K-points of the reciprocal lattice are found at $\vec{K} = \frac{1}{3}(\overrightarrow{k_1} - \overrightarrow{k_2})$, which results, combined with the periodic boundary condition, in

$$\vec{K} \cdot \overrightarrow{C_h} = \frac{1}{3}\left(\overrightarrow{k_1} - \overrightarrow{k_2}\right) \cdot (n\overrightarrow{a_1} - m\overrightarrow{a_2}) = \frac{2\pi}{3} \cdot (n - m). \tag{2.10}$$

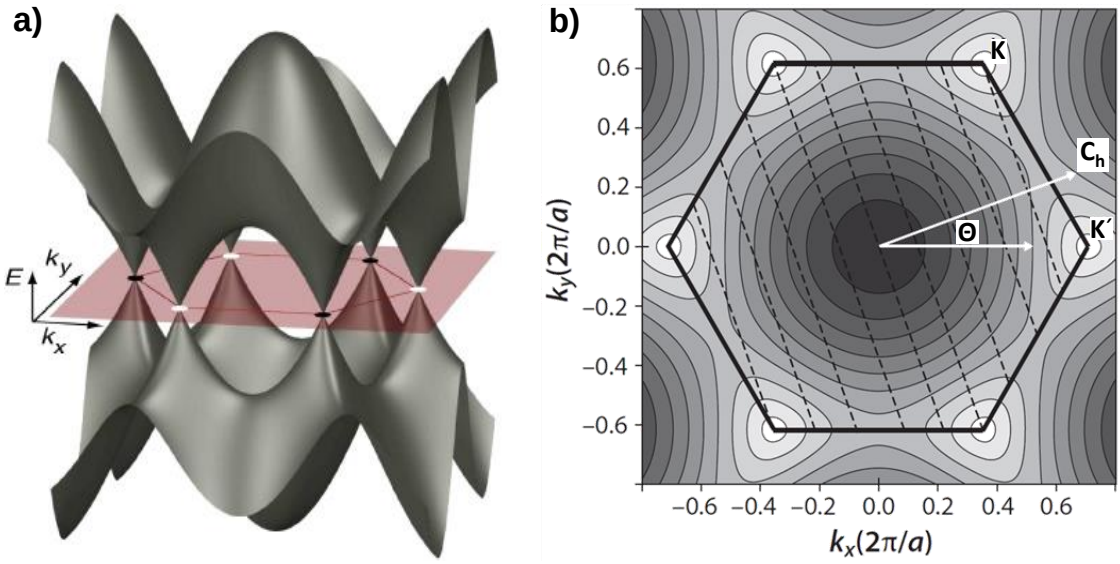

Figure 2.4. Dispersion relation of graphene. In a) a three-dimensional representation of the electronic dispersion relation of graphene is shown. In b) the first Brillouin zone of graphene is superimposed with the allowed k-vectors (dashed lines) of a metallic SWCNT. Taken from [75, 76], respectively.

Only the nanotubes with a chiral index (n, m) that fulfills the condition

$$\frac{(n-m)}{3} = q, \text{ where } q \in \mathbb{Z} \tag{2.11}$$

are metallic. The other way around this means that $2/3$ of all possible nanotubes are semiconducting, whereas the other third is of metallic character.

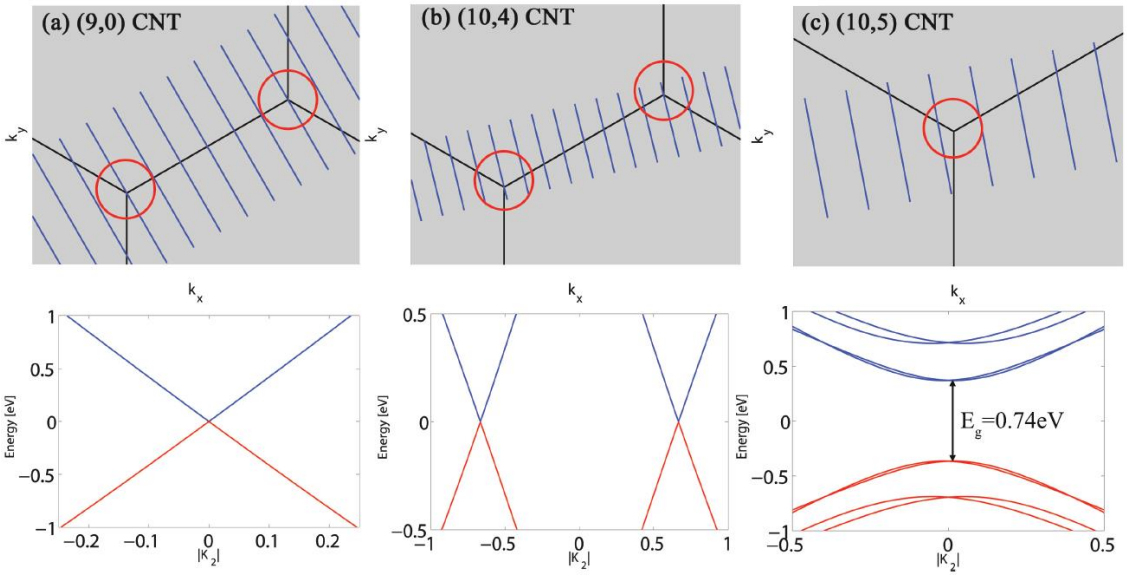

Figure 2.5. Allowed k-states for different nanotubes. The first Brillouin zone of a) a zig-zag (9,0), b) metallic chiral (10,4) and c) semiconducting chiral (10,5) along with the resulting energy dispersion for the respective SWCNTs. Taken from [77].

In the case of semiconducting SWCNTs or in mathematic terms where $(n - m)$ is not a multiple of three, a value of $\frac{2}{3d_t}$ is obtained for the closest misalignments of allowed $\overrightarrow{k_\perp}$ to the K-points. This results in a bandgap of [73]

$$E_g = 2 \cdot \left(\frac{\partial E}{\partial k}\right) \cdot \frac{2}{3d_t} \approx \frac{2a_{C-C}\gamma_0}{d_t} \approx \frac{0.7\ eV}{d_t(nm)}. \tag{2.12}$$

With γ_0 (≈2.9 eV) being the transfer integral between first neighbor π orbitals used in the tight-binding derivation of the energy dispersion of graphene.

2.5.1. Density of States

The density of states (DOS) $n(E)$ is the number of available states ΔN in a given energy interval ΔE with $\Delta E \rightarrow 0$. A one-dimensional system with energy bands that can be approximated by a parabolic shape near its extrema consists of singularities, where $n(E) = \frac{1}{\sqrt{E}}$ [73]. Those singularities, called van Hove singularities (VHS), are important for the physical properties of SWCNTs. The density of states can be obtained from

$$n(E) \propto \sum_i \int dk \delta(k - k_i) \left|\frac{\partial E_i^{\pm}}{\partial k}\right|^{-1}, \tag{2.13}$$

where the $E_i^{\pm}$ are the eigenvalues originating from the tight-binding calculations for graphene and the k_i result from the equation $E - E_i^{\pm}(k) = 0$ [74]. At VHS the density of states exhibits a maximum, which for example increases the probability for optical absorption, if a photon matches the energy difference between VHS in the valence and conduction bands [73].

2.5.2. Optical Properties

Spectroscopic methods are powerful tools in order to precisely determine the chirality of SWCNTs. Absorption and Raman spectra are directly related to the electronic band structure of SWCNTs and can be performed without damaging the SWCNTs. Optical processes start with the absorption of a photon, which excites an electron into a higher state. Due to the SWCNT's absorption of light in the visible spectrum, suspended SWCNTs even show distinct colors depending on the present nanotube enrichment [78].

2.5.3. Absorption of Photons

Electronic states accumulate in the VHS, which as a consequence dominate optical absorption of SWCNTs. To describe optical properties of carbon nanotubes after excitation of one electron by a photon one assumes an electron transition between two VHS (see Figure 2.6a).
Excitations perpendicular to the tube axis are strongly suppressed due to depolarization fields [79]. Absorption of light polarized parallel to the tube axis must fulfill the condition $\Delta m = 0$ with m being the azimuthal quantum number [71]. Therefore optical transitions occur mostly between sub-bands of the same $|m|$ resulting in distinct transition energies E_{ii}, where $i \in \mathbb{N}$.

Possible transitions are shown in Figure 2.6a. Transitions between the lowest energy (first from Fermi level) VHS in the valence and conduction band are indicated by E_{11}. Higher order transitions are named analogously. To analyze spectra of absorption energies and Raman shift the so called Kataura plot is inevitable.

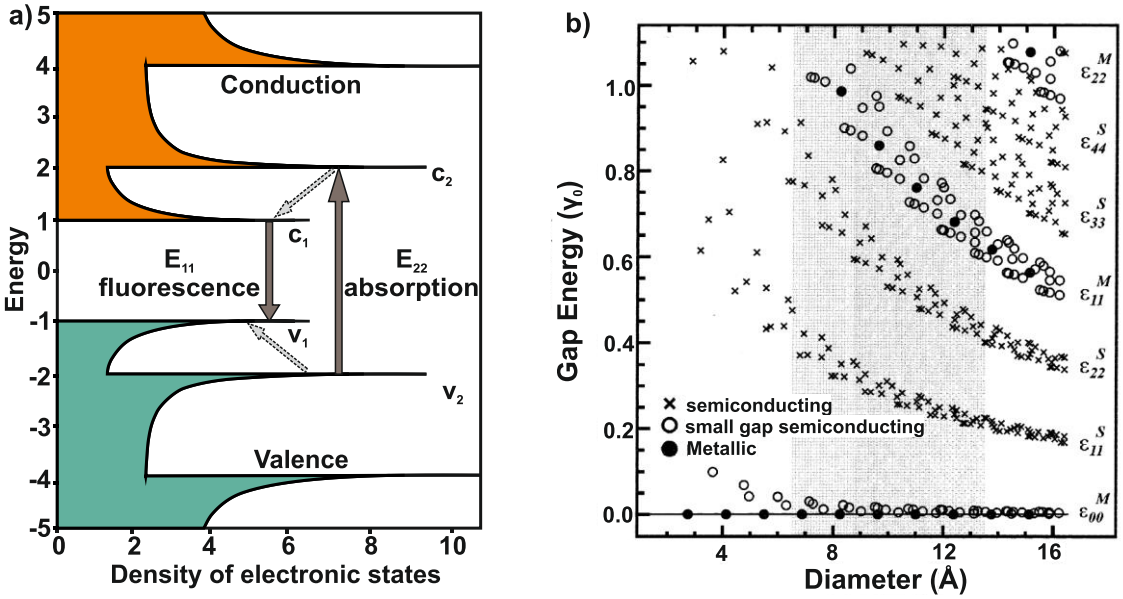

Figure 2.6. Optical transitions between VHS of SWCNTs and the Kataura plot. a) A schematic DOS for a single semiconducting SWCNT. Optical excitations are marked by dark gray arrows and non-radiative relaxations are marked by dashed light gray arrows. b) Kataura Plot: Gap energies for symmetric interband transitions in SWCNTs as a function of their diameter. The grey shaded area marks the diameter range of HiPco SWCNTs. Modified from [56, 80], respectively.

This Kataura plot shows the transition energies $E_{ii}(d_t)$ between the mirror symmetric VHS in dependence of the tube diameter d_t (Figure 2.6b) for both metallic as well as semiconducting SWCNTs. Since raw SWCNTs are featured in this thesis, a great variety of SWCNTs with diverse chiralities and therefore different absorption lines is contained. Interaction with their surrounding e.g. in form of bundling and their natural line width surfactants lead to a broadening of the absorption peaks in absorbance spectra [81].

2.5.4. Raman Spectroscopy

Raman scattering is the name for inelastic scattering of light by emission or absorption of one optical phonon in honor of C. Raman [82]. Raman spectra reveal the phonon frequencies of a given material by measuring the intensity of the scattered light as a function of energy loss. If the incoming photon's energy is close to an electronic transition the Raman intensity is greatly enhanced, which is called resonant Raman scattering. The VHS of SWCNTs lead to an even greater intensity of the measured signal, meaning for nanotubes it is possible to examine different chiralities and measure their characteristic Raman spectrum. It was shown that resonant Raman spectroscopy is a very sensitive characterization tool for SWCNTs [83-88].

Important Raman Modes of SWCNTs

The most important Raman modes of SWCNTs are the radial breathing mode (RBM) and the G-band. For further evaluation of SWCNT material also the D-mode must be considered as it is linked to structural defects. These optical features of SWCNT will be discussed shortly in the following.

The RBM is a low frequency mode that corresponds to a collective vibration of the nanotube in radial direction. This can be visualized as a periodic increase and subsequent decrease in diameter of the SWCNT as illustrated in Figure 2.7. This vibration is unique for each chirality SWCNT. Typical values are 130 - 350 cm^{-1} when focusing on nanotube diameters of SWCNTs used throughout this thesis (0.7 and 1.8 nm).
To investigate the chirality or the diameter distribution in a given sample of SWCNT the relation of the RBM to the diameter must be known [89]

$$\omega_{RBM} = \frac{A}{d_t} + B, \tag{2.14}$$

where the parameters A and B are empirically determined parameters. Values of $A = 215$ cm^{-1} and $B = 18$ cm^{-1} were reported for dispersed [90] and $A = 248$ cm^{-1}, $B = 0$ cm^{-1} for substrate bound SWCNTs [91].
To excite the RBM of a given SWCNT the exciting laser's energy has to match the S_{22} transition of a semiconducting or the M_{11} transition of a metallic SWCNT (lasers in the visible spectrum).

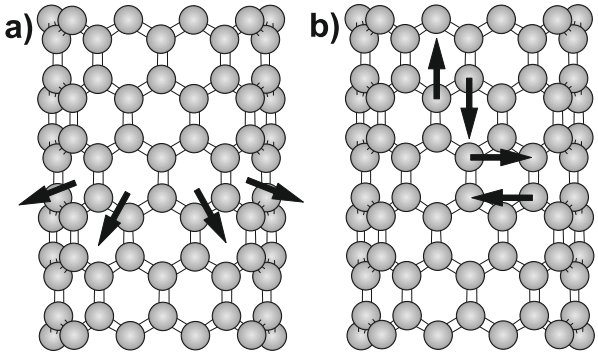

Figure 2.7. Carbon atom vibrations leading to distinct excitation modes in SWCNTs. In a) the RBM vibration and in b) the G^+ and G^- modes are presented for better visualization of the vibrational proceedings within the nanotube during Raman spectroscopy.

The high energetic G-band corresponds to a tangential vibration of two carbon atoms as indicated in Figure 2.7 leading to Raman shifts of 1550 - 1600 cm^{-1} [92]. For SWCNTs in contrast to graphene, the G-band is split into two components called $G^+$and G^- due to vibrations along the nanotube axis (longitudinal optical phonons) or along the circumference (transversal optical phonons), respectively. The G-band peaks depend onto the chirality of the nanotube but the exact relation is not yet fully understood. However, a Breit-Wigner-Fano line shape of the G-band is

considered an indicator for a metallic SWCNT. A Lorenz profile is associated with a semiconducting SWCNT (Figure 2.8).

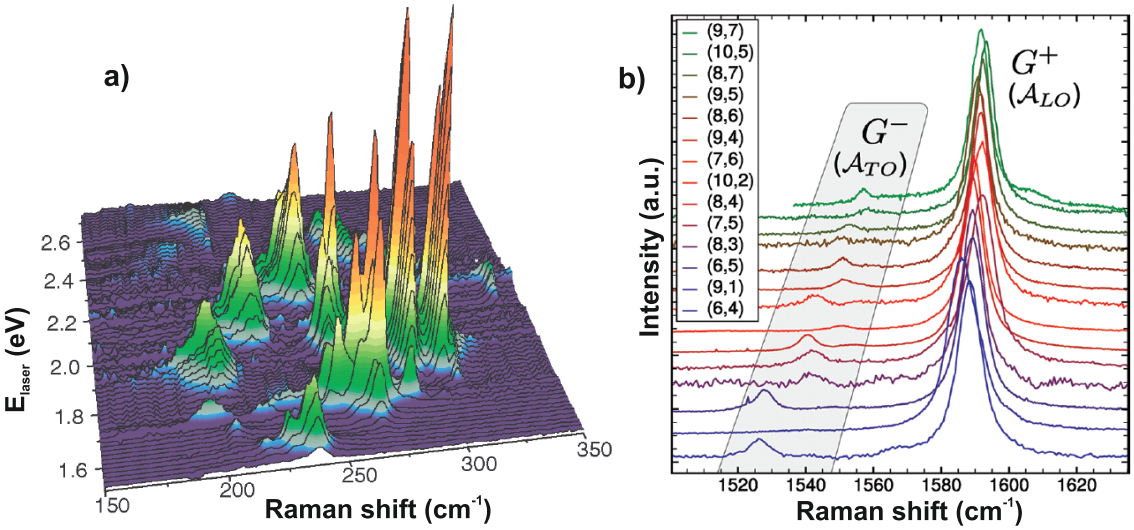

Figure 2.8. Typical Raman spectra for SWCNTs. In a) the RBM of small diameter SWCNTs dispersed in aqueous SDS are shown while in b) the G-modes of different small diameter nanotubes are shown with their respective chiral index. Both the RBM as well as the G^- modes are shown to depend strongly on the excited SWCNT. Modified from [81] and [93], respectively.

The *D*-mode is excited, when an electron is resonantly scattered twice, first at a phonon but also at a defect site. The *D*-mode is therefore correlated to the number of defects in the SWCNT. Typical values for the *D*-mode in SWCNTs are around 1350 cm^{-1}. Defects include for example vacant spaces in the lattice, or non-carbon atoms that were incorporated in the SWCNT structure [94]. The ratio between the intensity of the *D*-mode and the *G*-mode is often used as indication for the crystallinity of the SWCNT [63].

2.6. Centrifugation

This section gives an overview over established theoretical considerations of centrifugation experiments including sedimentation theory and density gradient centrifugation.

The basic principles of centrifugation rely on the exerting of centrifugal forces onto particles dispersed or dissolved in liquid media.

In case of a liquid medium containing dispersed high density particles, the sedimentation of each particle can be described following the theoretical considerations in section 2.6.1. It is derived that each particle's sedimentation velocity depends mostly on particle size.

The case, where the particles are dispersed in liquid media that contain dissolved high density media is the basis for density gradient centrifugation. The centrifugal forces urge the dissolved high density medium to gradually build a density gradient during centrifugation. The dispersed particles follow their sedimentation directed to the bottom of the centrifugation vessel (Swinging

bucket rotors) as long as the density of the dispersed particles is greater than the density of the surrounding medium. The formation of a density gradient is a continuous process, which takes place at the same time as the particles are following their respective isopycnic point, which is the point that matches the particles' buoyant density. Balanced forces of diffusion, friction and of the centrifugal field lead to the state, in which the gradient's form is not changing further. This state is called equilibrium state of the gradient. By choosing sophisticated layering of the density medium prior to centrifugation and compatible centrifugation times, dynamic (non-equilibrium) gradients have proven to be suitable for effective separation of particles including SWCNTs [34, 35, 95-100] by density. This is described in section 2.6.2.

2.6.1. Svedberg's Simplified Theory

In this section a short introduction into the theory of preparative centrifugation will be presented. At first the mechanical theory based on the work of Svedberg is shown to illustrate the sedimentation of particles, followed by a thermodynamic approach leading to the famous Lamm equation describing the gradient formation of density media as in [44].
There are three forces present in the centrifugation cell (see Figure 2.9) that influence dissolved or dispersed particles. The centrifugal force, generated by the spinning of the rotor, acts radially against the buoyant force and the frictional force for each particle. All forces act either radially or inversely radial eliminating the need for a vector description. The centrifugal acceleration $\omega^2 \cdot r$ induces a centrifugal force of

$$F_c = \omega^2 \cdot r \cdot m_p, \qquad (2.15)$$

where m_p is the mass of the particle, ω is the angular frequency and r is the distance of the particle from the rotational axis.

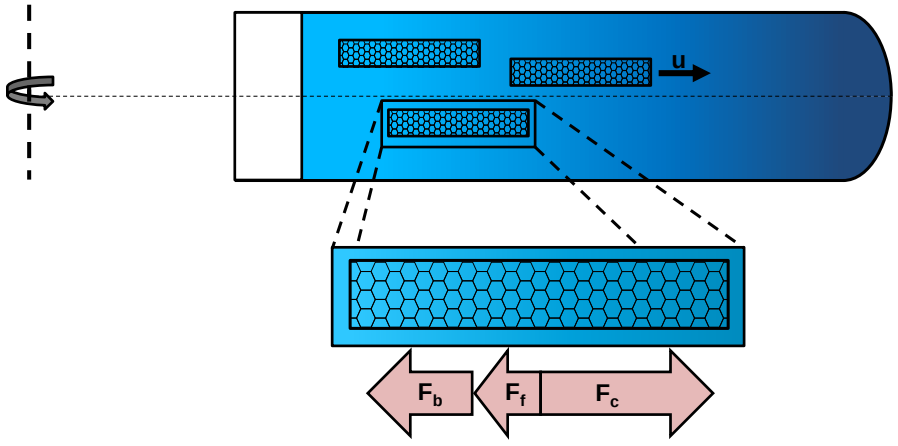

Figure 2.9. Forces acting on SWCNTs (black rods) during centrifugation in a density medium. Within a density gradient the particles are drifting towards their isopycnic points. The centrifugal force urges the particles towards the outside of the rotation, which is the bottom of the centrifugation tube. The frictional and buoyant forces act against this movement until the particle has found the place of matching density in the gradient. Once the forces match the movement is not further accelerated. But since the gradient building density medium is also shifting, the process is dynamic until the gradient reaches an equilibrium point and the particles have found their isopycnic points.

The centrifugal force increases linearly with r and is partially matched by the buoyant force, which acts according to Archimedes

$$F_b = -\omega^2 \cdot r \cdot m_{dm}, \tag{2.16}$$

where m_{dm} is the mass of the particle's surrounding density medium that is displaced by the particle. The frictional force matches another part of the centrifugal force. The frictional force is proportional to the sedimentation velocity u of the particle

$$F_f = -f \cdot u. \tag{2.17}$$

Here the frictional coefficient is represented by f. Equilibrium is reached, when the forces balance

$$F_c = -F_f - F_b. \tag{2.18}$$

In this case the sedimentation velocity is not accelerated further.

After expressing the mass of the dissolved density medium m_{dm}, which is displaced by the particle, as the product of the volume of the particle and the density ρ_{dm} of the density medium in equation 2.18, one obtains inserting (2.15), (2.16) and (2.17)

$$\frac{V_p(\rho_p - \rho_{dm})}{f} = \frac{u}{\omega^2 \cdot r} \equiv s. \tag{2.19}$$

Here the sedimentation coefficient s was defined for sedimentation analysis independent of the angular velocity. Now following Einstein's theory for spherical particles the frictional coefficient relates to the coefficient for diffusion D according to

$$f = (6 \cdot \pi \cdot \eta \cdot r_p), \tag{2.20}$$

where η is the kinematic viscosity of the density medium. Using $V_p = \frac{4}{3}\pi {r_p}^3$ leads to

$$r_p = \sqrt{\frac{9 \cdot \pi}{2 \cdot \omega^2 \cdot r} \cdot \frac{\eta \cdot u}{(\rho_p - \rho_{dm})}} \quad \text{or} \quad u = \frac{2}{9 \cdot \pi} \cdot \omega^2 \cdot r \cdot \frac{(\rho_p - \rho_{dm})}{\eta} \cdot r_p^2. \tag{2.21}$$

This way the actual sedimentation velocity of the particles can be related to three main factors: The centrifugal force, the viscosity as main aspect of the diffusion coefficient in the density medium and the size of the dispersed particles [101].
The sedimentation velocity depends mainly on the size of the particles. If the centrifugal force exerted onto the particles is increasing the sedimentation velocity also increases proportionally as direct result. Usually a constant centrifugal field is applied. A direct influence is also given through the viscosity of the density medium. The lower the viscosity, the faster the particles sediment to the bottom of the centrifugation vial. That also means that temperature, which has an influence on the viscosity as well as diffusion itself, influences the sedimentation velocity.

2.6.2. Density Gradient Formation

The thermodynamic part of preparative (ultra)centrifugation theory is used to describe the change of the gradient medium concentration as a function of time and the radial position within the centrifugation tube [102, 103]. A volume element dV in an ultracentrifugation cell, which rotates at an angular velocity ω, is considered to derive the mass transport due to sedimentation. This volume element extends from r to $r + dr$. The transported mass through a given surface per unit time by sedimentation is given by the product of the surface area, the sedimentation velocity u and the concentration of the solute. As mentioned above the centrifugal acceleration scales with the radial distance according to $\omega^2 \cdot r$. The area within a centrifuge tube is given by $\pi \cdot z^2$. Here z is the radius of the tube. The sedimentation velocity was defined as $u = s \cdot \omega^2 \cdot r$, leading to a sedimentation caused mass change per unit time of

$$\frac{dm_s}{dt} = c \cdot \pi \cdot z^2 \cdot u = c \cdot \pi \cdot z^2 \cdot s \cdot \omega^2 r. \tag{2.22}$$

The second mass transport mechanism is captured in Fick's first law[44].

$$\frac{dm_D}{dt} = -D \cdot \pi \cdot z^2 \cdot \frac{\partial c}{\partial r}, \tag{2.23}$$

where D is the coefficient for diffusion and $\frac{\partial c}{\partial r}$ is the concentration gradient along the radius. The net mass transport across the surface at a certain radial position r per unit time is obtained when combining equations (2.22) and (2.23)

$$\frac{dm}{dt} = \pi \cdot z^2 \left(cs\omega^2 r - D \cdot \frac{\partial c}{\partial r}\right). \tag{2.24}$$

The quotient of the change in mass per unit time $\frac{dm}{dt}$ and volume element dV gives the change of the concentration in each volume element

$$\frac{\partial c}{\partial t} = \frac{\frac{dm}{dt}}{dV} = \frac{dm}{dt} \cdot \frac{1}{\pi z^2 \partial r}. \tag{2.25}$$

The following expression for the change in concentration with the radial position r

$$\frac{\partial c}{\partial t} = \frac{\partial}{dr}\left(D \frac{\partial c}{\partial r} - cs\omega^2 r\right), \tag{2.26}$$

leads to the Lamm equation [104] by assuming that D and s are independent of the radial position

$$\frac{dc}{dt} = D\left(\frac{\partial^2 c}{\partial r^2}\right) - s\omega^2\left(c + r\frac{\partial c}{\partial r}\right). \tag{2.27}$$

Any experiment performed in a preparative ultracentrifuge can be described by this general differential equation. When equilibrium between diffusion and sedimentation of the binary mixture, forming the density gradient, is reached, the gradient has attained its final form.

2.6.3. Hermans-Ende Theory

In order to understand how density profiles evolve during centrifugation experiments it is necessary to understand the equilibrium form of a gradient. This problem of describing the density profile of a gradient was addressed by Hermans and Ende in 1963 [105]. This theory has been extended in [102, 106, 107] and gives

$$\rho(r) = a + b \cdot exp(c \cdot r^2), \tag{2.28}$$

hinting an exponential increase of the density with the radius. Density profiles of any initial form tend to reach this exponential shape during centrifugation.
Parameters a, b, and c are radius independent constants taking real mixtures into account. The parameters can be obtained empirically by using density markers as for example in [102], where 11 markers were used to generate the profiles of seven Metrizamide gradients resulting in a set of parameters a, b, and c for this density medium.

2.7. Analytical Ultracentrifugation (AUC)

An analytical ultracentrifuge is an ultracentrifuge equipped with one or multiple optical detection systems. Those systems allow the detection of the sedimentation process taking place in the centrifuge [44]. Three different components are part of this system, the centrifuge itself, the rotor with the measurement cells and the optical detection system synchronized with the rotational frequency. A typical double slit measurement cell is shown in Figure 2.10a.

2.7.1. Absorption Optics AUC

When light passes through a solution with light absorbing particles it loses intensity summarized mathematically in Lambert-Beer's law [44]

$$A = \lg\left(\frac{I_0}{I}\right) = \varepsilon \cdot c \cdot d. \tag{2.29}$$

Here A is the absorbance, I the Intensity of light after the sample, the initial intensity I_0 and the extinction coefficient ε as well as d the thickness of the measurement cell. Figure 2.10b shows the setup of the absorbance spectroscopy ultracentrifuge schematically. A Xenon flash lamp releases µs light pulses that travel through the sample cell so that the intensity of the coming out light can be detected. The light flashes are triggered via a Hall-effect sensing device based on a magnet placed at the bottom of the rotor. Distinct wavelengths are selected by adjusting a grating in the range of 200 – 800 nm. Below the rotor, a movable lens-slit assembly is placed to focus the light onto a photomultiplier tube for radial positions that can be adjusted in 5 µm steps [44].

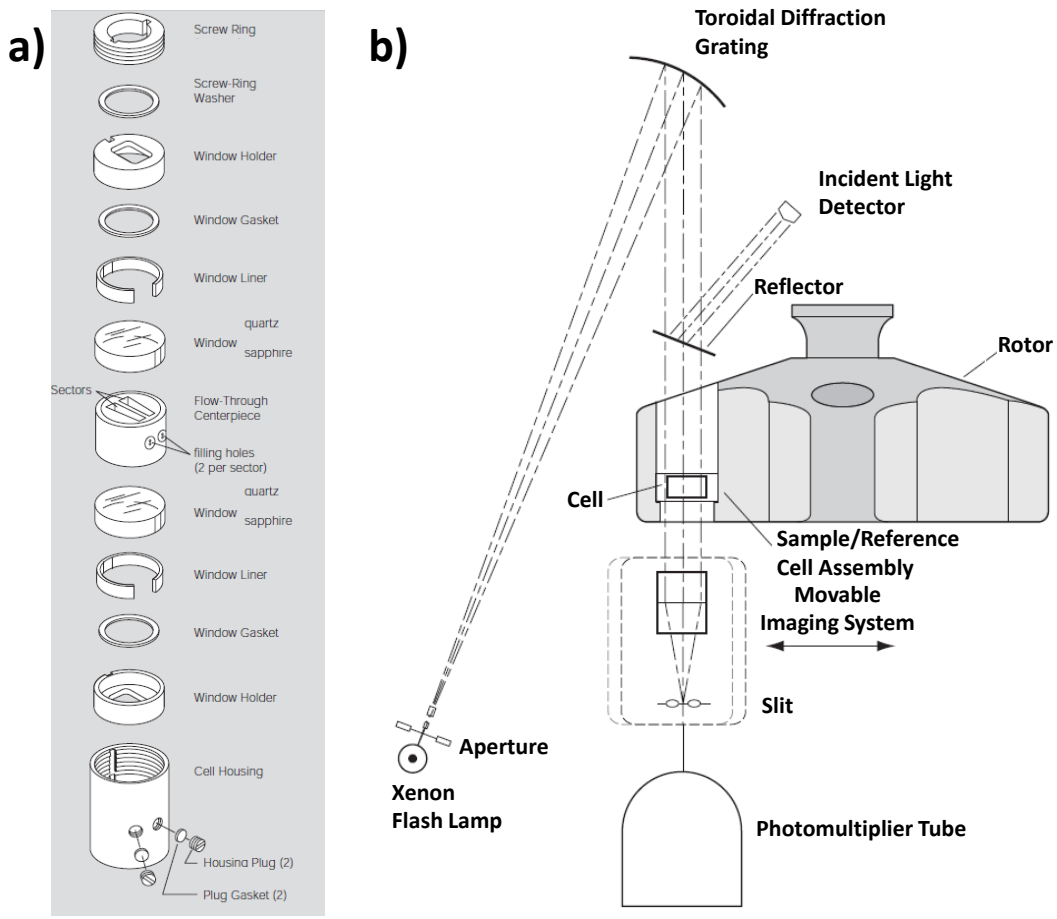

Figure 2.10. Assembly of absorption AUC and a single measurement cell are shown. In a) the assembly of a standard two chamber sector cell is shown. One chamber is used for the sample while the other contains the solvent as reference material. In b) a scheme of the absorbance optics AUC is presented. Light from a Xenon flash lamp is diffracted in a monochromator resulting in single wavelength that can be used to evaluate the sample. The radially movable imaging system focuses the light from certain points under the sample onto a detection system (photomultiplier). Pictures modified from [108].

2.7.2. Interference Optics AUC

In contrast to an ultracentrifuge equipped with absorbance optics, the interference system makes use of a laser diode set-up (675 nm). Here the light is directed in two parallel ways through the measurement cell (double sector cell). One beam is directed through the sample sector while the other one passes through the reference sector. The fact that the velocity of light depends on the refractive index of the medium it passes through leads to an interference pattern, when the beams are superimposed after passage through the cells. This pattern is proportional to the refractive index, which in turn is proportional to the concentration. The interference pattern is taken along the radial direction in the cell and consists of dark and light fringes in the plane of the CCD detection system (Double Slit experiment). The shift in stripes is counted in numbers of fringes $J(r)$. Via

$$J(r) = \frac{d \cdot \left(\frac{dn}{dc}\right)}{\lambda} \cdot c(r), \tag{2.30}$$

the concentration can be determined if the refractive index increment is known. Experimentally this can be achieved with high precision by testing a known concentration while recording the shift in fringes [44].

2.8. Mechanism behind Dispersing Nanotubes

A multitude of methods to separate SWCNTs according to electronic type has been reported already [25, 26, 29, 39]. Those methods rely on sonication to disperse SWCNTs, followed by subsequent centrifugation. This is because addressing the problem that SWCNT synthesis processes commonly result in a preponderance of non-nanotube carbonaceous material as well as residual metal catalyst impurities can be easily achieved by brief centrifugation of a dispersion as the sedimentation velocity depends mainly on particle size. The following paragraphs will give insight into the mechanism behind preparing stable dispersions of the highly hydrophobic SWCNTs in water.

2.8.1. Surfactants

To enable post-synthesis purification methods for SWCNTs the established procedure is based on the preparation of a stable dispersion of SWCNTs in water. However, all approaches are limited by the practical insolubility of SWCNTs in aqueous or organic solvents. The high polarizability and smooth surfaces cause SWCNTs to form bundles, where the SWCNTs are aligned parallel through high van-der-Waals forces [109, 110]. A popular route to overcome this limitation is to disperse carbon nanotubes in solvents by the use of amphiphilic surfactant molecules or polymers. Sodium dodecyl sulfate (SDS) and sodium dodecylbenzene sulfonate (SDBS) are widely used surfactants to disperse SWCNTs in water [27, 48, 55, 111]. Bile salt detergents such as sodium cholate (SC) or sodium deoxycholate (SDOC) are extremely efficient in individualizing single SWCNTs and show highly resolved optical absorption spectra [112-114].

Ultrasonication is applied to the raw SWCNT powder in aqueous surfactant systems to exfoliate the bundles of SWCNTs. The process of nanotube exfoliation is schematically shown in Figure 2.11b. The surfactants adsorb onto the SWCNTs surfaces and self-organize into supramolecular structures [24, 54, 115, 116]. Resulting from the dispersant adsorption is a lower buoyant density for the dispersant-SWCNT complex in comparison to bare SWCNTs. Different chiralities of SWCNTs lead to slightly different self-organized dispersant structures on the SWCNT surfaces [97]. Molecules that contain aromatic groups can form $\pi - \pi$ stacking interactions with the surface of carbon nanotubes. SDS and SDBS were shown to exhibit a similar behavior towards SWCNTs [117]. SDS and SDBS differ by the phenyl ring attached to SDBS (Figure 2.11a) making SDBS more effective as dispersant for SWCNTs. The structures of SDS, SDBS and the bile salt detergents are also shown in Figure 2.11a.

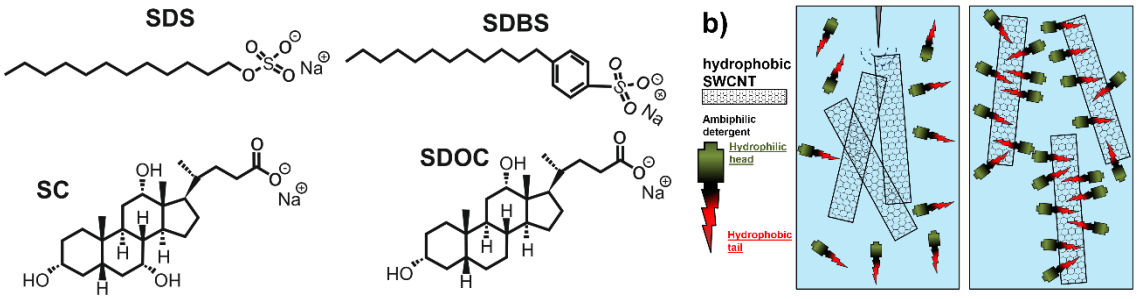

Figure 2.11. Various surfactant structures and a scheme of the exfoliation process of SWCNTs in water are depicted. In a) the structure of SDS, SDBS, SC and SDOC are presented. In b) the exfoliation process is illustrated schematically. The ultrasonication waves are indicated by dashed lines and the surfactant molecules are depicted with a green hydrophilic head and a red hydrophobic tail. On the left one can see the intact nanotube bundle with surfactant molecules surrounding the bundle. On the right the nanotubes have loosened due to the ultrasonication and surfactant molecules have attached to the newly opened surface, which results separated and stabilized SWCNTs by the surfactant molecules.

The effectivity of SC and SDOC in stabilizing individualized SWCNTs is attributed to the forming of homogeneous, stable micelles around the SWCNTs [118].

2.8.2. Polymeric Dispersants

Many surfactants have been evaluated under different conditions. With respect to electronic type separation of SWCNT, especially the pH-value has stepped into focus [51, 52, 119-121]. The pH is believed to induce an ongoing protonation of SWCNTs the more acidic the environment is. The protonation is starting with the metallic ones owing to their higher polarizability [122, 123]. Subsequently the small bandgap semiconducting ones are protonated and lastly the species with the largest bandgap. This protonation leads to less detergent adsorption onto the surface as fewer electrons are available for $\pi - \pi$ interaction [51, 121]. The high efficiency surfactants SC and SDOC are prone to flocculation under acidic pH values. This is one example why a search for stable dispersing agents exists. Custom designed polymers have evolved into a dispersing class that combines effectivity with stability under many desired conditions.

Polymer Wrapping

Large molecular size polymers adsorb differently onto the surface of SWCNTs compared to small surfactant molecules. Helical wrapping of long chained polymers (poly(phenylacetylene)) around SWCNTs was reported in 1999 [124]. Several reports of polymers in parallel alignment along the SWCNT axis have followed [125]. These configurations were found to be resulting from the stiffness of the polymer backbone with flexible backbone polymers more likely for helical wrapping [126] and stiff backbone polymers preferring the parallel alignment [127]. This was not only experimentally observed but can be simulated considering the binding energy between the polymer and the SWCNT for different constellations [128]. It was even shown that specific polymers favor exact curvatures in SWCNTs and therefore preferentially disperse certain chirality/diameter nanotubes [129, 130].

2.9. Transistors

Dekker et al. demonstrated the first SWCNT-FETs in 1998 at Delft University [131], soon followed by US groups at IBM [132] and Stanford University [133]. SWCNTs as active channel material in FETs can serve as p-type or an n-type semiconductor, with ballistic transport properties and mechanical robustness. SWCNTs are deposited onto substrates as individual tubes or networks of percolated tubes with few nanometer in thickness. Therefore FETs based on SWCNTs are best described as thin-film transistors (TFTs). To use carbon nanotubes as active semiconductors in TFTs, the SWCNTs are usually contacted with metal electrodes to apply operation voltages and carry current to the tubes. An issue arising from the metal electrode/SWCNT interface is the formation of a Schottky barrier due to differences between the metal's work function and the Fermi level of the SWCNTs. The height of the Schottky barrier for electrons or holes determines whether electron or hole transport is favorable. Therefore this depends on the relative height of the metal's work function compared to the Fermi level of the SWCNT. The layout of the gate electrode and dielectric significantly alters the behavior of a SWCNT-FET. In planar bottom or top gate architecture the SWCNT cannot experience the same electric field as for example in a top gate or wrap around gate configuration due to the thickness of SWCNT networks. Wrap gate configuration is also one possibility to passivate the channel and thus reduce the hysteresis while effectively gating the SWCNTs in the FET [134]. Alternative gating methods are for example the use of Ionic gels, which have high intrinsic capacitance and, as consequence, enable low voltage operation. The final part of this thesis is the use of semiconducting SWCNTs as active material in field-effect transistors (FETs). This section will give a short introduction into the mode of operation of carbon nanotube network based field-effect transistors.

2.9.1. Charge Transport in SWCNTs

It was shown that the allowed electronic states for SWCNTs are very limited compared to those of bulk graphite. Theoretically, the charge transport in SWCNTs follows a ballistic nature at low temperatures as generally described for 1D-quantum wires. In a quantum wire, the mean free path of charge carriers exceeds the individual tube length [57]. This means that the conduction for SWCNTs takes place in well-separated discrete electron states without resistance by inelastic scattering by phonon-electron interaction or present defects [14]. For metallic SWCNTs the mean free path can be more than several µm and for semiconducting SWCNTs around 300 nm have been found [135]. Assuming that ohmic contacts were established between the electrodes and the carbon nanotube, the current I through a nanowire in the ballistic regime is given by

$$I = \frac{2e^2}{h} M \frac{(\mu_1 - \mu_2)}{e}, \qquad (2.31)$$

where the μ_i are the chemical potentials of the connected electrodes. M is the number of conduction channels for an electron of wave vector $k > 0$. The conductance G of the nanowire is given by

$$G = \frac{2e^2}{h} M. \quad (2.32)$$

Two fold band degeneracy at the Fermi level leads to two conduction channels per SWCNT [73], which yields an ideal quantum resistance per nanotube of

$$R_{qNt} = \frac{h}{4e^2} = 6.5\ k\Omega. \quad (2.33)$$

If the distance between the electrodes exceeds the mean free path of a charge carrier, ballistic transport cannot take place. Outside of the ballistic region the resistance of a nanotube scales with length and depends on parameters such as diameter or defect density. The resistance outside of the ballistic region therefore covers a range from R_{qNt}= 6.5 kΩ to several MΩ for very long SWCNTs [136]. At low temperatures (ballistic) single nanotube transistors with mobilities up to 100,000 cm²/Vs and at room temperature mobilities of up to 10,000 cm²/Vs have been demonstrated. An empirical relation between the zero field mobility and temperature as well as nanotube diameter has been found

$$\mu(d_t, T) = \mu_1 \left(\frac{300[K]}{T}\right) \left(\frac{d_t}{1[nm]}\right)^{\alpha}, \quad (2.34)$$

where μ_1= 12,000 cm²/Vs and α = 2.26. The zero field mobility depends on the diameter of the nanotube d_t mainly due to decreased scattering events in larger diameter nanotubes [137].

2.9.2. Charge Transport in Networks of SWCNTs

Experimentally, this thesis covers the electronic properties of SWCNT networks formed by many individual SWCNTs. A carbon nanotube ensemble placed on a substrate is considered a network once a percolation path between two separated contacts is established. The contacts in this thesis are in general spatially separated by a length exceeding those of individual nanotubes. Therefore ballistic transport is not expected. The charge transport of SWCNT network is governed by the number of percolation paths and intertube contacts, which are energetic barriers for charge transport. Those barriers result in resistance contributions up to MΩs, depending on the nanotube diameter, orientation and possible surfactant coverage on individual nanotubes. In addition to the intertube barriers, Schottky barriers between the nanotubes and the electrodes contribute to the total resistance.

In the case of very long channel length compared to the length of the individual tubes, the electrode nanotube Schottky barriers can be neglected [138]. Also for example, Gold or Palladium contacts have been proven to deliver nearly ohmic contacts [73, 139] due to work functions near the fermi level of SWCNTs. Pd is a noble metal with a high work function of $\Phi_m \sim 5.2\ eV$ in vacuum [73]. This enables contacts with small energetic barrier to the valence band of SWCNTs with diameters greater than 1.6 nm ($E_g < 0.6\ eV$) [73, 140]. In such a case the conductivity of the network is governed by the intertube junctions [141]. Since semiconducting nanotubes are intended for the networks, the focus is directed on the barrier between two semiconducting SWCNTs of different bandgaps. The work functions of the semiconducting

SWCNTs as well as its energy gap determine the height of the energetic barrier for both hole and electron transport. The overall resistance for such a network is given by

$$R_t = \frac{h}{4e^2} + R_C + R_{Channel}, \qquad (2.35)$$

where R_t defines the total resistance, R_c defines the contact resistance and $R_{channel}$ is the resistance of the nanotube channel due to carrier scattering events by defects, impurities or phonons. Experimentally, also the surfactant covering the tubes can be a limiting factor as it reduces the contact area between two nanotubes or imposes another energetic barrier for the nanotubes in a network. Also the overall occupancy of the channel area with nanotubes is important as the current scales proportionally to the number of established percolation paths, which is related to the SWCNT density.

Another parameter that can be investigated is the alignment of the nanotube with respect to the direction of the electric field between the contacts. In modeling the minimum resistivity of a nanotube network between two electrodes, or in other terms the ideal alignment was found to be a partially aligned network in the direction of the channel [142]. This optimizes the tradeoff between the overlap of the nanotubes and the charge transport between the contacts. For small channel devices that can be bridged by individual nanotubes, alignment in channel direction is obviously completely favorable over random placement of the SWCNTs.

2.9.3. Operation Principle of Field-Effect Transistors (FETs)

Field-effect transistors are three terminal devices consisting of a source, a drain and a gate electrode around a semiconducting channel. The schematic of a field-effect transistor is given in Figure 2.12. The semiconductor is connected to two contacts (drain and source) of different potential V_{DS} on opposing sides. In this setup a current between drain and source is allowed by modulating the resistance of the semiconductor via a second potential V_{GS} between source and gate electrodes.

The third electrode is the gate electrode, which is spatially separated and electrically insulated from the channel by a dielectric/insulator. The resistance of the semiconducting channel can be controlled by an external electric field applied between the source electrodes and the gate contact. In other words, in a MISFET (metal-insulator-semiconductor field-effect transistor) a current flow between the source and the drain contact is modulated by an external voltage. Therefore the modulation does only require a minimum amount of power, since no current flows between gate and source.

The electric field between source and drain is the driving force for the current flow. If zero voltage is applied between drain and source contacts, the field-effect transistor can be understood as a MIS-capacitator, which can be used to understand the gating principle of the transistor.

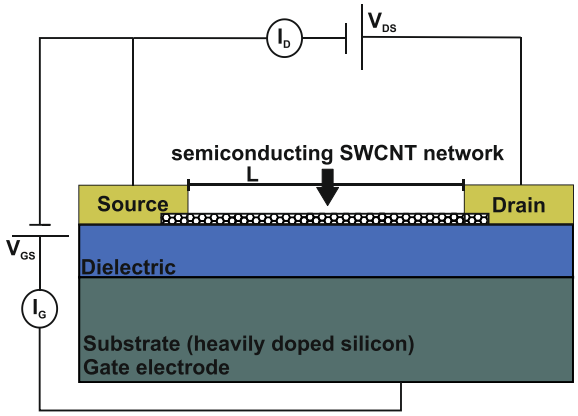

Figure 2.12. A schematic of a field-effect transistor. The three terminal (gate, source, drain) device in bottom gate bottom contact is controlled by firstly applying a voltage between drain and source to allow a current I_D. The resistance of the semiconducting network of SWCNTs is modulated by applying a second voltage between source and gate. The channel length L is denoted along with the voltages and the according currents.

Metal-Insulator-Semiconductor (MIS) Capacitor

The charge-carrier density for holes close to the valence band edge in an intrinsic, nondegenerate semiconductor is given by the expression

$$p = N_V \cdot exp\left(-\frac{E_F - E_V}{k_B T}\right), \tag{2.36}$$

where E_F and E_V denote the energy of the Fermi level and the valence band, respectively. N_V is the effective density of states in the valance band as defined in [143]. The charge-carrier density for electrons at the bottom of the conduction band depends analogue on the energy difference between the Fermi energy and the energy of the conduction band ($E_C - E_F$). The capacitance of a parallel plate capacitor is given by

$$C_{MIS} = \varepsilon_o \cdot \varepsilon_r \cdot \frac{A}{t_{Di}}, \tag{2.37}$$

where the vacuum- and dielectric permittivity are given by ε_o, ε_r, respectively. Parameter A represents the gate electrode area and t_{Di} it the thickness of the dielectric.
The band structure of a MIS-capacitor with an intrinsic semiconducting SWCNTs is shown in Figure 2.13 for n-and p-type operation.
It is to mention that adsorbed oxygen usually leads to p-type behavior in non-passivated SWCNTs [144]. Figure 2.13 bases on a high work function metal like palladium, gold or silver with the potential barrier Φ_{MI} between the metal and the insulator. Without any electric field applied between semiconductor and gate in Figure 2.13a, no band bending due to Fermi level adjustment occurs. The Fermi level of the metal and the semiconductor are assumed to be on the same level in this example. When a voltage is applied, a voltage drop occurs across the insulator and the semiconductor (see Figure 2.13b, c). Depending on the applied voltage between the gate electrode and the semiconductor either hole or electron accumulation is favored. In case of a positive voltage accumulation of electrons (b) or in case of a negative voltage accumulation of

holes (c) occurs in the respective bands at the interface between semiconductor and insulator as the charge carrier density depends on the energy difference between $(E_F - E_{C,V})$, respectively [143].

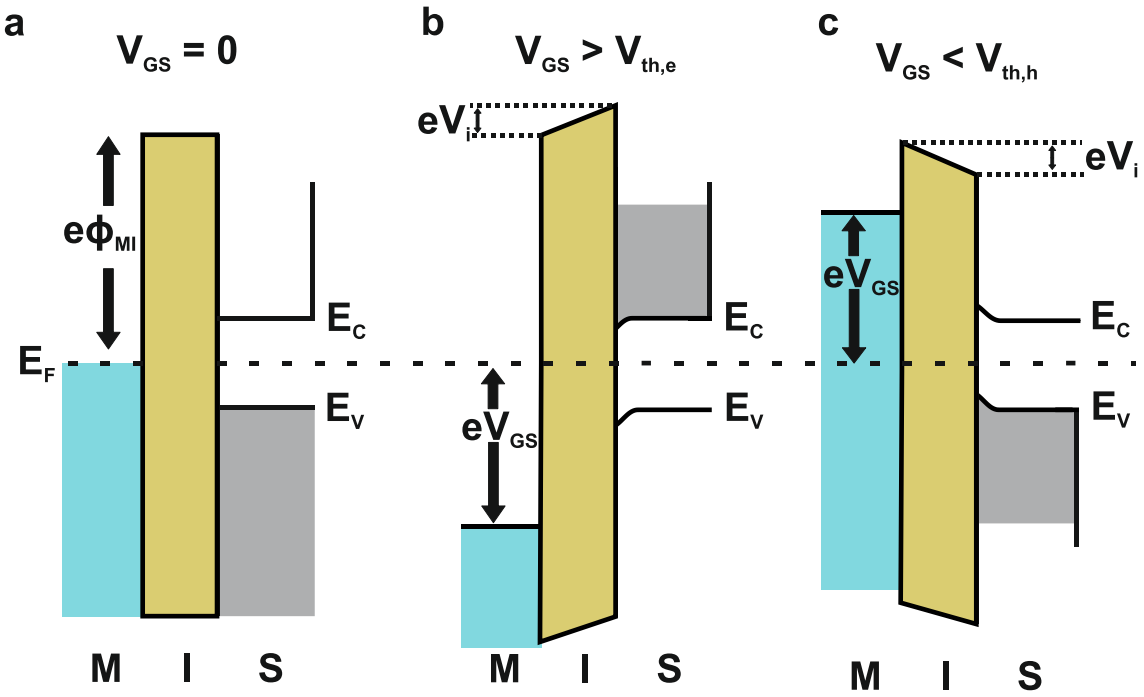

Figure 2.13. Band structure of MIS-capacitator. In a) no gate voltage is applied (flatband condition). The Fermi levels of the semiconductor and the metal are equal. No current can flow as the charge carrier density is not modulated. In b) a shift of the Fermi level within the metal has occurred. Electron accumulation in the conduction band occurs as a result of a positive voltage applied to the gate, which induces a band bending towards the Fermi level of the conduction band. In c) a negative voltage is applied to the gate. The Fermi level of the metal has shifted inducing band bending so that hole accumulation is favored.

Field-effect Transistor (FET)

In Drude's model [94] the current between source and drain called I_D is proportional to the conductivity σ of the semiconductor and the drain-source voltage V_{DS} along the channel.

$$I_D \propto \sigma \cdot V_{DS} = e \cdot p \cdot \mu \cdot V_{DS}. \tag{2.38}$$

Here, σ is the conductivity of the channel, μ is the intrinsic charge-carrier mobility, which is independent of the electrostatic potential. The density of charge carriers p is controlled by the gate-source voltage.

Following [143], TFTs can be approximated by the so-called charge-sheet model. This charge-sheet is of zero thickness so that across the charge sheet no voltage drop occurs. The amount of accumulated charge carriers Q_{acc} in the semiconductor is directly proportional to the capacitance C_{MIS}

$$Q_{acc} = C_{MIS} \cdot (V_G - V_{th}). \tag{2.39}$$

The charge-carrier density is modified as seen via V_{GS} and therefore the resistance of the semiconductor [143]. The TFT operation is distinguished between two different regimes. At first, I_D increases linearly (linear regime), with increasing V_{DS}. For $(V_{GS} - V_{DS}) < V_{th}$, the charge density under the drain contact is zero (pinch-off point) and the current saturates (saturation regime). The drain current I_D is described by the following equations in the two regimes, respectively. Figure 2.14 shows the different regimes in the characteristic transfer and output curve of a transistor.

$$I_D = \frac{\mu W C_{diel}}{L}\left((V_{GS} - V_{th})\, V_{DS} - \frac{V_{DS}^2}{2}\right), \tag{2.40}$$

where $|V_{GS} - V_{th}| > |V_{DS}|$ (linear regime).

$$I_D = \frac{\mu W C_{diel}}{2L}\,(V_{GS} - V_{th})^2, \tag{2.41}$$

where $0 < |V_{GS} - V_{th}| < |V_{DS}|$ (saturation regime).

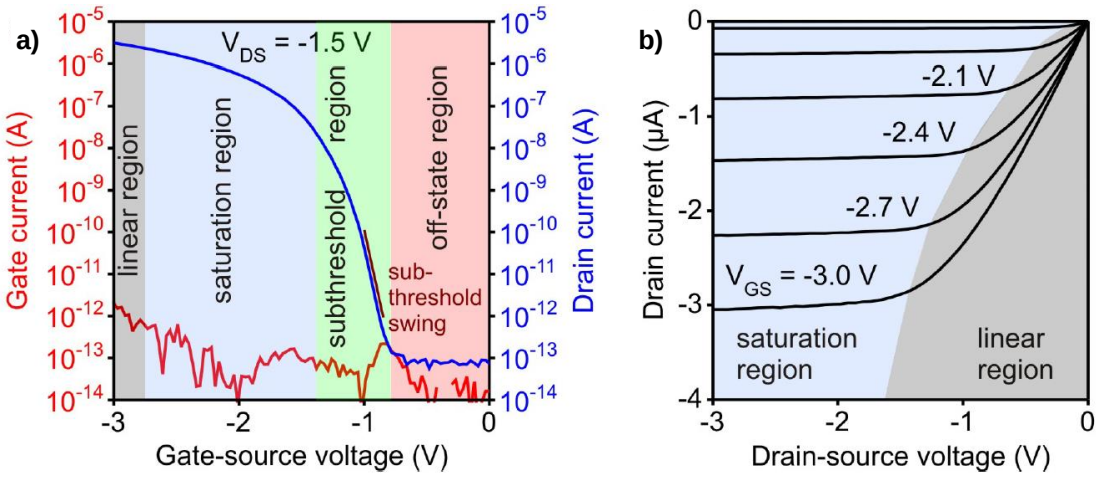

Figure 2.14. Transfer and output characteristics of a field-effect transistor. a) The transfer characteristic is the drain current (blue curve) as function of the gate-source voltage. This function is recorded at fixed drain source voltage (here -1.5 V) can be divided into the off-state (red), the subthreshold (green), the saturation (blue) and the linear region (gray), which are marked by the respective colors. The red curve shows current measured between gate and source. It gives the insulating qualities of the dielectric. b) The output curves give the drain current in relation to the drain-source voltage for fixed gate-source voltages. The current saturates once $V_{DS} > V_{GS} - V_{th}$ (saturation region). Taken from [145].

The charge-carrier mobility of the semiconductor μ $\left[\frac{cm^2}{Vs}\right] = \left[\frac{\frac{cm}{s}}{\frac{V}{cm}}\right]$ is introduced, which is the velocity of charge-carriers per electric field strength. The gate capacitance per unit area is C_{diel} and L and W are the length and width of the channel, respectively. C_{diel} is derived analogous to the MIS capacitance

$$C_{diel} = Q_S(V_{GS} - V_{th}) = \frac{\epsilon_0 \epsilon_R A}{t_{Di}}. \tag{2.42}$$

The threshold voltage V_{th} is defined as the minimum voltage required to induce strong inversion for silicon MOSFETs (metal-oxide-semiconductor field-effect transistors) [146]. In accumulation it describes the voltage necessary to induce a drain current with non-exponential slope.

2.9.4. Key Parameters of Thin Film Transistors (TFTs) in the Charge-sheet Approximation

The mobility of the charge carriers in a TFT can be derived from the equations for the drain current in the respective regimes. For the linear region the mobility is obtained by

$$\mu_{lin} = \frac{L}{C_{diel} W V_{DS}} \cdot \frac{\partial I_D}{\partial V_{GS}}. \tag{2.43}$$

And in the saturation regime one gets

$$\mu_{sat} = \frac{2L}{C_{diel} W} \cdot \left(\frac{\partial \sqrt{I_D}}{\partial V_{GS}} \right)^2. \tag{2.44}$$

The on/off current ratio (on/off ratio) is the ratio of the drain current in the on-state and the off-state. For technical applications this ratio should be as high as possible (>10^3 for analog, >10^6 for digital circuits).

2.9.5. Ionic Gel Gating

An (room temperature) ionic liquid is a salt in its liquid state if its melting point is below an arbitrary temperature such as 100°C [110]. The liquid can be gelled by addition of polymers or by adding nanoparticles. Below the melting point of the polymer, the formation of small crystals as solid phase in the liquid mixture is energetically favored and the polymer chains in solution form bridges between crystalline parts [147]. In this way they can be used as gate dielectric. The contained ions are free to orient and move in applied electric fields, which leads to the formation of a so-called Helmholtz layer at the interface to the gate electrode.

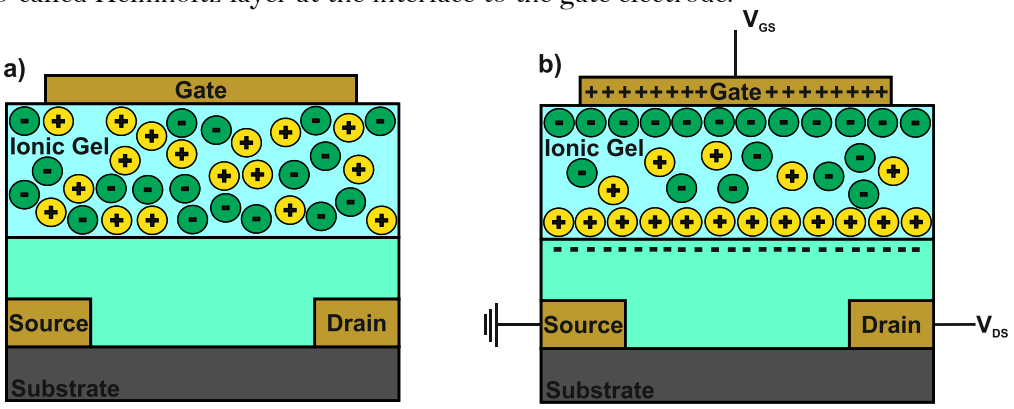

Figure 2.15. The ion-distribution within an ionic gel with and without an applied electric field. In a) no voltage is applied and therefore no spatial orientation of the ions is achieved. In b) a gate voltage is applied, which leads to an ion formation called electric double layer at the interfaces with the gate electrode and the semiconductor.

Ionic liquids offer very high intrinsic capacitances, which allow low voltage operation of devices gated in this fashion. Figure 2.15 shows schematically how an ionic gel is used as gating material. For nanotubes the use of ionic gels brings two advantages over bottom gate configuration transistors. Firstly the gel can surround the SWCNT network completely for effective gating. The second advantage is that the semiconductor can be passivated from the atmospheric surroundings by an IG, which have caused hysteresis effects in carbon nanotube FETs [148, 149].

2.10. X-Ray Photoelectron Spectroscopy (XPS)

Developed by Siegbahn et al. in 1957 [150], photoelectron spectroscopy is a method to evaluate the energy levels of atomic core electrons by the photoelectric effect, primarily in solids. XPS is used to evaluate the elemental composition of a material's surface due to finite penetration depth of the photons. The principle relies on the photoelectric effect, where electrons are emitted from a sample after radiation with electromagnetic waves (here X-rays). The X-rays often have an energy of ≈1,487 eV (Aluminum K_α) or ≈1,254 eV (Magnesium K_α). The energies of emitted electrons are characteristic for the original electronic state (atomic orbital).
If a light source with wavelength λ ionizes molecules or atoms, electrons are emitted. The electrons of kinetic energy E_{kin} from a distinct state of ionization with energy E_1 are measured by an energy analyzer. The conservation of energy requires that

$$E_{kin} = h\nu - E_1, \tag{2.45}$$

where $\nu = c/\lambda$. Therefore the kinetic energy of the measured electron directly gives the energy of the molecular orbital from where the electron was emitted. E_1 may be split into the binding energy E_B and the work function φ. This way also the binding energy can be recorded. Electrons can also be emitted as a result of energy transfer between electrons, when an outer shell electron fills the vacancy left behind from an initially emitted electron due to photon absorption. Those electrons are called Auger electrons. Their kinetic energy is independent of the excitation wavelength due to the fact, that it is an inner atomic process. Both processes are schematically drawn in Figure 2.16 [151]. The emitted photoelectrons are collected, filtered by their energy (concentric hemispherical analyzer) and counted using an electron multiplier detector. This gives a spectrum of electron intensity versus their kinetic energy or binding energy. An example spectrum of the binding energy of the iron catalyst in raw SWCNTs generated by XPS measurements are found in Figure 2.17.

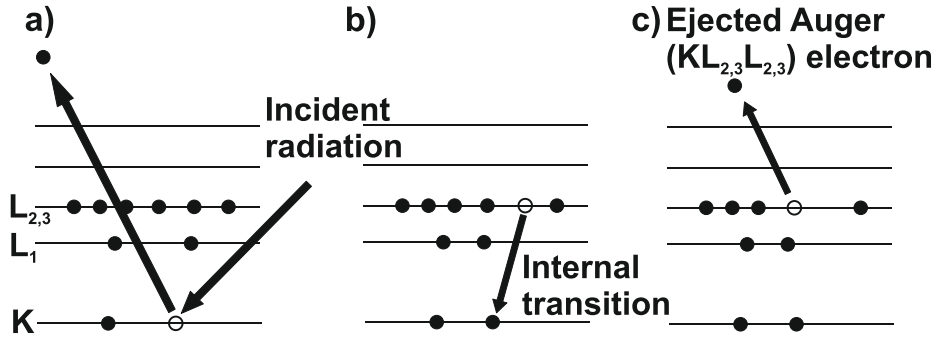

Figure 2.16. The photoelectric process with emission of Auger electron is shown schematically. In a) the photoelectric effect is schematically shown. An incident light beam (black arrow) causes an electron to be emitted from the K shell. In b) the vacant state in the K shell is taken by an electron from the L shell, under the emission of another L electron due to conservation of energy depicted in c).

The vacant space can also be taken by an electron from a higher order shell under the emission of an X-ray instead of the Auger-electron, after incident radiation and emission of an electron. This is element characteristic X-ray fluorescence and can be measured using a photodetector.

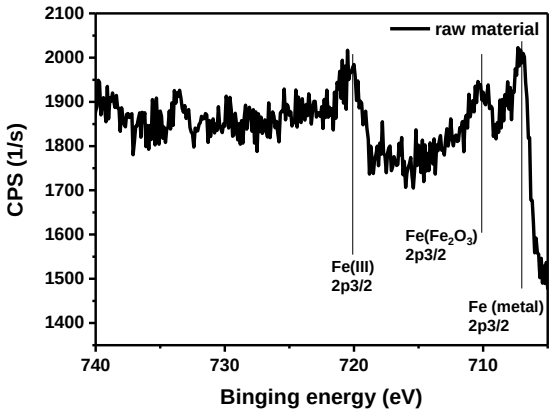

Figure 2.17. High resolution XPS scan of the iron catalyst peaks in raw HiPco SWCNTs.

2.11. Atomic Force Microscopy (AFM)

The atomic force microscope was developed by Binnig, Quate and Gerber in 1986 [152] and is nowadays an ubiquitously used method to evaluate surfaces on the nanometer scale. The principle of this measurement relies on moving a nanoscale stylus attached to a cantilever in a defined pattern across the surface of a sample (scanning). While the stylus moves across the surface, the cantilever bends towards or away from the surface due to attractive or repulsing forces. Those can be repulsive short range forces from e.g. the Pauli repulsion (electrons) or the Coulomb forces (nuclei) or attractive long range van-der-Waals forces. The deflection of the cantilever is monitored simultaneously to the lateral movement by a laser beam focused onto the back of the stylus. The reflected beam is directed onto a photodetector. This photodetector is sensitive to the position of the laser beam. The basic AFM set-up is illustrated in Figure 2.18. The AFM essentially operates in three different modes. The contact-, the non-contact- and the tapping-mode.

Contact Mode

In all contact mode operations the tip remains in direct mechanic contact to the surface of the sample. The contact mode itself is divided into a regulation for constant height or constant force. In case of constant height the cantilever stays on the same height during the scan process, the cantilever then bends according to the surface topography and depicts it.
In case of constant force regulation the cantilever is forced into a steady deflection. The information of the topography is generated by the feedback signal that is required to keep the cantilever in this position while different surface forces act.
A general drawback of the contact mode is that the surface can be deformed (problem for polymeric materials) in the process or breaking of the nanoscale stylus.

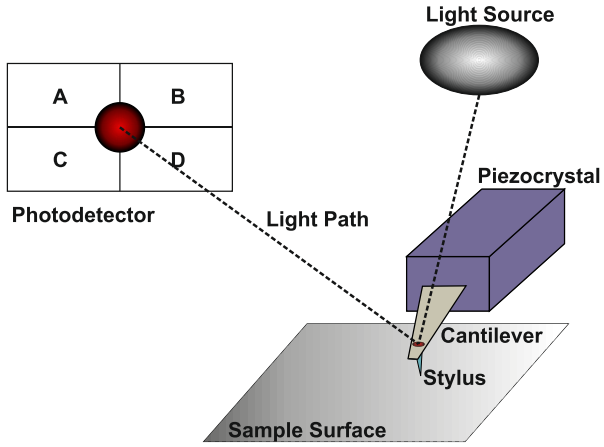

Figure 2.18. A basic AFM set-up. A stylus mounted at the tip of a flexible cantilever. The cantilever is driven by a piezocrystal, which allows lateral movement over the surface. The deflection is monitored by the movement of the light spot on the photodetector, which is triggered by the reflection from the back of the cantilever in the given mode of operation.

Non-Contact Mode

In the non-contact mode the tip of the cantilever does not encounter the surface. The cantilever is typically oscillated at its resonant frequency. The interactive forces such as long range van-der-Waals forces between the surface and the stylus damp the cantilever's oscillation frequency. The feedback loop combined with the decrease in frequency of the oscillation generates the average surface to stylus distance that images the topography of the sample surface.
The drawback is that under ambient conditions many samples adsorb monolayers of fluid, which can massively falsify images [153]. Therefore this mode is typically used in ultra-high vacuum and high vacuum and allows a lateral resolution down to 0.1 nm.

Tapping Mode

In the tapping mode the cantilever is driven to oscillate close to its first flexural resonance by an external actuator. Interaction forces (such as van-der-Waals) between tip and surface damp the

cantilever oscillation. A feedback adjusts the cantilever height in order to keep the oscillation amplitude constant. Based on this feedback signal the topography of the surface is obtained. During this mode the tip is brought into close contact to the surface at the lower turning point of the oscillation, which enables overcoming of the adsorbed fluid problem.
Additionally, changes in the oscillation frequency due to different mechanical or adhesive properties of the surface can be depicted as the phase signal between the drive frequency and the actual oscillation frequency.

2.12. Asymmetrical-Field Field Flow Fractionation (AF4)

The AF4 was invented by Giddings et al. in 1966 [154]. The method presents an analytical tool to separate particles in fluid suspensions or solutions depending on their different field flow mobilities. The method relies on pumping the analyte through a long, narrow channel. During the propagation in this channel the particles experience an additional flow field perpendicular to the direction of flow. The method can provide applicability to a wide range of colloidal sizes while maintaining high resolution. The principle bases on laminar flow of the particles. Since diffusion is correlated to the size of the molecules, separation will be achieved as the particles will travel with different velocities stemming from the parabolic flow profile in a channel. When considering two different size particles in the channel, the cross flow will force the particles towards the bottom of the channel as depicted in Figure 2.19.

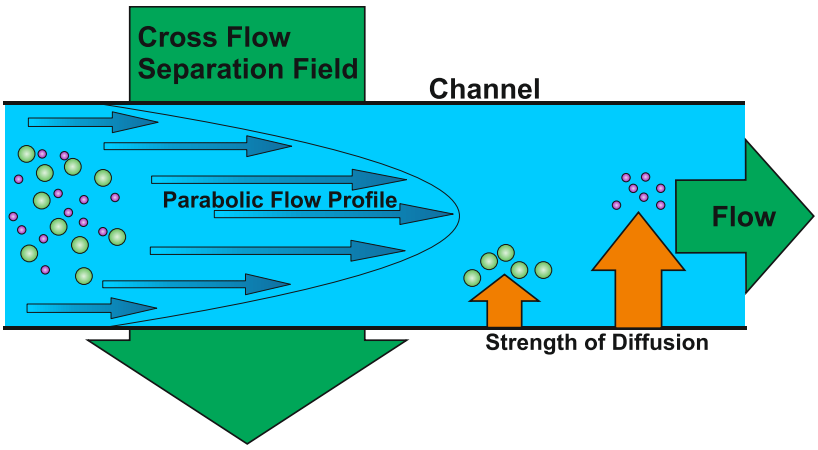

Figure 2.19. The asymmetrical-field field flow fractionation is shown schematically. The flow through a channel follows a parabolic shape, with the highest velocity in the middle of the channel. Due to different diffusion constants of differently sized particles in the stream the particles travel with different average velocities and are eventually separated.

The opposing force is diffusion. In equilibrium these two forces result in a particles distribution

$$c = c_0 \cdot exp\left(\frac{-x}{l}\right), \tag{2.46}$$

with x being the distance from the bottom of the channel and l being defined via

$$l = \frac{k_B T}{F}. \tag{2.47}$$

Here F is the force exerted by the cross flow. Smaller particles travel faster as their higher diffusion allows them to penetrate deeper towards the middle of the channel allowing for high efficiency separation with very good control via the cross flow field. Equipped with dynamic light scattering, refractive index and absorbance detectors the AF4 can deliver reliable information about molar mass and particle size. Particle size can even be dissected into hydrodynamic and gyration radius, which gives information about the mass distribution/shape of the particles. Experimentally, the cross flow is often regulated in a decreasing profile starting with high flow rates to separate very small particles and then slowly decreasing the flow to exploit the size differences between all the particles in an unknown sample.

2.13. Dynamic and Static Light Scattering (DLS, SLS)

Since Tyndall 1869 [155] and Rayleigh 1881 [156], light scattering has been used to determine the size of particles. Here two methods are shortly introduced while the complete theory of these light scattering methods can be found for example in [157-159].

Dynamic Light Scattering

Dynamic light scattering (DLS) is a method used to measure particle sizes via the time-dependent fluctuations in the scattering intensity as a result of particles undergoing random Brownian motion. The Diffusion coefficient and therefore particle size information can be obtained from these fluctuations. A monochromatic light beam, for example a laser, is directed onto a solution containing particles. The Brownian motion causes a Doppler shift when the light hits the moving particle, changing the frequency of the incoming light (typically 633 nm). This change is related to the size of the particle as smaller particles move faster. The correlation of the electric field $g^1(t)$ relates to the mentioned Doppler shift $S(\omega)$ via

$$g^1(t) \sim \int_0^\infty S(\omega) exp(-iq\omega t). \tag{2.48}$$

Here $g^1(t)$ is the autocorrelation function at a particular wave vector q, delay time τ and intensity I. Short times lead to high correlation as particles haven't had a chance to move far from their initial states. However, the correlation decays exponentially for monodisperse small particles and after long times there is no correlation between scattered intensity and their final states. The exponential decay is used to relate the particles to their size via their diffusion rate

$$g^1(t) = B \cdot exp(-q^2 Dt). \tag{2.49}$$

Here B is the signal to noise ratio and depends on the optical setup [160]. Via the Einstein relation $D = k_B T/(6 \cdot \pi \cdot \eta \cdot r_p)$, the diffusion coefficient is related to the hydrodynamic radius of the particles. The hydrodynamic radius gives a sphere equivalent radius approximation of the particles.
This technique is a popular method used to determine the size of particles in range from nanometer to several micrometer [161].

Static Light Scattering

In contrast to DLS, the static light scattering (SLS) is a technique that does not correlate the fluctuations but averages the total intensity of scattered light at a given angle via the Zimm relation [162]. In the Rayleigh-Debye-Gans approximation ($\frac{\lambda}{20} > d$, $qR_g < 2$), the Zimm equation relates the radius of gyration R_g to the measured intensity via

$$\frac{KC}{R_\theta} = \frac{1}{M_w}\left(1 + \frac{1}{3}q^2\langle R_g^2\rangle_z\right). \tag{2.50}$$

Here M_w is the molecular weight, R_θ is the Rayleigh ratio determined via a standard of known scattering (usually toluene), K is an optical constant related to the $\frac{dn}{dc}$ of the particle and the refractive index of the medium, C is the particle concentration, q is the scattering vector $q = \frac{4\pi}{\lambda}\sin\left(\frac{\theta}{2}\right)$ and $\langle R_g^2\rangle_z$ is the mean square radius of gyration [163]. The radius of gyration gives the distance from the axis of rotation where a point mass would be located that gives an equivalent inertia to the original particle.

2.14. Wilhelmy Plate (Tensiometry)

The Wilhelmy plate is a method used to determine the surface tension of a liquid. A plate of a couple of square centimeters is oriented perpendicular to the liquid/air interface in contact with both phases. The plate is connected to a balance so that the force exerted onto it by wetting is monitored. This force depends on the surface tension and follows

$$\sigma = \frac{F}{l\cos(\theta)}, \tag{2.51}$$

where σ is the surface tension and l is the wetted perimeter (two times the width plus two times the thickness of the plate) and θ is the contact angle between the plate and the liquid phase. The parameters can also be visualized in Figure 2.20.

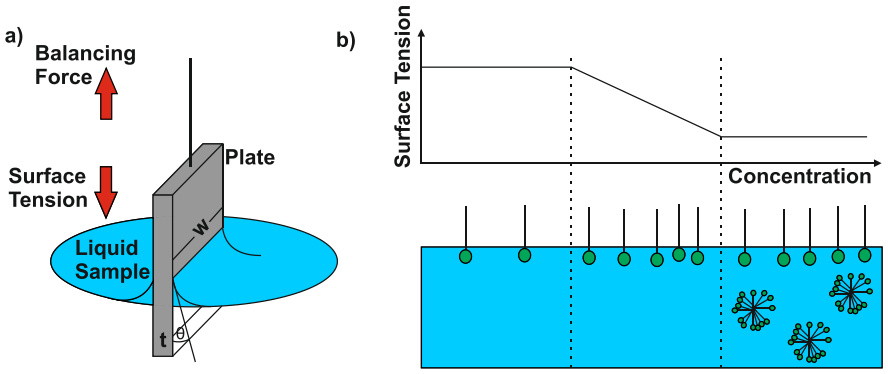

Figure 2.20. The Wilhelmy plate method. In a) a scheme of the Wilhelmy plate is shown. The plate is put in contact with the interface of a liquid and gas. The force exerted by the wetting of the plate is measured in dependence of the polymer/surfactant concentrations in the liquid phase. Panel b) shows the regimes of micelle formation and relation to the surface tension so that the critical micelle concentration can be deduced.

2.15. Density Determination by Oscillating U-Tube

Kratky et al. proposed a method to measure the density of fluids and gases based on the oscillation of a hollow tube [164]. A hollow U-shaped tube made of glass is electronically excited to oscillate undamped. The Eigen frequency of the U-tube is influenced by the medium inside the oscillating part. The higher the density the more mass takes part in the oscillation and therefore the longer the period. The density is determined by this sample depending Eigen frequency shifting in comparison to the densities of water and air. The period of the oscillation is given by

$$T_{Osc} = 2\pi \cdot \sqrt{\frac{m+\rho \cdot V}{K}}, \tag{2.52}$$

where m and V are the mass and the volume of the empty U-tube, respectively. The density ρ of the medium filled into the u-tube and the spring rate K of the U-tube are introduced. The density of the medium in the U-tube is given by

$$\rho = T^2 \cdot \frac{K}{4\pi^2 V} \cdot \frac{m}{V}. \tag{2.53}$$

Here two device specific constants can be introduced

$$A = \frac{K}{4\pi^2 V}, B = \frac{m}{V}, \tag{2.54}$$

so that equation (2.53) simplifies to

$$\rho = A \cdot T^2 - B. \tag{2.55}$$

A and B are determined via calibration using two different media (usually water and air) via

$$A = \frac{\rho_1 - \rho_2}{T_1^2 - T_2^2}, B = \frac{T_1^2 \cdot \rho_1 - T_2^2 \cdot \rho_2}{T_1^2 - T_2^2}. \tag{2.56}$$

2.16. Electrophoresis

Electrophoresis was developed in 1937 by Tiselius to separate particles in a liquid suspension. In our case the aim of this method is to measure the migration of charged particles due to application of an electric field.

The drifting velocity is induced by the electric field E and proportional to the charge of the particle. The mobility of particles in a liquid medium is directly measured via the Doppler shift of a laser aligned in direction of the electrodes. The charge of the particle is strongly influenced by adsorbed species to the surface of the particle [165]. The surface charges are screened by a diffusive layer of ions in aqueous systems. Within the screening ion layer, the zeta potential ζ-potential is defined as the potential difference between the dispersion medium and the stationary screening layer [166]. Overall the force acting on particles during electrophoresis is given by

$$F_{tot} = 0 = F_{el} + F_f + F_{ret}. \tag{2.57}$$

Following Smoluchowski's approach [167] the electrophoretic mobility μ_e can be expressed as

$$\mu_e = \frac{\varepsilon_r \varepsilon_0 \zeta}{\eta}, \tag{2.58}$$

where η is the viscosity of the dispersion medium. This early approach was used to relate the mobility to the screening layer, however, has been expanded to greater regions of validity [168].

3. Materials

This chapter's content are descriptions of the main materials used throughout this thesis. The carbon nanotubes used in this work are described in more detail. The class of polyarylether (PAE) polymers is introduced as dispersants including their synthesis. Also the density materials are listed. They were classified by viscosity measurements under the conditions used in centrifugation experiments. Other chemicals that were used for specific experiments are also listed in combination with the supplier.

3.1. Single-Walled Carbon Nanotubes (SWCNTs)

The SWCNTs used in this work originate from different production processes namely the "High pressure carbon monoxide" (HiPco), the arc-discharge process (AD) and the plasma torch (PT) process. The samples were acquired from NanoIntegris, Raymor Technologies and Carbonsolutions Inc., respectively.
Each sample contains multiple species of SWCNTs that have random diameters between 0.8 - 1.2 nm (HiPco), a diameter range around 1.4 nm (AD) and the diameter range of the PT-SWCNTs is centered at about 1.2 nm. Thus, a wide range of possible SWCNTs is covered providing different chiralities meaning also different band-gaps, radii of curvature, surface area, for both semiconducting and metallic types.
Statistically there are approximately 33% metallic and 67% semiconducting SWCNTs in every sample synthesized in the three introduced large scale production processes. The SWCNT supplier, synthesis process, batch numbers, mean diameter and SWCNT content of the raw materials according to the suppliers are summarized in Table 3.1.

Producer/ Supplier:	Process:	Batch Number:	Mean Diameter:	SWCNT Content:
Raymor	Plasma	RN-020	1.2 nm	30%
NanoIntegris	HiPco	R1-912 R1-901 HS 28030	1.0 nm	13% 10% 5%
Carbonsolutions	Arc-Discharge	P2	1.4 nm	90%

Table 3.1. Summary of the raw SWCNT materials used throughout this thesis.

3.2. Polyarylethers (PAEs)

All PAE polymers were provided by BASF Construction Solutions GmbH as research product synthesized by Annemarie Kühn in the lab of Alexander Kraus (BASF Construction Solutions GmbH). The general structure of the PAE polymer used in this work can be found in Figure 3.1. It has a hydrophobic backbone based on benzene rings, which are substituted with hydrophobic dodecyl side chains as well as hydrophilic polyethylenglycol (PEG) side chains and

phenoxyethanolphosphate groups. Our experiments showed that this polymer has a strong affinity to carbon nanotubes (CNTs) believed to be promoted by $\pi - \pi$ interactions with its aromatic backbone [169] and the hydrophobic interaction originating from the dodecyl side chains. The hydrophilic PEG side chains and the anionic phenoxyethanolphosphate moieties ensure an electrosteric stabilization of the individualized tubes and strongly prevent their re-agglomeration [48], due to the strong van-der-Waals forces between not functionalized SWCNTs.

PAE1 and PAE2 consist of different ratios of the same building blocks. The idealized structure is shown in Figure 3.1.

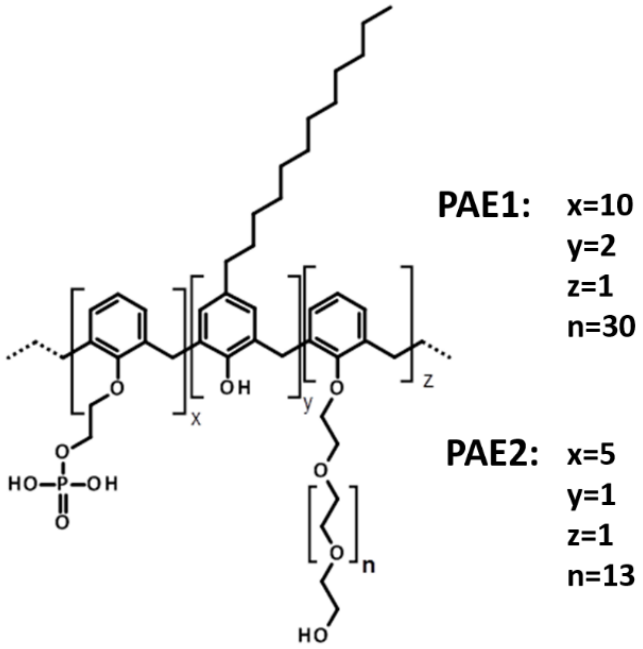

Figure 3.1. The general structure of the PAEs used for the separation of SWCNTs. The length of the PEG component is altered besides differences in the component ratio for PAE1 and PAE2, respectively.

Synthesis:

The PAEs (Figure 3.1) were prepared according to the following general phosphorylation and polycondensation procedure.

A reactor, equipped with heating and stirrer, was charged with 127 g of polyphosphoric acid (specified to have 85 % P_2O_5 content) and heated to 90°C. 138.2 g (1 mol) of phenoxyethanol was added to the stirred reaction mixture through a period of one hour. After the addition was finished, the reaction mixture was stirred for an additional hour. The reaction product contained 75 wt% of phenoxyethanol phosphoric acid monoester (ester of 1 mol of phenoxyethanol with 1 mol of phosphoric acid), 5 wt% of bis(phenoxyethanol)phosphoric acid ester (ester of 2 mols phenoxyethanol with 1 mol of phosphoric acid), 1 wt% of unreacted phenoxyethanol and 19 wt%

of unreacted phosphoric acid. The reaction product of the phosphorylation was used without further purification as starting material for the following polycondensation step.

General Polycondensation Procedure:

A corrosion-resistant reactor equipped with a stirrer and temperature control was charged with the starting materials listed in Table 3.2. Starting materials used for the synthesis of the PAEs. The exact amounts of the starting materials used for the synthesis of polymers PAE1 and PAE2 are listed in the given order:

1. poly(ethylenoxide)monophenylether (Ph-PEG)
2. phosphorylated phenoxyethanol (PPE)
3. dodecylphenol
4. paraformaldehyde or trioxan
5. methansulfonic acid 98 %

Upon completion of the addition of the acid, the reaction mix was heated to 95-100 °C. After 2 hours (for PAE1) and 3 hours (for PAE2) respectively the polycondensation reaction was finished and water was added. The solid content of obtained water solution of polymer PAE2 was 49.8 wt%. The polymer PAE1 was neutralized with NaOH to pH 7, and the solid content of the product was adjusted with water to 36.2 wt%.

Polymer	Ph-PEG M_w (g/mol)	Ph-PEG (g)	PPE[1] (g)	Dodecyl-phenol (g)	Trioxan (g)	Paraform-aldehyde (g)	CH_3SO_3H 98% (g)	M_w[2] Reaction product (g/mol)
PAE1	1500	60.7	87.20	20.40	0	16.33	2.39	8000
PAE2	750	37.51	54.55	13.51	9.03	0	2.92	6900

Table 3.2. Starting materials used for the synthesis of the PAEs. The exact amounts of the starting materials used for the synthesis of polymers PAE1 and PAE2 are listed.

(1) contains 75 wt% of phenoxyethanol phosphoric acid monoester, 5 wt% of bis(phenoxyethanol)phosphoric acid ester, 1 wt% of phenoxyethanol and 19 wt% of phosphoric acid.

(2) The molecular weights of the polymers were determined by using gel permeation chromatography method (GPC). Column combination: OH-Pak SB-G, OH-Pak SB 804 HQ and OH-Pak SB 802.5 HQ by Shodex, Japan; eluent: 80 Vol.% aqueous solution of HCO_2NH_4 (0.05 mol/l) and 20 Vol.% acetonitrile; injection volume 100 µl; flow rate 0.5 ml/min. The molecular weight calibration was performed with poly(styrene sulphonate) standards for the UV detector and poly(ethylene oxide) standards for the RI detector. Both standards were purchased from PSS Polymer Standards Service, Germany. In order to determine the molecular weight of the polymers, the result based on UV-detection (254 nm) was used, because the UV detector is only responsive towards the aromatic compounds and neglects inorganic impurities, that otherwise could falsify the results for the molecular weights.

Density of PAE1

The density of the as-synthesized polymer was determined to be 1.61 ± 0.02 g/cm³ by the oscillating U-tube method and extrapolation from water diluted samples to 100% polymer via volume. The density will be further discussed in section 5.1.

3.3. Density Materials

The density media used throughout this thesis is predominantly sodium polytungstate (SPT) but Iohexol or Iodixanol, CsCl and lithium tungstate have been used as well. Lithium tungstate was acquired from Polytungstates Europe. Sodium polytungstate was acquired as solution from TC-Tungsten Compounds GmbH. Iohexol (powder) and Iodixanol (solution) were purchased from Axis-Shield. Cesium Chloride was purchased from Alfa-Aesar. For a comparison of the different possible aqueous densities, the main parameters are summarized in Table 3.3.

Density Material:	Possible Density Region (g/cm³)	Viscosity (mPa·s) (at 25°C, 1.25g/cm³)
Sodium Polytungstate	1.0 - 3.0	1.1
Iohexol	1.0 - 1.4	4.1
Iodixanol	1.0 - 1.3	4.9
Cesium Chloride	1.0 - 1.9	0.9
Lithium Polytungstate	1.0 - 2.8	1.1

Table 3.3. Summary of the density media. The density media are summarized with the density region they can achieve in aqueous solution and a standard value for viscosity.

UV-vis-NIR Absorbance of Sodium Polytungstate (SPT)

The UV-vis-NIR absorbance of SPT is shown in Figure 3.2. An increase in absorbance is detected towards smaller wavelengths.

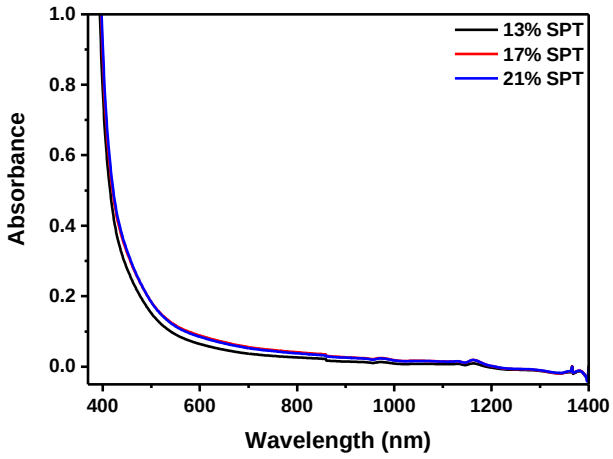

Figure 3.2. Spectra of different SPT concentrations that match the density of SWCNTs in density gradient centrifugation.

Below 400 nm the absorbance is out of the linear detection region for each aqueous concentration measured.

3.4. Surfactants

Sodium cholate and sodium deoxycholate were purchased from Alfa-Aesar and used as received. Cetyl trimethyl ammonium bromide was purchased from Amresco and sodium dodecylbenzenesulfonate was purchased from TCI and both were used as received.
The structures are displayed in Figure 2.11. Lupasol PN60, Tamol NN9401, Pluronic F68, F108, F127, PE10500 and Tetronic 90R4 were provided by BASF SE. Structures can be found in the appendix. The Pluronic names contain either F, P or L if they are a solid-, pasture like- or liquid-material, respectively. The structures of Pluronic and Tetronic are displayed in the appendix 10.1. The structure of Lupasol can be found for example online at www.care-chemicals-formulators.basf.com.
Tamol NN9401 is a Naphthalinesulfonic acid polycondensate sodium salt. The structure can be found in the appendix section 10.2.

3.5. Ionic Liquid

The Ionic Gel was formed from a mixture of 1-ethyl-3-methylimidazolium bis(trifluoromethylsulfonyl)imide ([EMIM][TFSI], BASF SE), poly(vinylidene-co-hexafluoropropylene) (p(VDF-HFP), Sigma Aldrich) and γ-butyrolactone (Sigma Aldrich), respectively. The Ionic Gel was prepared and deposited onto SWCNT transistor channels by Michel Kettner (FET systems, BASF SE).

3.6. List of Various Chemicals Used throughout this Thesis

Sodium Chloride (Sigma Aldrich), Tungsten(III) Oxide (Sigma Aldrich), 1M HCl (Bernd Kraft Ag), 1M NaOH (Bernd Kraft Ag).

3.7. Self Assembling Monolayers (SAMs)

Tetradecylphosphonic acid (SAM1) ($C_{14}H_{31}PO_3$) was dissolved to form a concentration of 0.45 g/L in isopropanol.
4-ethoxyphenylphosphonic acid (SAM2) ($C_8H_{11}P\ O_4$) was dissolved to result in a concentration of 0.34 g/L in isopropanol.

4. Methods

This chapter gives an overview over the methods and experimental details.

4.1. Dispersing SWCNTs in Water

Horn Sonicator

The SWCNTs (raw material) were typically dispersed into 2 wt% aqueous solutions of polyarylethers (PAEs) by permanent horn sonication (Dr. Hielscher Up 200s Tip: S2) for 1 h. The amplitude of the sonicator was set to 260 µm (100%) at a depth of immersion of approximately 2 cm. At this setting, a sonication power of 120 W is delivered into the liquid as determined by calorimetry [170].
The dispersions were set up to consist of 0.5 wt% SWCNT source material in 2 wt% of aqueous surfactant solution in a total of 50 g if not otherwise declared. During sonication the dispersion was placed in ice-cooled water bath. After the material had been dispersed, the pH-value of the dispersion was set to pH 4 by adding aliquots of 1 M HCl (Knick pH-Meter 766). Each source material contained significant amounts of carbonaceous impurities and metal catalyst impurities. The nanotube content is summarized in Table 3.1 in the materials chapter.

Cup Sonicator

The Branson Digital Sonifier 450 was equipped with a sonication chamber so that the sonication power from the horn is directed into a water flushable chamber (cup). This can be visualized by the photograph in Figure 4.1. The sonicator was inverted and the sonication cup is placed on top of the horn of the sonicator. The cup itself is equipped with a cooling water system. Via a three pipe system the water flow can be adjusted so that a constant temperature can be achieved during sonication. Teflon sample holders were custom built to fit in the chamber. A temperature sensor was installed in the middle of the cup to monitor the temperature during sonication. The power input into the cup is about 90 W at 50% amplitude. Samples that fit in the depicted sample holder (Figure 4.1) roughly take about 12% of the power, but the sonication is further damped by the vial the sample is placed in.

To disperse carbon nanotubes using the cup sonicator at 25°C the cooling water flow was set to maximum to ensure stable temperature conditions (24 - 25°C). Dispersing carbon nanotubes at 55°C requires exact water flow, which has to be adjusted manually. The cooling water flow was in principle set to a minimum flow. The vial containing the carbon nanotubes was placed in the cup after the water bath was already heated to 55°C by sonication pulses so that prior to inserting the sample stable temperature could be ensured. The sonicator was set to stop when temperatures higher than 55°C occurred in the cup starting again when the temperature dropped to 53°C. To avoid hearing damage the whole device is placed in a soundproof box.

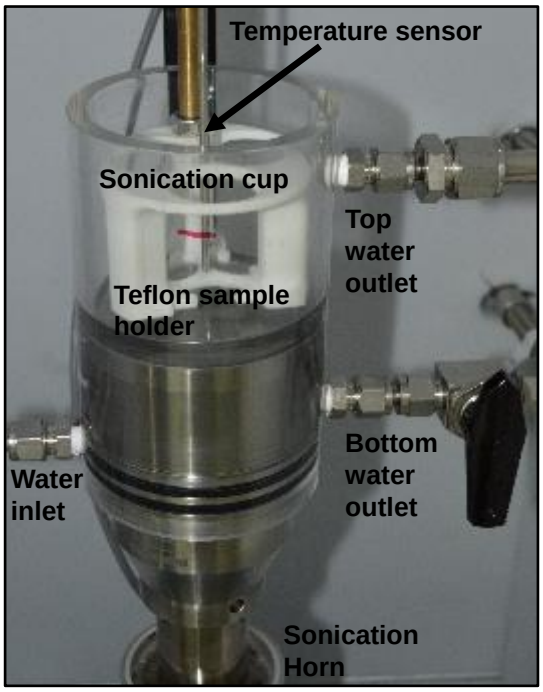

Figure 4.1. The cup sonicator is shown in a photograph. The samples can be placed in the sonication cup and are held by a ceramic tray, which can be exchanged for different vial sizes. Via the water inlet the chamber is flushed with cooling water of around 24°C. The bottom water outlet can be adjusted so that the flow can be regulated with in a very controlled way. The top water outlet assures that under maximum water inlet flow the cup does not overspill. By using a minimum flow of cooling water, the cup can maintain a water bath of high temperature during the sonication protocol.

4.2. Centrifugation Process

A standard centrifugation process to obtain individualized semiconducting SWCNTs or freestanding SWCNT sheets is described here. For centrifugation, a water based solution of sodium polytungstate (SPT, 25.5 wt%) also containing 2 wt% of PAE1 was prepared. The pH-value of this SPT column was controlled by adding 1 M HCl. The centrifugation vessel was loaded with 4.2 ml of SPT (pH 1.8) and 0.3 ml of the nanotube dispersion (pH 4) on top. Centrifugation (Beckman Coulter Optima XL) was performed applying a centrifugal field of approximately 10,000 x *g* for 25 h to yield semiconducting nanotubes in a Beckman Coulter SW 60Ti rotor.

In case of the freestanding SWCNT sheets the dispersion was prepared using PAE2 with shorter PEG sidechains compared to PAE1 (pH 2.5). For centrifugation 7.5 ml of the raw SWCNT dispersion was mixed with 7.5 ml of 20 wt% aqueous SPT solution (pH 2.5). The volume of the centrifugation vessel was changed from a 4.5 ml to a 29.5 ml tube. Two 7 ml columns of 64 wt% and 34 wt% SPT were set up on top of each other. As the topmost layer 15 ml of the SWCNT dispersion/SPT mixture was used. The pH-value of each layer was set to 2.5. Centrifugation was performed applying a centrifugal field of approximately 10,000 x *g* for 72 h in a Beckman Coulter SW 32Ti rotor. Centrifugation processes vary over the course of the thesis. The details will be mentioned again in the description of the respective experiments.

4.3. Post-Treatment of the Separated SWCNTs / Re-Dispersion into Semiconducting Inks

The extracted semiconducting SWCNT fractions that still contained SPT and the PAE1 polymer were slowly mixed with 1 M HCl. This leads to the agglomeration of SWCNTs. The agglomerated particles were collected after 2 h, diluted in DI-water and submitted to a 15 min run in the centrifuge at 10,000 x *g*. The supernatant was extracted and the pellet was swirled up by refilling the centrifugation vessel with DI-water. This maneuver was repeated six times. Afterwards the pellet was swirled up in DI-water containing 1 wt% of SDOC (pH 7.2). Bath-sonication for 30 min was used to disperse the SWCNTs again. The SWCNT sheet was collected and stored as obtained in a DI-water bath. A part of the sheet was transferred to a quartz wafer and was subsequently dried at 70°C.

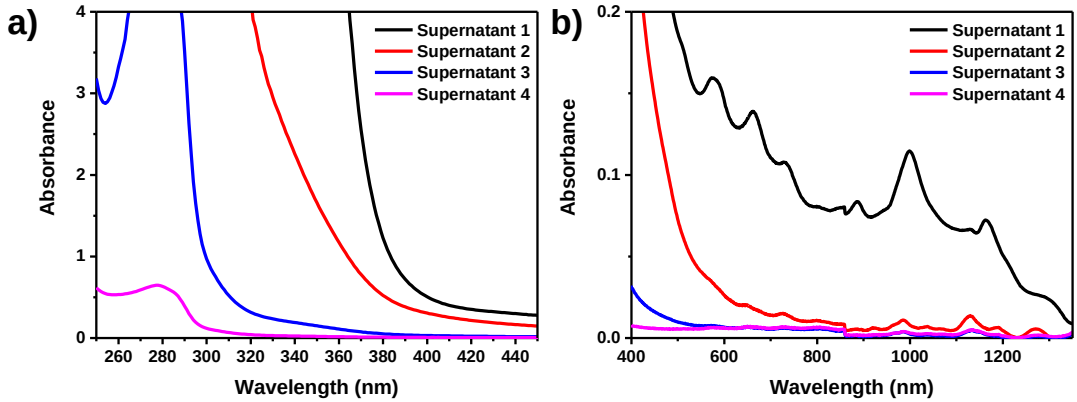

Figure 4.2. Analysis of the supernatant after pelletizing the SWCNT content extracted from a centrifugation run. In a) the SPT removal is tracked by the decreasing absorbance in the supernatant with each iteration. In b) the SWCNT content lost in each iteration is highlighted.

4.4. Nanotube Transistors

Network Transistors

For the SWCNT network transistor the conditioned sample was drop cast onto an aluminum oxide/silicon wafer (30 nm dielectric thickness) in single droplet steps at 70°C - 90°C substrate temperature. After evaporation of the water, the wafer was quickly dipped in 1 M HCl and afterwards placed in an Ethanol bath for 5 minutes. This procedure was repeated 30 times. The wafer was patterned with gold electrodes by vacuum evaporation. Channels of 50 µm length and 200 µm width were established. The characteristic curves were recorded with an Agilent B1500 Parameter Analyzer. Silicon oxide covered silicon wafers were also used (dielectric thickness 300 nm).

Self-Assembling Monolayers (SAMs)

Before immersing wafers in the SAM solutions, they were cleaned by an oxygen plasma for 2 minutes at 100 W. After cleaning the wafers were immersed in the respective dissolved SAM1 or SAM2 solutions for 24 h.

Freestanding Sheet Transistor

A part of the SWCNT sheet was deposited from a water droplet onto a quartz wafer and was subsequently dried at 70°C. Metal contacts were realized via thermal evaporation of gold through a shadow mask and formed a transistor channel of 1,000 µm width and 50 µm length. The IG was dried onto the sheet at 70°C and 5 mbar. A PEDOT:PSS gate electrode was drop-cast on top of the IG and dried for 30 min at 70°C to allow a better electrical contact between the IG and a probe needle.

4.5. Optical Characterization

UV-vis-NIR Absorption Spectroscopy

Optical analysis was performed recording the absorbance spectra of post-treated samples with the Perkin Elmer UV-vis-NIR Spectrometer Lambda 750 or Lambda 35 with 1 cm disposable cuvettes. The spectra were taken in ambient conditions. For low wavelength analysis, suprasil quartz cuvettes of 1 cm optical path length were used.

Raman Microscopy

Raman spectroscopy were recorded by the use of a ND-MDT Ntegra Spectra. The sample excitation was performed with a 514 nm and 633 nm emission wavelength laser. The laser was focused using an objective of 100 x magnification after finding the dried SWCNT spots in 10x magnification.

4.6. Atomic Force Microscopy

The morphology of SWCNT networks was determined by tapping-mode AFM (Bruker Dimension Icon). The SWCNT films were established on silicon substrates as described for the transistor measurements.

4.7. XPS Measurements

The XPS analyses were carried out with a Phi Versa Probe 5000 spectrometer using monochromatic Al Kα radiation (49 W).
XPS can detect all elements except hydrogen and helium, probes the surface of the sample to a depth of 5 - 7 nanometers, and has detection limits ranging from 0.1 to 0.5 atomic percent depending on the element. The instrument work function was calibrated to give a binding energy

(BE) of 84.00 eV for the Au $4f_{7/2}$ line of metallic gold and the spectrometer dispersion was adjusted to give a BE of 932.62 eV for the Cu $2p_{3/2}$ line of metallic copper.
The built in Phi charge neutralizer system was used on all specimens. To minimize the effects of differential charging, all samples were mounted insulated against ground.
Survey scan analyses were carried out with an analysis spot of 100 x 1400 μm^2 area, a pass energy of 117 eV and an energy step size of 0.5 eV. High resolution analyses were carried out on the same analysis area with a pass energy of 23.5 eV and an energy step size of 0.1 eV. S11 spectra have been charge corrected to the main line of the carbon 1s spectrum set to 284.5 eV as a typical value quoted for the energy of the peak of aromatic carbon.
C1s-Spectra were analyzed using CasaXPS (Casa Software Ltd) software version 2.3.16 using Shirley background subtraction in the energy region of 280 - 298.5 eV. Sp2-hybridized carbon was described by a Lorentzian asymmetric line shape with tail damping as provided by the software with an asymmetry index of 0.0913 allowed to vary its FWHM in the range of 0.7 to 1.3 eV. All other peaks were fitted using a sum function of 90%-Gaussian-10%-Lorentzian as provided from the software accounting for the presence of functional groups (Hydroxyl, carboxyl, Epoxy, as well as resonances from the aromatic system (shake-up structures and plasmon resonances) as given in the literature [171]. Relative sensitivity factors as provided by the instrument manufacturer were used for quantification. XPS measurements were performed with Arkadius Boron in the laboratory of Sabine Hirth (BASF SE).

4.8. Density Profile Measurements

The density profiles of gradients after centrifugation were measured by splitting the gradient into multiple fractions. Starting with the extraction of the topmost fraction, the centrifugation tube was emptied, using a cut pipette to extract very homogeneously from the complete surface (thereby mostly avoiding the drawback introduced for extraction of DGU nanotube bands (see Figure 1.3)), followed by the extraction of the lowest fraction. Each extorted volume was weighed and diluted with a certain amount of water to yield at least 2 ml of solution. The diluted fractions were homogenized on a rotating tray for at least 2 h. The density was measured twice, each time using 1 ml of the diluted fractions by employing a Kratky-balance (Anton Paar Density Meter DMA 5000M). The measured densities were corrected for the dilution factor including error propagation from dilution and standard deviations if multiple measurements could be conducted per sample.

4.9. Asymmetrical-Field Flow Fractionation (AF4) Analysis

The AF4 was performed using the separation system Eclipse AF4 from Wyatt Technology. The PAE sample was concentrated as 0.3 wt% (3 g/L) aqueous solution with 0.05M $NaNO_3$ and injected into the channel equipped with a 5k Dalton RC-membrane (Millipore). The detector flow was 0.5 ml/min. During the measurement an exponentially decreasing cross flow was used. The cross flow decreased from 4 ml/min to 0.1 ml/min over a period of 35 min. The separation system was equipped with a light scattering system (DAWN Helios-II) and a refractive index measurement system (Optilab T-rEX) both from Wyatt Technologies.

4.10. Electrophoretic Mobility

All measurements were carried out with the Zetasizer Nano from Malvern in pH-range from 2 to 11. The measurements were started at the original pH-value after dilution (7.3). The pH-value was adjusted with HCl and NaOH. All samples were measured at a background electrolyte concentration of 10 mmol/L KCl.

4.11. Viscometry

Kinematic viscosity measurements of all density media were performed with a shear rheometer (Anton Paar MCR 302). The density media were dissolved in DI-water to yield to give a density of 1.255 ± 0.005 g/cm³ and were measured at 25°C. The device rotates a cylinder within the medium at a given rate of rotation and measures how much force is necessary to achieve these rates. The viscosities of fluid samples are calculated from calibration with media of known viscosity.

4.12. Determination of Critical Micelle Concentration (CMC)

The PAE1 polymer was used in 1 wt% aqueous concentration to determine the critical micelle concentration of the PAE1 polymer. The polymer was stepwise diluted at 23°C while the surface tension was measured using the Krüss K100.

4.13. Refractive Index Measurements

The refractive index of various polymeric solutions were measured at 25°C using the Bellingham+Stanley Ltd. RFM 340 Refractometer. Approximately 1 ml of the respective solution was used and the recorded values were averaged over 10 measurements after thermal equilibrium was reached.

5. Characterization of Aqueous PAE/SWCNT Dispersions and Benchmark Dispersants

This chapter gives insight into how SWCNTs were dispersed with different dispersants including the PAE polymer and the subsequent characterization of PAE/SWCNT dispersions. Multiple experiments were set up to explore the properties of different dispersions and to classify the PAE dispersant among other polymeric dispersants.

At first, the PAE polymer is evaluated by looking into critical parameters connected to the dispersing ability for SWCNTs. Here, it must be recalled that the PAE polymer used in this thesis was custom synthesized and used as polymerized. However, polymerization typically leads to a polydispersity in the final product. The chemical structures can only be given idealized but in reality vary strongly. This is reflected by the molecule sizes, molecule weight or chemical molecule structure.

This is the reason why the first step in characterizing the PAE/SWCNT dispersions, was collecting data on the PAE polymer batch before moving over to analyzing the dispersing behavior in the ensuing sections.

5.1. Analysis of PAE Polymer

Molecular Weight Distribution of PAE1

To characterize the PAE polymer, the molecular weight distribution was measured by Asymmetrical-Field Field Flow Fractionation (AF4) as it is more precise compared to GPC measurements [154]. The molecular weight distribution is depicted in Figure 5.1a and shows two peaks. One corresponding to a molecular weight at the peak of about 8,800 Dalton and a second one with a molecular weight at the peak of 78,000 Dalton.

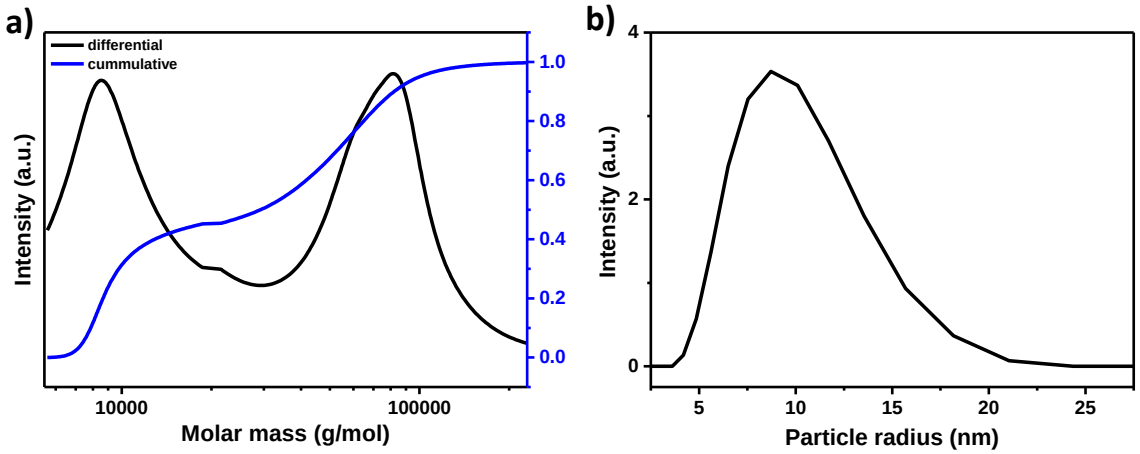

Figure 5.1. Molecular weight and size distribution of the PAE1 polymer. In a) the molecular weight distribution is shown differential (black) and cumulative (blue) as obtained by AF4 measurements. In b) the size distribution as measured by dynamic light scattering is shown for the PAE1 polymer in low concentration. The peak is linked to the individual polymeric dispersant but also to micelles starting to form at concentrations above the critical micelle concentration (CMC).

Dynamic light scattering (DLS) measurements of the PAE1 polymer in a low concentration (10 mg/L) were performed to complement the molecular weight distribution. However, DLS cannot resolve differences in particle size between 9,000 and 80,000 Dalton. One broad peak is observed corresponding to the polymer and micelle sizes present in the solution shown in Figure 5.1b.
The molecules of 8,800 Dalton were ascribed to the individual polymer, while the larger molecules were ascribed to micelle formation. To gain access to the particle sizes, a quasi-elastic light scattering detector (QELS) was used in the AF4 setup. This way the hydrodynamic radius R_h of the polymers and micelles at peak maximum was determined. The data analysis shows that the solution polymers have a radius of about 2 nm while the hydrodynamic radius of the micelles is almost twice as large.
The absolute values should be handled with care, however, the ratio of 2 between the hydrodynamic radii of individual polymers and micelles would fit a lateral extension of the micelle twice the size of the monomer as proposed in [172].

UV-vis-NIR Absorbance Spectrum of PAE

The UV-vis-NIR absorbance of the PAE1 polymer was recorded. A peak is observed at 278 nm. This peak was used for a concentration/absorbance calibration. Using this calibration the polymer concentration can be determined for unknown PAE1 concentrations. The complete calibration is summarized in the appendix.

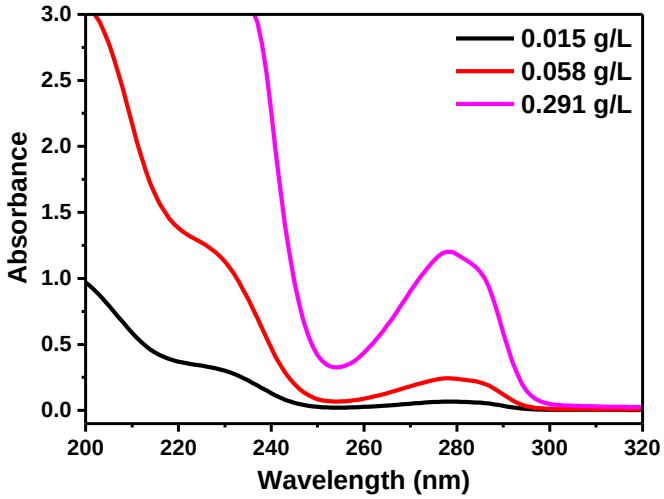

Figure 5.2. UV-vis-NIR absorbance of the PAE1 polymer.

Density of PAE1 Polymer

Additionally, the polymer density was measured via oscillating U-tube measurements and extrapolating the water diluted densities of the as-synthesized batch to 100% of polymer. This is done by calculating the partial specific volumes and averaging over multiple concentrations. The density was determined to be 1.61 ± 0.02 g/cm³. The measured density, however, is believed to be dominated by byproducts of the reaction (salts formed during neutralization of the low pH from the polymerization) and thus does not reflect the actual polymer density. The individual moieties of the PAE1 polymer have densities between 0.9 and 1.2 g/cm³. Additionally, the

complexes formed by SWCNTs and PAE1 will be shown to possess a buoyant density of about 1.15 g/cm³.

5.2. Effects of Dispersant Concentrations

Critical Micelle Concentration (CMC) of PAE1

A critical parameter that characterizes a dispersant is its critical micelle concentration (CMC). The CMC is the concentration of the dispersant in water, which if exceeded leads to the formation of micelles. The surpassing of the CMC improves the effective stabilization of SWCNTs in water using various surfactants [173]. The CMC was determined by concentration dependent surface tension measurements.

Figure 5.3a shows the surface tension in dependence on the concentration of PAE1 polymer given into the aqueous solution. The CMC was extracted from the graph to be about 0.370 g/L (0.037 wt%) by the interpolation of linear fits. Relating the CMC of the PAE1 polymer to the stability of the dispersions of PAE and SWCNTs was done by setting up PAE1 concentrations from 10^{-3} to 10 g/L. Each solution was used to disperse SWCNTs by sonication.

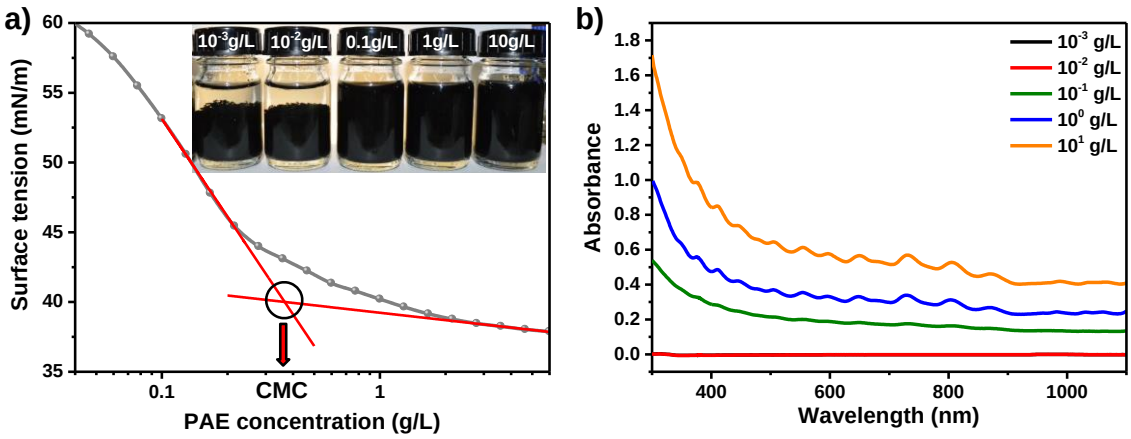

Figure 5.3 The formation of micelles in an aqueous PAE1 solution and its relation to the stability of a PAE1/SWCNT dispersions. In a) the surface tension was measured and related to the forming of micelles. The extrapolation to find the CMC is done in a logarithmic plot to minimize errors. In b) the absolute absorbance of SWCNT dispersions with different PAE1 concentrations was measured. Micelles starting to form at concentrations above the critical micelle concentration (CMC) support the individualization of SWCNTs, as evidenced by diameter-specific UV-Vis-NIR peaks.

The resulting dispersions are shown in an inset in Figure 5.3a. The PAE1 concentrations range from 10^{-3} to 10 g/L, where effective dispersing of SWCNTs is starting from 1 g/L. Each of the dispersions was centrifuged shortly (30 min 250,000 x *g*) to evaluate the nano content (individualized and small bundles of SWCNTs) in each dispersion. This is done by measuring the absolute absorbance of the supernatant by UV-vis-NIR spectroscopy [49]. The absolute absorbance spectra of the extracted supernatant after centrifugation are shown in Figure 5.3b. Before going into a detailed analysis of SWCNTs spectra (found in 0) only the appearance of peaks and the total absorbance will be considered. It is shown that nanotubes (peaks) are found

at concentrations of and above 0.1 g/L. Exceeding the CMC of 0.37 g/L supports the stabilizing of SWCNTs as an increasing total absorbance is recorded from 0.1 - 10 g/L of PAE concentration. The appearance of SWCNTs in the supernatant at a concentration below the CMC can be explained. For ethylene oxide/propylene oxide type polymers it was found, that micelles do not form at a fixed concentration but rather over a wide concentration range [174]. The same is expected in the micellization of aqueous solution of the PAE1 polymer due to its polyethylene oxide moieties (see 3.2) and the polydispersity of the as polymerized PAE1 polymer, in line with the change of dispersing action over a wide range from 0.1 to 10 g/L.

Aqueous Dispersion of SWCNTs

The exceeding of the CMC was shown to support the dispersing of SWCNTs in water. The evaluation of SWCNT dispersions was enabled by UV-vis-NIR spectroscopy, but individual peaks still remain to be assigned. Here, the characterization of SWCNT dispersions by UV-vis-NIR spectra will be presented for the different SWCNT materials that are used in this work.

The PAE dispersant (PAE1) was used to disperse three different raw SWCNTs materials. Here all three different SWCNT sorts (HiPco, Arc Discharge (AD) and Plasma Torch (PT)) were dispersed via horn sonication in different aqueous PAE1 concentrations. After sonication, the dispersions (0.5 ml) were diluted to 1/5 by volume using the respective aqueous PAE1 solution. The absolute UV-vis-NIR absorbance spectra are shown in Figure 5.4 for each combination of polymer concentration and SWCNT raw material. In literature it was already shown that the dispersing of SWCNTs does not depend on the dispersant to nanotube ratio, but rather on the total concentration of dispersant in the solution [49]. The spectra reveal the characteristic absorption peaks of SWCNTs.
For the small diameter HiPco material multiple peaks are observed resulting from metallic M11 and semiconducting S22 transitions in the visible region. Semiconducting S11 transitions appear between 1000 - 1350 nm.
The larger diameter plasma tubes show only slightly pronounced peaks between 600 - 700 nm from metallic M11 transitions and between 800 - 1100 nm from semiconducting S22 transitions. The shift in wavelengths of same order transitions compared to the HiPco spectra results from the different diameter distribution.
For the AD nanotubes the peaks appear clearer and are redshifted further so that semiconducting S33 transitions can be observed from 400 - 550 nm. Metallic M11 transitions are found from 600 - 800 nm and semiconducting S22 transitions are starting from 900 nm and extend to 1200 nm.
The individual transitions are differently strong pronounced, which results mainly from the relative content of nanotube material. While 90 wt% of the raw material are nanotubes in the AD sample, the diameter wise comparable PT sample contains only 30 wt% of nanotubes. On the other hand different diameter SWCNTs show differently pronounced absorbance peaks [49]. For HiPco SWCNTs the diameter distribution is shifted so that the higher order transitions lie in the visible region, resulting in distinct peaks although the raw materials contained only 5 – 13 wt% of nanotubes (here 5 wt%).

The comparison of all spectra shows that 0.1 wt% (1 g/L) of polymer is enough to effectively disperse the three SWCNT sorts, however for HiPco SWCNTs 2 wt% (20 g/L) of PAE1 polymer shows the highest yield. The Plasma grown SWCNTs show similar yield for all PAE concentrations, and for the AD nanotubes the highest yield is obtained using 1 wt% of PAE1.
All three SWCNT sorts result in acceptable dispersions using the PAE1 dispersant and will be used in centrifugation experiments (see chapter 6). However, the absorbance is not within the linear region of the detection system so no direct quantitative comparison between the materials can be performed here.

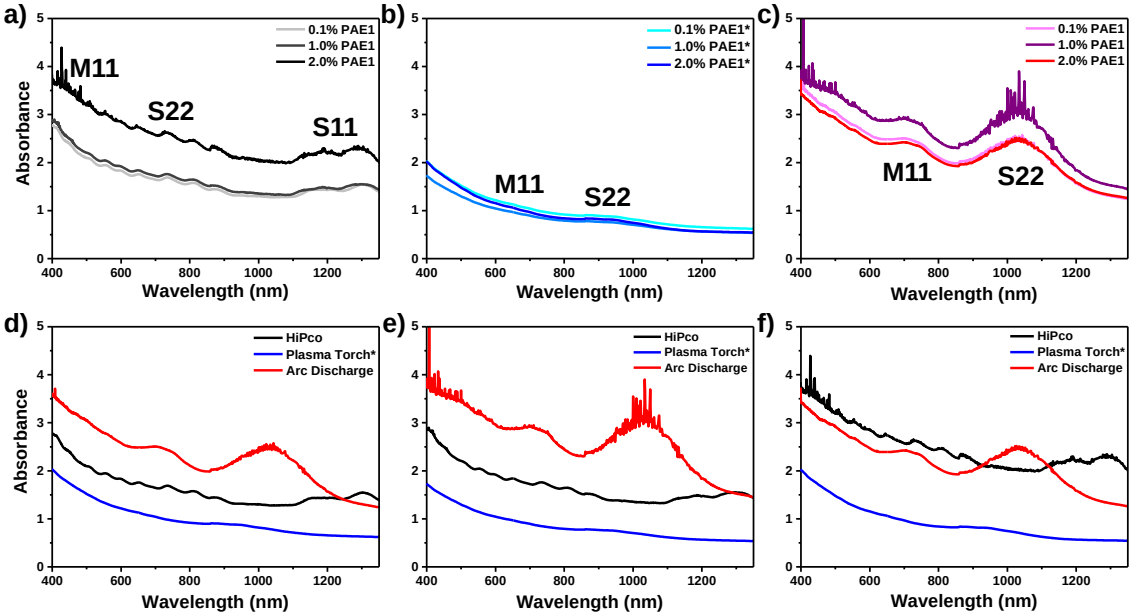

Figure 5.4. Absolute absorbance spectra of SWCNTs dispersed with different concentrations of PAE1. UV-vis-NIR absorbance spectra are shown in a) for 0.5 wt% HiPco material dispersed with different aqueous concentrations of the PAE1. In b) the Plasma grown- and in c) the Arc-discharge SWCNTs are shown for the same concentrations. Spectra marked with an asterisk * were additionally diluted to 1/5 of the concentration described. In d), e) and f) the different SWCNTs are shown for one fixed concentration of aqueous PAE1. All spectra taken in 1 cm cuvettes.

5.3. Effects of Dispersion Temperature

Dispersing SWCNTs in Dependence on Temperature

The complex colloidal system formed by the combination of PAE1 as the stabilizing dispersant and different sorts of SWCNTs in water is the foundation of this work. The initial combination of both under the influence of ultrasonication was probed in various directions. Above, a dependence of the SWCNT dispersion on the polymer concentration was discussed. In this section, the temperature during the dispersing by sonication is monitored and controlled. Typically, an ice cooled water bath is applied to cool the dispersion, because it has been shown to support the preparation of a practicable dispersion of nanotubes [36, 119, 175].

For an investigation of the temperature's influence on the resulting dispersion quality, the absorbance was measured after different sonication times at two different temperatures. Room temperature and 55°C were used to complement the horn sonication cooled with ice displayed in the previous section.
Exact controlling of the temperature during horn sonication is hindered by evaporation losses of the solvent due to the requirement of an open setup. Therefore the cup sonication system was used. This sonication setup was depicted in Figure 4.1. The sonicator sonicates the interior of a cup mounted on top of an inverted horn sonicator. This cup was flushed with an adjustable water flow. The temperature was controlled between the temperatures of the connected tap water lines and higher temperatures of about 55°C, where the water flow is low so that this temperature was maintained. In detail, during this experiment the temperature varied either between 25 - 26°C for the first temperature dependent dispersion measurements or between 53 - 55°C for the second measurement row.
The analysis was performed using 1 ml of the resulting dispersion, extracted from the meniscus area after selected times of sonication in the two different temperature ranges. The respective samples were measured versus the respective reference solution in disposable 1 cm cuvettes at room temperature. Each spectrum was recorded after the as extracted 1 ml were allowed to settle for 20 min. This way larger agglomerations were excluded from the signal.

Extraction times were 2 min, 5 min, 10 min, 30 min and 60 min of sonication time. To extract samples from the 55°C dispersions, the dispersion was cooled to 25°C and reheated before the dispersing process was continued. This procedure was performed to hinder the deposition of material to the sidewalls of the pipettes.
The sonicator system was set to 50% amplitude for the complete duration of the sonication process.
The raw material is only marginally dispersed in 60 min of sonication, however, this experiment aims at optimizing temperature.
By selecting low dispersing power the onset of dispersed material accumulating in the liquid phase could be monitored in small steps between initially wetting the raw material in the polymer solution and a nanomaterial containing dispersion.

Different dispersants were tested in combination with HiPco SWCNTs. Those dispersants were the surfactant sodium cholate hydrate (SCH), the PAE1 polymer and the polymeric dispersant Pluronic F108 (F108). Figure 5.5a, d show the spectra of the samples taken after 2 min, 5 min, 10 min, 30 min and 60 min of sonication time for a 2 wt% SCH/0.5 wt% SWCNT dispersion prepared in both temperature ranges, respectively. Figure 5.5b, e and 5.4c, f show the spectra for samples taken after the same sonication times for the 2 wt% PAE1/0.5 wt% SWCNT dispersion and the 2 wt% F108/0.5 wt% SWCNT dispersion prepared in both temperature ranges, respectively.
Starting with the spectra for SCH at 25°C, the absolute spectra in Figure 5.5a, b, c show that the dispersion process starts noticeably after 30 min of cup sonication. The same observation can be deduced from Figure 5.5b for PAE1. The dispersing process for F108 in Figure 5.5c, however, starts promptly and nanotubes are noticeably found in the supernatant already after 2 min of

sonication. Comparing the spectra taken for each dispersant after 60 min at 25°C reveals that SCH and PAE1 disperse SWCNTs comparably, while F108 can disperse a larger amount of SWCNTs at 25°C in this setup.

When moving the observation to the 55°C spectra of SCH in Figure 5.5d it is shown that the dispersion process is accelerated and SWCNTs are found in the supernatant already after 2 min. After 10 min of sonication at 55°C the same amount of nanotubes as after 60 min of sonication at 25°C using SCH.

When considering the polymeric dispersants PAE1 and F108, the complete opposite is found in Figure 5.5e, f. The preparation of a SWCNT dispersion is hindered to a great extent. In both cases the absolute absorbance drops to about one third of the total absorbance seen at 25°C comparing the 60 min spectra. This shows that at higher temperatures the formation of the two polymeric SWCNT dispersions is suppressed, while the surfactant SCH actually shows greater affinity for dispersing SWCNTs in terms of the shorter time necessary to achieve the same absorbance.

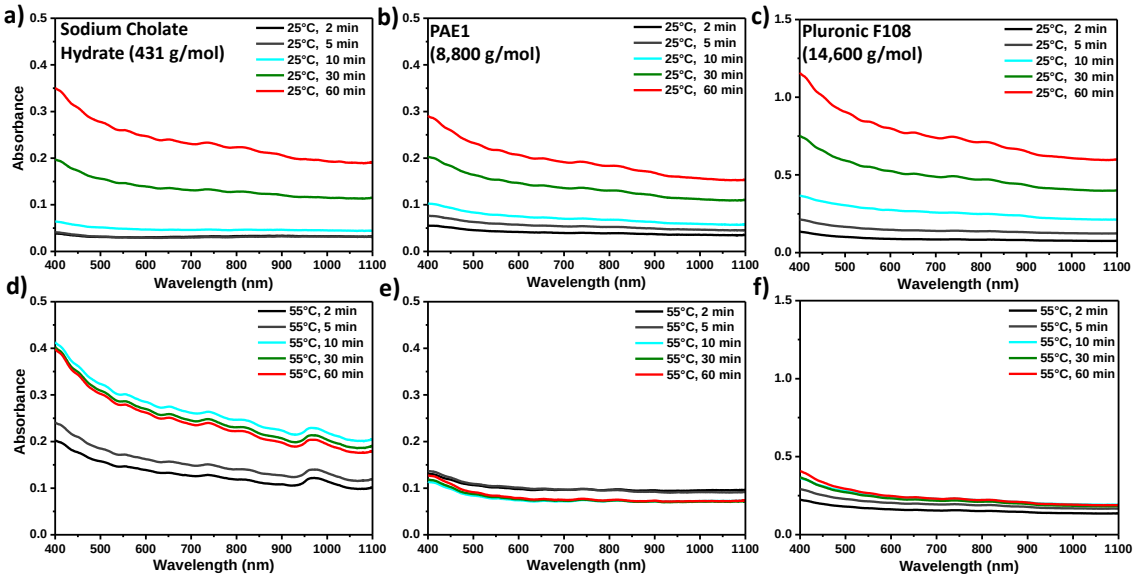

Figure 5.5. Spectra of SWCNT dispersions prepared at different temperatures. Ambient conditions are shown in a), b), c), while temperature conditions of 55°C are depicted below in d), e), f). In a) and d) spectra of SWCNT dispersions in aqueous sodium cholate hydrate are shown for both temperatures, respectively. In b), e) the dispersions were prepared using the PAE1 and in and c), f) Pluronic F108 was used.

Figure 5.6 shows the onset of dispersing raw HiPco SWCNT material in water by the use of different surfactants by the normalized spectra from Figure 5.5 in the same order of panels.

For SCH the normalized 2 min and 5 min spectra show no peaks. This means that nanotubes are firstly found in the extracted samples after 10 min of sonication time at 25°C. At 55°C the SCH dispersion contains nanotubes already after 2 min, which is shown by the abundance of the distinct peaks in the 2 min spectrum.

In case of the polymeric dispersants, the normalized spectra in Figure 5.6b, e and c, f show the features of SWCNTs at each time and temperature. The dispersions already contain nanotubes

after 2 min of sonication. This shows that although the polymeric dispersants used are noticeably restricted in their dispersing ability, the mechanism is not completely lost.

The normalized spectra can also be used to evaluate the nanotube diameter distribution with time in the dispersion.

For all dispersants the peak distribution found in the spectra shows no differences. That means no selectivity for any diameter range is observed in the arising nanotube dispersions. However, it must be noted that SCH shows a peak in absorbance at 970 nm only at 55°C. This peak is not observed in any other sample. This could indicate an increased individualization of the small diameter (6,5) (S11 at 975 nm) or (7,3) (S11 at 992 nm) SWCNT [55].

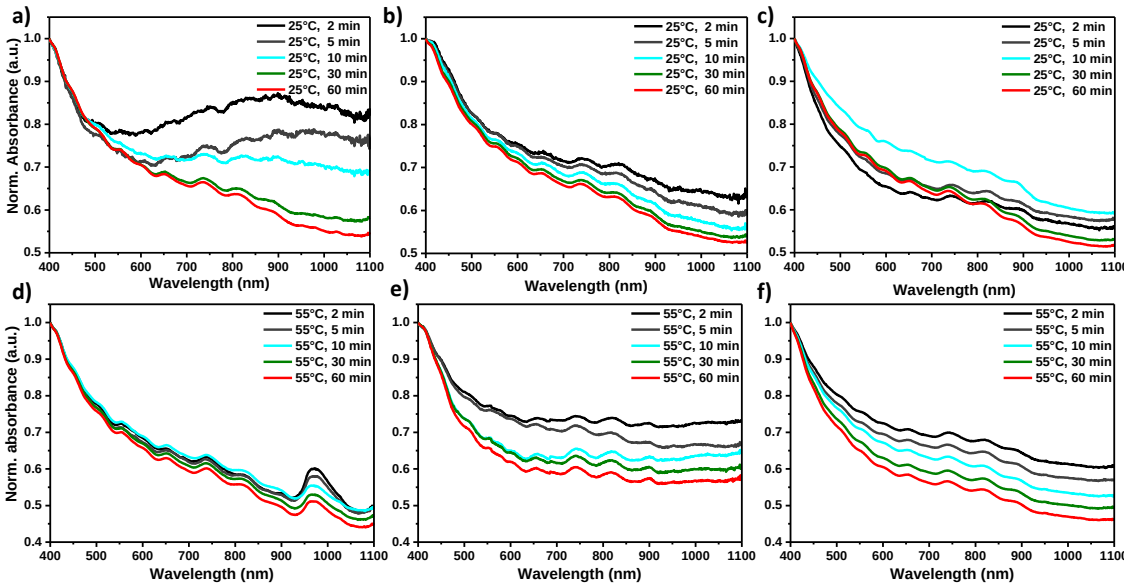

Figure 5.6. Normalized (400 nm) spectra of SWCNT dispersions prepared at different temperatures. Ambient conditions are shown in a), b), c), while temperature conditions of 55°C are depicted below in d), e), f). In a) and d) normalized spectra of SWCNT dispersions in aqueous sodium cholate hydrate are shown for both temperatures, respectively. In b), e) the dispersions were prepared using the PAE1 and in and c), f) Pluronic F108 was used.

The quality of the dispersions is summarized in Figure 5.7 as the integral absorbance area in the 400 - 1100 nm interval for each time of sonication, temperature and dispersant. The qualities of the polymeric dispersions at 55°C never reach the same level that was already obtained after 30 min, 25°C for PAE1 and for F108.

At low temperature 25°C, SCH shows a linear dependence of dispersion progress with sonication time. At higher temperatures (55°C) the dispersion progress is accelerated and reaches a plateau level after 10 min.

For the polymeric dispersants the dispersion progress with time appears similar for both temperatures. The PAE1 polymer shows linear dependency of dispersion progress on time at 25°C. However, there is no dependence of the dispersion on sonication time at 55°C. This behavior is also observed for Pluronic F108, but yielding a higher absolute absorbance at both temperatures, meaning more dispersed material is found using F108.

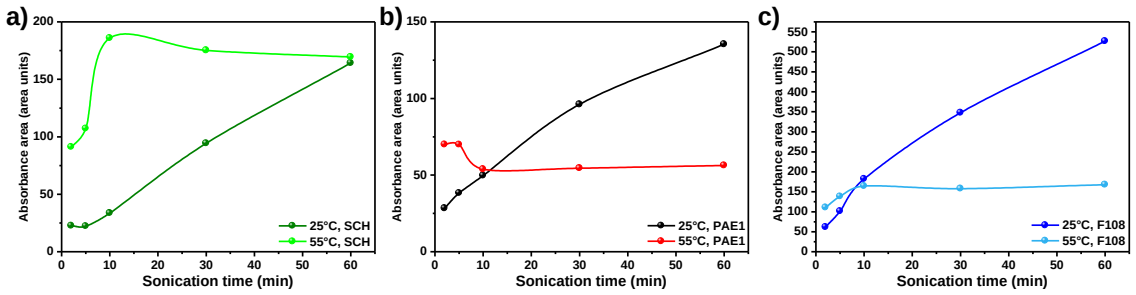

Figure 5.7. The quality of the dispersions is shown depending on time of cup sonication. In a) the area under the absorbance spectra from Figure 5.4a, d is shown. In b) the area under the absorbance spectra from Figure 5.4b, e is shown. In c) the area under the absorbance spectra from Figure 5.4c, f is shown.

Table 5.1 shows the increment of linear fits to the data displayed in Figure 5.7. This increment can be seen as a rate of dispersion progress for the different dispersants in the two temperature regions. The figures indicate that the polymeric dispersants have reached a plateau level for dispersing material when moving to higher temperatures so that no more material can be dispersed.

However, also the surfactant SCH reaches a plateau level after 10 min of sonication at 55°C. The plateau in arising dispersions seems to be a general feature of dispersions sonicated at 55°C.

Dispersant:	Rate of dispersion progress: (25°C) [1/min]	Rate of dispersion progress: (55°C) [1/min]
SCH	2.5±0.1	12.3±2.8/-0.3±0.1
PAE1	1.8±0.2	-0.2±0.2
F108	7.9±0.7	-0.7±0.4

Table 5.1. The development of SWCNT dispersions with SCH, PAE1 and F108. The dependence on sonication time and temperature are summarized. The dispersion rate for SCH at 55°C was divided into two region, before and behind the plateau level.

Summarizing this experiment, higher temperatures during sonication induce a plateau level for dispersing material in aqueous dispersant solutions in our given setup (sonication power, time). The exfoliation is hindered with the tested polymeric dispersants. However, temperature also shifts the affinity of SCH so that rapid dispersing of SWCNTs results until the plateau level is reached. When additionally considering the photographs of the dispersions shown in the Appendix (Figure 10.4 & Figure 10.5) after the given sonication times for both temperatures, larger agglomerates were observed at higher temperature. Similar results were found, when heating a dispersion, previously formed in an ice cooled water bath, was probed. This led to bundling of SWCNTs [176]. The results discussed above showed how the preparation of dispersions is limited at high temperatures. The observed effect was tremendous, especially for

the tested polymeric dispersants (PAE1, Pluronic F108). The dispersions prepared at 55°C lost about 66% of absorbance compared to dispersions prepared at 25°C in the same setup.

Temperature Influence on Dispersants

In this section the molecule sizes of the three dispersants including sodium cholate hydrate (SCH) in the absence of SWCNTs are investigated in dependence on the surrounding temperature by DLS. Thirty measurements at each temperature were averaged. In Figure 5.8 the hydrodynamic radii distribution as determined by DLS measurements of SCH (a), PAE1 (b), and F108 (c) are shown. The size distribution of all dispersants feature one peak, which can be related to the individual molecules and foremost the formed micelles at 20 g/L for each surfactant or polymer. When focusing on SCH, the distribution experiences a small shift towards smaller sizes. This indicates that slightly less micelles are present corresponding to more individual surfactant molecules as a result of the temperature increase. For the PAE1 polymer the particle size distribution shift slightly to larger particle sizes after heating from 25°C to 55°C. However, the results for SCH and PAE1 have to be handled with care as can hardly resolve particles on a 1 nm scale. When considering the Pluronic F108 solution, the particle size distribution shows one large peak at 25°C at approximately 6 nm. This peak shifts and only one single peak at 20 nm average size is observed after heating the solution to 55°C.

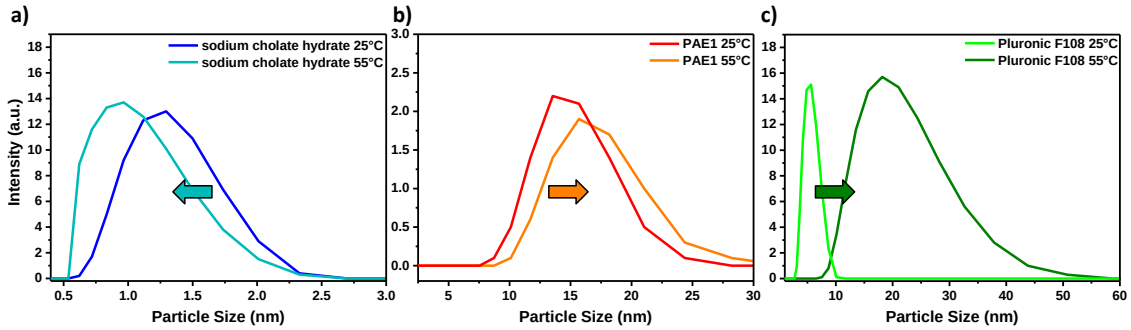

Figure 5.8. DLS measurements for the hydrodynamic size distributions of three dispersants in aqueous solutions (20 g/L) at different temperatures. The particle size distribution of SCH (a), PAE1 (b) and F108 (c) was measured at 25°C and 55°C.

While the results for SCH and the PAE1 polymer cannot give a clear indication of why the dispersing of SWCNTs at 55°C is promoted or hindered compared to the lower temperature dispersion process, the particle size distributions of Pluronic F108 shows a clear difference with increasing temperature.

The shift towards greater particle sizes in the aqueous F108 solution indicates that fewer individual polymer molecules are present and can support effective stabilization of SWCNT material as it was observed at 55°C. The polymer particles assembled into larger structures. This indicates increased micelle formation. Actually the CMC was found to be temperature dependent using Pluronic polymer F127 or F108 [177, 178]. The temperature dependency can be visualized as a micellization boundary in a temperature concentration plot.

The small shift towards smaller particle sizes with SCH meaning less micelles could explain the faster stabilization of the nanotube material as observed. However, the absolute absorbance after 60 min of sonication stayed unaffected by the increase in temperature, indicating that the amount of dispersed SWCNTs did not alter and the surfactant concentration did not change noticeably. However, increased diffusion of the SCH molecules at higher temperatures could be a factor resulting in faster dispersing without resulting in a higher yield.

Temperature Dependent CMC

The temperature dependence of the CMC of the tested dispersants SCH, PAE and F108 differed significantly. The individual dispersant's CMCs are plotted in dependence on the temperature in Figure 5.9 to indicate the micellization boundaries. In Figure 5.9 micelles form in the regions above the indicated lines between the measured or reported CMCs.

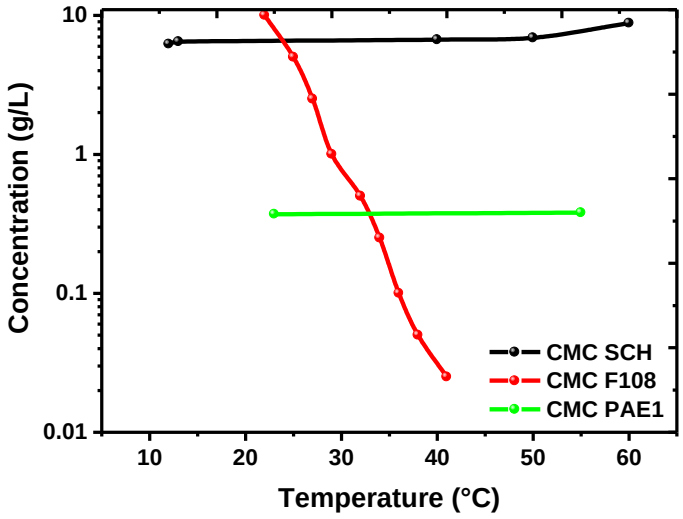

Figure 5.9. The CMC of different dispersants is plotted as function of the temperature and concentration. Values for F108 and SCH were taken from [178, 179], respectively.

For higher temperatures the CMC of SCH increases slightly leading to a lower degree of micellization in aqueous solution [179]. Fewer micelles are present in the solution the higher the temperature is. However, more molecules are not automatically related to better stabilization as shown by concentration dependent dispersing of SWCNTs in [49]. In the present study it is observed that the total amount of dispersed nanotubes stays unaffected, although the dispersing of nanotubes seems to be accelerated at higher temperature.

The opposite behavior was reported for F108 [178]. The CMC decreases with increasing temperatures so that at 55°C many micelles have formed at an aqueous concentration of 2 wt%. This can be correlated to reducing the polymer concentration in the solution, which subsequently limits the dispersing capability of nanotubes.

The CMC of the PAE1 polymer was not found to be temperature dependent. Therefore it cannot be linked to the decreased dispersing ability at 55°C. The broad molecular size distribution of the

PAE1 polymer leads to an average CMC value. The differences in CMC induced by temperature cannot be determined by surface tension measurements. Increased micellization can be a factor, when considering the hindered dispersability of SWCNTs at high temperatures with F108. For the PAE1 polymer this cannot be confirmed with the obtained data.
To explain why both polymeric dispersant lose 2/3 of their dispersing ability at 55°C compared to 25°C, one can focus on the similarities in their chemical structure. Both polymers include PEO chains. PEO chains were found to dehydrate with increasing solution temperatures [180, 181]. The dispersion subsequently loses steric stabilization and aggregation is favored as found for both polymers.

5.4. Effects of Dispersion pH

pH Influence on SWCNT Dispersion with PAE1

An aqueous 2 wt% PAE1 and 0.5 wt% HiPco SWCNT dispersion was probed with respect to the pH value. The response of the dispersion was monitored by UV-vis-NIR spectroscopy after changing the pH value of the dispersion using 1M HCl or 1M NaOH, respectively. The dispersion was diluted by a factor of 100 prior to adjusting the pH value. Photographs of the dispersions after 24 h are displayed in Figure 5.10.

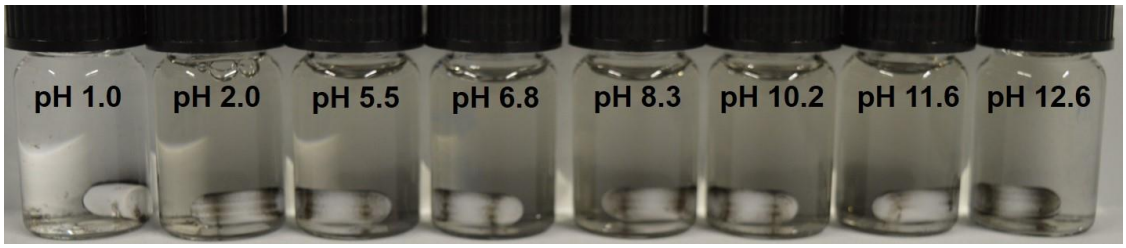

Figure 5.10. Photographs of the pH dependent dispersions. A dispersion with 2 wt% PAE1 and 0.5 wt% raw HiPco SWCNT material was diluted by a factor of 100. 8 different vials were set up at different pH values as labelled in the Figure. UV-vis-NIR spectra of each dispersion were recorded 5 min and 24 h after adjusting the pH, respectively.

UV-vis-NIR spectra were recorded 5 min after setting the pH value and after additional 24 h of resting. The spectra are shown in Figure 5.11. The absolute absorbance drops to lower values with time for each pH. The strongest pH response is found at pH 1.0, where the SWCNTs agglomerated visibly within 24 h (see Figure 10.6 for photographs of the dispersion after 96 h). The smallest differences are found in basic pH conditions. The difference at pH 7 is best explained by the dilution of the dispersion (less absolute dispersant concentration). Compared to this dilution induced loss, the dispersions are stable above pH 2 over a time period of 24 h. However, the stability of the dispersion is lost at pH 1.0 within 24 h. The distribution of nanotube peaks does not change, for any pH value with time.

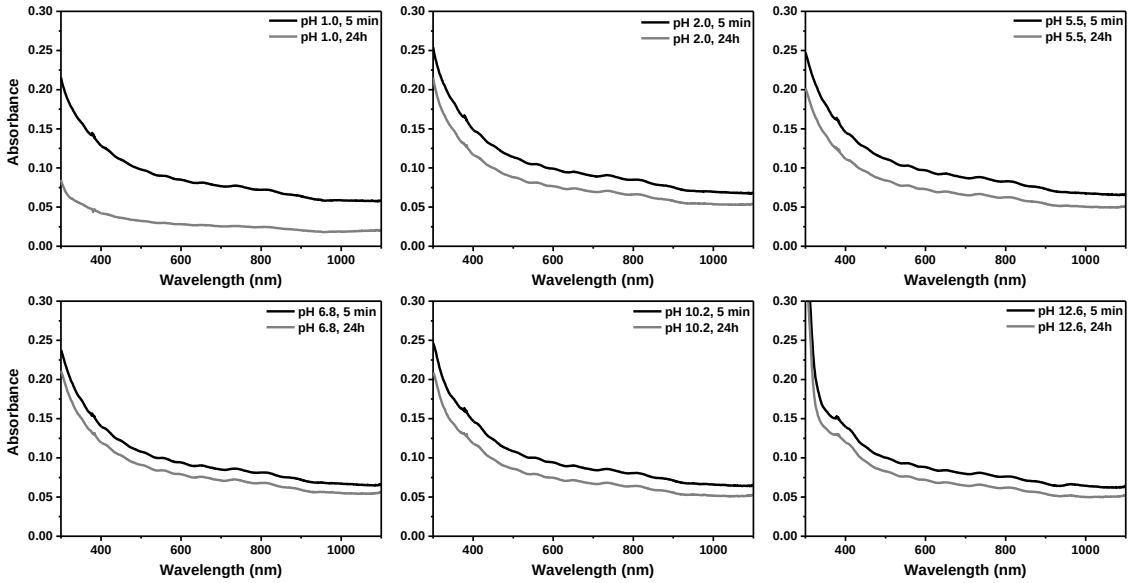

Figure 5.11. Dispersions of 2 wt% PAE1 with HiPco SWCNTs at different pH values. The absolute absorbance of the dispersions is shown at different pH values for different times. Spectra were taken 5 minutes after the dispersion was pH modified for acidic and basic pH conditions between pH 1.0 to 12.6 and 24 h after the pH modification.

These differences between the spectra at 5 min and 24 h were additionally captured in Figure 5.12 as the difference in area between the respective spectra for each pH value. From a trend line inserted to follow the data one could assume that the dispersion at pH 2 is also not stable. Indeed, the corresponding dispersion was found completely agglomerated after 2 weeks of resting.

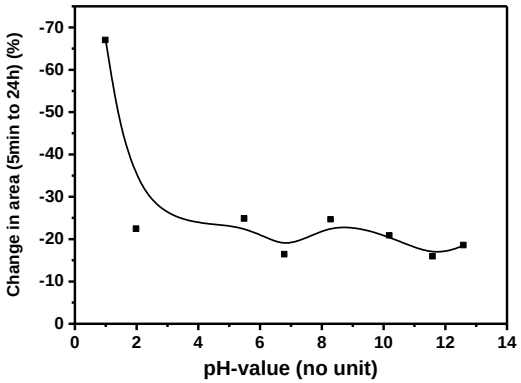

Figure 5.12. The loss in yield after 24 h of dispersions set to different pH values is illustrated. The area changes between the different time spectra in Figure 5.11 and between the spectra of different times for two additional pH values are shown in %. This indicates the time dependent loss of stability with respect to pH values of the dispersion. A trend line (B-spline) was inserted as guide for the eye.

Electrophoretic Mobility

The PAE1 dispersion was tested for its electrophoretic mobility to complement the influence of different pH conditions onto the dispersion. To remove all carbonaceous impurities from the raw

dispersion, the HiPco SWCNTs dispersed with PAE1 were submitted to density gradient ultracentrifugation (DGU) at neutral pH to. In detail 0.5 ml of the PAE1 nanotube dispersion (set to pH 4) were loaded on top of a density column (4 ml of 25.5 wt% of SPT at pH 7) and centrifuged at 40,000 x *g* for 10 h. After extraction of the SWCNTs they were pelletized by centrifugation in DI-water, rinsed with DI-water and re-dispersed in an aqueous solution of PAE1 (2 wt%).

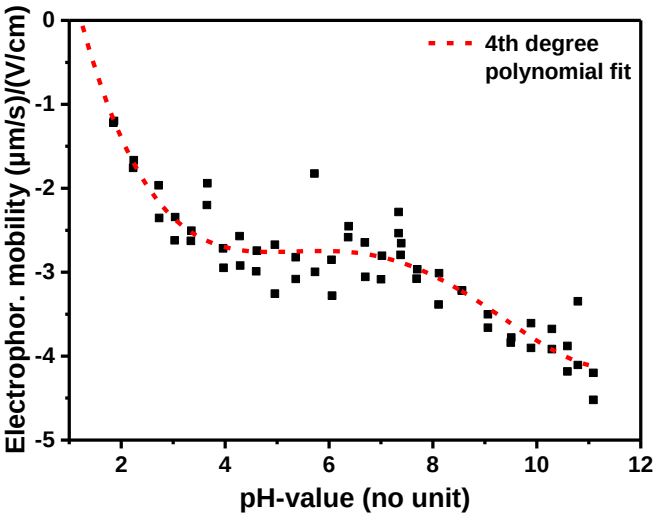

Figure 5.13. Electrophoretic analysis of SWCNTs dispersed with PAE1. The electrophoretic mobility was measured for different pH values. The electrophoretic mobility decreases significantly in the critical pH-region below 3, due to neutralization of surface charges. A fourth degree polynomial is fitted to the data to indicate the trends.

The electrophoretic mobility was subsequently measured and is shown Figure 5.13. At neutral pH the absolute value of electrophoretic mobility of the PAE1/SWCNT complex is 3 (µm/s)/(V/cm) due to the surface charges. A decrease in the absolute value of the electrophoretic mobility was observed below pH 3, which could correspond to a decrease in surface charges as consequence of protonation of the phosphoric acid group of the PAE1 polymer (pK_a = 2.15) [182]. This means the PAE1/SWCNT complex is neutralized, when lowering the pH, especially when then pH is lower than 2.15. Extrapolating the measurement to pH 1 would result in zero mobility, which corresponds well to the instability of the dispersion at this pH value, which was observed and described in section 5.4. In acidic environment the electric field is also screened by the increasing amount of H^+ ions in solution resulting in decreasing mobility

The conclusion from these measurements is a negative surface charge of single-walled carbon nanotubes dispersed by PAE1 molecules. This negative charge is neutralized by adding protons to the solution. If the PAE1/SWCNT dispersion is highly acidified, the dispersion aggregates rapidly, because the neutralization of the surface charges leads to instability of the dispersion.

5.5. Benchmarking of Dispersant's Adsorption and Effectiveness

Adsorption of PAE1 and Other Benchmark Dispersants onto Different SWCNTs

In this section the amount of polymer adsorbed onto the surface of the SWCNT materials is determined. The adsorbed polymer amount was determined by measuring the absorbance of the free polymer in the supernatant of the nanotube dispersions and calculating the concentration of the adsorbed portion via the extinction coefficient from calibration concentrations for PAE1 or via refractive indices for the Pluronics. The calibration graphs and calculations are summarized in the appendix section 10.7.
The aqueous polymer concentrations were set up in the given concentrations displayed in Figure 5.14. Typically, 30 g of total dispersion were prepared using 2.5 wt% of SWCNT material by 36 min of horn sonication. The supernatant samples were comprised of the complete supernatant (only the material that stuck to the bottom of the centrifugation vessel was discarded), which was extracted after centrifuging three times at 250,000 x g for 4 h from each dispersion. It is assured that most SWCNTs are pelletized by this procedure, leaving only free (non-adsorbed) dispersant in the supernatant. For the PAE1 polymer the concentration was determined by the absorbance of its characteristic absorbance peak at 278 nm in diluted (1/100 by weight) fractions of the samples. For the Pluronic polymers no such characteristic peak exists and the calculation of the concentration was performed after measuring the refractive index of the supernatant at 589 nm. Unfortunately, at this wavelength contributions from residual nanotubes in the supernatant cannot be excluded completely. Therefore and from error propagation in the calculations large errors of 0.5 g/L were included in the graph. The measured refractive indices for the Pluronics and Tetronic absorbance values for PAE1 are summarized in the appendix section 10.7.

In Figure 5.14 the adsorption of a PAE1 polymer, set at different concentrations, on HiPco raw material with a 5 wt% SWCNTs content (as delivered) is presented. Purified samples with higher SWCNT content are also tested in combination with selected concentrations.
At low polymer concentrations, a very steep increase in adsorption can be seen. At concentrations above 15 g/L, the strong increase is greatly reduced and the amount of adsorbed polymer remains almost constant with an average value of about 1.25 g/L. Clearly, at higher amount of polymers the carbon surface is saturated leading to a plateau region. The pre-plateau adsorption data can be fit with a Langmuir isotherm (black line) and is added here as a guide to the eye. This good fit might also suggest that the PAE1 adsorbs as a single layer as long as free surface sites are available.
For an initial polymer concentration of about 50 g/L a slight decrease in the adsorption can be seen. The decrease in adsorption at extremely high concentrations is known in literature and is not specific to this system [183]. This could be due to the polymer's broad polydispersity.
It remains unanswered, which part in the broad molecular weight distribution is responsible for the dispersing qualities of PAE1. The molecular weight is linked to the length of the polymer chain. If polymers of different size are present in a solution, the adsorption was shown to be competitive. In competitive adsorption it was reported that long chain molecules adsorb rather

than short chain molecules and this competitive adsorption is believed to cause the decrease in adsorbed material at higher concentrations [184].

In order to evaluate the influence of the SWCNT content, adsorption at higher initial PAE1 concentration (20 g/L) on materials with higher SWCNT content was also measured. Also here a concentration of 25 g/L was used but for raw SWCNTs from HiPco materials and arc discharge containing 80 wt% and 90 wt% of SWCNTs, respectively. The adsorption on both samples is comparable to the adsorption on the material with only 5 wt% SWCNT content. This shows that the adsorption of the PAE1 polymer is not strongly dependent on the carbon morphology nor on the SWCNT mean diameter. Apparently, the PAE1 dispersant does not discriminate between different carbon surfaces.

For three further polymers the concentrations of adsorbed polymer were measured using 30 g/L as input concentration with the same HiPco starting material (5% SWCNTs). The three polymers included Pluronic F68, Pluronic F108 and Pluronic PE10500. They show lower adsorption than the PAE1 polymer in this concentration. This result fits to the SWCNT contents measured and depicted in Figure 5.15. Pluronic F68 showed no quality in dispersing individual HiPco SWCNTs, however, it still adsorbs to the surface of the raw HiPco carbon material. From literature it is known that polymeric dispersants usually discriminate between sources of carbon material thereby strongly depending on the mean diameter in case of SWCNTs [49]. In detail Pluronic polymers showed different dispersing qualities firstly depending on the diameter of the nanotubes and secondly when considering only one SWCNT material depending on their dispersant structure. Most relevant for Pluronic polymers is the ratio of the PEO to PPO chain lengths decisively determines the adsorption properties on different SWCNTs [48].

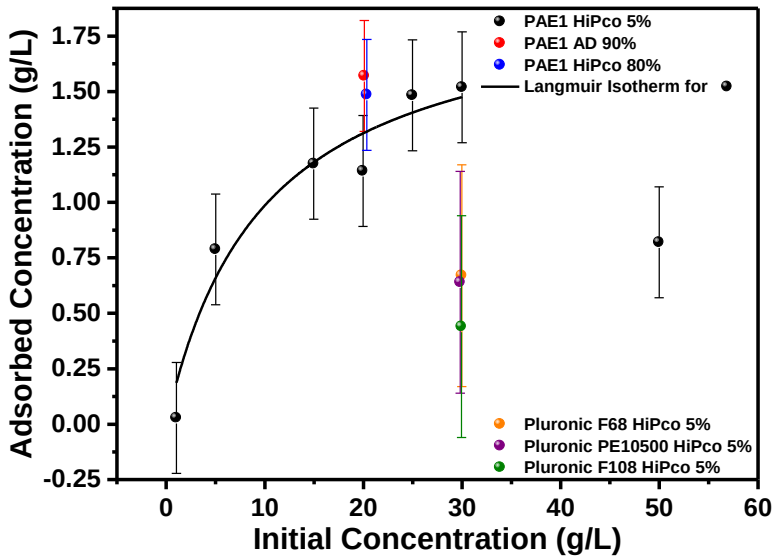

Figure 5.14. The adsorption of polymers on SWCNT material in aqueous dispersion. The adsorption isotherm of PAE1 was measured on 2.5 wt% SWCNT material for different initial PAE1 concentrations at pH 7 via absorbance. Point measurements using other SWCNT materials and or Pluronic dispersants are also displayed. The HiPco PAE1 dispersion roughly follows a Langmuir isotherm for ideal adsorption. It is shown that higher nanotube contents in the raw material do not influence the amount of adsorbed material of PAE1 polymer. For 30 g/L it is shown that other polymers do not adsorb to the same degree as the PAE1 polymer onto the available surfaces.

Dispersions of HiPco SWCNTs with Polymeric Dispersants

In a test of polymeric dispersants in combination with HiPco SWCNTs the resulting dispersions were tested regarding the highest SWCNT content in the dispersion. To analyze this SWCNT content the dispersions were prepared at a concentration of 2 wt% of the given polymers. This concentration was selected because it widely exceeds the CMCs reported for each dispersant [177, 178, 185, 186]. Here PAE1, Pluronic F68, Pluronic F108, Pluronic F127 and Tetronic 90R4 were tested with 0.5 wt% of raw HiPco material. The SWCNT content was isolated via neutral DGU using 1 ml of the respective dispersion on 3.5 ml of 1.26 g/cm³ SPT solution at 40,000 x *g* for 14 h. The resulting separation of SWCNT material is shown in the appendix Figure 10.7. The fractions were collected, diluted, pelletized and re-dispersed in of the according 2 wt% aqueous polymer.

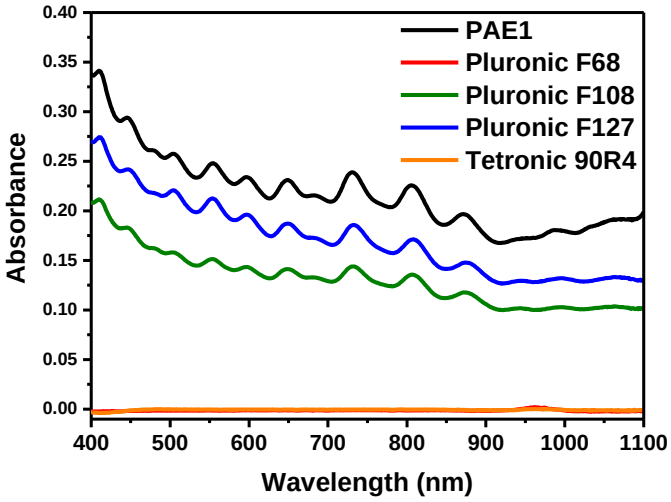

Figure 5.15. Absorbance spectra of SWCNTs dispersed with different polymeric dispersants. The SWCNT content separated from raw dispersions of 0.5 wt% HiPco powder in aqueous 2 wt% of various dispersants is measured via UV-vis-NIR absorbance spectroscopy. The PAE1 shows the highest SWCNT content for the various tested polymeric dispersants.

Therefore UV-vis-NIR spectra reflect the individualized SWCNT content in the SWCNT dispersions. The DGU process was introduced to separate the actual amount of SWCNTs that is accessible in a centrifugation based separation process, because bundled SWCNTs would contribute to absorbance spectra but are generally not accessible for electronic type sorting in centrifugation runs.

Pluronic F68 as well as Tetronic 90R4 did not disperse any HiPco SWCNTs. This is captured by UV-vis-NIR measurements of the extracted SWCNT fractions after centrifugation in Figure 5.15. Pluronic F108 and Pluronic F127 do disperse HiPco material, however, the PAE1 polymer shows the highest amount of SWCNT material within the 1 ml sample of the dispersion.

5.6. Stability of SWCNT Dispersions

Before setting up separation experiments, the PAE1 based dispersion was tested regarding any effects different environments could induce to the SWCNT dispersion. With regard to establishing a centrifugation based separation method especially density media must be tested in combination with the PAE1 dispersion. Density media are essential during centrifugation experiments and were tested in combination with the dispersion to evaluate possible interactions. A density medium that was found to stand out in its interaction with PAE dispersions was sodium polytungstate (SPT).

In this section the interaction between SPT and SWCNTs dispersed with the PAE1 polymer is probed by using a dispersion of Plasma grown nanotubes. Dispersions from Plasma nanotubes offer the possibility of examining the absorbance spectra, which unanimously divide into metallic and semiconducting transition regions of the nanotubes [56, 187]. This way selectivity with respect to electronic nature can be monitored by absorbance measurements alone.

The Plasma nanotube dispersion (0.5 ml) was mixed into environments that simulate the conditions of weak field centrifugation (WFC) [53] at only 1 x *g*.

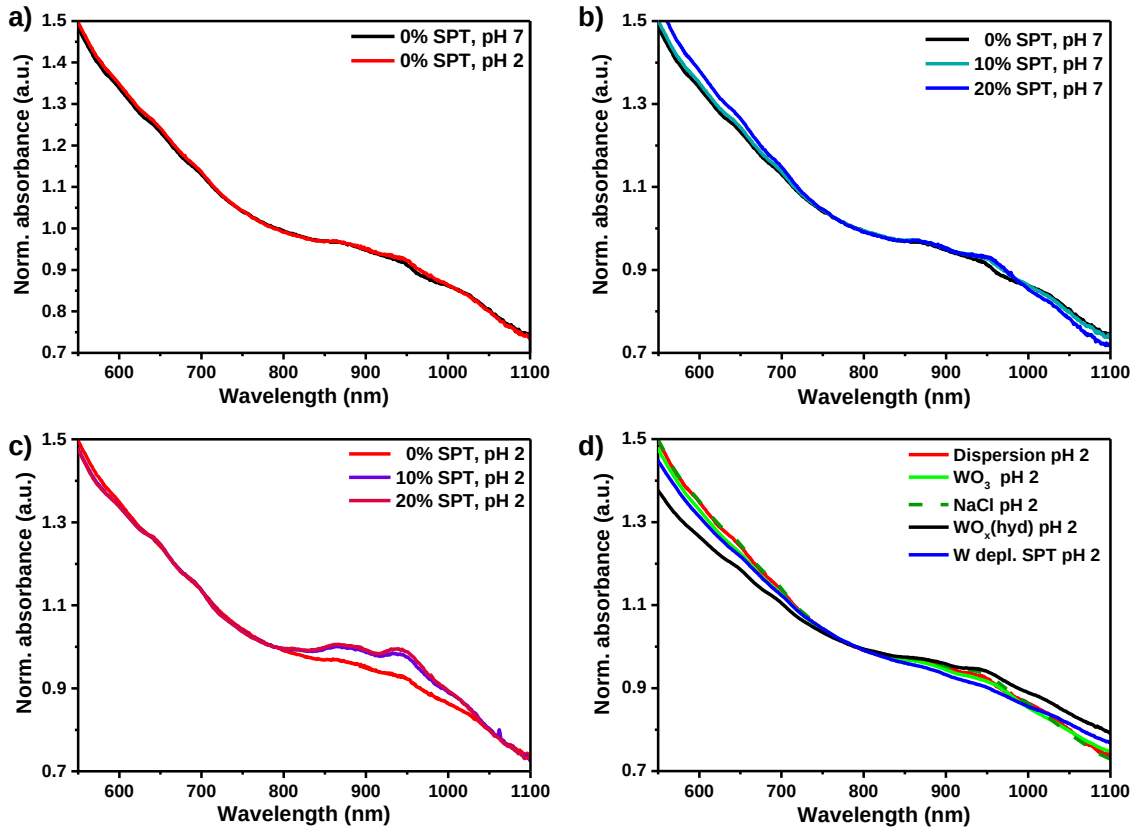

Figure 5.16. The response of a PAE1 dispersion with HiPco SWCNTs to various changes in the environment. a) SWCNT content extracted from the supernatant of HiPco SWCNTs dispersed in 2 wt% PAE1 that were previously set to pH-values of 7.0 and 2.0. The samples were pelletized and re-dispersed in 0.5 wt% aqueous SDOC and measured at pH 7.0. In b) the samples were extracted from dispersions at constant pH 7.0 including different concentrations of SPT. In c) the extracted samples were collected from nanotube dispersions with different SPT concentrations at constant acidic pH 2.0. d) Samples of nanotube dispersions with different NaCl concentrations at pH 2.0.

Here, these WFC environments consisted of 10 g of water with or without aqueous SPT as density medium in different concentrations at neutral or acidic pH values. After one week 2 ml of each mixture were extracted and the carbon content was pelletized by ultracentrifugation. The obtained pellet was thoroughly rinsed with DI-water and re-dispersed in 0.5 wt% of aqueous SDOC at pH 7. UV-vis-NIR absorbance spectra were recorded afterwards. Figure 5.16 shows the absorbance of the extracted samples from each environment.

In Figure 5.16a, the pH value of the dispersion is varied without the addition of SPT. The recorded spectra were normalized to the absorbance at 790 nm. They do not differ after pH variation of the dispersion for one week. This indicates that no selective interaction of PAE1 and SWCNTs of only one electronic type is introduced by the pH variation alone. The same result was previously observed for different pH values in combination with a HiPco SWCNT dispersion.

Figure 5.16b shows the dispersion after addition of certain concentrations of SPT. It is shown that the nanotube dispersion is also not largely influenced by the abundance of SPT in the mixture without additionally introducing an acidic environment. A selectivity with respect to one electronic kind of SWCNTs is not observed.

In Figure 5.16c the influence of the combination of SPT and acidic conditions is investigated and clearly a selectivity in the electronic type of the SWCNTs is triggered. The absorbance in the semiconducting transition region has increased while the absorbance in the metallic transition region is similar compared to the unchanged dispersion. In order to further investigate the observed effect a series of experiments was set up simulating different SPT moieties.

In Figure 5.16d different chemicals were used to simulate the SPT moieties from the dissociation of SPT in water at acidic conditions. To select chemicals, which can simulate the ions that are present in solution after dissolving SPT, the dissociation of SPT in water and the production of SPT are used. Sodium polytungstate is prepared by the dissolution of $3Na_2WO_4 \cdot 9WO_3 \cdot H_2O$ crystals

$$3Na_2WO_4 \cdot 9WO_3 \cdot H_2O \rightarrow Na_6[H_2W_{12}O_{40}] \qquad (5.2)$$

[95]. Dissolved SPT dissociates into sodium ions and a complex tungstate ion as given in the following reaction [188].

$$Na_6[H_2W_{12}O_{40}] \rightarrow 6\,Na^+ + (H_2W_{12}O_{40})^{6-} \qquad (5.1)$$

Acidified tungstate solutions yield paratungstate, metatungstate and tungstic acid solid phases [189, 190]. Dissolved polynuclear species in acidified tungstate solutions have been reported as various hexatungstate ions and also a tritungstate ion with unknown structures [190, 191].

Therefore, at first sodium chloride was used to test the dependence of the observed effect on the sodium concentration. The simulation of sodium was done by evaluating similar molar sodium concentration from dissolving NaCl instead of SPT.

To secondly simulate the tungsten moiety in solution three experiments were conducted. In the first experiment tungsten oxide WO_3 was used. In the second experiment precipitated tungsten oxide hydrates from a heavily acidified SPT solution were employed [190, 192] and in the third experiment the remaining tungsten depleted SPT supernatant was used. In the acification of SPT, a white powder (unspecified, but presumably tungsten oxide hydrates [192]) precipitated as a result and was collected. The supernatant as well as the white powder were collected individually. The depletion of tungsten in the supernatant was tracked by X-ray fluorescence. The original SPT solution contained a ratio of 0.06 of sodium to tungsten. After acidification and resetting the pH to neutral pH 7 by addition of small aliquots of 1M HCl or 1M NaOH, respectively, this Na/W ratio was determined to be 0.15 showing the enrichment of sodium over tungsten in the remaining liquid phase. In this evaluation the addition of sodium from the addition of less than a one milliliter of 1 molar NaOH was neglected. 5 wt% of WO_3 or the white powder were added to the vials with acidified (pH 2) dispersion. In case of the tungsten depleted supernatant, 1 ml of was added to the vial with acidified (pH 2) dispersion.

With the addition of NaCl, the previously shown effect of semiconductor enrichment in the SWCNT dispersion is not observed as the spectra remain unchanged (Figure 5.16d, red and dotted green). It is hinted that the sodium concentration has no role in the observed selectivity of PAE1/SWCNT interaction.

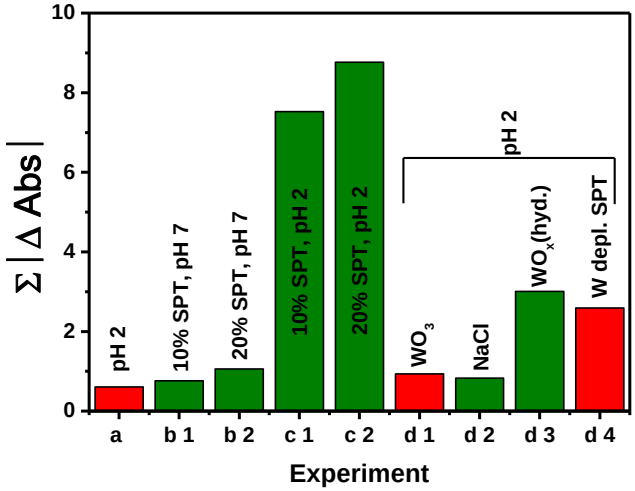

Figure 5.17. The absolute values of the areal differences between the spectra displayed in Figure 5.16 in the semiconducting transition range. The spectra from the experiments submitting the PAE1 dispersion to different environments are evaluated to show the differences in semiconducting transitions induced by the environmental changes. Each bar corresponds to one experiment. The larger the bars are the greater the semiconducting enrichment is in the dispersions. Green bars represent a positive area difference after reference subtraction red bars represent negative area differences after reference subtraction.

The addition of 5 wt% of tungsten oxide (WO_3) does not change the absorbance of the nanotube dispersion either (Figure 5.16d, red and green), indicating no change in the nanotube distribution

within the dispersion nor any electronic enrichment. The same is observed when considering the addition of the tungsten depleted SPT solution.
The spectrum after addition of tungsten oxide hydrates (white powder from acidification of SPT) as precipitated from the SPT solution indicates that this addition induces a change in nanotube composition compared to the original dispersion that is closest to the one observed in acidic SPT environments (Figure 5.16d, red and dotted black). However, the nanotube distribution does not reach the same level of electronic type enrichment as it was achieved by the use of as received SPT.
The introduction of the tungsten depleted SPT solution also hardly alters the normalized spectrum of the dispersion (Figure 5.16d, red and blue). The absolute absorbance spectrum revealed an overall decrease in metallic and semiconducting absorbance. However, the dispersion in this vial was found to be completely agglomerated after 2 weeks.
The evaluation of the spectra was complemented with an evaluation of the semiconducting area between the spectra after addition of the individual chemicals, acidification or both and the respective reference spectra given in each panel of Figure 5.16. The area was evaluated in the semiconducting transition region between 800 – 1025 nm. These results are summarized in Figure 5.17. The electronic kind enrichment observed when introducing SPT to an acidified dispersion of SWCNTs with PAE1 is clearly reflected by the area difference.

Tungsten oxide hydrates (white powder from heavily acidified SPT) induce an effect that comes closest to this observed selectivity. However, the spectrum taken after addition of the tungsten oxide hydrates also shows the greatest difference to the reference spectra at wavelengths above 1,025 nm. In this regime the acidified SPT spectra in experiment c1 and c2 are approaching the reference spectra, so that the difference in area might be resulting from a different effect. However, the tungsten oxide hydrates were confirmed in this experiment to play a key role in the effect of selective stabilization of semiconducting SWCNTs, since sodium and the tungsten depleted SPT solution were shown to not be capable of inducing the selectivity effect observed with SPT.

5.7. Time Dependence of Agglomeration of SWCNTs

In order to visualize what happens to the nanotubes that are not found in the supernatant after exposing the dispersion to different environments, a video was recorded of different SWCNT dispersions put into an environment, where the dispersions were previously found unstable. The detailed understanding of the PAE1-SWCNT interaction and its pH dependency is under investigation, but its complete chemical basis it is beyond the scope of this work. Nevertheless, the recorded video helps to visualize the onset of agglomeration in the case of unsorted SWCNTs versus a stable dispersion of semiconducting SWCNTs at low pH levels. In order to visualize agglomeration and sedimentation, the pH value of the dispersed SWCNTs was set to 1.0. In this regime both SWCNT dispersions are not stable (see 0). The video recorded the first 40 minutes after the pH value was adjusted. Individual shots of specific times after acidification of the dispersions are displayed in Figure 5.18.

The SWCNT fractions in the video were collected from neutral and acidic WFC in SPT. It will be displayed in chapter 6, that WFC under pH neutral conditions leads to the separation of electronically unsorted SWCNTs, while acidification of the SPT column in WFC leads to the separation of semiconducting SWCNTs.
The video was merged from two 20 min videos. In the 15 seconds in between the videos, the illumination of the samples was optimized. Therefore the starting image appears darker. Within this timeframe recorded, agglomeration is starting and the ensuing sedimentation of the agglomerates can be observed in the unsorted SWCNT dispersion, while the enriched semiconducting fraction remains stable. Finally, the complete agglomeration of both fractions was only observed after 5 hours, indicating a different susceptibility to agglomeration for both dispersions.

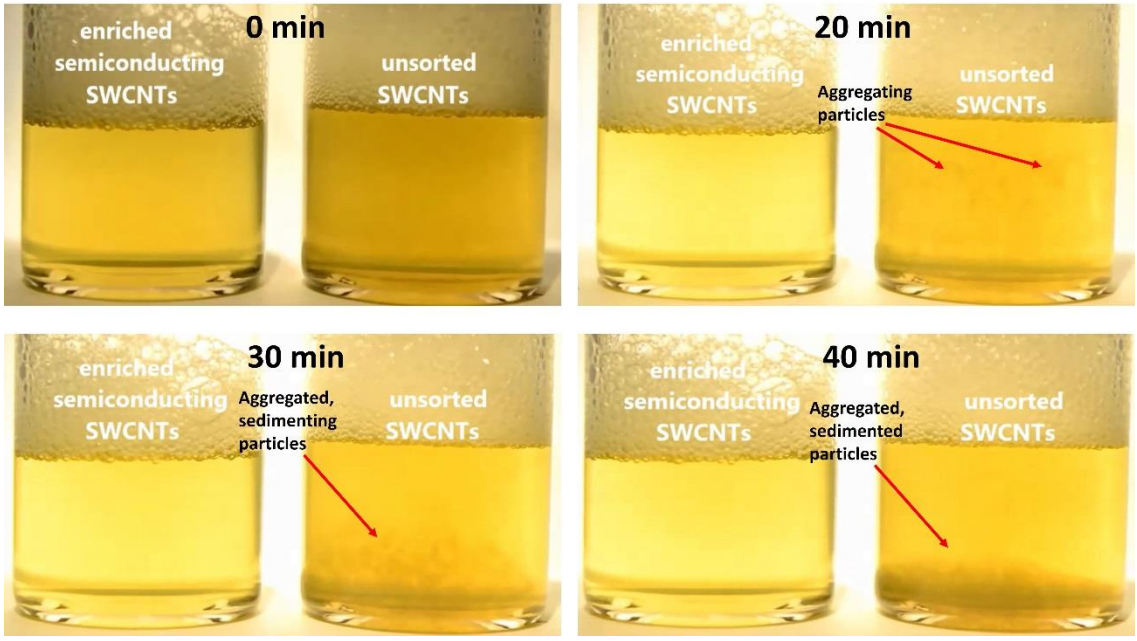

Figure 5.18. Agglomeration behavior of different dispersions. From top left to bottom right, individual shots from a video taken of two acidified (pH 1.0) dispersions enriched with semiconducting SWCNTs and unsorted SWCNTs are displayed for ongoing times after acidification. 20 minutes after acidification the illumination of the samples was slightly increased. The onset of agglomeration occurs after 20 min in the unsorted sample, after 30 min the particles in the unsorted sample do not agglomerate further, but sediment to the bottom of the glass vial. This sedimentation has ended 40 min after the initial acidification.

A different timescale for agglomeration of both heavily acidified samples indicates how differently the electronic types of SWCNT react to environmental changes. The video was recorded using a Nikon D3200.

6. Weak Field Centrifugation as SWCNT Separation Method

This section describes the development of a centrifugation based separation method for semiconducting SWCNTs. After having observed that PAE1/SWCNT dispersions show different behavior when put in contact to different environments as described in chapter 5, centrifugation is explored as separation approach in this chapter. Especially after introducing SPT solutions, selectivity effects of the dispersing properties of the PAE1 polymer with SWCNTs were observed. Combining these effects with centrifugation can be used to develop a separation process for SWCNTs by electronic type. In this process the observed agglomeration must be induced selectively to metallic SWCNTs to effectively sort them by their size dependent sedimentation during centrifugation experiments. The main objective of this thesis was the development of a method that provides electronic enrichment of nanotubes by using only weak centrifugal fields (<15,000 x *g*). Therefore the gradient forming behavior of SPT is firstly targeted in the following and put in comparison to different density media in weak centrifugal fields.

6.1. Non-Equilibrium Gradient Formation in Weak Centrifugal Fields

A first step to prepare the separation of SWCNTs is investigating SPT as density material for centrifugation. The observed selectivity for semiconducting SWCNTs in a PAE1/SWCNT dispersion induced by acidified SPT environments hint that SPT should be used as density medium during centrifugation. In literature mostly high viscosity density media are selected, because their forming of density gradients can be well controlled by selecting the centrifugation times and fields. SPT is a very low viscosity density medium. In weak centrifugal fields, the density gradient formation of the different density materials has not been previously reported. Thus this chapter starts with an experiment that was designed to compare different density materials under WFC conditions.

Aqueous solutions of common density media were prepared to illustrate differences in density gradient formation. The selected media were Sodium Polytungstate (SPT) [193], Caesium Chloride (CsCl) [193], Iohexol (Iohex) [97] and Iodixanol (Iodix) [34].
For a comparison of the density gradient formation, the density of each medium in aqueous solution was set to approximately 1.24 g/cm³. Each solution was then centrifuged (Beckman Optima XL) at 40,000 x *g* in a SW60 Ti rotor for 11 h. Afterwards, each centrifugation tube was separated into 15 fractions, decanted, diluted and the density was measured with an Anton Paar DMA 5000M. The density profiles for each density medium were calculated and are shown in Figure 6.1. Centrifugation as well as the density measurements were carried out at 25°C. The density medium that reacts the most to the applied centrifugal force is SPT, whereas the other density media react only very slightly (Iodix, Iohex) or do not show a density profile different from the starting solution (CsCl). For Iodix and Iohex that is due to their high viscosity. The high viscosity hinders the forming of a gradient compared to a lower viscosity density medium like SPT in WFC. However, when using low viscosity density media like CsCl, the centrifugal field is not strong enough to induce a gradient to the very small molecules [194].

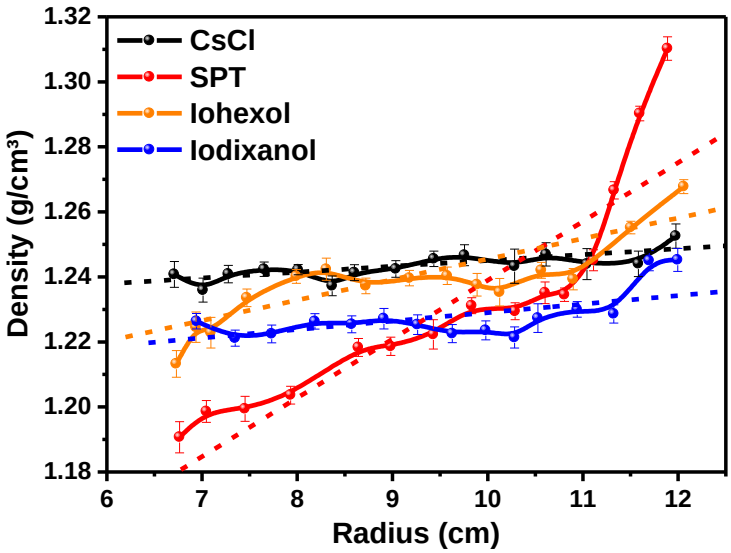

Figure 6.1. Analysis of density gradient formation in WFC. The density gradient profiles of different media with approximately the same loading density (1.24 g/cm³) after centrifugation at 40,000 x *g* for 11 h. The aqueous solution of CsCl does not show density gradient formation at all. Iohexol and Iodixanol exhibit slight density gradient formation. SPT on the other hand shows the most pronounced density gradient formation of the tested media. Error bars indicate the experimental error from dilution of the as extracted samples. The linear fits are shown as dashed lines.

Linear fits to the graphs show the average increment in the density gradient formation within the centrifugation tube. The slopes of these fits are listed here: SPT ≈ 0.02 g/cm⁴, Iohex ≈ 0.006 g/cm⁴, Iodix ≈ 0.003 g/cm⁴, CsCl ≈ 0.002 g/cm⁴. SPT shows the steepest gradient at 40.000 x *g*. When moving to standard lab scale centrifugal fields, the increment in the density profile will be weakened.

Thus, two tungstate based density media SPT and Lithium polytungstate (LPT) were used to test their behavior in even weaker centrifugal fields in the next section.

6.2. Density Media Suitable for Weak Centrifugal Fields

SPT advanced from the previous discussion as most suitable density medium for weak field centrifugation. This was in addition to having shown to induce selectivity effects in SWCNT dispersions stabilized with PAE1. In the next step two tungstate based density media are compared in weak field centrifugation. The closely related density media SPT and LPT were tested regarding differences in gradient formation when moving to even weaker centrifugal fields of about 10,000 x *g*. Therefore solutions of about 1.25 g/cm³ were prepared. In two separate experiments they were centrifuged for 5 h or 29 h. The resulting density profiles were measured and are shown in Figure 6.2.

A comparison of the density profiles reveals that the density profile of LPT is slightly more pronounced after 5 h of centrifugation. After 5 h of centrifugation both density media (LPT and SPT) are characterized by a stable (isoconcentration) plateau region from 1.5 – 4.2 cm into the centrifugation tube. Theoretically this plateau region is known when centrifuging only one density column, especially for high viscosity density media. In literature this is well described as

density barrier method [195]. In the last years the term self-forming or self-generating density gradient was made popular as used for example in [50, 51] or [99], respectively.
After 29 h of centrifugation the density profile of LPT is noticeably steeper. Both density media, LPT and SPT, show a point of stable density (isoconcentration point) at approximately 3 cm into the centrifugation tube. This point can be visualized as a pivot point for of the density profile. The steeper increase in density observed at the bottom of the centrifugation tube using LPT compared to SPT shows a faster accumulation of tungstate molecules. Therefore the overall shape of the LPT profile after 29 h is also closer to the theoretically predicted equilibrium density gradient form, which has an exponential shape (see equation (2.28)).

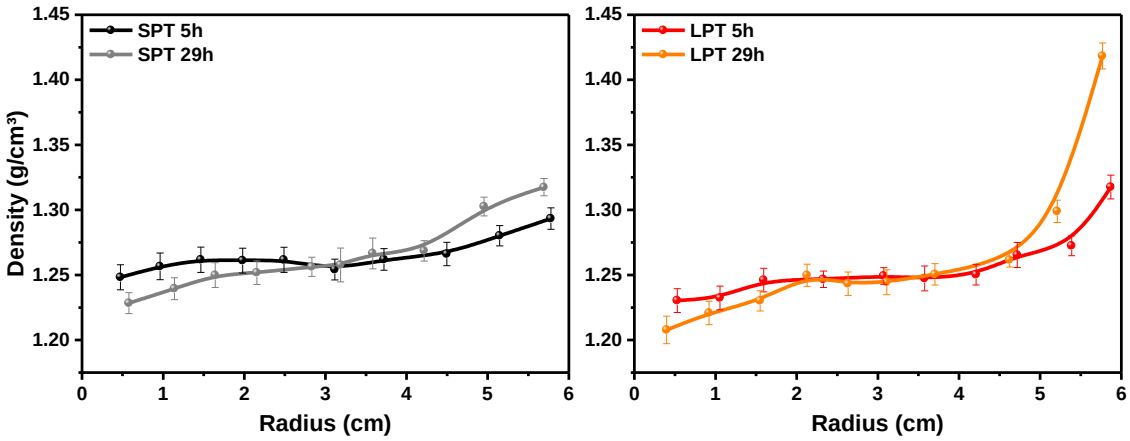

Figure 6.2. Analysis of density gradient formation in WFC with LPT and SPT. The density gradient profiles of LPT and SPT at approximately the same initial loading density (1.25 g/cm³) after centrifugation at 10,000 x *g* for 5 h and 29 h are shown. The density profile of LPT responds slightly differently compared to SPT. While SPT shows an isoconcentration point [194] where the density is unchanged over the course of centrifugation, LPT shows a plateau region of stable density extending 1 cm in both directions from the isoconcentration point observed in SPT. Isoconcentration points are marked by a red circle.

The comparison of both profiles with time shows that SPT yields a well controllable density barrier. The LPT profile quickly forms an equilibrium gradient shape and is thus less favorable for density barrier centrifugation. Unwanted nanoparticles cannot reach the bottom of the tube due to the strong increase in density and the wanted particles are not trapped in the top area but rather in the middle of the tube. The observed gradient formation of SPT was in detail described in [193] and is explained by a sedimentation potential. This means that electrostatic repulsion and attraction between the dissociated ions influences (hinders) the gradient formation for SPT. In LPT this effect is not observed in this experiment as the gradient formation shows a comparably steeper increase in density at the bottom of the centrifugation tube.
For the purpose of separating nanomaterial in weak centrifugal fields it is also critical that diffusion between manually established density barriers enables diffusive movement of nanoparticles. In detail, the nanoparticles must have space to distribute, in between the densities of the superimposed dispersion and the density barrier. If diffusive broadening of those density barriers is not given, particles accumulate at such an interface and can aggregate depending on their individual interactions. This is schematically drawn in Figure 6.3 to support a visualization.

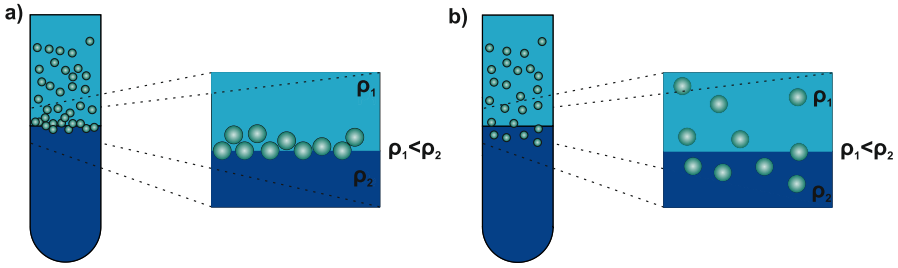

Figure 6.3. Scheme of centrifugation of a superimposed dispersion on a density barrier with and without diffusive broadening of the density barrier. In a) the density barrier does not allow fast diffusive broadening. As a consequence the particles are trapped at the density interface due to the centrifugal force and aggregate in the worst case. In b) the diffusive broadening of the density barrier allows the particles to penetrate to a certain degree into the initial density barrier so that aggregation of the particles can be prevented.

If metallic and semiconducting SWCNTs agglomerate equally at the interface, the access point to separate both types of SWCNTs is lost. This is why the diffusive broadening of SPT was tested. A density column (1.0 g/cm³) was leveled on top of a SPT column of density 1.26 g/cm³. The combination was centrifuged at 10,000 x *g* for 18 h. The resulting density profile after 18 h of centrifugation is shown in Figure 6.4. After 18 h of centrifugation the density profile shows two regions of interest.

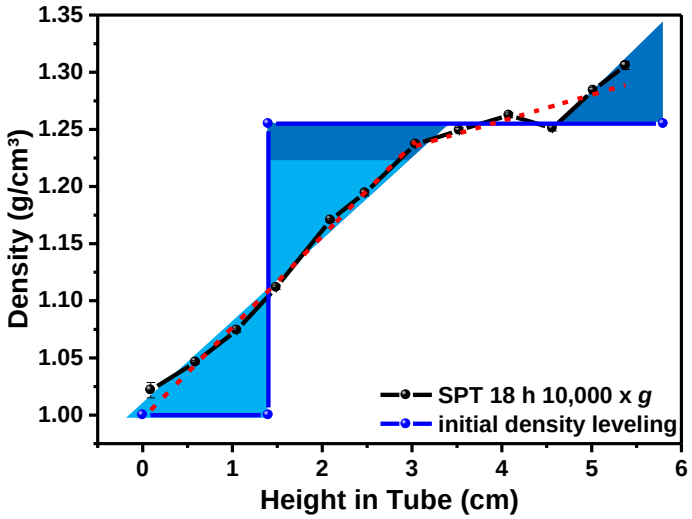

Figure 6.4. Density profile of a bottom column of 80% SPT column and top column of 20% water centrifuged for 18 h. A density column of SPT at 1.26 g/cm³ formed the bottom column (80%) and a density column of DI-water (20%) formed the top column to simulate top loading of a SWCNT dispersion. After 18 h of centrifugation at 10,000 x *g* the density profile was measured (black), while the initial leveling of density columns is indicated by the blue lines. An almost linear gradient formed in the region of the initial density interface. While in the lower part of the gradient a plateau region was maintained with slight increase in density in the bottom accumulation zone. In the top part of the profile the diffusion transport is indicated by highlighting same area triangles in orange, while the sedimentation induced transport mechanism is highlighted by red marked shapes. Dashed red lines show linear fits in the different regions.

An almost linear increment between the initial density layers of 1.0 g/cm³ and 1.26 g/cm³ at (0 - 3 cm) with a slope of 0.08 g/cm⁴. And a second plateau region (3 - 5.5 cm) where the increase in

density is comparably reduced to 0.02 g/cm^4. The linear fits shown as dashed yellow lines in Figure 6.4 for clarity.
The density profile shows that stable dispersed SWCNTs (1.15 g/cm^3 [33, 50]) would accumulate at about 2 cm into the centrifugation tube. This nearly linear density increment region is a result of back diffusion of SPT molecules into the initial water column. This diffusion process is highlighted by same area triangles in light blue. This way the transport mechanism by diffusion is separated from the sedimentation, which is highlighted in dark blue. The small discrepancies in the red areas can be explained by the very strong increase in density towards the bottom of the centrifugation tube (at 6 cm), which is not measureable with high accuracy.

Overall it is found that SPT meets the requirement of forming a stable density barrier in weak field centrifugation, while also allowing diffusive movement. If a nanotube dispersion (≈1.0 g/cm^3) is superimposed on a high density column of SPT (1.26 g/cm^3) the SWCNTs (1.15 g/cm^3) should not aggregate due to spatial compression as result of the centrifugal force.

6.3. pH Influence during WFC Separation

In this section we turn to the systematic investigation of how the pH value influences centrifugation experiments with the PAE1 dispersion on SPT. It was observed that only under acidic pH conditions a selectivity was observed in the PAE1/SWCNT dispersion. It was also demonstrated that the stability of the dispersion is completely lost when moving to very acidic environments (pH 1.0) in chapter 5. Centrifugation of a SWCNT dispersion superimposed onto a density barrier of SPT will be the basis of the next sections, to investigate different parameters.

Acidic Conditions

Clearly, the acidity of the heavy liquid SPT strongly influences the stability of the SWCNT dispersion and thus separation. pH dependent separation by WFC was set up for a PAE1/HiPco SWCNT dispersion. The separation results after systematic pH variation of the SPT column are shown in Figure 6.5a. Here, 0.5 ml of a SWCNT dispersion at pH 4 were top-loaded onto 4 ml SPT columns with their pH values varying between 1 and 6. Figure 6.5b shows the corresponding normalized UV-vis-NIR absorbance spectra of the extracted and purified top bands (red boxes in Figure 6.5a). At pH 1 all nanotubes sediment and no separation is observed.
Apparently, at very low pH values the stabilization of the SWCNTs is fully lost. In fact, electrophoretic mobility measurements on HiPco CNTs dispersed with the PAE1 polymer reveal a strong decrease in the surface charges below pH 3 (section 5.4). This leads to lower electrostatic repulsion and thus also to the formation of larger SWCNT bundles and aggregates. As a consequence of the increase in hydrodynamic size and density these bundles move to the bottom of the tube even at low centrifugal fields (even at 1 x *g* as shown in chapter 5). For pH values between 4 and 6, the centrifugation stage only leads to a separation of the individualized, but electronically unsorted species of SWCNTs from the carbonaceous impurities in the raw dispersion. Obviously, SWCNTs of all electronic types are equally stabilized under these conditions. Moreover, it was previously demonstrated that at this low centrifugal field the

formation of an equilibrium density gradient is not expected either. That is why banding, i.e. separation according to chiralities, is not observed [44]. Only the absorbance spectra for the separated fractions at intermediate pH levels 2 and 3, show a decreased absorbance in the metallic M11 transition region [196] (red shaded area in Figure 6.5b).

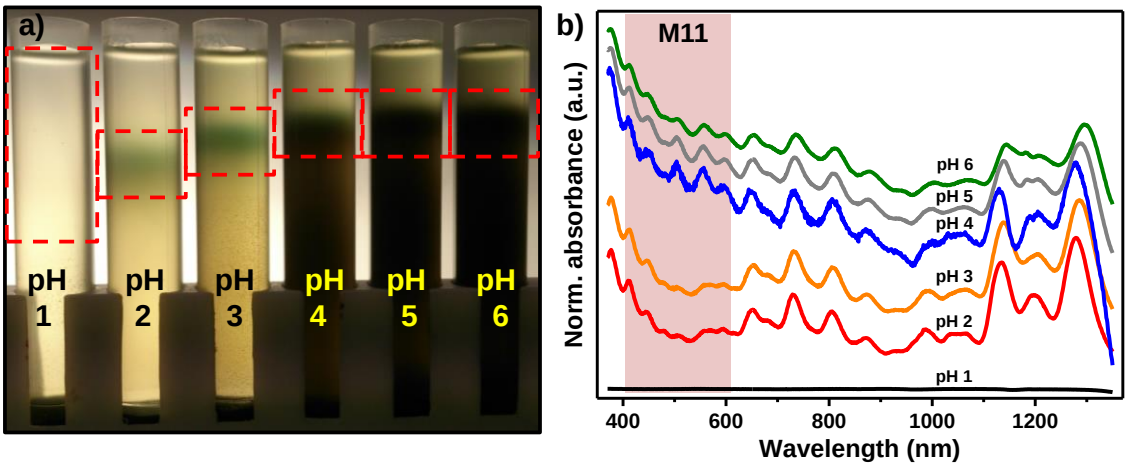

Figure 6.5. The pH dependency of the weak field SWCNT separation. In a) a photograph of the resulting separation of SWCNTs from the raw dispersion after 32 h of centrifugation at 10,000 x *g* for increasing pH-values. In b) normalized (to peak at ≈1270 nm) UV-vis-NIR absorbance measurements of the separated fractions (red boxes). The spectrum of the pH 1 fraction was not normalized due to a lack of optical transitions. Spectra were offset into the y-direction for clarity.

This is a clear indication for the enrichment with semiconducting SWCNTs. In fact, under these conditions a selective protonation of the sidewalls of metallic carbon nanotubes compared to semiconducting SWCNTs is predicted [121]. Consequently, the PAE1 dispersant predominantly stabilizes semiconducting SWCNTs while partially detaching from the significantly protonated metallic ones that hold fewer adhesion sites available [51]. The agglomeration and sedimentation observed at lower pH values is obviously under these conditions mainly affecting the metallic nanotubes and not their semiconducting counterparts. Moreover, even at such low centrifugal fields excellent spatial separation was achieved between the semiconducting band and the rest of the sample. In contrast to most common separation media, the low viscosity heavy liquid (SPT) [193] can rapidly form dynamic density gradients in WFC. The well dispersed semiconducting nanotubes (lower density) are withheld at the upper part of the centrifugation vessel due to the formation of a density barrier [195] as explained in Section 6.2.

Basic Conditions

Under specified acidic conditions it was shown that centrifugation of a PAE1/SWCNT dispersion on a SPT column can lead to an enrichment of semiconducting SWCNTs in the separated fraction. In reported experiments [51] the opposite of enriched metallic species was observed when moving from acidic to basic conditions. To test the behavior of PAE1 dispersed SWCNTs in basic conditions 3 different amounts of dispersion were set up for centrifugation at pH 8.3. The

pH-value of the SPT/PAE1 column was initially set to pH 12 but wasn't stable and settled within 30 minutes to pH 8.3. This pH value did not change further. Figure 6.6 shows the resulting separation of different loading amounts of dispersion at basic pH conditions. An absorbance spectrum shows that no enrichment with respect to electronic type is achieved by centrifugation at 10,000 x *g* for 18h.

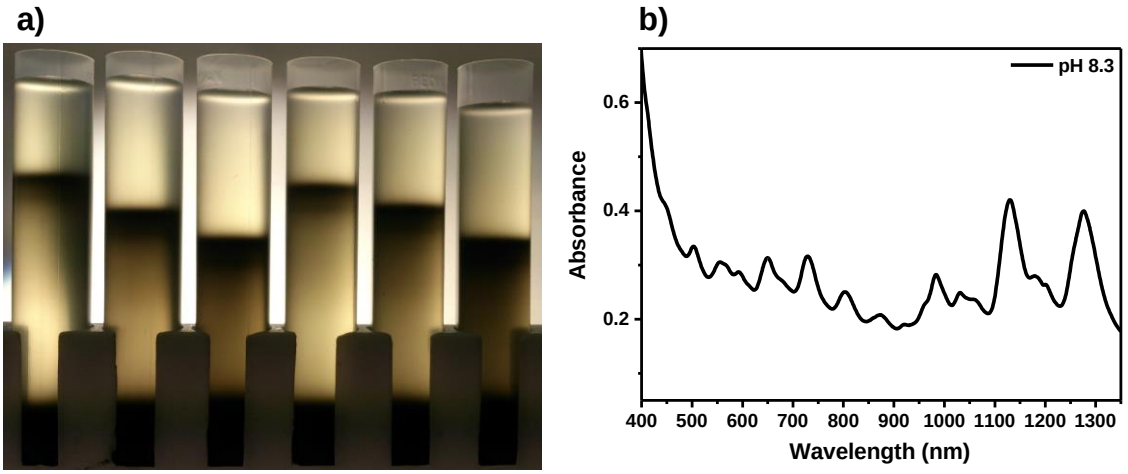

Figure 6.6. The weak field SWCNT separation is shown at basic pH conditions for three different loading amounts. In a) a photograph of the resulting separation of SWCNTs from the raw dispersion after 18 h of centrifugation at 10,000 x *g* at pH 8.3. The six centrifugation tubes can be divided into groups of three, the so called A-sample and B-sample from different centrifugation runs. In b) a UV-vis-NIR absorbance spectrum of the separated fraction (tube 1) is shown.

6.4. Temperature Influence during WFC Separation

In further experiments the favorable environment of SPT and acidic pH for selective PAE1/SWCNT interaction was tested regarding an influence of temperature. When initially dispersing carbon nanotubes increasing the temperature usually has a negative influence [176] on the individualization of SWCNTs (see 5.3). After varying the temperature during initial dispersion of carbon nanotubes, increased temperatures were found to lead to an enhanced amount of agglomerated particles within the dispersion even for prolonged sonication times with the PAE1 polymer. This led to the general question of how much the temperature influences the SWCNT/PAE1 interactions. To illustrate this in detail the WFC process was tested at pH 2.0 [53] for fixed g-force, pH-combination (dispersion pH 4, SPT column pH 1.8), density barrier and time of centrifugation at different temperatures.

In this experiment the dispersion of HiPco nanotubes was used in 2 wt% aqueous PAE1. A series of WFC experiments varying the temperature during centrifugation was carried out and is illustrated in Figure 6.7. The temperature was controlled between 10°C and 35°C in steps of 5°C. The separation process of semiconducting from metallic SWCNTs is clearly hindered at low temperatures (Figure 6.7a). The semiconducting enrichment improves for the given

centrifugation conditions (10,000 x *g*, 18 h) with increasing temperatures. This is revealed by the spectra in Figure 6.7b when comparing the absorbance in the metallic transition region.

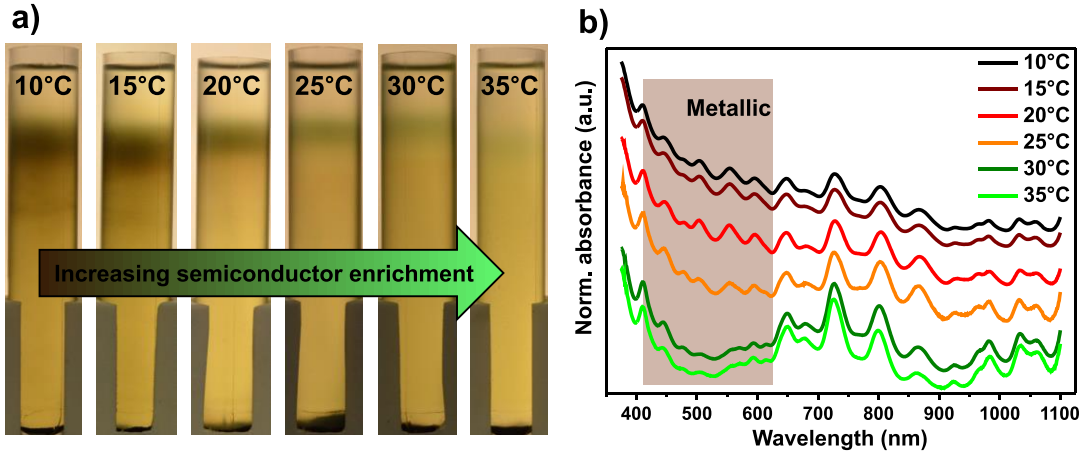

Figure 6.7. Temperature dependent WFC separation of HiPco SWCNTs. a) WFC (10,000 x *g*) is performed for 18 h at different temperatures for steady loading amounts (0.5 ml) of SWCNT dispersion. In b) the nanotube fractions were analyzed by UV-vis-NIR spectroscopy. The grey shaded area indicates the region of metallic M11 transitions. Spectra were offset into the y-direction for clarity.

The position of the SWCNT band observed in Figure 6.7a is at the initial leveled density interface for each tube. The band width decreases as the amount of SWCNT material decreases following the separation mechanism. However, the temperature increase has an attenuating influence on the viscosity [197] of the density barrier medium (SPT). This directs the density border into faster diffusive softening and therefore a higher scattering of the SWCNTs along their isopycnic point [44]. This is observed especially for the 35°C experiment where the SWCNT band is clearly broadened within the density barrier region between the initial densities of the dispersion (close to 1 g/cm³) and the SPT column (1.26 g/cm³). Centrifugation for 25 h was previously found (section 6.3) to be necessary to reach the same enrichment found here at 30°C after just 18 h. The selection mechanism reduces the nanotube content with increasing temperature, while at the same time diffusion is promoted and the nanotube band is blurred. Comparing the absolute spectra (not shown) of 30°C and 35°C, where semiconducting enrichment does not increase further, a lower SWCNT content was observed for the 35°C sample.

The above described experiment proofs that WFC relies not only on protonation but also on selective colloidal aggregation that can be boosted at higher temperatures. Nanoparticles and colloidal systems in general tend to lose their stability and agglomerate at higher temperatures [45, 46]. Actually, aggregation in homogeneous systems is often a result of van der Waals [176, 198] interaction between individual SWCNTs. For nanotubes, the van der Waals-London pair interaction energy depends on the diameter [199].

6.5. Overview of WFC Separation Process

The WFC separation approach that is presented in this section is enabled by the combination of two key elements: Firstly, dispersions based on PAE comb polymers with tailored amphiphilic properties are utilized and secondly, low viscosity aqueous solutions of heavy liquids are necessary. The comb polyarylether (PAE) polymers have a strong amphiphilic character and were shown to act as highly potent dispersants for SWCNTs. Under acidic pH conditions and after addition of SPT to the dispersion it was shown that semiconducting SWCNTs were better supported than metallic SWCNTs within the dispersion.
The low viscosity aqueous heavy liquid solutions, sodium polytungstate (SPT), was shown to meet the requirements to form diffusion softened density barriers when applied as density and therefore separation media for SWCNT purification. Centrifugation was selected as separation procedure, because the majority of separation techniques require individualized SWCNTs from dispersions. (Ultra-) Centrifugation of as prepared dispersions is required in most separation methods prior to the actual separation stage to remove the bundled nanotubes and catalytic impurities along with amorphous carbon material from dispersions [36, 200]. This additional step is associated with the loss of semiconducting nanotubes and thus reduces the yield to a large extent. This step is naturally not required when moving to WFC as the separation method. The loss in yield should be prevented by separating SWCNT material from the present impurities in the same step that is supposed to eliminate the metallic SWCNTs from the raw dispersion.

Different parameters have been highlighted in the previous sections. The pH as well as temperature, time of centrifugation and loading amounts are factors that can be varied to obtain different results. It was shown that favorable combinations exists that result in semiconductor enrichment in the separated SWCNT fraction. This section is supposed to give an overview over the separation process for HiPco SWCNTs for a fixed temperature of 25°C in WFC (10,000 x *g*) as it was established during this thesis. The conditions displayed here were used to prepare the semiconducting SWCNT samples that yielded the best performance in field effect transistors.
Therefore the separation method is schematically depicted in Figure 6.8. HiPco SWCNTs were dispersed by horn sonication in an aqueous solution of the polymeric dispersant (Figure 6.8a). Without any pre-separation, the dispersion, set to pH 4, was then loaded on top of an SPT column within a centrifugation vessel (Figure 6.8b). This is followed by a single centrifugation step employing a weak centrifugal field of about 10,000 x *g*. Photographs of different final separation states are depicted in Figure 6.8c. They represent the separation results from the procedure described above when performed under three different conditions. When the initial SPT solution is neutralized, i.e. set to pH 7, it is observed that the SWCNTs were only separated from the carbonaceous impurities which have accumulated at the bottom of the vessel (Figure 6.8c-1) after 25 h of WFC. As discussed, WFC under acidic conditions (~ pH 1.8) leads to a different separation result. A single (green-blue) band was isolated in the upper part of the centrifugation vessel, while impurities and bundled tubes accumulated at the bottom (Figure 6.8c-2). Optical and electrical analysis confirm a high purity separation of semiconducting SWCNTs (details will be discussed in chapter 7).

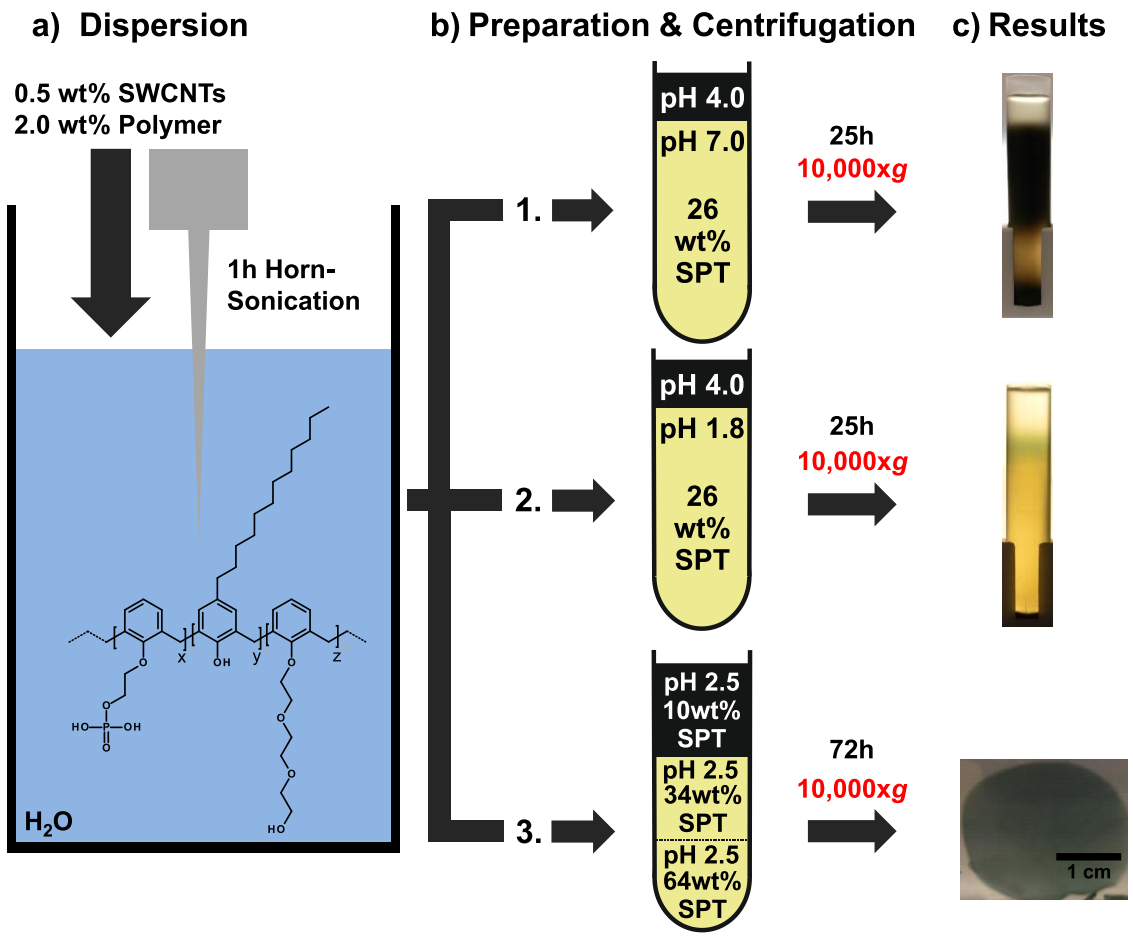

Figure 6.8. The separation process is shown schematically. a, Raw HiPco SWCNTs are dispersed in an aqueous solution of the PAE dispersant. The general structure of the PAEs is shown. The exact compositions of the PAEs are detailed in the Supporting Information. b, The neutral (1.), acidic (2.) and acidic layered (3.) preparation of the separation medium and dispersion prior to centrifugation. c, Photographs of the tubes after centrifugation at 10,000 x *g* reveal the separation of electronically unsorted SWCNTs under neutral (1.) and semiconducting SWCNTs under acidic (2.) conditions during centrifugation. The freestanding SWCNT sheet (3.) is shown after extraction from the centrifugation vessel and transfer into a DI-water bath.

We have also investigated the case, in which the initial SPT loading in the tube and the molecular weight of the polyethylenglycol side chain in the PAE polymer were altered. Three acidic aqueous SPT solutions (pH 2.5) with decreasing concentrations were layered on top of each other in the centrifugation vessel (Figure 6.8b-3). In this experiment the SWCNT dispersion (pH 2.5) was mixed into the topmost SPT layer prior to loading. The molecular weight of the polyethylenglycol side chain in the PAE polymer was decreased from 1500 g/mol (PAE1) to 750 g/mol (PAE2) as compared to the previous runs. Under these conditions and for the first time, the self-organization of SWCNT sheets of high lateral extension was observed after 72 h of WFC. They can be easily extracted as flexible freestanding high purity semiconducting sheets with a diameter in the centimeter range and thickness of about 100 nm (Figure 6.8c-3).

The observation of self-organized freestanding sheets under WFC conditions may be surprising at first glance (Figure 6.8c-3). For this experiment the three layered SPT solutions were set to pH 2.5. Clearly, the semiconducting-metallic SWCNTs separation mechanism can be rationalized by taking into account the results presented in the previous sections. The formation of the sheet-like structure is believed to be favored by an increased spatial compression in the centrifugation vessel as it was depicted in Figure 6.3. In fact, the SPT concentrations of the two top layers correspond to densities of about 1.09 g/cm³ and 1.36 g/cm³, respectively. The buoyant density of the polymer-SWCNT pair is expected to be within this range [34]. Denser bundles and aggregates may easily penetrate this density interface and precipitate towards the bottom of the tube. The stabilized semiconducting SWCNTs, however, will accumulate at this interface and aggregate. It is important to mention that the molecular weight of the used PEG side chains was decreased to 750 g/mol. Thus, the degree of steric stabilization is reduced and will further facilitate the formation of these condensed sheet-like structures compared to the use of PAE1.

Before presenting the optical and electrical investigations of the separated band and the extracted freestanding sheets, the focus in the next sections will be on understanding the separation mechanism and different results depending on the process conditions applied (e.g. different SWCNT materials).

6.6. Diameter Dependence of WFC Process

After showing that the PAE1 polymer can effectively disperse HiPco SWCNTs, the quality of dispersions obtained using PAE1 and nanotubes produced via different synthesis methods were investigated. The arc discharge (AD) and plasma torch (PT) processes lead to the production of larger diameter SWCNTs (1.0 - 1.8 nm) [64, 201] (See 5.2 for spectra of the dispersed SWCNTs). In Figure 6.9 pH dependent WFC separation was carried out [53] for all three types of SWCNTs. On top, photographs of the WFC separation are shown. To understand the large contents of black material in the HiPco and PT samples it must be noted that the actual SWCNT content was only 5% or 30%, respectively. In the AD sample the amorphous content was only 10%. Underneath the photographs of the pH dependent WFC, the UV-vis-NIR spectra of the separated fractions are shown.

A volume of 0.5 ml nanotube dispersion set to pH 4 was superimposed onto an SPT column (≈ 4 ml) of different pH values and submitted to WFC for 18 h. Electronic type separation is reached for HiPco SWCNTs under different pH conditions than for the larger diameter plasma torch or arc discharge SWCNTs. This is made evident by the spectra in Figure 6.9. They show how the electronic type enriching pH range shifts for the larger diameter arc discharge SWCNTs towards less acidic conditions (pH 5). It appears that the larger the mean diameter of the nanotubes sample is, the less acidic the environment has to be in order to reach effective electronic type separation. Moreover, for HiPco nanotubes stability is completely lost at pH 1, while for PT nanotubes the stability is widely lost up to pH 2. The larger diameter AD tubes lost their stability up to pH 3.

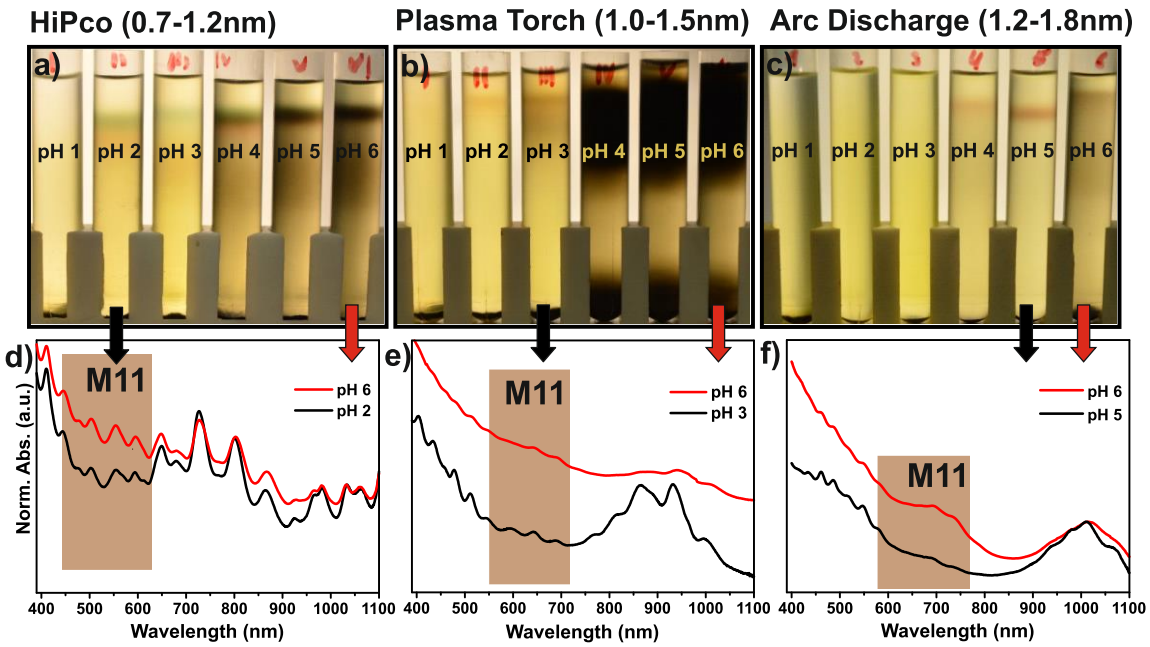

Figure 6.9. The WFC was carried out with SWCNT dispersions from different raw materials. In a) HiPco SWCNTs (mean diameter 1.0 nm) are separated by WFC (10,000 x g) in an 18 h run at different pH conditions. In b) AD SWCNTs (mean diameter 1.3 nm) and c) PT SWCNTs (mean diameter 1.5 nm) are separated by WFC (10,000 x g) in an 18 h run at different pH conditions. At the bottom normalized absorbance spectra of the separated fractions from the upper part of tubes for each SWCNT sample are shown. Spectra were offset for clarity.

This behaviour could be explained by the fact that larger diameter semiconducting nanotubes possess smaller band gaps, which makes them prone for protonation in less acidic environment [121]. Protonation is expected to result in a negative image charge on the SWCNTs that adversely affects the SWCNT / PAE interaction [121]. Subsequently, higher pH values are required to reach a regime where the stability of the semiconducting SWCNTS is not lost. Metallic SWCNTs possess no band gap and should be protonated regardless of their diameter.
Out of the diameter dependent pH shift, one could conclude that semiconducting enrichment in WFC is mainly driven by the strength of protonation. To better understand the separation mechanism, we performed further experiments where the centrifugation temperature was varied. However, colloidal stability was already shown to be relevant in enabling WFC as separation for SWCNTs. This suggests that the pH shift, observed in
Figure 6.9, could be resulting from the altered protonation and van der Waals-London interaction of larger diameter nanotubes.

6.7. Agglomeration of Metallic SWCNTs

As the video in chapter 5 (section 5.7) demonstrated, the SWCNTs in the dispersion aggregated during acidic WFC. The acidic conditions in combination with SPT additionally induced a selectivity in the SWCNTs found in the supernatant. After adding the weak centrifugal field to this system this selectivity was exploited to enrich dispersions with semiconducting SWCNTs.

In this chapter the induced aggregation will be investigated by testing the sedimentation coefficient in analytical ultracentrifugation (AUC) experiments.

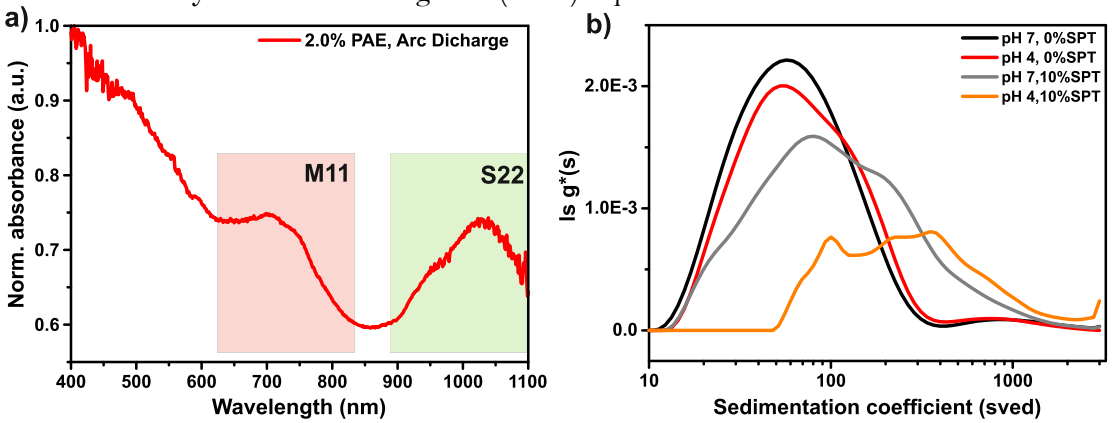

Figure 6.10 Arc Discharge SWCNTs were submitted to AUC to analyze the sedimentation coefficient in dependence on the present environment. a) The absorbance of an arc-discharge nanotube dispersion is shown to illustrate the metallic and semiconducting regions in excitation wavelengths. In b) the sedimentation coefficient distribution is plotted after the dispersions were mixed into the different environments of SPT and pH.

Aggregation of particles can be traced by following the sedimentation velocity by AUC approaches [202-204]. This approach has been widely used especially for dispersed particles as sedimentation depends largely on particle size [101]. The arc discharge nanotube dispersion was selected to trace the agglomeration of metallic SWCNTs as the metallic transitions can be clearly distinguished by selecting the correct transition region and the raw material contained 90% of SWCNTs. This metallic M11 transition region is highlighted in Figure 6.10a. Single wavelength AUC was performed at 700 nm to investigate metallic SWCNTs in a centrifugal field of 10,000 x *g*. At 700 nm only metallic SWCNTs absorb light. Semiconducting SWCNTs do not show an isolated absorbance band below 800 nm, the detection limit of the system (compare Figure 6.10a). In Figure 6.10b the sedimentation coefficient (SedCo) distribution of the SWCNTs (fitted with SEDFIT [205], see appendix 10.10 for a screenshot) is shown for the dispersion without SPT under neutral and acidic pH conditions as well as for the dispersion mixed into 10% SPT and the same pH modifications. When acidifying the dispersion without SPT a slight increase in sedimentation velocity is observed. The differences when adding SPT to the mixture is that for both pH conditions the SedCo increases, showing an increase in average particle size. At neutral pH the difference is owed to an increase in particle size, because the SedCo reduces when the solution has a higher density [202]. However, the mixture still contains individualized SWCNTs as the SedCo distribution starts between 10 - 20 sved (typical for SWCNTs [202, 204]). In the acidified mixture with SPT the SecCo distribution starts at 50 sved hinting that no individualized SWCNTs exist in the mixture anymore. The observed increasing SedCo shows that metallic SWCNTs agglomerated during the discussed WFC experiments. Agglomeration leads to an increased sedimentation velocity even for small bundles, because the sedimentation velocity depends on the squared particle radius (see equation (2.21)). Agglomeration is therefore a large factor in enabling a separation method for SWCNTs at only 10,000 x *g*.

7. Optical Analysis of Separated Fractions

This chapter covers the analysis of the separated fractions obtained via the WFC process as depicted in the overview in Figure 6.8.

7.1. UV-vis-NIR Absorbance and Raman Spectroscopy of HiPco SWCNTs

The purity and quality of the separated fractions of semiconducting SWCNTs were analyzed using UV-vis-NIR absorption and Raman spectroscopy. In UV-vis-NIR spectroscopy SWCNTs absorb light that is characteristic and depends on their chirality. For polychiral samples as treated in this thesis, metallic and semiconducting transitions occur in different wavelength regions depending on the diameter distribution of the SWCNT sample.

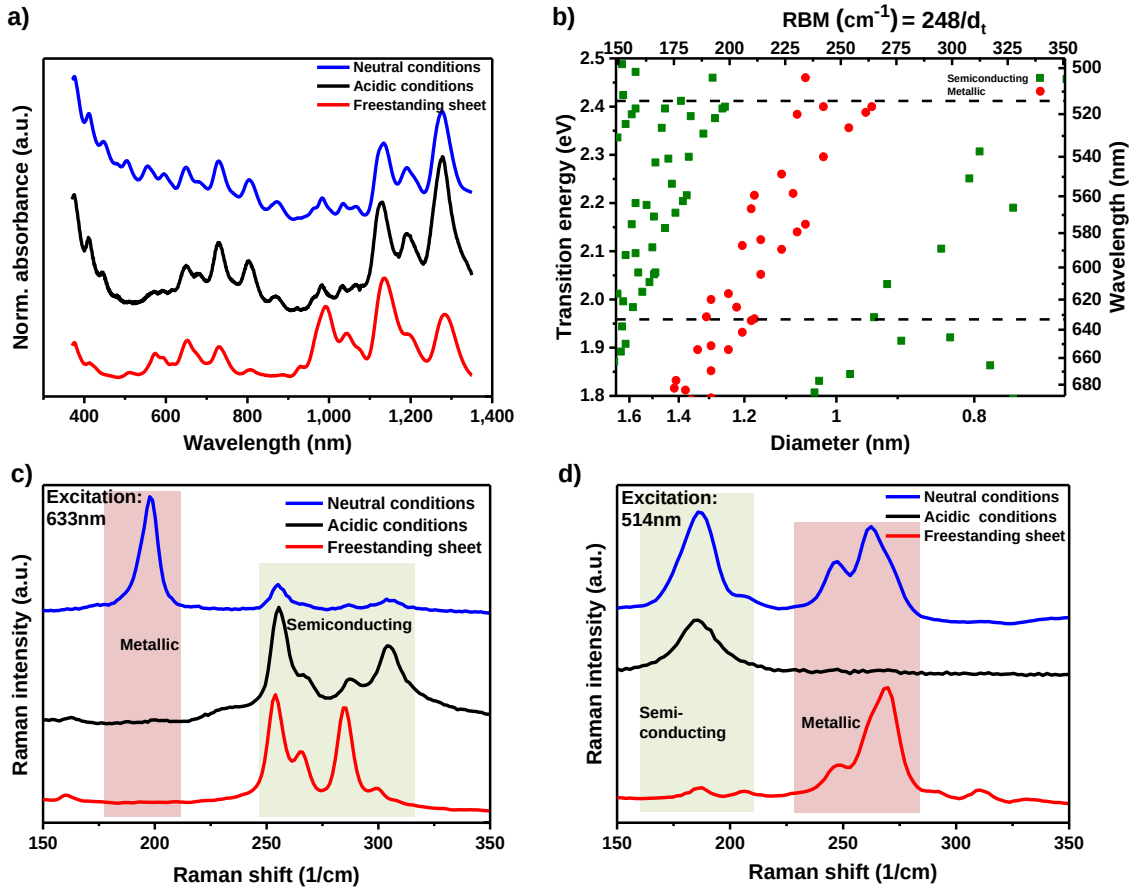

Figure 7.1. Optical analysis of the separated fractions. In a) normalized UV-vis-NIR spectra after pH-neutral separation of HiPco SWCNTs (blue), acidic conditions (pH 1.8, black) and the freestanding sheet (pH 2.5, red). In b) the Kataura plot was reproduced from calculations following [57] shown in the diameter range of HiPco SWCNTs. E22 transitions were taken from [55]. Red dots indicate metallic SWCNTs, green dots show semiconducting SWCNTs. The dashed lines in b) indicate the laser wavelengths used for Raman spectroscopy. In c), d) normalized Raman signals of SWCNTs obtained at neutral (blue), acidic conditions (pH 1.8, black) and the freestanding sheets (pH 2.5, red) were recorded at 633 nm excitation and 514 nm, respectively. All spectra were offset into the y-direction for clarity.

In the case of HiPco SWCNTs these regions overlap for first order metallic M11, the third order semiconducting S33 and second order semiconducting S22 transitions [206]. However, decreased absorbance in the M11 transition region can give for any sample a hint for electronic type separation. In Raman analysis, the excitation wavelength is critical as it determines, which chiralities respond to the excitation. Only nanotubes with transitions that are close to the excitation energy can be excited. For a complete analysis of polychiral SWCNTs it would therefore be necessary to employ tunable excitation systems. Single-wavelengths Raman spectroscopy in the M11 or S22 regions of a HiPco sample can excite SWCNTs and therefore give a first hint of how purified a sample is.

Figure 7.1a shows the normalized absorbance spectra of three SWCNT samples separated as described in Figure 6.8, i.e. under neutral (pH = 7, fraction 1) and acidic conditions (pH = 1.8, fraction 2) as well as the freestanding SWCNT sheet after its transfer to a quartz substrate. All spectra were background corrected to eliminate the contribution of their respective environment (surfactant solution or support). Both absorbance spectra of fraction 2 and of the sheet show a strong decrease in the absorbance in the metallic M11 transition region (≈400 – 600 nm) compared to the absorbance of fraction 1. However, the absorbance spectra of both semiconducting nanotube enriched samples are not identical between 900 nm and 1,100 nm. These differences indicate a slightly different enrichment with respect to certain semiconducting chiralities/ diameters for fraction 1 and 2, respectively.

The strong suppression of the absorption in the metallic region confirms the advanced electronic type separation of the new method. The exact quantification of the semiconducting purity on the basis of absorbance spectra as suggested in [207] is difficult for HiPco SWCNTs as detailed in Appendix Section 10.9, where the AD and PT samples are also evaluated for purity.

Raman spectroscopy was performed to further investigate the quality of the separated SWCNT fractions. The Kataura plot in Figure 7.1b relates optical transitions of nanotubes to their diameter or radial breathing mode (RBM), respectively. It has to be noted, that single wavelength excitation Raman spectroscopy gives insight into only a small fraction of SWCNT chiralities. Two excitation wavelengths, at 633 nm and 514 nm, were used to evaluate the SWCNT species [85, 91, 208]. The RBMs of all collected fractions excited at the given wavelengths are shown in Figure 7.1c, d being in line with the previous observations on this sample, fraction 1 reveals strong RBMs in both the metallic and semiconducting regime. In contrast, for fraction 2 (pH 1.8) only RBMs associated with semiconducting SWCNTs were excited. These findings underline once more the highly efficient separation by electronic type under the experimental conditions described above. In the case of the freestanding sheet semiconducting RBMs were excited at both laser wavelengths, but peaks originating from metallic RBMs were also detected when excited by the 514 nm laser. The observation of metallic RBMs in the sheet indicate the presence of residual metallic tubes which were sequestrated in the freestanding sheet. This might indicate that at pH 2.5 the separation of semiconducting from metallic SWCNTs is not complete even after long centrifugation times. These findings might be further influenced by the diameter distribution of the nanotubes observed in the freestanding sheet, which is shifted to smaller diameter SWCNTs compared to fraction 2 [200].

7.2. Temperature Dependent Semiconducting Purity

In order to quantify the temperature effect on the semiconductor enrichment, UV-vis-NIR spectra of the SWCNT fractions extracted from the upper part of the tube, were recorded. Subsequently, the ratio of the area under the M11 (424 – 627 nm) transition region and the area under the S22 (627 – 943 nm) transition region in normalized (peak at 727 nm) absorbance spectra was calculated. In Table 7.1 the exact values obtained in the calculation are summarized.

Temperature (°C)	M11 / S22 Area ratio
10	0.79116
15	0.81115
20	0.77129
25	0.68319
30	0.56536
35	0.57209

Table 7.1. Summarizing the temperature dependent semiconducting purity. For the tested temperatures the purity of the SWCNT fractions was evaluated by integration of the S22 and M11 peak areas (without background subtraction). The calculated areas were used to form the A(M11)/A(S22) ratio. The smaller this ratio is the higher is the semiconducting purity of the extracted fractions at pH 2.0.

In Figure 7.2, this ratio and its relative change are plotted against the separation temperature. At low temperatures, the M11/S22 ratio has a value of about 0.8.

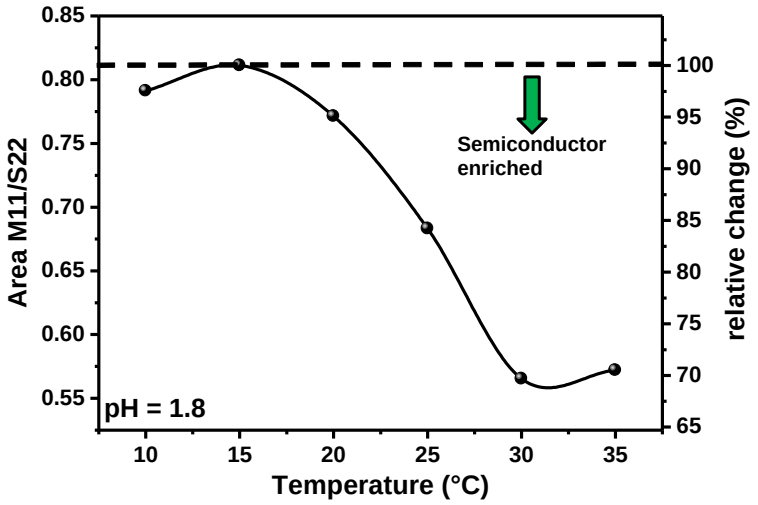

Figure 7.2. The nanotube fractions from the upper part of the tubes were analyzed using normalized (peak 727nm) UV-vis-NIR spectra. The area ratio determined from the normalized spectra in Figure 6.7 is plotted for each temperature. The area ratio between the M11 transitions and S22 transitions was formed is plotted here as a function of temperature.

This value corresponds to a statistical SWCNT mixture without electronic type enrichment. This was calculated with a pH neutrally separated sample. For temperatures above 20°C, the decrease in this ratio proofs an increase in the purity of the semiconducting SWCNT. For the separation temperature of 30°C, a total decrease in M11/S22 ratio of about 30% is calculated. This value remains almost a constant for even higher temperatures.
The plateau region at higher temperature shows that electronic type separation cannot be further improved by higher temperatures. At lower temperatures the plateau level gives the ratio of an unsorted HiPco SWCNT dispersed with SDOC. These findings were surprising, since it has been reported that in DGU under acidic conditions semiconducting SWCNTs can be better separated at lower temperatures [52]. This is best explained by a loss of colloidal stability leading to aggregation as observed in [209] and therefore effective sedimentation even in a weak centrifugal field of only 10,000 x *g*.

7.3. Selective PAE1 Adsorption on Metallic and Semiconducting SWCNTs

Selective desorption of the PAE1 polymer from the surface of metallic SWCNTs is believed to be triggering the agglomeration of metallic SWCNTs during the WFC separation method. To analyze the surface of SWCNTs the method of choice is X-ray photoelectron spectroscopy (XPS). XPS can deliver crucial information about elements present in the first few nanometer of a given sample. To prove the presence or absence of PAE1 polymer on the SWCNT surface, the characteristic phosphorous groups can be used. In the case of WFC separation semiconducting SWCNTs can be obtained in reasonable purity.

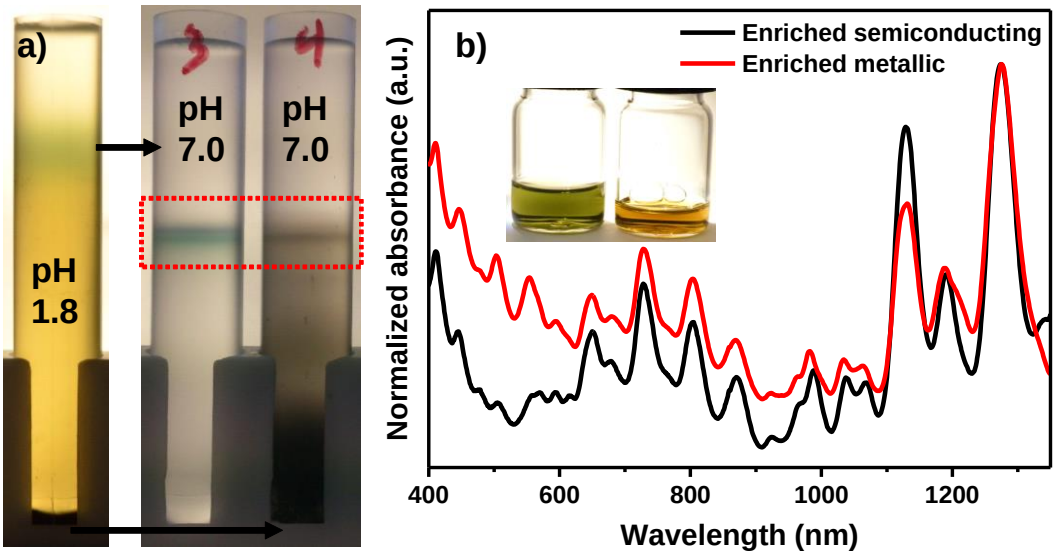

Figure 7.3. Analysis of the fractions used for XPS measurements. In a) parts of the separated top and bottom fractions from electronic sorting were transferred to neutral DGU (40,000 x g, 18 h) in Iohexol to isolate the electronically enriched fractions (dashed red box). In b), the normalized (peak at 1,275 nm) UV-Vis-NIR spectra reveal the electronic enrichment within each sample. The differences in absorbance in the M11 transition region (400 - 600 nm) indicate these findings. An inlet shows the coloring of the extracted samples.

A second fraction enriched with metallic SWCNTs had to be obtained for this experiment. To obtain metallic SWCNTs, the larger agglomerates and bundled SWCNTs were removed from the initial raw dispersion (PAE1) by a 15 min ultracentrifugation run at 250,000 x *g* and subsequent collection of the supernatant. After removing agglomerates and bundled SWCNTs from the dispersion, WFC was applied as introduced. A sample enriched with semiconducting SWCNTs was collected from the top of the centrifugation tube as indicated in Figure 7.3. A fraction enriched with metallic SWCNTs was collected from the bottom fraction in the centrifugation tube. To reveal the electronic character of both SWCNT fractions, parts of the top and bottom SWCNT fractions were extracted, set to neutral pH value and centrifuged on a neutral 40 wt% Iohexol gradient with 2 wt% PAE1 at 250,000 x *g* for 18 h. The individualized SWCNT fractions were extracted, diluted with water, pelletized by ultracentrifugation (4 h, 250,000 x *g*), rinsed with DI water and afterwards re-dispersed in 2 wt% aqueous sodium cholate. The obtained samples were analyzed by UV-vis-NIR (Figure 7.3) to reveal the corresponding electronic characters of both SWCNT fractions.

The other part of the electronically enriched top and bottom fractions of SWCNTs were analyzed by X-ray photoelectron spectroscopy (XPS) to investigate differences in adsorption of the PAE1 dispersant. For that purpose, both as-extracted electronically enriched SWCNT fractions were diluted in DI-water, pelletized by ultracentrifugation at 250,000 x g, wet deposited on a silicon wafer and dried for 3 weeks in a vacuum oven (55°C). The raw HiPco SWCNT material was used as reference material. An overview over the difference spectra obtained from XPS measurements is found in Figure 7.4.

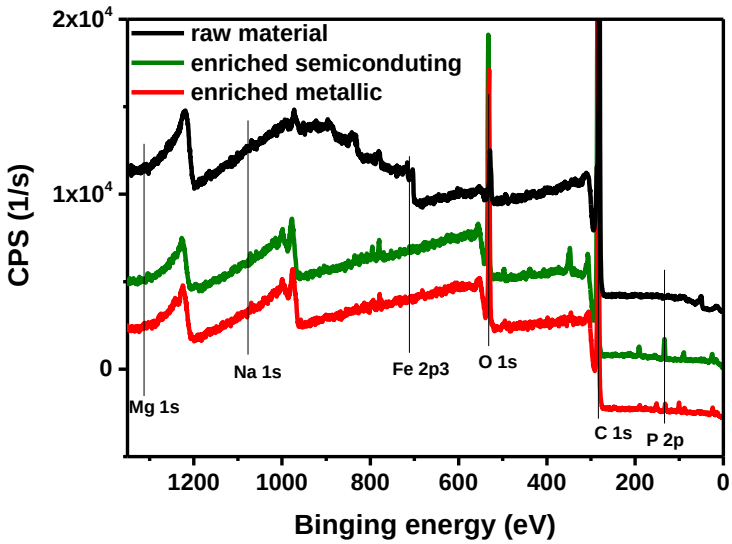

Figure 7.4. Overview over the different XPS spectra from enriched metallic, semiconducting and raw SWCNTs. Relevant peaks are named according to the element and its electron transition.

The phosphorous P 2p peak was used for the phosphorous elemental percentage analysis. The spectra of the corresponding binding energy is shown enlarged in Figure 7.5.

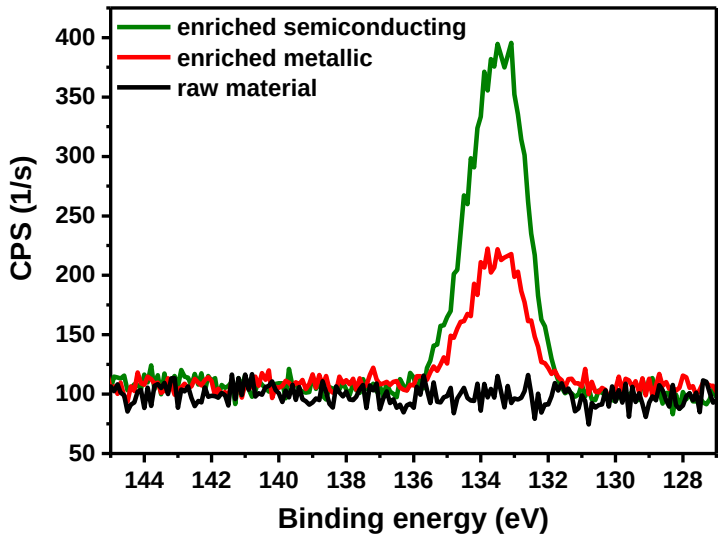

Figure 7.5. The Phosphorous 2p peak in the three tested samples. The spectra were offset for clarity.

The normalized elemental analysis is summarized in Figure 7.6. Phosphorous is an element that can be unambiguously ascribed to the PAE1 (see Figure 3.1). The normalized atomic concentrations reveal that the relative amount of phosphorous within the enriched metallic SWCNT fraction is lower than the phosphorous content within the enriched semiconducting sample. Also, the raw reference material shows no phosphorous content. This reveals that the polymeric coating of metallic SWCNTs with PAE1 is at least partially removed by the acidic environment. The reference material also reveals remaining iron catalyst from the production process. The iron is removed by the separation process in the ultracentrifuge as evident by the lack of the iron signal in the separated samples.

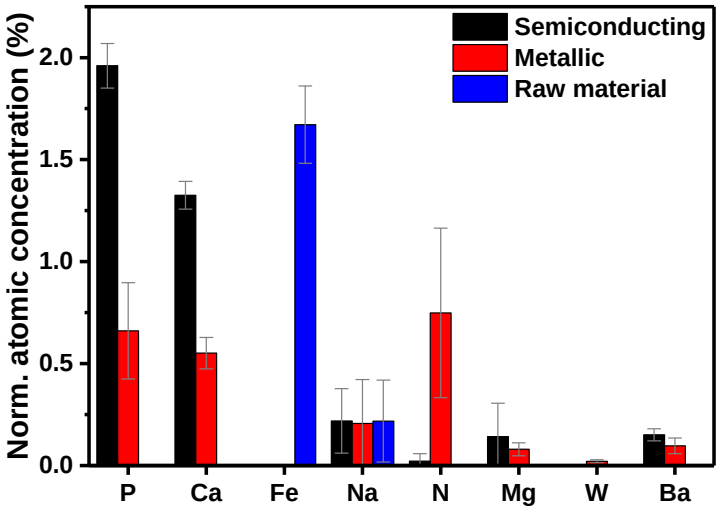

Figure 7.6. Comparing polymeric adsorption on electronically sorted SWCNT fractions after separation. The normalized atomic concentrations of electronically enriched fractions of SWCNTs as well as for the raw material are shown as determined by XPS measurements. The atomic concentrations are normalized to the carbon content. The carbon and oxygen concentrations are not shown to depict the less abundant elements in detail. Errors bars indicate the statistical variation from measuring multiple spots on each sample.

8. SWCNT Based Field-Effect Transistors

In the last part of this study, the electronic characteristics of field-effect transistors based on the separated SWCNT material is presented. The two most important figures of merit of FETs are the charge-carrier mobility μ and the ratio between the current passing through the transistor in the on and the off state ($I_{on/off}$-ratio) [149]. The lateral dimensions of such FETs are typically in the >10 µm range, meaning that the channel does not consist of a single but a percolating network of a large number of SWCNTs. Such a network naturally exhibits a high amount of junctions between individual SWCNTs that limit μ [210]. The resistance of each junction critically depends on the chemical purity of the sidewalls of the SWCNTs. The removal of the surfactant used for separation or dispersion of carbon nanotubes is very important. In a FET composed of a SWCNT-network, μ and the on/off ratio also correlate with the SWCNT density in the channel. The larger the total density of tubes, the larger also μ, since more tubes contribute to the overall current. At the same time, however, the on/off ratio will typically decrease, as the density of residual metallic SWCNTs also increases. In the worst case such high densities may lead to a shortening of the channel and to a strongly decreased on/off ratio. Therefore, a good approach to investigate the degree of purity for separated SWCNTs is to deposit a very dense network as semiconducting channel.

In the following, two SWCNT fractions with enriched semiconducting character were used as defined in chapter 7. The definitions from chapter 7 included, "fraction 1" to name the electronically unsorted SWCNTs from pH neutral WFC.

"Fraction 2" denotes the individually dispersed as extracted semiconducting fraction from WFC separation at low pH. The as extracted sheet like structures of enriched semiconducting character were named "freestanding sheets".

FETs were fabricated in three different configurations. These are: Bottom-contact, Back-gate, (BCBG), Bottom-contact, top-gate (BCTG) and Top-Contact, back-gate (TCBG). Figure 8.1 shows FETs with top contact and bottom contact configuration. Bottom or top source and drain contacts were used in combination with either top or bottom gate configuration.

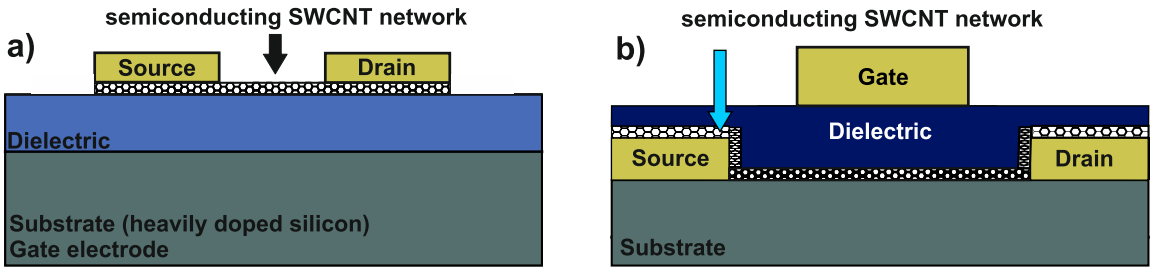

Figure 8.1. Figure 8.1a shows a schematic of a SWCNT-BGTC transistor and in Figure 8.1b a TGBC configuration. In a) source and drain contact were evaporated onto the wafer after deposition of the SWCNT network. In b) bottom contact configuration: the drain and source contacts were evaporated onto the wafer before drop casting a SWCNT network on top of the contacts. Here, the device is top gated.

8.1. Transistor from As-Extracted Semiconducting SWCNTs (Fraction 2)

To demonstrate the applicability of our SWCNTs, field-effect transistors (FETs) were realized from fraction 2 as it was extracted from the centrifugation vials. The FET measurements were set up on silicon oxide coated silicon wafers. The first separation of semiconducting SWCNTs was obtained in a levelled gradient of SPT at pH 2.3. This experiment was not detailed as part of this thesis, however, the separated fraction can be understood as a "fraction 2 equivalent" obtained at pH 2.3. The resulting fraction of individualized enriched semiconducting SWCNTs was used as extracted from the centrifugation tube to build a FET. Besides optimized conditions for better semiconducting purity, this fraction did not differ from fraction 2 as obtained at pH 1.8. The residual SPT content was approximately 17 wt%, which corresponds to a density of 1.15 g/cm³. The FETs were set up by evaporation of gold through shadow masks to establish a pattern of source and drain contacts on the silicon/silicon oxide wafer (length: 50 µm, width: 200 µm). Drop casting of the SPT rich SWCNT dispersion in between two contacts was used to complete a bottom gate bottom contact configuration. The wafer was afterwards immersed in water to reduce the content of residual water soluble SPT and dispersant.

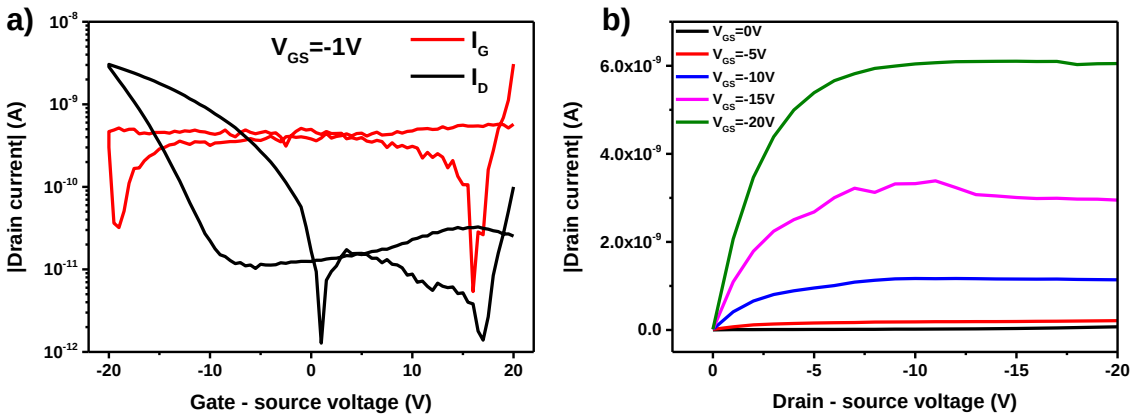

Figure 8.2. Transfer and Output characteristics of a network transistor on Si/SiO_2 in bottom gate bottom contact configuration without SPT removal.

Figure 8.2 includes the transfer and output characteristics of the realized SWCNT FET. At a drain-source voltage of -1 V, p-type transistor behavior is observed. The drain current shows an on/off ratio of 2.3 x 10^3, the field effect mobility from the forward sweep (black arrow) was determined to be 5.6 x 10^{-4} cm^2/Vs. The field effect mobility is very low compared to reported SWCNT transistors from centrifugation based separation procedures (20 cm^2/Vs) [35]. This indicates that the residual SPT greatly enhances the contact resistance between the SWCNTs in the channel. The next step in improving the transistor performance was therefore to reduce/remove the residual SPT content from the as-extracted fraction 2.

8.2. Transistor from Fraction 2 after SPT Removal

To enhance the mobility of the FETs fabricated in section 8.1, the first step was the removal of residual SPT from the extracted samples. A comparably simple approach is the use of ultracentrifugation to pelletize the SWCNT content in the aqueous extracted sample. To pelletize the SWCNTs in the sample the density of the aqueous mixture has to be reduced so that the formation of a density gradient during centrifugation is prevented. This is achieved by diluting the as extracted fractions. This pelletizing procedure was performed iteratively. The extracted SWCNT fraction was centrifuged 4 times at 250,000 x *g* for 4 h and each time the supernatant was discarded and the centrifugation tube was refilled with DI-water. After pelletizing the SWCNTs at the bottom of the centrifugation tube, they were collected and re-dispersed in 2 wt% aqueous sodium cholate hydrate.

The strong reduction of SPT was verified by UV-vis-NIR measurements, which were shown in the methods section 4.3.

Here, a series of measurements were performed using multiple channel lengths of gold contacts that were covered by drop casting the SPT reduced SWCNT/sodium cholate hydrate dispersion onto a silicon/aluminum oxide (30 nm) wafer. However, inhomogeneous covering of the individual channels by the SWCNT networks lead to varying results. The wafer was afterwards immersed in water to reduce the content of residual water soluble SPT and dispersant. In Figure 8.3 the transfer and output characteristics are shown for an established transistor in a 20 µm channel between two gold contacts (width: 1000 µm).

The FET showed an improved transistor performance in terms of on/off ratio and field effect mobility. The mobility increased to 2.6 x 10^{-3} cm^2/Vs and the on/off ratio was determined as 5 x 10^4. The mobility of the transistor is still below reported values (20 cm^2/Vs), however, the on/off ratio increased as result of optimized purity from optimized WFC conditions as well as better gating of the channel by the aluminum oxide dielectric and due to increased mobility.

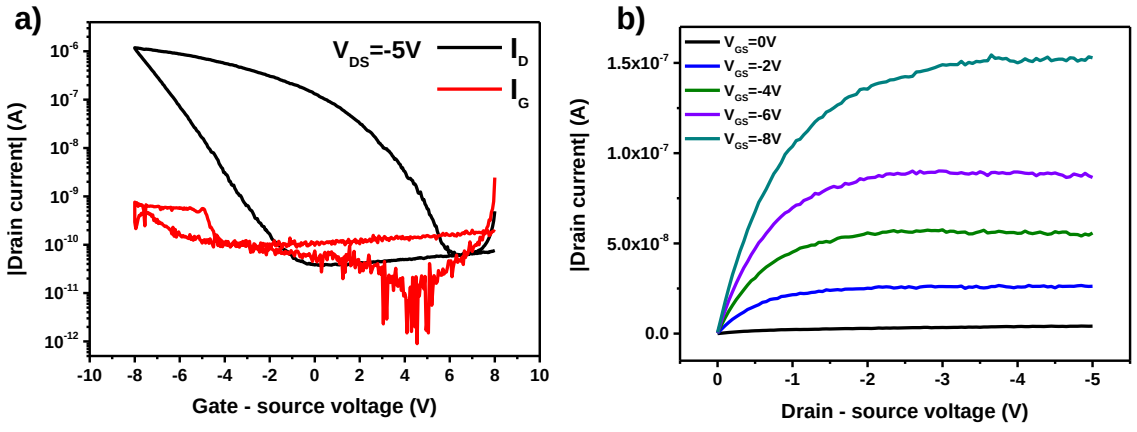

Figure 8.3. Transfer and Output characteristics of a network transistor on Si/Al_2O_3 after SPT removal.

8.3. Transistor from Fraction 2 in Bottom Gate Configuration with Surface Functionalization

To further optimize the conditions of SWCNT network formation, self-assembling monolayers (SAMs) were tested. SAMs offer a high quality surface, tunable surface energy and can shield the deposited SWCNTs from adsorbed species on the wafer surface. Those species, if in contact with the SWCNT network, can form trapping sites for charge carriers. Using SAMs the emerging nanotube networks are shielded from defects and traps on the surface of the Al_2O_3, which results in a decrease of the large hysteresis measured before. Field-effect transistor measurements were set up with SPT depleted SWCNT inks on Al_2O_3 covered silicon wafers. In this experiment the wafers were covered with two different self-assembling monolayers (SAMs). The first one is tetradecylphosphonic acid (SAM1) and the other one is 4-ethoxyphenylphosphonic acid (SAM2). SAM1 results in a more hydrophobic surface while SAM2 gives a rather more hydrophilic surface. The re-dispersed SWCNT after SPT removal were drop casted onto a silicon wafer covered with aluminum oxide + SAM. Golden contact pattern were evaporated onto the wafers patterned by shadow masks.

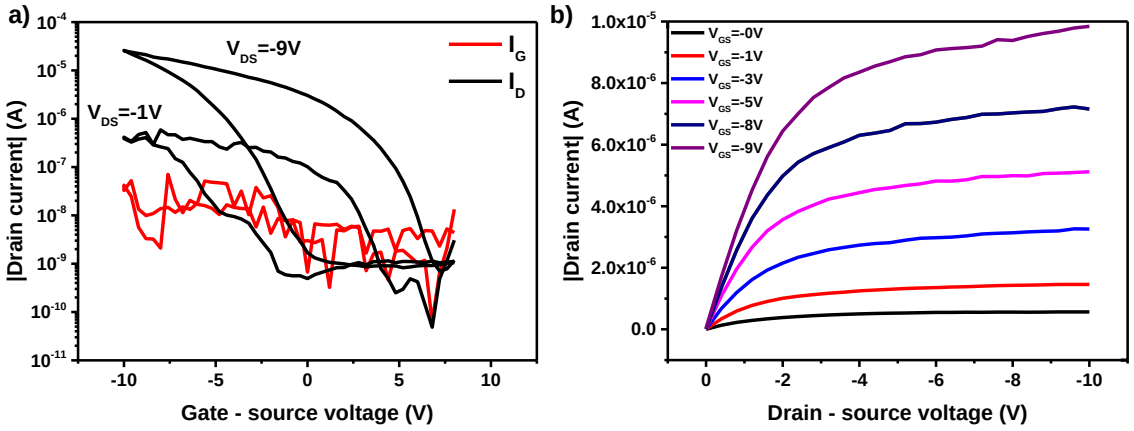

Figure 8.4. Mobility, Transfer and output line of a drop casted transistor in top contact bottom gate configuration from the fraction 2 material on a SAM1 covered Al_2O_3/silicon wafer.

In Figure 8.4 and Figure 8.5 the transfer and output characteristics of silicon/aluminum oxide wafers with SAM1 and SAM2 are shown, respectively. Using SAM1 the field effect mobility increased to 0.2 cm^2/Vs with an on/off ratio of 2 x 10^4. With the use of SAM2 the field effect mobility increased to 0.4 cm^2/Vs with an on/off ratio of 1 x 10^5, with a comparably smaller hysteresis. In both cases, the hysteresis is smaller than without the use of a SAM. Experimentally, it must be noted that only after several measurement sweeps at a source- drain voltage of -9 V the transistor operation was stable. This was expected as the network of SWCNTs could not be immersed in water after drop casting onto the SAM covered wafers.

Immersion in water resulted in the loss of the percolating network of SWCNTs. This was tested before and after establishing the contact patterns, which means that the network was very weakly bound to the SAM covered substrates. Therefore the residual surfactant and polymer could not be further reduced after deposition.

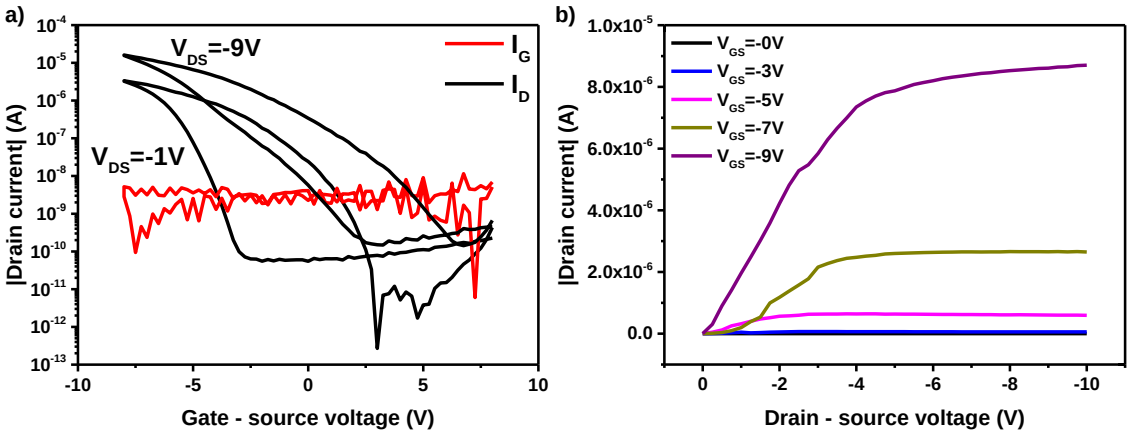

Figure 8.5. Mobility, Transfer and output line of a drop casted transistor in top contact bottom gate configuration from the fraction 2 material on a SAM2 covered Al_2O_3/silicon wafer.

8.4. Transistor from Fraction 2 after SPT and Polymer Removal

After observing that the hysteresis can be reduced using SAMs it was also confirmed that the main enabler for establishing a low resistance network in the discussed transistor experiments must be the removal of residual polymer/dispersant on the individual SWCNTs.
In this section a transistor will be discussed that was fabricated by drop casting another polymer reduced fraction 2 after SPT removal onto an silicon wafer covered with aluminum oxide. To enable post deposition cleansing of the SWCNT network the wafer was not covered with a SAM. The as extracted fraction 2 material was collected in a glass vial after centrifugation. Subsequently, the pH of the as extracted volume was set to pH 1.0. This acidification was shown to induce reversible protonation of the SWCNT sidewalls and therefore hinder surfactant/SWCNT interaction. Therefore, at this pH the stabilization of SWCNTs by the PAE1 polymer is limited. After 24 h of resting the SWCNT material was found to have formed a gray cloud-like structure (see Figure 8.6).

Figure 8.6. Extracted semiconducting SWCNTs without removal of SPT after 24 h of acidification (pH 1.0).

The sedimented SWCNT cloud was collected, diluted with DI-water and four times iteratively pelletized at 10.000 x *g*. The supernatant was exchanged after each centrifugation step. In the last step the SWCNT pellet was re-dispersed in 2 wt% sodium cholate hydrate (SCH).

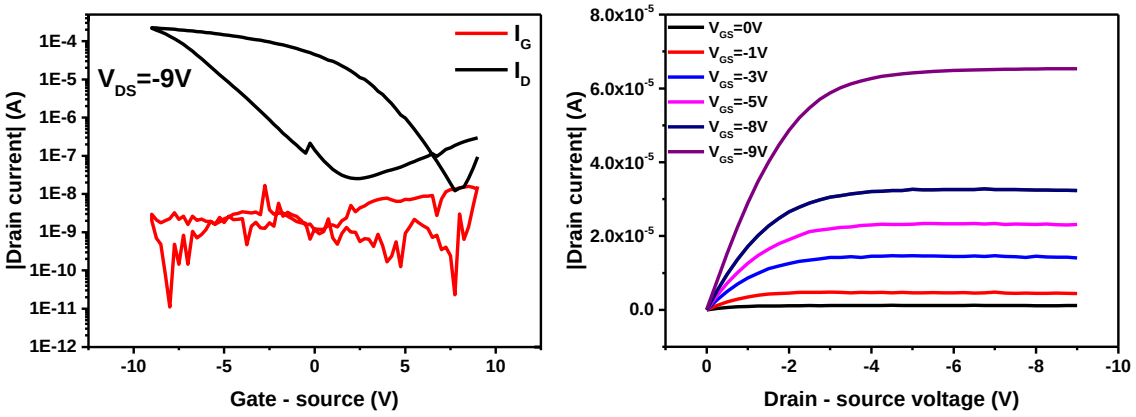

Figure 8.7. Transfer and Output characteristics of a fraction 2 network transistor on Al_2O_3/silicon wafer after polymer reduction.

The transistor configuration was established by drop casting the dispersion onto an aluminum oxide covered silicon wafer after a pattern of gold contacts was evaporated onto the wafer. In Figure 8.7, the transfer and output characteristics of a typical bottom gate bottom contact transistor is shown. The mobility increased to 3.0 cm^2/Vs with an on/off ratio of 1 x 10^4. The mobility increase is mainly ascribed to a reduction of the amount of polymer as consequence of the acid treatment.

8.5. Transistor from Fraction 2 with Bottom Gate after Additional Polymer Removal

In this section the best performing transistor is shown. As the previous sections demonstrated, the applicability of SWCNTs in transistors from the introduced separation process depends largely on the protocol of SPT and polymer removal from the as extracted semiconducting SWCNTs. After showing that SPT and polymer removal lead to an improved mobility of the SWCNT networks the network establishing protocol was further improved. Here, improving the experimental transistor protocol included cleansing steps in between the drop casted aliquots of SWCNT ink. The wafers were immersed in ethanol and 1-M hydrochloric acid after the drying of each droplet to reduce the content of the residual surfactant and polymer. To demonstrate the applicability of the SWCNTs that showed the highest purity in optical analysis, field-effect transistors were once more realized from fraction 2 on aluminum oxide coated silicon wafers. Before deposition on the wafer the SWCNTs were therefore first separated from residual SPT and excess polymer (as described in 4.3 and 4.4) and then re-dispersed in sodium deoxycholate hydrate (SDOC) [210]. The schematic of a transistor, an atomic force microscope (AFM) picture of the thin-film morphology as well as the transfer and output curves are shown in Figure 8.8. A top-contact, bottom-gate structure was used for the device testing (Figure 8.8a). The AFM image (Figure 8.8b) shows that the network exhibits a very high density of SWCNTs. Still, the transfer curves of the transistors (Figure 8.8c) show a p-type field-effect transistor with high on/off ratio (10^5).

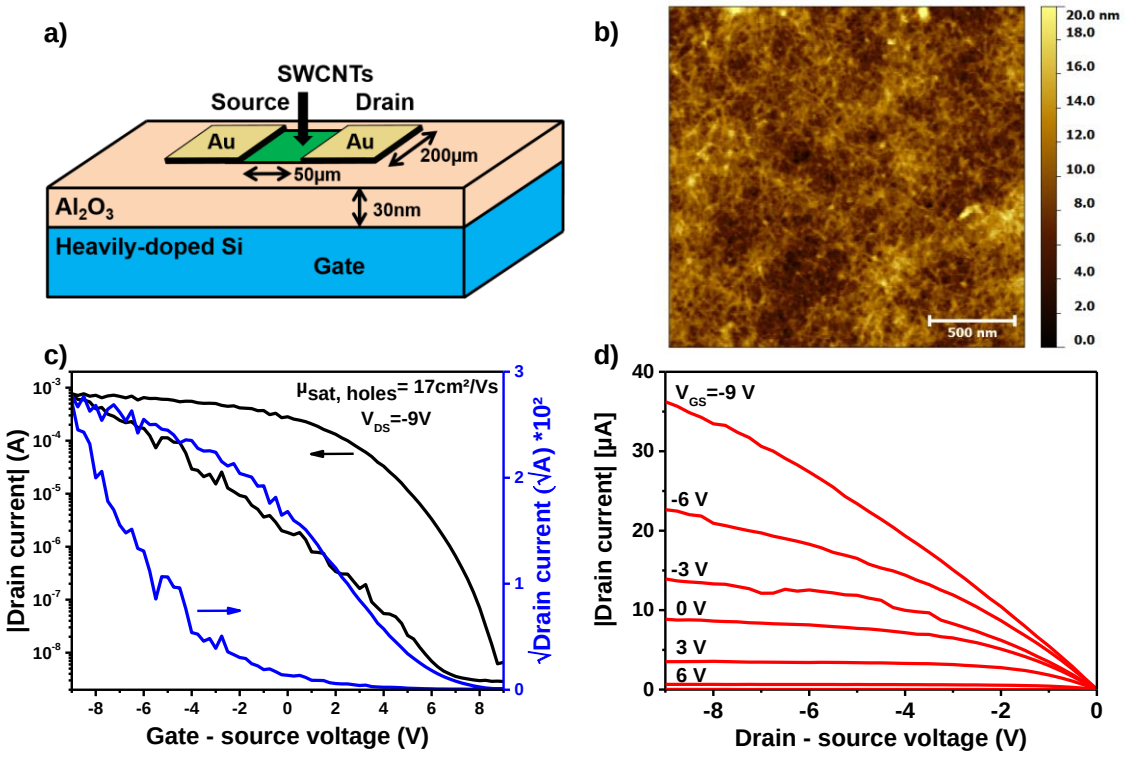

Figure 8.8. Morphology and electronic characteristics of a SWCNT-network transistor. In a) Transistor configuration with semiconducting SWCNT material in green. In b) AFM image of the SWCNT network revealing the morphology of the thin film. In c) the transconductance (linear fits to $\sqrt{I_D}$ resulted in a slope of − 0.0028 for the p-region) and in d) output curve of a transistor.

Even though the AFM analysis indicates that the nanotubes were not completely liberated of the polymer and surfactant by our cleaning protocol the device shows a remarkable field-effect mobility up to 17 cm²/Vs comparable to literature results with similar, plain transistor configuration [35, 211]. The large hysteresis indicates a high density of trapping sites that is typical for this kind of device configuration i.e. no SAM passivation [148] and can be overcome by using different dielectric layouts as reported previously [134].An improved cleaning protocol of the deposited SWCNTs or a more favorable contact configuration could also lead to better injection and improved transistor performance [212-214]. However, the large charge carrier mobility with concomitantly large on/off ratio reveal that the tubes obtained by our method are suitable as channel material for thin-film transistors for example for use in OLED displays.

8.6. Transistor from Fraction 2 in Bottom Gate and Ionic Gel Gate Configuration

In this section a functioning transistor in bottom gate configuration was additionally top gated by an ionic liquid. In Figure 8.9 the transfer characteristic of the transistor bottom-gated with silicon oxide and top gated with the IG are shown, respectively. The top-gate structure was established by drying the IG on the channel between contacts that were already tested in bottom gate configuration.

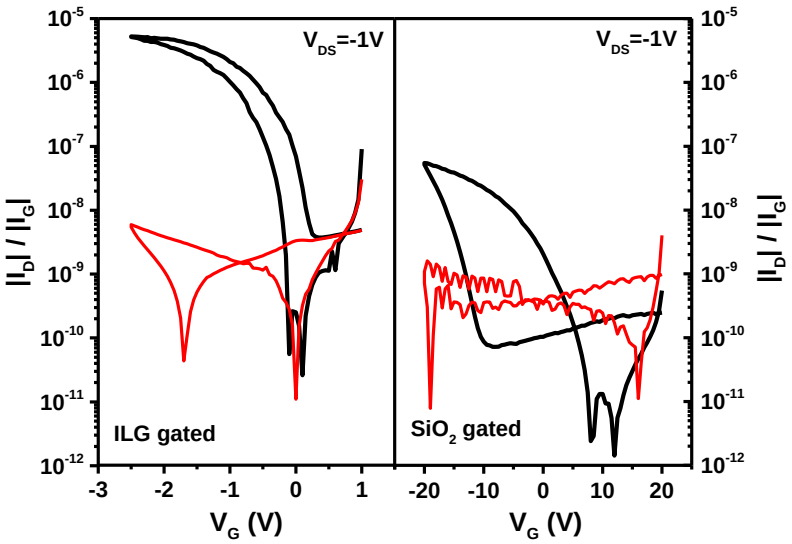

Figure 8.9. Transfer curve of a SWCNT transistor gated by an IG or with SiO_2. The voltage between source and drain was -1V.

The IG was subsequently equipped with a PDOT/PSS gate electrode. The first difference observed in this transistor configuration is the significantly reduced hysteresis and the lower voltages necessary for transistor operation. This is caused by the large capacitance of the IG. The on-state current is enhanced by two orders of magnitude, while the off-state current is enhanced by 1.5 orders of magnitude. Overall a higher on/off ratio is observed in the IG top-gate configuration. The ionic gel was therefore shown to be suitable for use in combination with SWCNTs to improve the transistor properties of an existing percolating network.

8.7. Freestanding Sheet of Enriched Semiconducting SWCNTs

FETs were also prepared based on the freestanding SWCNT sheet (Figure 8.10). The sheet used is approximately 100 nm thick (section 8.8) and was deposited on a quartz wafer for UV-vis-NIR analysis. Therefore cannot be contacted with conventional (bottom gate) gating methods. Therefore an ionic gel (IG) was utilized as gate dielectric, to measure its electronic properties. The ions contained in the gel can penetrate and therefore gate the SWCNTs throughout the entire sheet [215]. A micrograph (Figure 8.10a) shows the layout of the SWCNT sheet device on a quartz wafer. Capacitance measurements, transconductance and output characteristics of the sheet transistor are summarized in Figure 8.10b – d. In Figure 8.10b the area normalized capacitance of the IG at 1 Hz for different gate-source voltages is found [216]. The area used for normalization was $W \cdot L$, which is the interface between IG and the SWCNT sheet in the on-state. It is found that the transistor shows even for high $V_{ds} = -1$ V a notable on/off behavior (10^3) (Figure 8.10c), which is a good indication for the high purity of the SWCNTs given that this transistor device is composed of a 100 nm dense SWCNT network and the channel is only 50 µm in length. The hysteresis is negligible mainly due to screening of the nanotube channel by the IG and measurement in vacuum [148]. This also leads to the characteristic ambipolar transistor behavior for SWCNTs as it was reported previously [217-219].

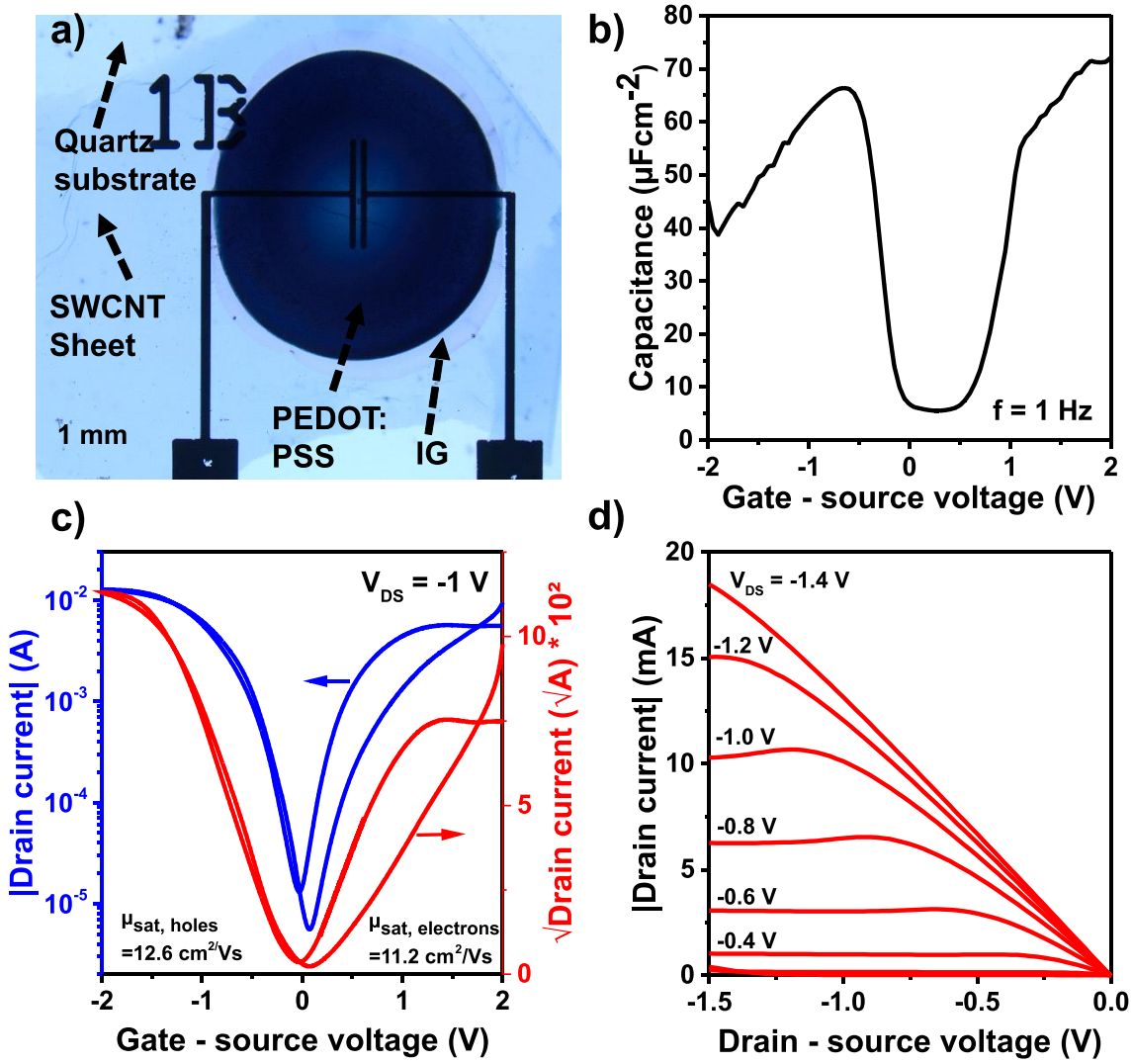

Figure 8.10. Morphology and electronic characteristics of a SWCNT-sheet transistor. In a) a dark field microscopy image of the sheet transistor covered with IG and PEDOT:PSS (dark blue), SWCNT sheet (intermediate blue) and quartz wafer (light blue) is shown. The channel configuration can be seen through the IG. In b) the area normalized capacitance of the IG measured at 1 Hz (interface between IG and SWCNT sheet: 7.02 mm^2) is shown. In c) the transconductance (linear fits to $\sqrt{I_D}$ gave slopes of −0.091 for the p-region and 0,079 for the n-region) and in d) the output curve of the transistor are shown.

The sheet transistor has a hole mobility of 12 cm^2/Vs and an electron mobility of 11 cm^2/Vs calculated by using the peak capacitance for electron (55 $\mu F/cm^2$) and hole (66 $\mu F/cm^2$) conductance in the corresponding voltage range of transistor operation (±1 V). This mobility can be improved in the future by removing the polymer content from the sheet which remains from the separation stage. The mobility of the transistor is furthermore limited by the carrier injection at the metal contacts (Figure 8.10d) due to the top contact top gate configuration applied for the measurements.

8.8. Freestanding Sheet in AFM

The thickness of the freestanding sheet was determined by drying it on a silicon wafer. In Figure 8.11 the sheet is shown in photograph, micrograph and AFM resolution. By measuring the topography of the sheet over an area including a hole scratched into it, the thickness of the sheet could be approximated to be 104 ± 3 nm.

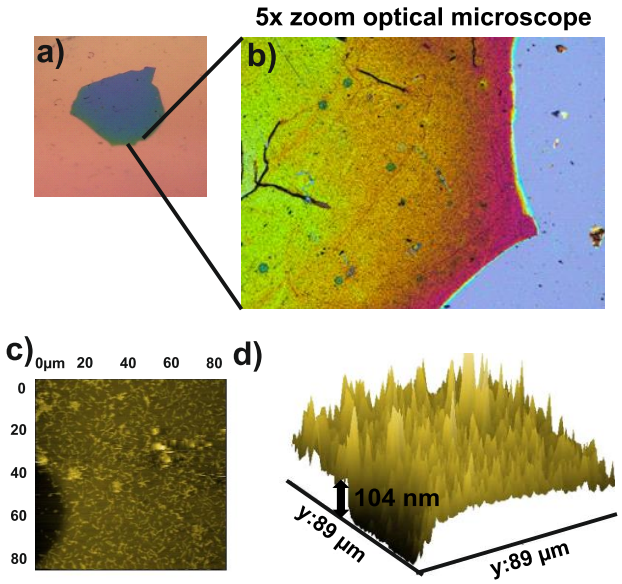

Figure 8.11. Photographs and AFM images of the freestanding sheet on a silicon wafer. In a) and b) a photograph and a micrograph of the dried sheet on the wafer are shown. In c) an AFM picture was taken after scratching a hole into the freestanding sheet so that the AFM stylus captures the height difference. In d) the AFM picture is shown again in 3 dimensions.

9. Summary and Outlook

9.1. Summary

Semiconducting SWCNTs can be considered the future semiconductor material. They have already outperformed silicon in transistor application in terms of on state current density and thus bear the potential to eventually replace silicon completely [220]. However, semiconducting SWCNTs cannot be produced in large scale without their metallic counterparts. To enable the future application of semiconducting SWCNTs in electronic devices, a scalable post-synthesis separation method is sought to provide SWCNTs highly enriched with semiconducting SWCNTs.

Lab scale preparation and subsequent centrifugation of SWCNT dispersions with polymeric dispersants that selectively stabilize semiconducting SWCNTs has delivered SWCNTs with very high semiconducting purity. However, this approach often requires the use of environmentally unfriendly and inflammable organic solvents with additional expensive and laborious ultracentrifugation to result in the desired semiconducting purity. These drawbacks prevent the expansion of SWCNT separation to economic scales and thus the market breakthrough of SWCNT semiconductor devices.

The focus in this work was to develop and establish a scalable method (see Figure 9.1) able to enrich semiconducting SWCNTs. The presented method relies on selective interactions between tailor-made amphiphilic polymers and semiconducting SWCNTs in the presence of low viscosity separation media. The method is simple and scalable, as it only requires a single weak field centrifugation (WFC, i.e. <10,000 x *g*) step of the SWCNT dispersion stabilized by a polymeric dispersant. As dispersant a polyarylether (PAE) polymer was found to enable effective stabilization of SWCNTs in water. In the preparation of SWCNT dispersions with the PAE polymer, non-selective and strong adsorption of the dispersants onto nanostructured carbon surfaces was found. The adsorption of the PAE polymer was found to be independent of SWCNT diameter and SWCNT content in a raw as-produced SWCNT powder. This enables the WFC method to separate SWCNTs independent of their diameter or their synthesis process.

Figure 9.1. Photograph of 100 ml sorted semiconducting SWCNTs. The SWCNTs were freed of SPT, which results in the multitude of pelletized SWCNTs that can be observed in the vial. The green color is preserved despite a high SWCNT concentration.

Selectivity for semiconducting SWCNTs was achieved by introducing the SWCNT dispersions to an acidic environment of aqueous sodium polytungstate (SPT). SPT a density medium used for the separation of minerals but had not been used in combination with carbon nanoparticles. Under these conditions, the mode of action behind the separation mechanism was found to be strongly connected to selective colloidal stability and protonation of the SWCNT polymer complexes. This was investigated by evaluating the separation of semiconducting SWCNTs in dependence on the centrifugation temperature. Here it was found that decreasing the temperature during centrifugation had an attenuating effect on the semiconducting purity of the separated SWCNT fraction. However, at room temperature or further elevated temperatures high purity individualized semiconducting SWCNTs or even self-organized semiconducting sheets were separated from an as-produced SWCNT dispersion via a single-WFC run.

The semiconducting purity of the separated SWCNTs was evaluated by optical spectroscopy methods. The enriched electronic character was proven via the UV-vis-NIR absorbance spectra in combination with single-wavelength excitation Raman spectroscopy. In this evaluation the freestanding sheets of enriched semiconducting SWCNTs showed the presence of residual metallic SWCNTs, while for the separated individualized semiconducting SWCNTs no such presence could be detected. The purity of the sorted SWCNTs is equal to or exceeds the purity achieved with multichiral separation of HiPco SWCNTs by other methods [27, 221-223].

The applicability of the separated fractions was evaluated starting with the approach of drop casting the as separated SWCNTs or placing the freestanding sheet from solution onto silicon wafers. In individual steps the drawbacks of residual density material and polymeric dispersant were investigated and the transistor performance was improved.
Using the individualized semiconducting SWCNTs as well as the sheet as semiconductor channel in FET setups resulted in transistors with on/off ratios of 10^5 and field effect mobilities as high as 17 cm^2/Vs comparable to separated large diameter SWCNTs from other separation processes in similar transistor configuration [35]. However, the mobility is lower than the mobility (147 – 297 cm^2/Vs) reported for more sophisticated SWCNT FETs (dielectric material and architecture and or deposition method of SWCNTs including the formation of SWCNT arrays) [149, 224, 225].
Although the freestanding sheet is composed of not only semiconducting SWCNTs, transistor behavior was observed after top gating it with an ionic gel. The performance in terms of on/off ratio was $>10^3$ with a field effect mobility of 12 cm^2/Vs.

9.2. Outlook

Within this thesis a method to enrich semiconducting SWCNTs mainly based on weak field centrifugation was developed. This new separation method is shown to be able to provide high purity enriched semiconducting HiPco SWCNTs. Although HiPco SWCNTs are the focus, the feasibility for large diameter arc discharge or plasma torch SWCNT dispersions was also demonstrated. This was done, however, without optimizing the centrifugation parameters in order to obtain higher semiconducting purity in the separated fractions.

Improving purity and yield of the separated fractions could be further optimized. Improved parameters such as, increasing the loading amount, decreasing centrifugation run time and finding the optimum solution pH could be identified using a statistical experiment plan (SEP). A SEP can give information about the dependence of purity and yield onto each relevant parameter. An analysis would be set up to optimize the yield (comparison of total UV-vis-NIR absorbance of extracted fractions) and the purity (ratio of area under M11 and S22 transitions in UV-vis-NIR absorbance) for SWCNT dispersions of any diameter. Furthermore such a SEP could be performed for any diameter SWCNT material.

Apart from optimizing the conditions for purity and yield, the separation process itself could be further simplified. Colloidal stability and subsequent agglomeration of SWCNTs was found to be important for the separation process. The extracted SWCNTs samples could thus be filtered to sort out small bundles of nanotubes that hadn't settled completely to the bottom of the centrifugation tube within the time of centrifugation. Using this step one could further reduce the necessary g-force or centrifugation time, because only the largest bundles have to be sorted out before filtering the smaller bundles. In the future, it is even imaginable that a SWCNT dispersion, free of amorphous carbon, only has to be put into an electronic enrichment favoring environment with subsequent filtering to enable effective semiconductor enrichment. The aggregated metallic SWCNTs could be efficiently sorted out without the necessity of centrifugation.

For HiPco SWCNTs a reliable WFC process resulting in very high semiconducting purity was established. However, the transfer of the optically determined purity of the extracted semiconducting SWCNTs into FET devices with very high mobilities was prevented. In the presented device testing, the residual polymeric dispersant on the SWCNT sidewalls was the largest hurdle in front of better device performance. Without effective removal of the polymer from the SWCNT sidewalls, the polymer leads to high contact resistance within the nanotube networks.

A strict polymer removal protocol should be developed to enable future boosts in FET performance with SWCNT from the WFC method. An approach for polymer removal could deduced from the experiments on temperature dependent preparation of dispersions. The affinity to effectively disperse SWCNTs with the PAE1 polymer was found to be temperature dependent, while for other surfactant a less pronounced dependency was found. An exchange of the PAE

dispersant with standard surfactants in the extracted SWCNT fractions could be developed by using heating and or sonication.

Post deposition polymer removal approaches could also be investigated. After deposition of nanotubes on a substrate, the networks can be cleansed by the use of acids. Hydrochloric acid (HCl) was already used to destabilize the as extracted separated SWCNTs. Different acids could be used in different concentrations to systematically investigate the immersion time and its effect on polymer removal. Subsequently annealing of the SWCNT network substrates could be investigated as well. Annealing is already widely used to eliminate other dispersants from SWCNT sidewalls after their deposition [220, 224, 226].

Nevertheless, a complete protocol for thorough polymer removal has to be found to limit the contact resistance of SWCNT networks in electronic application. Once the contact problems can be overcome, the semiconducting purity could be evaluated for each fractionated semiconducting SWCNT sample in complete detail via electronic device testing.

Electronic device testing can focus on establishing many short channel (< length of nanotube) devices to test the semiconducting purity via the on/off ratio of the SWCNTs. Further testing could base around alignment of the nanotube networks in larger channel devices, also contact metals and dielectric configurations as well as thickness and density of SWCNT networks [149, 220, 224, 225].

10. Appendix

10.1. Structures of Pluronic F68, F108, F127, PE10500 and Tetronic 90R4

The structures of the Pluronic and Tetronic polymers is shown in Figure 10.1. The rounded molecular weights and composition in terms of ethylene oxide and propylene oxide of the used polymers are listed in Table 10.1.

Polymer	Molecular Mass (Da)	PEO (Da)	PPO (Da)
F68	8,400	6,720	1,680
F108	14,600	11,680	2,920
Pluronic F127	12,600	8,820	3,780
PE10500	6,500	3,250	3,250
Tetronic 90R4	7,200	2,800	4,200

Table 10.1. The molecular weights and distribution into the different polymer groups are listed.

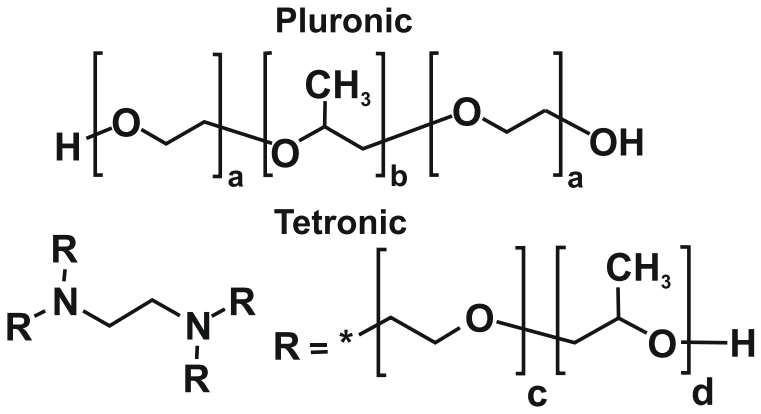

Figure 10.1. Structures of Pluronic and Tetronic polymers. The different molecular masses result from the different compositions of the PEO to PPP chains for Pluronic polymers and the number of the respective groups also displayed for the Tetronic polymers.

10.2. Structure of Tamol NN9401

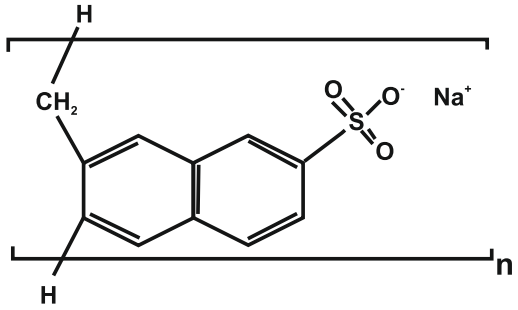

Figure 10.2. Chemical structure of Tamol NN9401.

10.3. EDIPS SWCNTs Dispersed with PAE1

Besides the discussed SWCNT material also SWCNTs from the EDIPS production process by Mejo were tested regarding dispersing qualities. The PAE polymer was used in 2 wt% aqueous solution and proofed to be able to disperse the SWCNTs (mean diameter 1.5 nm) from this production route. This corresponds well with the carbon material independent absorption of PAE1 on carbon surfaces especially SWCNTs of different diameters. The UV-vis-NIR spectrum in Figure 10.3 shows the typical S22 transition region between 850 and 1200 nm, the M11 transitions between 600 and 800 nm and even smaller S33 transitions below 600 nm.

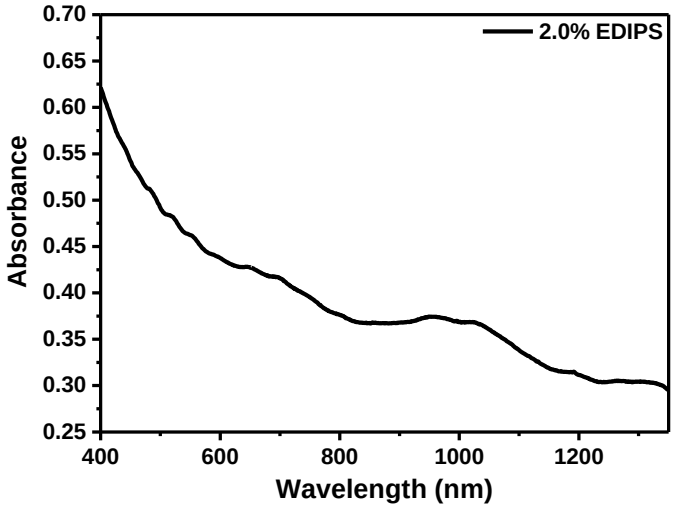

Figure 10.3. A UV-vis-NIR spectrum of EDIPS SWCNTs (mean diameter 1.5 nm) dispersed using 2 wt% PAE1.

10.4. Photographs of Temperature Dependent Dispersions

Photographs of the temperature dependent dispersion series were taken after different times as labeled in Figure 10.4 and Figure 10.5. The corresponding experiment is found in section 5.3.

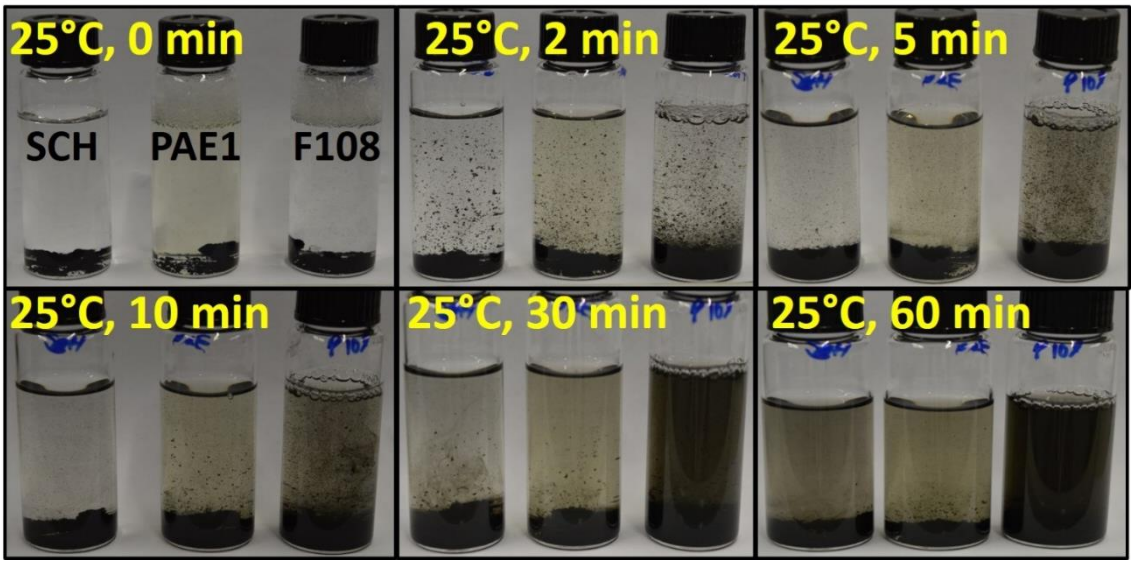

Figure 10.4. Photographs of temperature and time dependent SWCNT dispersions. The left dispersion features aqueous sodium cholate hydrate, the middle dispersion is comprised of aqueous PAE1 and the right dispersion was set up with Pluronic F108. The time dependent evolution of the dispersion is shown at 25°C.

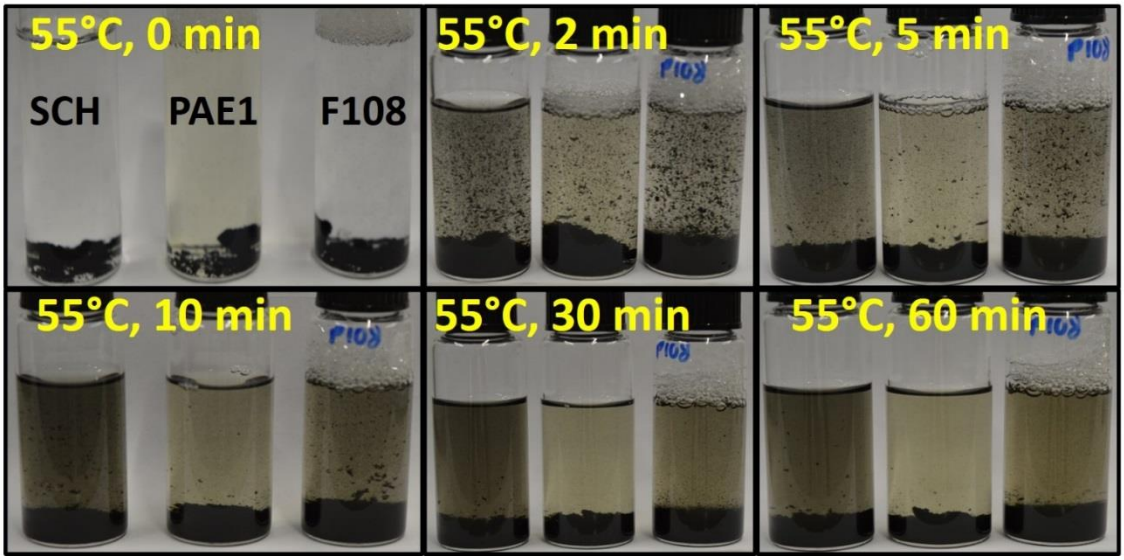

Figure 10.5. Photographs of temperature and time dependent SWCNT dispersions. The left dispersion features aqueous sodium cholate hydrate, the middle dispersion is comprised of aqueous PAE1 and the right dispersion was set up with Pluronic F108. The time dependent evolution of the dispersion is shown at 55°C. (The photograph at 0 min, was taken from the 25°C testing to avoid a blank space in this figure as no 2nd photograph of the wetted raw material was taken).

10.5. Photographs of pH Dependent Dispersions

Photographs of the pH variation of a PAE1 dispersions as described in section 5.4.

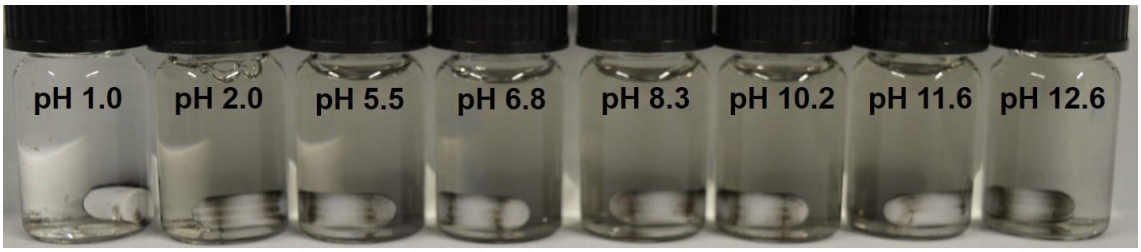

Figure 10.6. Photographs of pH modified PAE1 dispersions after 96 h.

10.6. Neutral DGU of Stable Dispersions

Dispersions prepared with various polymeric dispersions were analyzed regarding their SWCNT content. A neutral DGU step at 40,000 x *g* was applied for 14 h to sort the HiPco SWCNT material from the amorphous carbon. The density material was SPT.

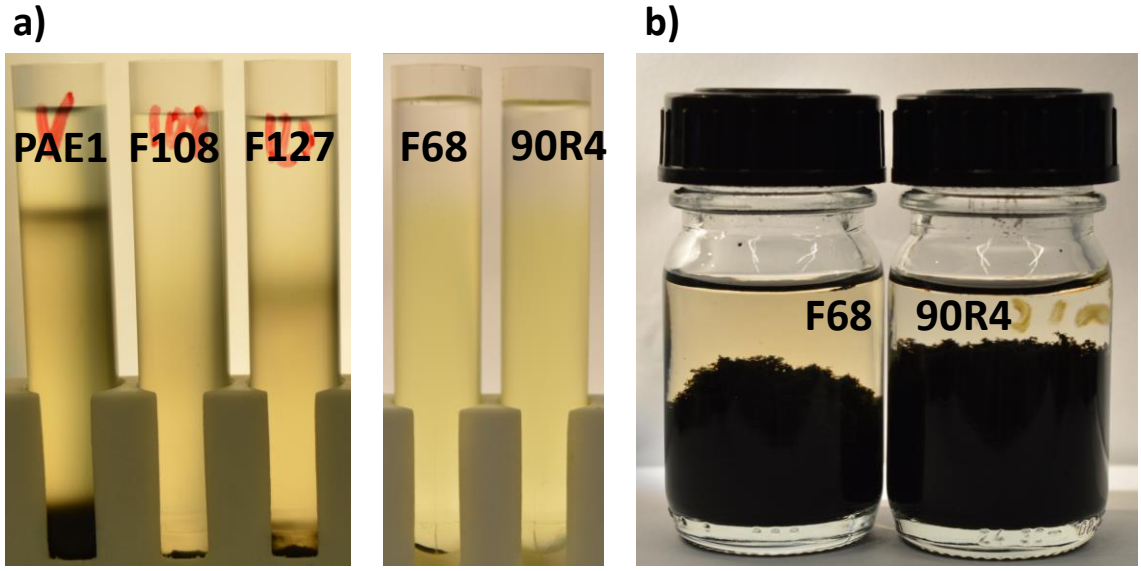

Figure 10.7. Neutral DGU of stable polymeric dispersions. In a) from left to right, 1 ml of a raw HiPco dispersion with 2 wt% aqueous PAE1, Pluronic F108, Pluronic F127, Pluronic F68 and Tetronic 90R4, respectively were centrifuged on a neutral column (3.4 ml) of aqueous SPT (26 wt%) at 40,000 x g for 14 h. In b) the unstable dispersions of HiPco SWCNTs with Pluronic F68 and Tetronic 90R4 are shown before centrifugation.

10.7. Calculations of Polymer Adsorption

Calibration and Calculation of PAE1 Adsorption

The absorbance was measured for different PAE1 concentrations to subsequently calibrate both parameters. The calibration concentrations of the aqueous PAE1 polymer between 1 and 30 g/L were diluted by a factor of 100 to have the peak absorbance of the polymer in the linear regime of the detector system (Perkin Elmer 35). In Figure 10.8 the absorbance of the polymeric solutions is shown and in Figure S1b the absorbance at 278 nm was plotted over the concentration. A linear fit was used to describe the data. An error of 0.25 g/L was used from error propagation from the fit and measurements uncertainty.

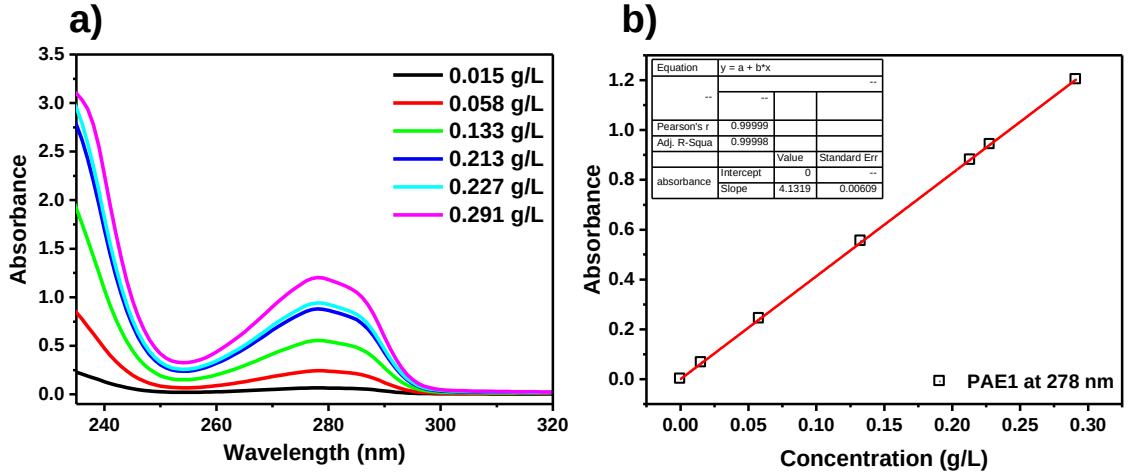

Figure 10.8. Calibration of the absorbance at 278 nm for PAE1 polymer solutions of different concentrations.

The absorbance of the supernatants (obtained as described in 5.5) was used to calculate the corresponding adsorbed polymer concentrations. The connected values are summarized in Table 10.2.

Measured Absorbance (diluted) (a.u.)	Concentration (diluted) (g/L)	Concentration (g/L)	Input Concentration (g/L)	Adsorbed Polymer Concentration (g/L)
0.036	0.00883	1.012	01.04	0.028
0.181	0.04374	4.232	05.02	0.788
0.667	0.16142	13.785	14.96	1.175
0.743	0.17982	18.808	19.95	1.142
1.232	0.29822	23.484	24.97	1.482
1.163	0.28157	28.481	30.00	1.519
1.171	0.28334	49.160	49.98	0.820

Table 10.2. Calculations of adsorbed PAE1 polymer concentration. The measured absorbance at 278 nm from the supernatants of PAE1 SWCNT dispersions and subsequent calculation of free and adsorbed polymer concentrations.

Calibration and Calculation of Pluronic Polymer Adsorption

The refractive index was measured for different concentrations of the Pluronic Polymers for calibration. The calibration concentrations of the aqueous Pluronic F68 and F108 polymers were set up between 1 and 50 g/L. The refractive index was measured and is plotted versus concentration in Figure 10.9.

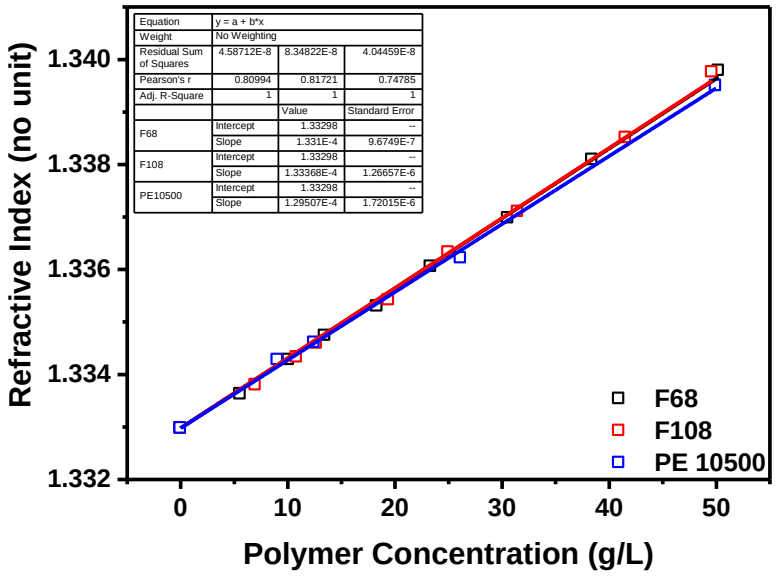

Figure 10.9. Calibration of the refractive indices for Pluronic polymer solutions.

The refractive indices of the supernatants as described in the 0 were used to calculate the corresponding adsorbed polymer concentrations. The connected values of the point measurements are summarized in Table 10.3. A rounded error of 0.5 g/L was assumed resulting from 0.1 g/L from measurements of the RI of pure water and the supernatant, respectively and the error propagation from the increment of the linear fit of 0.25 g/L.

Polymer	Refractive Index	Free Polymer Concentration (g/L)	Initial Polymer Concentration (g/L)	Adsorbed Polymer Concentration (g/L)
F68	1.33688	29.31	29.98	0.67
F108	1.33691	29.51	29.95	0.44
PE10500	1.33676	29.18	29.82	0.64

Table 10.3. Calculations of adsorbed Pluronic polymer concentration. The measured refractive index from the supernatants of SWCNT dispersions and subsequent calculation of free and adsorbed polymer concentrations.

10.8. Lower pH Limit in PAE1 Semiconductor Enrichment

For 18 h of WFC using HiPco SWCNTs, the lower pH limit to achieve a separation was probed. Figure 10.10 shows the resulting separation state of HiPco SWCNTs after WFC at very low pH. At pH 1.5 all nanotubes especially the semiconducting ones lose their stability and cannot be separated from their metallic counterparts. Additionally below pH 1.8, an increasing part of the SWCNT dispersion adhered to the centrifugation tube sidewalls.

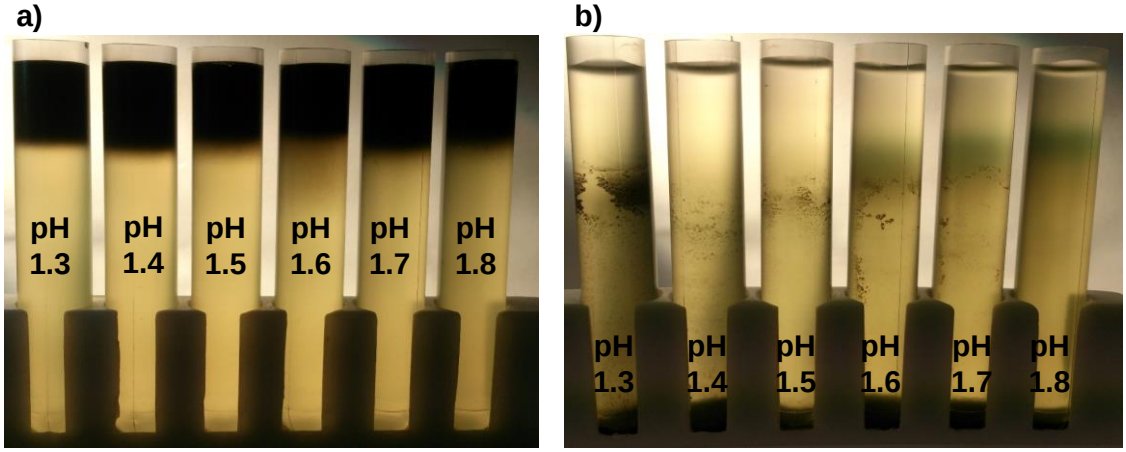

Figure 10.10. Lower pH limit for WFC separation of HiPco SWCNTs. The PAE1 WFC separation is probed in between pH 1 and pH 2, where the stability of all electronic type SWCNTs was found to be lost. The displayed range is between pH 1.3 – 1.8, where the stability is clearly vanishing below pH 1.6 after 18 h of centrifugation at 25°C, 10,000 x *g*.

10.9. Estimation of Semiconducting Purity from UV-vis-NIR Spectra

HiPco

The semiconducting purity of SWCNT samples may be calculated via the UV-vis-NIR spectra [207]. Therefore the semiconducting S22 and metallic M11 transitions have to be identified. For large diameter SWCNTs (1.5 nm) these two transition regions can be individually detected enabling to calculate the semiconducting purity. For small diameter HiPco SWCNTs (1 nm) the metallic M11 transitions overlap to a larger extend with the S33 and S22 transitions of the semiconducting nanotubes [55, 227]. However, the proposed method requires the peak areas to be identified unambiguously. Thus this method tends to underestimate the semiconducting purity of the fractionated HiPco samples if the overlap area is ascribed to the metallic SWCNTs or might overestimate the semiconducting purity if the overlapping area is ascribed solely to the semiconducting SWCNTs. Yet, here a purity estimating calculation is included for the separated SWCNTs (pH 1.8). The UV-vis-NIR spectra (Figure 10.11) reveal an area of decreased absorbance between 450 nm and 560 nm. This region was therefore ascribed to the M11 transitions and used to estimate the semiconducting purity.

In order to estimate the semiconducting purity of the separated nanotube fraction from acidic conditions (pH 1.8), the combined area A(S22) of the semiconducting absorption peaks and the combined area A(M11) of the metallic absorption peaks were calculated after background

subtraction. The background fit was performed using an exponential S14 decay ($C + a \cdot exp(-\lambda b)$ according to [207] the semiconducting percentage purity (SPP) of enriched semiconducting HiPco fractions can be obtained by the following equation

$$\mathrm{SPP} = \frac{1}{1 + \frac{A(M11)}{f \cdot A(S22)}} \tag{10.1}$$

Where f is 1.05, a factor determined for HiPco SWCNTs [207].
The respective areas were calculated to be A(M11) = 0.1293 and A(S22) = 8.1691. Using these values and equation (10.1) the SPP was estimated to be 98.5%. This estimation must be handled with caution, since the metallic M11 and the semiconducting S22/S33 transitions cannot be clearly distinguished. For the freestanding sheet, however, the diameter range of the included nanotubes is shifted so that an estimation on the base of HiPco material is not reasonable. The spectrum used for the evaluation is shown in Figure 10.11.

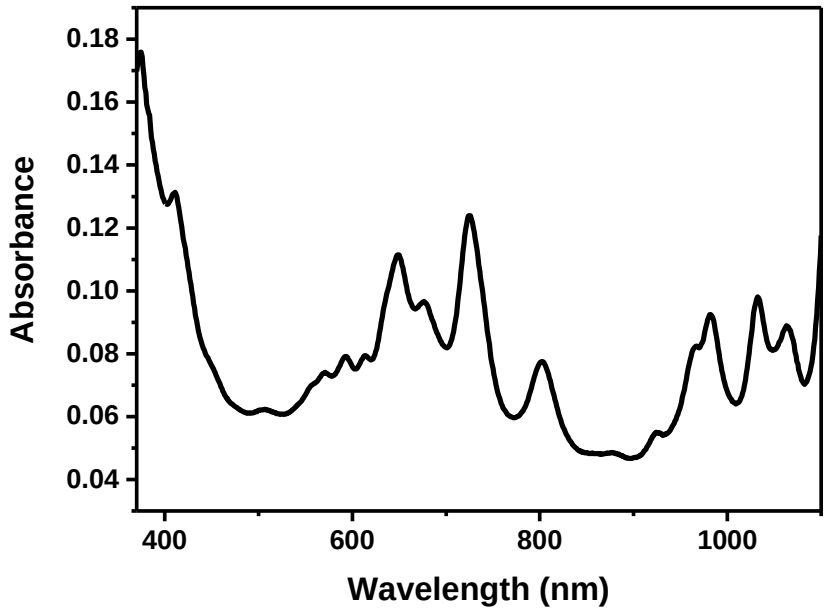

Figure 10.11. Spectrum used for the evaluation of the achieved purity during separation of HiPco SWCNTs.

Arc-Discharge

The separation of AD samples was not further optimized and the purity estimated from the optical absorbance as described and depicted in 6.6 was 99.4% with A(M11) = 0.7842 and A(S22)= 2 · 48.8557, where due to limits in the detection system the S22 area could not be recorded completely. The peak measured was integrated from 790 to 1000 nm and the resulting area was multiplied by a factor of 2 to at least give an estimation of the semiconducting purity. Here a value of 1.24 was used as value for f as determined for large diameter SWCNTs in [207].

Plasma-Torch

The separation of PT samples was not further optimized and the purity estimated from the optical absorbance as described and depicted in 6.6 was 96.7% with A(M11) = 0.2505 and A(S22)= 5.9812. Here a value of 1.24 was used as value for f as determined for large diameter SWCNTs in [207].

10.10. Sedfit Analysis of Sedimentation Coefficients of Metallic SWCNTs

In section 6.7 the agglomeration of metallic AD SWCNTs was investigated by AUC. In order to evaluate the sedimentation coefficients during the experiment the software Sedfit was used. A screenshot of the fits can be found in Figure 10.12. On top the measured data is displayed along with the fits made by the program. In the middle panel the residuals are displayed and on the bottom the resulting distribution of the sedimentation coefficient is shown.

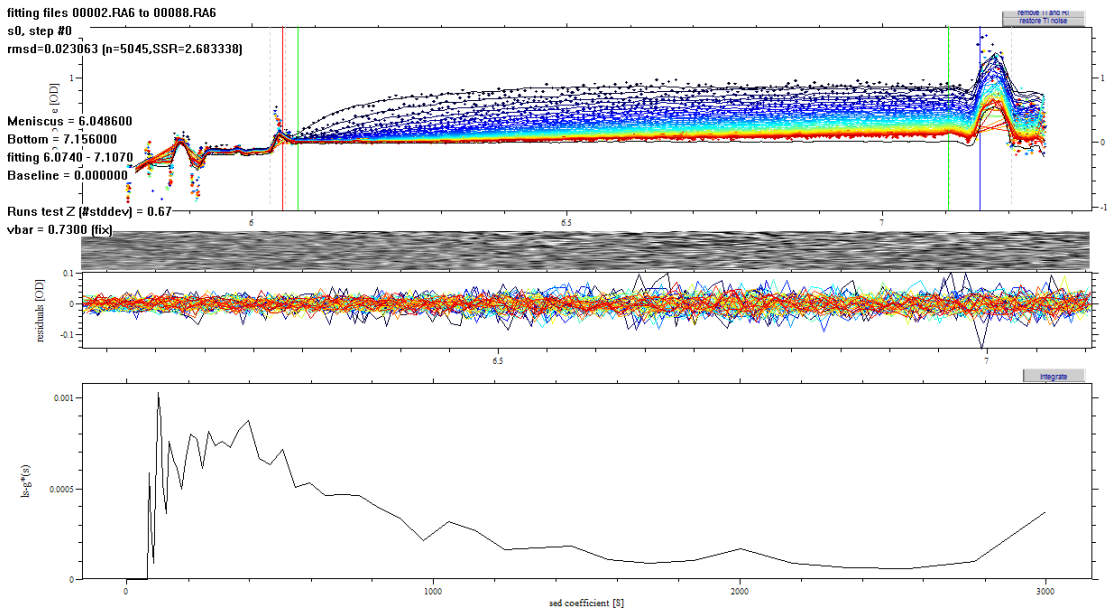

Figure 10.12. Screenshot of Sedfit as applied to evaluate the sedimentation of an AD dispersion with PAE1 in WFC conditions.

10.11. Different Dispersants in WFC

In this section, a variety of different surfactants and polymeric dispersants are probed for suitability in WFC separation. The widely used surfactants sodium cholate [33] and sodium deoxycholate [39, 228] are not suitable for use in acidic environments as they are prone to flocculation below pH 7 and could not be tested. The dispersions were prepared via 1 h of horn sonication of raw as-produced SWCNT (HiPco Batch: R1-912) material in DI-water with cetyl trimethyl ammonium bromide (CTAB), Lupasol PN60, Pluronic PE6800 and PE10500, Tamol NN9401, sodium dodecylbenzenesulfonate (SDBS), respectively. The overall composition of the dispersions is always 0.5 wt% of SWCNT raw material and 2 wt% of dispersant. UV-vis-NIR spectra of the resulting dispersions are displayed in Figure 10.13.

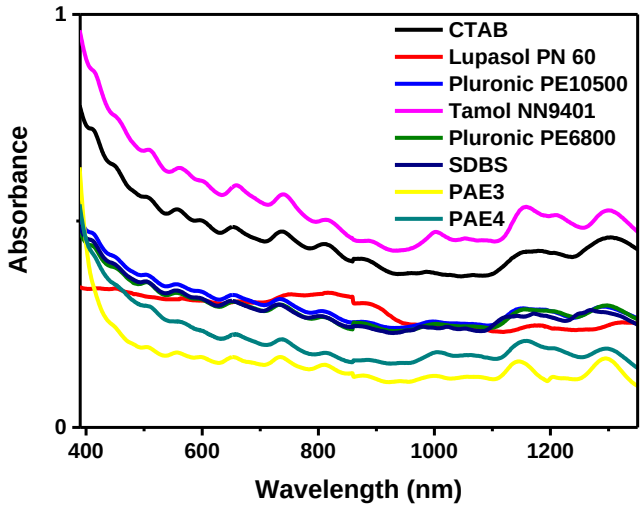

Figure 10.13. UV-vis-NIR spectra of HiPco SWCNT dispersions with different dispersants.

Lupasol PN60 is not capable of stabilizing small diameter HiPco SWCNTs in water. SDBS and the Pluronic polymers namely PE10500, PE6800 show dispersing properties as well as Tamol and CTAB. UV-vis-NIR spectra (Figure 10.13) revealed very similar peak positions, which shows that no significant differences between the metallic to semiconducting ratio existed in the initial dispersions.

SPT Concentration (wt.%)	Density (g/cm^3)
21	1,20
32	1,37
64	2,04

Table 10.4. Density columns used for WFC of different dispersants. The dispersants were cetyl trimethyl ammonium bromide (CTAB), Lupasol PN60, Pluronic PE6800 and PE10500, Tamol NN9401 and sodium dodecylbenzenesulfonate (SDBS).

To test the dispersions under WFC conditions density gradients of SPT were set up according to Table 3.1. Each gradient was set up equally and supplied with the same amount of SWCNT material (0.5 ml). All dispersants were tested using this stacked gradient. This is because this experiment was performed before the separation process was established as in section 6.5. The stacked gradient used was actually the one that resulted in the prototype separation achieved with either PAE1 or PAE2. The dispersion (0.5 ml) was superimposed on the density material column and the resulting separations achieved with all dispersants are shown in Figure 10.14. Figure 10.14a shows the loading of the different dispersions on the stacked gradient, the subsequent results of centrifugation are displayed in Figure 10.14b.

CTAB and Lupasol PN60 cannot stabilize HiPco SWCNTs so that a separation was not achieved. This is observed in Figure 10.14b, where tubes 1 and 2 show no separated SWCNT band. The material heavily agglomerated and penetrated into the bottom density layer of more than 2.0 g/cm³. With the Pluronic polymers (Figure 10.14 tubes 3 and 5) a lot of stable material is observed, while Tamol (Figure 10.14b tube 4) and SDBS (Figure 10.14b tube 6) even show bands of separated SWCNT material in the top region of the gradient.

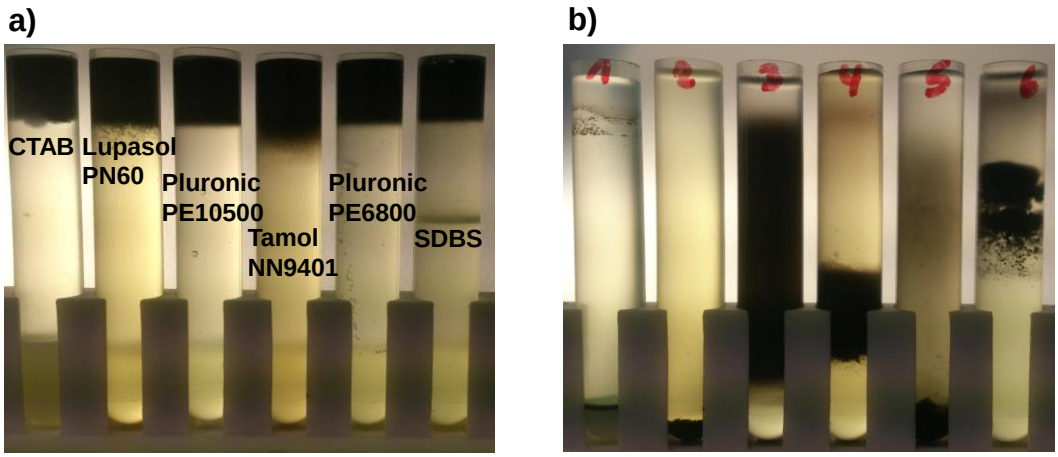

Figure 10.14. WFC separation of HiPco SWCNTs with different dispersants. In a) the loading of different dispersions and b) the resulting separations after pH 4 centrifugation for 18 h at 10,000 x *g*.

In case of isolated bands the material was carefully extracted, in case of no visible banding the complete supernatant was extracted and analyzed by UV-vis-NIR spectroscopy. Figure 10.15 shows the absorbance spectra of the extracted supernatants. It is proven that the supernatants from CTAB and Lupasol PN 60 do not contain SWCNTs. Pluronic PE 10500 and Pluronic PE 6800 show slightly different spectra. Both spectra differ in the stabilization of SWCNTs with transitions around 1000 nm for Pluronic PE 10500, besides showing no indication of electronic type enrichment.

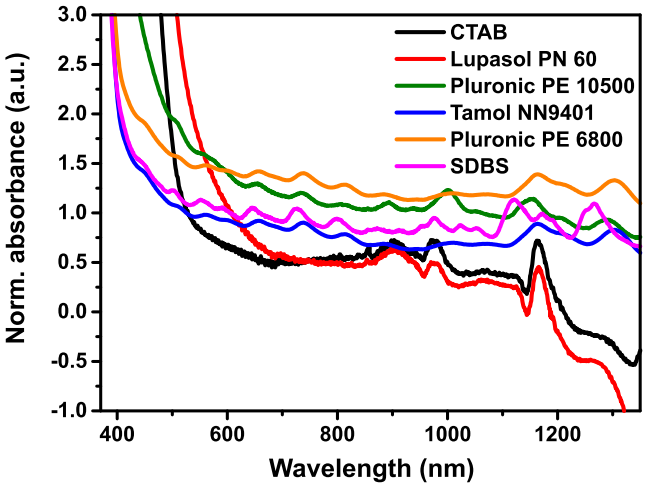

Figure 10.15. Analysis of the supernatant after centrifugation of dispersions from different dispersants as depicted in Figure 10.14b. The normalized absorbance is shown for supernatants from dispersions with CTAB, Lupasol PN 60, Pluronic PE 10500, Tamol NN9401, Pluronic PE 6800, SDBS. The spectra are offset for clarity.

10.12. Solvent/Acid Treatment of SWCNT Films on Silicon Wafers

To reduce the impact of polymer onto the contact resistance of deposited SWCNT networks the effects of an ethanol and a nitric acid bath were tested.

The SWCNTs were deposited on a silicon wafer. Figure 10.16a shows a micrograph of the as dried SWCNT ink on the wafer. In Figure 10.16b the SWCNT network is depicted by AFM after the wafer was immersed in a 1M-nitric acid bath for 20 min. In Figure 10.16c an AFM image of the SWCNT network is depicted the same wafer was immersed in an ethanol bath for 20 min and Figure 10.16d shows an AFM of the SWCNT network after the wafer was annealed at 350°C for 30 min. Nitric acid is shown to isolate the polymer/surfactant bearing SWCNTs as network on the wafer. Subsequent immersing of the wafer in an ethanol bath reduces the width of the nanotube/polymer complex. Annealing however, shows a greater impact on the width of the nanotube/polymer complex. This hints a removal of polymer from the surface of the nanotubes by the process. Height profiles were extracted from ach AFM image and are shown in Figure 10.17.

In the extracted profiles the height of the nanotubes can be observed. The height of the nanotubes was reduced from 10 - 20 nm to 1 - 7 nm after ethanol washing. After annealing the profile shows heights of 1 - 5 nm, however, the profile is more homogeneous. Especially the AFM image after annealing suggests, that an additional solvent rinsing step should be applied to remove the residual surfactant and polymer particles observed in Figure 10.16d.

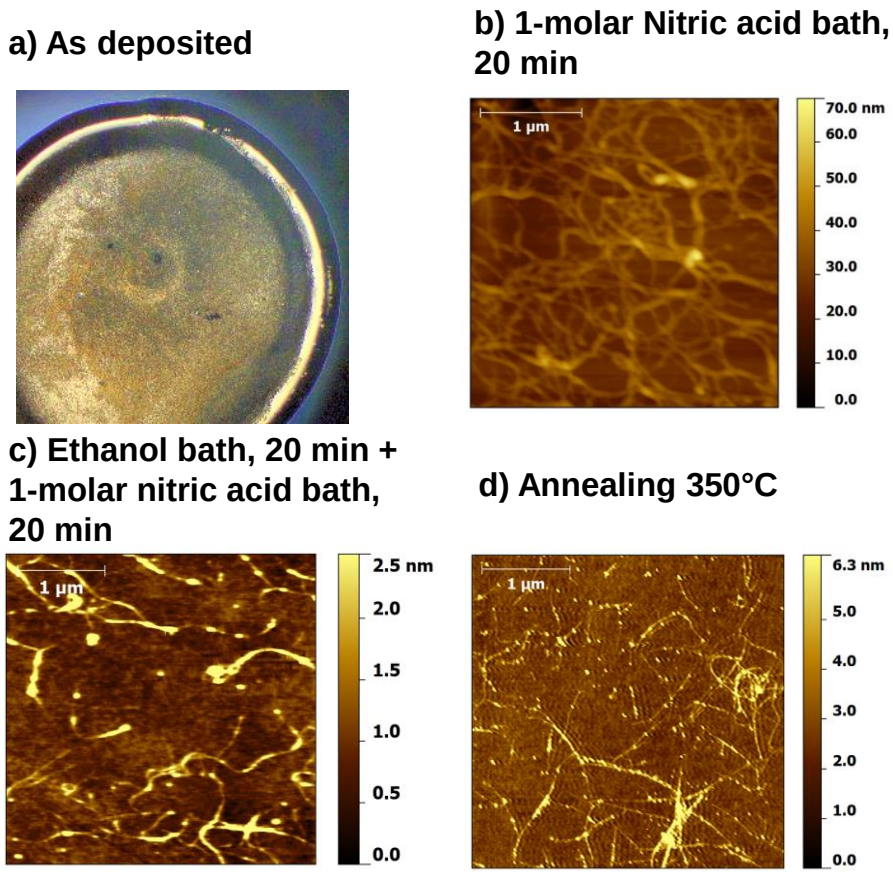

Figure 10.16. Subsequent washing steps of SWCNT Ink drop casted onto a silicon wafer. In a) a micrograph of an as deposited droplet of SWCNT ink is shown. In b) an AFM image is shown of the wafer after it was immersed in a bath of 1-M nitric acid. In c) an AFM image is displayed after the wafer was immersed in an ethanol bath for 20 min. In d) the wafer experienced additional annealing for 30 min at 350°C.

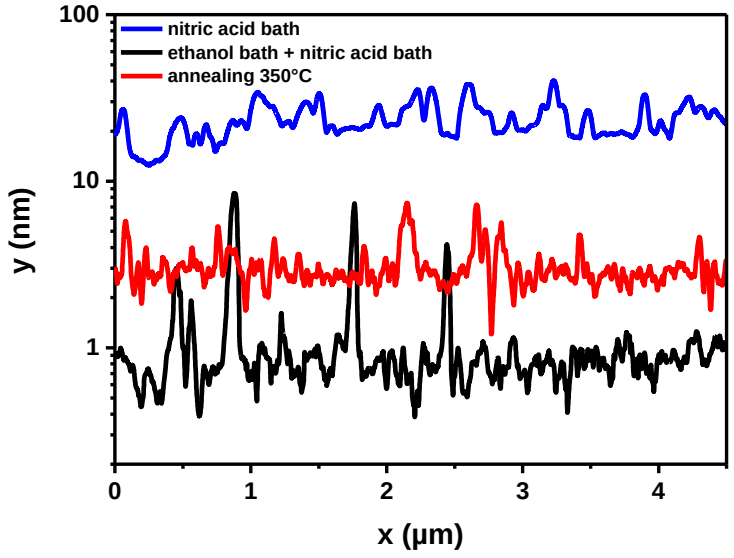

Figure 10.17. Height profiles extracted from the AFM images after several washing steps applied to a SWCNT network on a silicon wafer.

10.13. Transmission Electron Microscopy of SWCNTs

Both fractions, enriched individualized semiconducting SWCNTs and the freestanding sheets with enriched semiconducting character were analyzed under the transmission electron microscope. Figure 10.18 shows the image of individualized SWCNTs and Figure 10.19 shows the freestanding SWCNT sheet in high resolution TEM. It is found that the polymeric dispersant adsorbs as a thick layer around the SWCNTs.

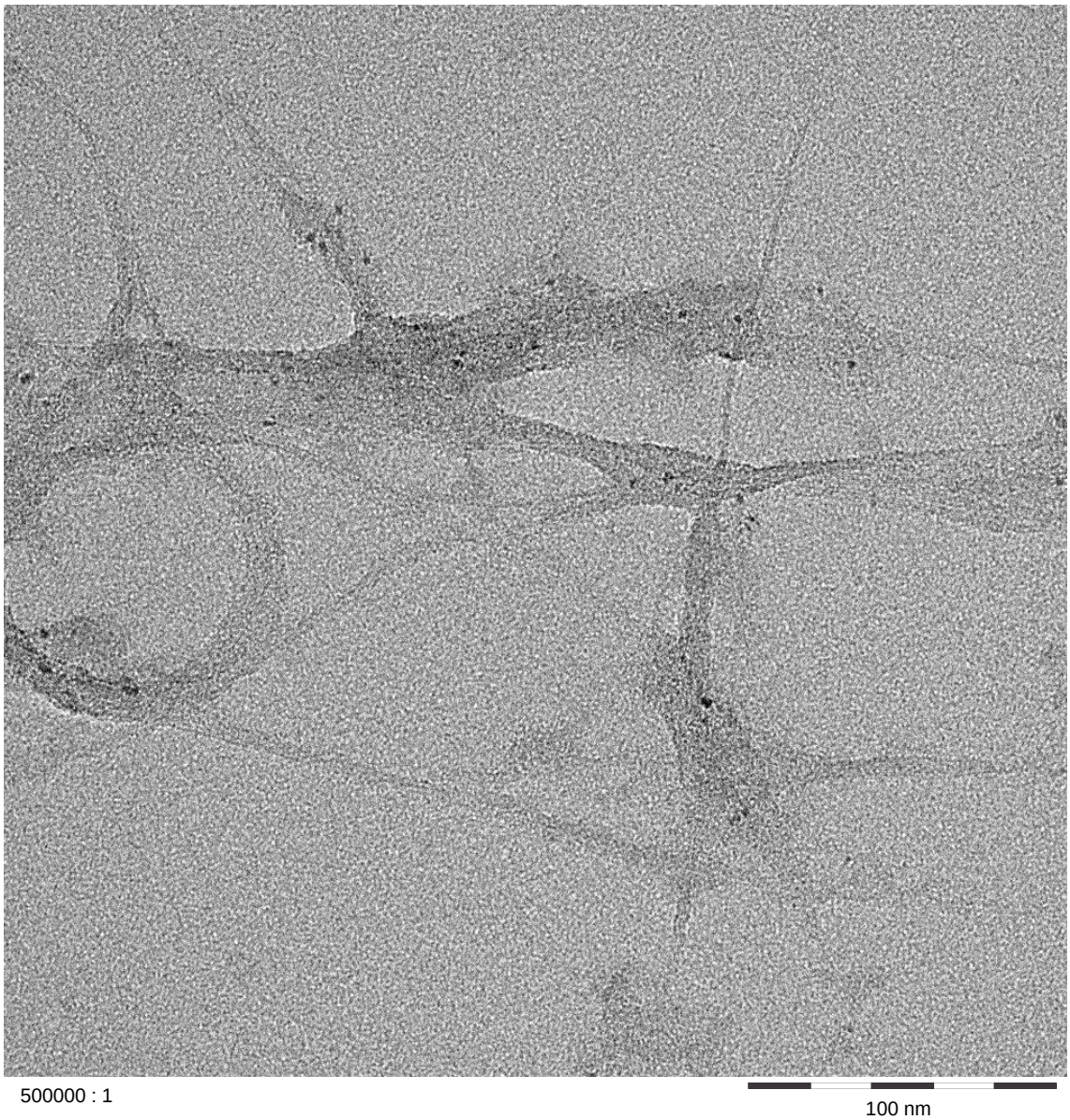

Figure 10.18. Individualized enriched semiconducting SWCNTs in TEM. The picture was taken by Ulrich Flörchinger in the laboratory of Philip Müller (BASF SE).

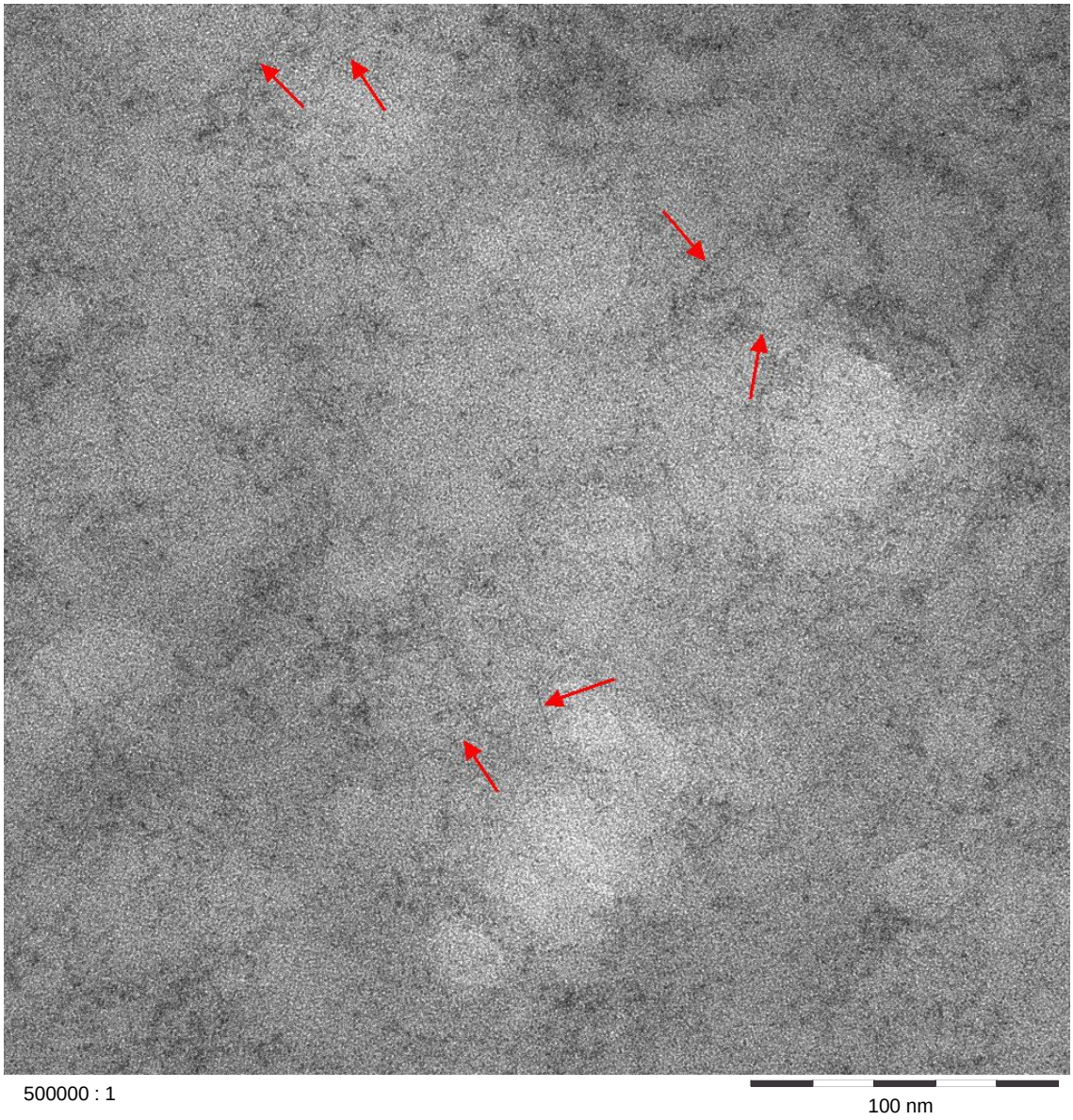

Figure 10.19. Freestanding SWCNTs sheets with enriched semiconducting character in TEM. Red arrows indicate possible SWCNTs incorporated into the largely polymeric freestanding sheet matrix. The picture was taken by Ulrich Flörchinger in the laboratory of Philip Müller (BASF SE).

11. Publications & Patents

- J. Walter, K. Löhr, E. Karabudak, W.G. Reis, J. Mikhael, W. Peukert, W. Wohlleben, H. Cölfen, *Multidimensional analysis of nanoparticles with highly disperse properties using multiwavelength analytical ultracentrifugation.* ACS Nano, DOI: 10.1021/nn503205k (2014).

- W.G. Reis, A. Kraus, J. Mikhael, M. Kaiser, M.G. Schwab, R.T. Weitz, M. Kettner, *Separation of semi-conducting and metallic single-walled carbon nanotubes using a polytungstate.* Patent WO 2016/046153 A1 (2016).

- W.G. Reis, R.T. Weitz, M. Kettner, A. Kraus, M.G. Schwab, Ž. Tomović, R. Krupke, J. Mikhael, *Highly efficient and scalable separation of semiconducting carbon nanotubes via weak field centrifugation.* Scientific Reports, DOI: 10.1038/srep26259 (2016)

- W.G. Reis, R.T. Weitz, Ž. Tomović, R. Krupke, J. Mikhael, *Wide dynamic range enrichment method of semiconducting single-walled carbon nanotubes with weak field centrifugation.* Scientific Reports, DOI: 10.1038/srep44812 (2017).

12. Acknowledgements

From day one the years spend on this project became a journey, in which time flew by between the first introduction to nanotubes and writing down a thesis. And most journeys are made fascinating by all the people that you meet along the way. I certainly would not have been able to finish this PhD without the contributions of each one around me. I am very glad for the support throughout the entire time. First of all, I want to mention my family, friends and colleagues, who influenced my work and certainly played their part in growing the ability in me to complete this thesis.

The most important people, who actually set up the whole project, with me as an external PhD student from TU Darmstadt in BASF SE, were Jules Mikhael, Thomas Weitz, Zeljko Tomovic, Matthias Schwab and of course Ralph Krupke.

I want to thank Jules Mikhael for his everlasting enthusiasm to not only design experiments and create insight into new findings, but to teach me the substantial parts of working scientifically precise. There could not have been a better mentor to support me become the best scientist I can be. I am deeply thankful for all the inspiration, trust and opportunities I enjoyed while being part of his lab not only but especially during the last year of my PhD.

I also want to thank Thomas Weitz, who similarly to Jules Mikhael shared a deep passion for new findings and often sparked the drive in me to put in more work and thought at every stage of this PhD. He provided me with advice and was there for scientific discussions helping me not only to build a structured thesis but teaching me to be successful.

The role of Ralph Krupke has to be highlighted. He provided me with scientific advice and insight at critical stages of my PhD. He helped to ensure that I was building a successful thesis from the first day on to this day.

I would like to express gratitude to my committee members, Professor Schneider and Professor Stark for being interested in the project and being part of my PhD jury.

I want to thank Matthias Schwab, Zeljko Tomovic and again Jules Mikhael and Thomas Weitz for designing the whole project in BASF SE and trusting me with developing the experiments that are featured in this thesis. At this point I also want to thank the people in the background Norbert Wagner, Jochen Brill, Erik Waßner as well as Josef Wünsch, Jens Rieger and Jürgen Barwich, whose groups I was part of in BASF SE.

I specifically want to thank Jules' co-lab leaders Wendel Wohlleben and Volodymyr Boyko. They helped me out a lot of times, stayed long hours in the lab and even read some of my earliest thesis drafts, which was not always the easiest job to do.

The next group I specifically want to express my gratitude to are all the lab members, who first instructed me on basically every device or measurement method that is displayed in this thesis and secondly worked with me on an everyday basis.
This includes, especially, my next desk colleagues in the fractionation lab, who were Sven Machauer, Michael Kaiser, Christian Dammbrück, Claudia Bänsch, Klaus Vilsmeier, Kai Werle, Stefan Herrmann, Katharina Stürmer, Maxime Schleyer and Andreas Hopf and of course the people from other labs I enjoyed to work with Elisabeth Wagner, Thomas Kolb, Ute Benkert, Bernd Miltner, Mathias Bach, Werner Wacker and Peter Schuler.
I also want to mention the complete CMIC Team Benjamin Rietz, Tanja Brunner, Nadja Obst, Waldemar Bartuli and Thorsten Wombacher. Here of course, I do not want to forget my Postdoc colleagues Nils-Eike Weber, Andreas Müller, Andrew Strudwick and Amit Kumar Roy, who helped me with discussions and instructed me to use the combined AFM/Raman, pyrolysis oven or the SEM.

I want to thank the guys that I directly worked with on multiple occasions and or proofread excerpts of this thesis, which are Arkadius Boron, Sabine Hirth, Roelf-Peter Baumann, Tobias Umbach, Bernhard von Vacano, Michel Kettner, Ilja Vladimirov, Subramanian Vaidyanathan, Daniel Kälblein. Here I also want to thank Alexander Kraus & Annemarie Kühn, who designed and synthesized the PAE polymers.

I want to mention the lab team from the OFET department Georg Schneider, Thomas Trapp, Daniel Bahl, Thomas Musiol, Thomas Rosenkranz, Michael Eustachi and Dieter Freyberg, who always supported my work and shared their equipment with me.

A lot of the mentioned collaborators, paper co-authors or supervisors became great friends in the last years and had a direct impact on my professional and personal development.

I would like to express special thanks to the "late night shift" people in BASF SE, who I cannot mention by names but shared everything with me meaning their laughs and frustrations, food and motivation as lab companions. I am very thankful to have met you guys.

Most importantly this thesis would have never been possible without the support of my family.
My deepest gratitude goes to all of you, my parents, siblings, and everybody else at home, who have always been there for me and will always be my source of energy, especially Katharina.
Thank you.

13. List of Figures

14. List of Tables

Personal Information

Name:	Wieland Gabriel Reis
Date of birth:	06/27/1987
Place of birth:	Cologne
Nationality:	German

Working experience

09/2011 – 12/2012	Research assistant at the Max-Planck Institute for Nuclear Physics in Heidelberg.

Studies

07/2013 – 11/2016	External PhD thesis in BASF SE under supervision of Prof. Ralph Krupke at the material science department at the Technical University Darmstadt. PhD Thesis at the Material Physics Department of BASF SE Ludwigshafen on „Electronic Type Separation of Single-Walled Carbon Nanotubes by Weak Field Centrifugation“.
10/2010 – 03/2013	Master of Science in physics at the Ruprecht-Karls-University Heidelberg. The Master thesis at the Material Physics Department of BASF SE Ludwigshafen on the „Advanced Sorting of Carbon Nanotubes by Density Gradient Ultracentrifugation and their Application in Organic Transistors“.
10/2007 – 08/2010	Bachelor in physics at the Ruprecht-Karls University Heidelberg. Bachelor Thesis on „Neutralization of Aluminum Cluster Anions by Laser Induced Delayed Emission in an Electrostatic Ion Trap“ at the Max-Planck Institute for Nuclear Physics in Heidelberg.

Education

05/2004 – 05/2006	Abitur (Siegtal-Gymnasium Eitorf)
07/2003 – 05/2004	Collins Hill High School Lawrenceville/Suwanee
07/1997 – 06/2003	Siegtal-Gymnasium Eitorf

15. References

1. Bardeen, J. & Brattain, W. H. The transistor, a semi-conductor triode. *Phys. Rev.* **74,** 230-231 (1948).
2. Crothers, B., End of moore's law: It's not just about physics, in *Cnet.* 2013.
3. Kurzweil, R. *The singularity is near: When humans transcend biology* (Penguin, 2006)
4. Kroto, H. The stability of the fullerenes cn, with n = 24, 28, 32, 36, 50, 60 and 70. *Nature* **329,** 529-531 (1987).
5. Gibson, J. A. E. Early nanotubes? *Nature* **359,** 369-369 (1992).
6. Iijima, S. Helical microtubules of graphitic carbon. *Nature* **354,** 56-58 (1991).
7. Iijima, S. & Ichihashi, T. Single-shell carbon nanotubes of 1-nm diameter. *Nature* **363,** 603-605 (1993).
8. Carver, R. L. *et al.* A model for nucleation and growth of single wall carbon nanotubes via the hipco process: A catalyst concentration study. *Journal of Nanoscience and Nanotechnology* **5,** 1035-1040 (2005).
9. Dürkop, T., Kim, B. M. & Fuhrer, M. S. Properties and applications of high-mobility semiconducting nanotubes. *J. Phys. Condens. Matter* **16,** R553 (2004).
10. Dürkop, T., Getty, S. A., Cobas, E. & Fuhrer, M. S. Extraordinary mobility in semiconducting carbon nanotubes. *Nano Lett.* **4,** 35-39 (2004).
11. Cao, Q. *et al.* End-bonded contacts for carbon nanotube transistors with low, size-independent resistance. *Science* **350,** 68-72 (2015).
12. Dresselhaus, S., Dresselhaus, G. & Eklund, P. C. *Science of fullerenes and carbon nanotubes: Their properties and applications* (Elsevier Science, 1996)
13. Torres, T. *Carbon nanotubes and related structures. Synthesis, characterization, functionalization, and applications.* Angew. Chem. Int. Ed. Vol. 50. (WILEY-VCH Verlag, 2011)
14. Harris, P. J. F. *Carbon nanotube science: Synthesis, properties and applications* (Cambridge University Press, 2009)
15. M. Rafique, J. I. Production of carbon nanotubes by different routes-a review. *Journal of Encapsulation and Adsorption Sciences* **1,** 29-34 (2011).
16. Eatemadi, A. *et al.* Carbon nanotubes: Properties, synthesis, purification, and medical applications. *Nanoscale Research Letters* **9,** 1-13 (2014).
17. Smiljanic, O., Stansfield, B. L., Dodelet, J. P., Serventi, A. & Désilets, S. Gas-phase synthesis of swnt by an atmospheric pressure plasma jet. *Chem. Phys. Lett.* **356,** 189-193 (2002).
18. Okuno, J. *et al.* Label-free immunosensor for prostate-specific antigen based on single-walled carbon nanotube array-modified microelectrodes. *Biosens. Bioelectron.* **22,** (2007).

19. Takahashi, T., Takei, K., Gillies, A. G., Fearing, R. S. & Javey, A. Carbon nanotube active-matrix backplanes for conformal electronics and sensors. *Nano Lett.* **11,** 5408-5413 (2011).

20. Ma-Hock, L. *et al.* Comparative inhalation toxicity of multi-wall carbon nanotubes, graphene, graphite nanoplatelets and low surface carbon black. *Particle and fibre toxicology* **10,** 1 (2013).

21. Bandyopadhyaya, R., Nativ-Roth, E., Regev, O. & Yerushalmi-Rozen, R. Stabilization of individual carbon nanotubes in aqueous solutions. *Nano Lett.* **2,** 25-28 (2002).

22. Wang, H. Dispersing carbon nanotubes using surfactants. *Current Opinion in Colloid & Interface Science* **14,** 364-371 (2009).

23. Bahr, J. L., Mickelson, E. T., Bronikowski, M. J., Smalley, R. E. & Tour, J. M. Dissolution of small diameter single-wall carbon nanotubes in organic solvents? *Chem. Commun.* 193-194 (2001).

24. Strano, M. S. *et al.* The role of surfactant adsorption during ultrasonication in the dispersion of single-walled carbon nanotubes. *Journal of Nanoscience and Nanotechnology* **3,** 81-86 (2003).

25. Krupke, R., Hennrich, F., Löhneysen, H. v. & Kappes, M. M. Separation of metallic from semiconducting single-walled carbon nanotubes. *Science* **301,** 344-347 (2003).

26. Moshammer, K., Hennrich, F. & Kappes, M. Selective suspension in aqueous sodium dodecyl sulfate according to electronic structure type allows simple separation of metallic from semiconducting single-walled carbon nanotubes. *Nano Res.* **2,** 599-606 (2009).

27. Liu, H., Tanaka, T., Urabe, Y. & Kataura, H. High-efficiency single-chirality separation of carbon nanotubes using temperature-controlled gel chromatography. *Nano Lett.* **13,** 1996-2003 (2013).

28. Duesberg, G. S., Muster, J., Krstic, V., Burghard, M. & Roth, S. Chromatographic size separation of single-wall carbon nanotubes. *Appl. Phys. A* **67,** 117-119 (1998).

29. Nish, A., Hwang, J.-Y., Doig, J. & Nicholas, R. J. Highly selective dispersion of single-walled carbon nanotubes using aromatic polymers. *Nat. Nanotechnol.* **2,** 640-646 (2007).

30. Hwang, J.-Y. *et al.* Polymer structure and solvent effects on the selective dispersion of single-walled carbon nanotubes. *JACS* **130,** 3543-3553 (2008).

31. Blanch, A. J., Lenehan, C. E. & Quinton, J. S. Dispersant effects in the selective reaction of aryl diazonium salts with single-walled carbon nanotubes in aqueous solution. *J. Phys. Chem. C* **116,** 1709-1723 (2011).

32. Huang, H., Maruyama, R., Noda, K., Kajiura, H. & Kadono, K. Preferential destruction of metallic single-walled carbon nanotubes by laser irradiation. *J. Phys. Chem. B* **110,** 7316-7320 (2006).

33. Ghosh, S., Bachilo, S. M. & Weisman, R. B. Advanced sorting of single-walled carbon nanotubes by nonlinear density-gradient ultracentrifugation. *Nat. Nanotechnol.* **5,** 443-450 (2010).
34. Arnold, M. S., Stupp, S. I. & Hersam, M. C. Enrichment of single-walled carbon nanotubes by diameter in density gradients. *Nano Lett.* **5,** 713-718 (2005).
35. Arnold, M. S., Green, A. A., Hulvat, J. F., Stupp, S. I. & Hersam, M. C. Sorting carbon nanotubes by electronic structure using density differentiation. *Nat. Nanotechnol.* **1,** 60-65 (2006).
36. Khripin, C. Y., Fagan, J. A. & Zheng, M. Spontaneous partition of carbon nanotubes in polymer-modified aqueous phases. *JACS* **135,** 6822-6825 (2013).
37. Fagan, J. A. *et al.* Isolation of specific small-diameter single-wall carbon nanotube species via aqueous two-phase extraction. *Adv. Mater.* **26,** 2800-2804 (2014).
38. Fagan, J. A. *et al.* Isolation of >1 nm diameter single-wall carbon nanotube species using aqueous two-phase extraction. *ACS Nano* **9,** 5377-5390 (2015).
39. Gui, H. *et al.* Redox sorting of carbon nanotubes. *Nano Lett.* **15,** 1642-1646 (2015).
40. Newburgh, R., Peidle, J. & Rueckner, W. Einstein, perrin, and the reality of atoms: 1905 revisited. *Am. J. Phys.* **74,** 478-481 (2006).
41. Reis, W., Advanced sorting of carbon nanotubes and their application in organic transistors. 2013, University of Heidelberg.
42. *The nobel prize in chemistry 1926.* 2014 [cited 2016 5 July]; Available from: http://www.nobelprize.org/nobel_prizes/chemistry/laureates/1926/.
43. *The nobel prize in physics 1926.* 2014 [cited 2016 5 July]; Available from: http://www.nobelprize.org/nobel_prizes/physics/laureates/1926/.
44. Maechtle, W. & Börger, L. *Analytical ultracentrifugation of polymers and nanoparticles* (Springer Berlin Heidelberg, 2006)
45. Franklin, A. D. *et al.* Sub-10 nm carbon nanotube transistor. *Nano Lett.* **12,** 758-762 (2012).
46. Sun, D.-M. *et al.* Mouldable all-carbon integrated circuits. *Nat. Commun.* **4,** (2013).
47. Tullo, A. H., Global top 50 chemical companies, in *Chem. Eng. News.* 2015. p. 14-26.
48. Moore, V. C. *et al.* Individually suspended single-walled carbon nanotubes in various surfactants. *Nano Lett.* **3,** 1379-1382 (2003).
49. Blanch, A. J., Lenehan, C. E. & Quinton, J. S. Optimizing surfactant concentrations for dispersion of single-walled carbon nanotubes in aqueous solution. *J. Phys. Chem. B* **114,** 9805-9811 (2010).
50. Antaris, A. L., Seo, J.-W. T., Green, A. A. & Hersam, M. C. Sorting single-walled carbon nanotubes by electronic type using nonionic, biocompatible block copolymers. *ACS Nano* **4,** 4725-4732 (2010).

51. Antaris, A. L. *et al.* Probing and tailoring ph-dependent interactions between block copolymers and single-walled carbon nanotubes for density gradient sorting. *J. Phys. Chem. C* **116,** 20103-20108 (2012).

52. Homenick, C. M. *et al.* High-yield, single-step separation of metallic and semiconducting swcnts using block copolymers at low temperatures. *J. Phys. Chem. C* **118,** 16156-16164 (2014).

53. Reis, W. G. *et al.* Highly efficient and scalable separation of semiconducting carbon nanotubes via weak field centrifugation. *Sci. Rep.* **6,** 26259 (2016).

54. O'Connell, M. J. *et al.* Band gap fluorescence from individual single-walled carbon nanotubes. *Science* **297,** 593-596 (2002).

55. Weisman, R. B. & Bachilo, S. M. Dependence of optical transition energies on structure for single-walled carbon nanotubes in aqueous suspension: An empirical kataura plot. *Nano Lett.* **3,** 1235-1238 (2003).

56. Bachilo, S. M. *et al.* Structure-assigned optical spectra of single-walled carbon nanotubes. *Science* **298,** 2361-2366 (2002).

57. Saito, R., Dresselhaus, G. & Dresselhaus, M. S. *Physical properties of carbon nanotubes* (Imperial College Press, 1998)

58. Prasek, J. *et al.* Methods for carbon nanotubes synthesis—review. *J. Mater. Chem.* **21,** (2011).

59. Iijima, S. & Ichihashi, T. *Single-shell carbon nanotubes of 1-nm diameter* 1993)

60. Yoshinori, A. & Sumio, I. Preparation of carbon nanotubes by arc-discharge evaporation. *Jpn. J. Appl. Phys.* **32,** L107 (1993).

61. Karthikeyan, S., Mahalingam, P. & Karthik, M. Large scale synthesis of carbon nanotubes. *E-Journal of Chemistry* **6,** (2009).

62. Keun Su, K. *et al.* Large-scale production of single-walled carbon nanotubes by induction thermal plasma. *J. Phys. D: Appl. Phys.* **40,** 2375 (2007).

63. Hahn, J., Han, J. H., Yoo, J.-E., Jung, H. Y. & Suh, J. S. New continuous gas-phase synthesis of high purity carbon nanotubes by a thermal plasma jet. *Carbon* **42,** 877-883 (2004).

64. Kim, K. S., Imris, M., Shahverdi, A., Alinejad, Y. & Soucy, G. Single-walled carbon nanotubes prepared by large-scale induction thermal plasma process: Synthesis, characterization, and purification. *J. Phys. Chem. C* **113,** 4340-4348 (2009).

65. Ren, Z., Lan, Y. & Wang, Y. *Aligned carbon nanotubes: Physics, concepts, fabrication and devices* (Springer Berlin Heidelberg, 2012)

66. José-Yacamán, M., Miki-Yoshida, M., Rendon, L. & Santiesteban, J. Catalytic growth of carbon microtubules with fullerene structure. *Appl. Phys. Lett.* **62,** 202-204 (1993).

67. Harris, J. D., Raffaelle, R. P., Gennett, T., Landi, B. J. & Hepp, A. F. Growth of multi-walled carbon nanotubes by injection cvd using cyclopentadienyliron dicarbonyl dimer and cyclooctatetraene iron tricarbonyl. *Materials Science and Engineering: B* **116,** 369-374 (2005).

68. Li, Y. *et al.* Preferential growth of semiconducting single-walled carbon nanotubes by a plasma enhanced cvd method. *Nano Lett.* **4,** 317-321 (2004).

69. Nikolaev, P. *et al.* Gas-phase catalytic growth of single-walled carbon nanotubes from carbon monoxide. *Chem. Phys. Lett.* **313,** 91-97 (1999).

70. *Carbon nanotubes*, ed. M. Endo, S. Iijima, and M.S. Dresselhaus (Pergamon, 1996)

71. Meyyappan, M. *Carbon nanotubes: Science and applications* (CRC Press, 2004)

72. Samsonidze, G. G. *et al.* The concept of cutting lines in carbon nanotube science. *Journal of Nanoscience and Nanotechnology* **3,** 431-458 (2003).

73. Javey, A. & Kong, J. *Carbon nanotube electronics* (Springer US, 2009)

74. Thomsen, C., Reich, S. & Maultzsch, J., *Electronic properties of carbon nanotubes*, in *Carbon nanotubes*. 2007, Wiley-VCH Verlag GmbH. p. 31-65.

75. Eva, Y. A., Guohong, L. & Xu, D. Electronic properties of graphene: A perspective from scanning tunneling microscopy and magnetotransport. *Rep. Prog. Phys.* **75,** 056501 (2012).

76. Ando, T. The electronic properties of graphene and carbon nanotubes. *NPG Asia Mater* **1,** 17-21 (2009).

77. Hazeghi, A., Carbon nanotube electronics. 2011, Stanford University.

78. Hároz, E. H. *et al.* Unique origin of colors of armchair carbon nanotubes. *JACS* **134,** 4461-4464 (2012).

79. Benedict, L. X., Louie, S. G. & Cohen, M. L. Static polarizabilities of single-wall carbon nanotubes. *Physical Review B* **52,** 8541-8549 (1995).

80. Hagen, A. & Hertel, T. Quantitative analysis of optical spectra from individual single-wall carbon nanotubes. *Nano Lett.* **3,** 383-388 (2003).

81. Fantini, C. *et al.* Optical transition energies for carbon nanotubes from resonant raman spectroscopy: Environment and temperature effects. *Phys. Rev. Lett.* **93,** 147406 (2004).

82. Raman, C. V. & Krishnan, K. S. A new type of secondary radiation. *Nature* **121,** 501-502 (1928).

83. Araujo, P. T. *et al.* Resonance raman spectroscopy of the radial breathing modes in carbon nanotubes. *Physica E: Low-dimensional Systems and Nanostructures* **42,** 1251-1261 (2010).

84. Dresselhaus, M. S., Dresselhaus, G., Jorio, A., Souza Filho, A. G. & Saito, R. Raman spectroscopy on isolated single wall carbon nanotubes. *Carbon* **40,** 2043-2061 (2002).

85. Kukovecz, A., Kramberger, C., Georgakilas, V., Prato, M. & Kuzmany, H. A detailed raman study on thin single-wall carbon nanotubes prepared by the hipco process. *EPJ B* **28,** 223-230 (2002).

86. Lebedkin, S., Arnold, K., Kiowski, O., Hennrich, F. & Kappes, M. M. Raman study of individually dispersed single-walled carbon nanotubes under pressure. *Physical Review B* **73,** 094109 (2006).

87. O'Connell, M. J., Sivaram, S. & Doorn, S. K. Near-infrared resonance raman excitation profile studies of single-walled carbon nanotube intertube interactions: A direct comparison of bundled and individually dispersed hipco nanotubes. *Physical Review B* **69,** 235415 (2004).

88. Saito, R., Takeya, T., Kimura, T., Dresselhaus, G. & Dresselhaus, M. S. Raman intensity of single-wall carbon nanotubes. *Physical Review B* **57,** 4145-4153 (1998).

89. Alvarez, L. *et al.* Resonant raman study of the structure and electronic properties of single-wall carbon nanotubes. *Chem. Phys. Lett.* **316,** 186-190 (2000).

90. Maultzsch, J., Telg, H., Reich, S. & Thomsen, C. Radial breathing mode of single-walled carbon nanotubes: Optical transition energies and chiral-index assignment. *Physical Review B* **72,** 205438 (2005).

91. Jorio, A. *et al.* Structural (n, m) determination of isolated single-wall carbon nanotubes by resonant raman scattering. *Phys. Rev. Lett.* **86,** 1118-1121 (2001).

92. Jorio, A. *et al.* G-band resonant raman study of 62 isolated single-wall carbon nanotubes. *Physical Review B* **65,** 155412 (2002).

93. Telg, H. *et al.* Chiral index dependence of the g+ and g– raman modes in semiconducting carbon nanotubes. *ACS Nano* **6,** 904-911 (2011).

94. Hunklinger, S. *Festkörperphysik* (Oldenbourg Verlag, 2009)

95. Hoover, M. D., Finch, G. L. & Castorina, B. T. Sodium metatungstate as a medium for measuring particle density using isopycnic density gradient ultracentrifugation. *J. Aerosol Sci* **22,** 215-221 (1991).

96. Yanagi, K., Iitsuka, T., Fujii, S. & Kataura, H. Separations of metallic and semiconducting carbon nanotubes by using sucrose as a gradient medium. *J. Phys. Chem. C* **112,** 18889-18894 (2008).

97. Backes, C., Hauke, F., Schmidt, C. D. & Hirsch, A. Fractioning hipco and comocat swcnts via density gradient ultracentrifugation by the aid of a novel perylene bisimide derivative surfactant. *Chem. Commun.* 2643-2645 (2009).

98. Nishide, D., Liu, H., Tanaka, T. & Kataura, H. Sorting single-wall carbon nanotubes combining gel chromatography and density-gradient ultracentrifugation. *physica status solidi (b)* **247,** 2746-2749 (2010).

99. Feng, Y., Miyata, Y., Matsuishi, K. & Kataura, H. High-efficiency separation of single-wall carbon nanotubes by self-generated density gradient ultracentrifugation. *J. Phys. Chem. C* **115,** 1752-1756 (2011).

100. Scharfenberg, L. & Mertig, M. Semiconducting enrichment of arc discharge single-walled carbon nanotubes by density gradient ultracentrifugation. *Physica Status Solidi a-Applications and Materials Science* **212,** 1395-1398 (2015).

101. Lauth, G. J. & Kowalczyk, J. *Einführung in die physik und chemie der grenzflächen und kolloide* (Springer Berlin Heidelberg, 2015)

102. Mächtle, W. & Lechner, M. D., *Evaluation of equilibrium and nonequilibrium density gradients in an analytical ultracentrifuge by calibration with marker particles*, in *Analytical ultracentrifugation vi*, W. Borchard and A. Straatmann, Editors. 2002, Springer Berlin Heidelberg: Berlin, Heidelberg. p. 1-10.

103. Börger, L. & Lechner, M. The preparative dynamic density gradient method. *Colloid. Polym. Sci.* **284,** 405-412 (2006).

104. Lamm, O. The theory and method of ultra centrifuging. *Z. Phys. Chem. A-Chem. T* **143,** 177-190 (1929).

105. Hermans, J. J. & Ende, H. A. Density gradient centrifugation of a polymer-homologous mixture. *Journal of Polymer Science Part C: Polymer Symposia* **1,** 161-177 (1963).

106. Lechner, M. D. & Borchard, W. The influence of strong centrifugal force fields on solutions: I. Improved hermans–ende equation. *Eur. Polym. J.* **35,** 371-376 (1999).

107. Lechner, M. D. Static density gradient centrifugation; extended hermans-ende equation. *Macromol. Rapid Commun.* **18,** 781-786 (1997).

108. Ralston, G. B. *Introduction to analytical ultracentrifugation* (Beckman Instruments, 1993)

109. Georgakilas, V. *et al.* Organic functionalization of carbon nanotubes. *JACS* **124,** 760-761 (2002).

110. Guldi, D. M. & Martín, N. *Carbon nanotubes and related structures: Synthesis, characterization, functionalization, and applications* (John Wiley & Sons, 2010)

111. Blanch, A. J., Quinton, J. S. & Shapter, J. G. The role of sodium dodecyl sulfate concentration in the separation of carbon nanotubes using gel chromatography. *Carbon* **60,** 471-480 (2013).

112. Hertel, T. *et al.* Spectroscopy of single- and double-wall carbon nanotubes in different environments. *Nano Lett.* **5,** 511-514 (2005).

113. Backes, C. *et al.* Determination of the surfactant density on swcnts by analytical ultracentrifugation. *Chem. Eur. J.* **16,** 13176-13184 (2010).

114. Fagan, J. A. *et al.* Centrifugal length separation of carbon nanotubes. *Langmuir* **24,** 13880-13889 (2008).

115. Richard, C., Balavoine, F., Schultz, P., Ebbesen, T. W. & Mioskowski, C. Supramolecular self-assembly of lipid derivatives on carbon nanotubes. *Science* **300,** 775-778 (2003).

116. Yurekli, K., Mitchell, C. A. & Krishnamoorti, R. Small-angle neutron scattering from surfactant-assisted aqueous dispersions of carbon nanotubes. *JACS* **126,** 9902-9903 (2004).

117. Islam, M. F., Rojas, E., Bergey, D. M., Johnson, A. T. & Yodh, A. G. High weight fraction surfactant solubilization of single-wall carbon nanotubes in water. *Nano Lett.* **3,** 269-273 (2003).

118. Wenseleers, W. *et al.* Efficient isolation and solubilization of pristine single-walled nanotubes in bile salt micelles. *Adv. Funct. Mater.* **14,** 1105-1112 (2004).

119. Flavel, B. S., Kappes, M. M., Krupke, R. & Hennrich, F. Separation of single-walled carbon nanotubes by 1-dodecanol-mediated size-exclusion chromatography. *ACS Nano* **7,** 3557-3564 (2013).

120. Hirano, A., Tanaka, T., Urabe, Y. & Kataura, H. Ph- and solute-dependent adsorption of single-wall carbon nanotubes onto hydrogels: Mechanistic insights into the metal/semiconductor separation. *ACS Nano* **7,** 10285-10295 (2013).

121. Strano, M. S. *et al.* Reversible, band-gap-selective protonation of single-walled carbon nanotubes in solution. *J. Phys. Chem. B* **107,** 6979-6985 (2003).

122. Joselevich, E. & Lieber, C. M. Vectorial growth of metallic and semiconducting single-wall carbon nanotubes. *Nano Lett.* **2,** 1137-1141 (2002).

123. Heo, K. Y., Lee, K. W., Kim, K. M. & Kim, H. J. Self-selective separation of single-walled carbon nanotubes via a hydroxyl group reaction. *Electrochem. Solid-State Lett.* **12,** K71-K73 (2009).

124. Tang, B. Z. & Xu, H. Preparation, alignment, and optical properties of soluble poly(phenylacetylene)-wrapped carbon nanotubes. *Macromolecules* **32,** 2569-2576 (1999).

125. O'Connell, M. J. *et al.* Reversible water-solubilization of single-walled carbon nanotubes by polymer wrapping. *Chem. Phys. Lett.* **342,** 265-271 (2001).

126. Von Bargen, C. D. *et al.* Origins of the helical wrapping of phenyleneethynylene polymers about single-walled carbon nanotubes. *J. Phys. Chem. B* **117,** 12953-12965 (2013).

127. Naito, M. *et al.* Stiffness- and conformation-dependent polymer wrapping onto single-walled carbon nanotubes. *JACS* **130,** 16697-16703 (2008).

128. Kang, Y. K. *et al.* Helical wrapping of single-walled carbon nanotubes by water soluble poly(p-phenyleneethynylene). *Nano Lett.* **9,** 1414-1418 (2009).

129. Gerstel, P. *et al.* Highly selective dispersion of single-walled carbon nanotubes via polymer wrapping: A combinatorial study via modular conjugation. *ACS Macro Letters* **3,** 10-15 (2014).

130. Berton, N. *et al.* Selective dispersion of large-diameter semiconducting single-walled carbon nanotubes with pyridine-containing copolymers. *Small* **10,** 360-367 (2014).

131. Tans, S. J., Verschueren, A. R. M. & Dekker, C. Room-temperature transistor based on a single carbon nanotube. *Nature* **393,** 49-52 (1998).

132. Martel, R., Schmidt, T., Shea, H. R., Hertel, T. & Avouris, P. Single- and multi-wall carbon nanotube field-effect transistors. *Appl. Phys. Lett.* **73,** 2447-2449 (1998).

133. Soh, H. T. *et al.* Integrated nanotube circuits: Controlled growth and ohmic contacting of single-walled carbon nanotubes. *Appl. Phys. Lett.* **75,** 627-629 (1999).

134. Franklin, A. D. *et al.* Carbon nanotube complementary wrap-gate transistors. *Nano Lett.* **13,** 2490-2495 (2013).

135. Javey, A., Guo, J., Wang, Q., Lundstrom, M. & Dai, H. Ballistic carbon nanotube field-effect transistors. *Nature* **424,** 654-657 (2003).

136. Li, S., Yu, Z., Rutherglen, C. & Burke, P. J. Electrical properties of 0.4 cm long single-walled carbon nanotubes. *Nano Lett.* **4,** 2003-2007 (2004).

137. Perebeinos, V., Tersoff, J. & Avouris, P. Electron-phonon interaction and transport in semiconducting carbon nanotubes. *Phys. Rev. Lett.* **94,** 086802 (2005).

138. Ma, Y. *et al.* Improved conductivity of carbon nanotube networks by in situ polymerization of a thin skin of conducting polymer. *ACS Nano* **2,** 1197-1204 (2008).

139. Bachtold, A. *et al.* Contacting carbon nanotubes selectively with low-ohmic contacts for four-probe electric measurements. *Appl. Phys. Lett.* **73,** 274-276 (1998).

140. Kim, W. *et al.* Electrical contacts to carbon nanotubes down to 1nm in diameter. *Appl. Phys. Lett.* **87,** (2005).

141. Skákalová, V., Kaiser, A. B., Woo, Y.-S. & Roth, S. Electronic transport in carbon nanotubes: From individual nanotubes to thin and thick networks. *Physical Review B* **74,** 085403 (2006).

142. Behnam, A., Guo, J. & Ural, A. Effects of nanotube alignment and measurement direction on percolation resistivity in single-walled carbon nanotube films. *J. Appl. Phys.* **102,** 044313 (2007).

143. Sze, S. M. & Ng, K. K. *Physics of semiconductor devices* (John wiley & sons, 2006)

144. Collins, P. G., Bradley, K., Ishigami, M. & Zettl, A. Extreme oxygen sensitivity of electronic properties of carbon nanotubes. *Science* **287,** 1801-1804 (2000).

145. Ante, F. S., Contact effects in organic transistors. 2011, École polytechnique fédérale de Lausanne.

146. Klauk, H. Organic thin-film transistors. *Chem. Soc. Rev.* **39,** 2643-2666 (2010).

147. Jansen, J. C., Friess, K., Clarizia, G., Schauer, J. & Izák, P. High ionic liquid content polymeric gel membranes: Preparation and performance. *Macromolecules* **44,** 39-45 (2011).

148. Kim, W. *et al.* Hysteresis caused by water molecules in carbon nanotube field-effect transistors. *Nano Lett.* **3,** 193-198 (2003).

149. Sangwan, V. K. *et al.* Fundamental performance limits of carbon nanotube thin-film transistors achieved using hybrid molecular dielectrics. *ACS Nano* **6,** 7480-7488 (2012).

150. Nordling, C., Sokolowski, E. & Siegbahn, K. Precision method for obtaining absolute values of atomic binding energies. *Phys. Rev.* **105,** 1676 (1957).

151. Watts, J. F. & Wolstenholme, J. An introduction to surface analysis by xps and aes. *An Introduction to Surface Analysis by XPS and AES, by John F. Watts, John Wolstenholme, pp. 224. ISBN 0-470-84713-1. Wiley-VCH, May 2003.* 224 (2003).

152. Binnig, G., Quate, C. F. & Gerber, C. Atomic force microscope. *Phys. Rev. Lett.* **56,** 930-933 (1986).

153. Johnson, D., Hilal, N. & Bowen, W. R., *Chapter 1 - basic principles of atomic force microscopy*, in *Atomic force microscopy in process engineering.* 2009, Butterworth-Heinemann: Oxford. p. 1-30.

154. Giddings, J. C., Yang, F. & Myers, M. N. Flow-field-flow fractionation: A versatile new separation method. *Science* **193,** 1244-1245 (1976).

155. Tyndall, J. On the blue color of the sky, the polarization of skylight, and polarization of light by cloudy matter generally. *Journal of the Franklin Institute* **88,** 34-40 (1869).

156. Young, A. T. Rayleigh scattering. *Appl. Opt.* **20,** 533-535 (1981).

157. Goldburg, W. Dynamic light scattering. *Am. J. Phys.* **67,** 1152-1160 (1999).

158. Pecora, R. *Dynamic light scattering: Applications of photon correlation spectroscopy* (Springer Science & Business Media, 2013)

159. Schurtenberger, P. & Newman, M. E. Characterization of biological and environmental particles using static and dynamic light scattering. *Environmental particles* **2,** 37-115 (1993).

160. Brown, W. *Dynamic light scattering: The method and some applications* Vol. 49. (Oxford University Press, USA, 1993)

161. Berne, B. J. & Pecora, R. Dynamic light scattering with application to chemistry, biology and physics. *Courier Dover, New York* (1976).

162. Zimm, B. H. & Dandliker, W. B. Theory of light scattering and refractive index of solutions of large colloidal particles. *The Journal of Physical Chemistry* **58,** 644-648 (1954).

163. Brown, B., Parker, C. B., Stoner, B. R. & Glass, J. T. Growth of vertically aligned bamboo-like carbon nanotubes from ammonia/methane precursors using a platinum catalyst. *Carbon* **49,** (2011).

164. Kratky, O., Leopold, H. & Stabinger, H. Dichtemessungen an flüssigkeiten und gasen auf 10^{-6} g/cm^3 bei 0.6 cm^3 präparatvolumen. *Z. angew. Phys* **27,** 273-277 (1969).

165. Hanaor, D., Michelazzi, M., Leonelli, C. & Sorrell, C. C. The effects of carboxylic acids on the aqueous dispersion and electrophoretic deposition of zro$_2$. *J. Eur. Ceram. Soc.* **32,** 235-244 (2012).

166. Lyklema, J. Fundamentals of interface and colloid science. Solid-liquid interfaces. **2,** (1995).

167. Smoluchowski, M. Contribution à la théorie de l'endosmose électrique et de quelques phénomènes corrélatifs. *Pisma Mariana Smoluchowskiego* **1,** 403-420 (1924).

168. Hunter, R. J. *Zeta potential in colloid science: Principles and applications* Vol. 2. (Academic press, 2013)

169. Backes, C. *et al.* Enhanced adsorption affinity of anionic perylene-based surfactants towards smaller-diameter swcnts. *Chem. Eur. J.* **16,** 13185-13192 (2010).

170. Taurozzi, J. S., Hackley, V. A. & Wiesner, M. R. Ultrasonic dispersion of nanoparticles for environmental, health and safety assessment–issues and recommendations. *Nanotoxicology* **5,** 711-729 (2011).

171. Leiro, J. A., Heinonen, M. H., Laiho, T. & Batirev, I. G. Core-level xps spectra of fullerene, highly oriented pyrolitic graphite, and glassy carbon. *J. Electron. Spectrosc. Relat. Phenom.* **128,** 205-213 (2003).

172. Debye, P. & Anacker, E. Micelle shape from dissymmetry measurements. *The Journal of Physical Chemistry* **55,** 644-655 (1951).

173. Utsumi, S. *et al.* Rbm band shift-evidenced dispersion mechanism of single-wall carbon nanotube bundles with naddbs. *J. Colloid Interface Sci.* **308,** 276-284 (2007).

174. Holland, R. J., Parker, E. J., Guiney, K. & Zeld, F. R. Fluorescence probe studies of ethylene oxide/propylene oxide block copolymers in aqueous solution. *The Journal of Physical Chemistry* **99,** 11981-11988 (1995).

175. Haggenmueller, R. *et al.* Comparison of the quality of aqueous dispersions of single wall carbon nanotubes using surfactants and biomolecules. *Langmuir* **24,** 5070-5078 (2008).

176. Wang, D. & Chen, L. Temperature and ph-responsive single-walled carbon nanotube dispersions. *Nano Lett.* **7,** 1480-1484 (2007).

177. Lin, Y. & Alexandridis, P. Temperature-dependent adsorption of pluronic f127 block copolymers onto carbon black particles dispersed in aqueous media. *J. Phys. Chem. B* **106,** 10834-10844 (2002).

178. Alexandridis, P., Nivaggioli, T. & Hatton, T. A. Temperature effects on structural properties of pluronic p104 and f108 peo-ppo-peo block copolymer solutions. *Langmuir* **11,** 1468-1476 (1995).

179. Paula, S., Sues, W., Tuchtenhagen, J. & Blume, A. Thermodynamics of micelle formation as a function of temperature: A high sensitivity titration calorimetry study. *The Journal of Physical Chemistry* **99,** 11742-11751 (1995).

180. Smith, G. D. & Bedrov, D. Roles of enthalpy, entropy, and hydrogen bonding in the lower critical solution temperature behavior of poly (ethylene oxide)/water solutions. *J. Phys. Chem. B* **107,** 3095-3097 (2003).

181. Dormidontova, E. E. Role of competitive peo-water and water-water hydrogen bonding in aqueous solution peo behavior. *Macromolecules* **35,** 987-1001 (2002).

182. Razaq, M., Razaq, A., Yeager, E., DesMarteau, D. D. & Singh, S. Perfluorosulfonimide as an additive in phosphoric acid fuel cell. *J. Electrochem. Soc.* **136,** 385-390 (1989).

183. Paria, S. & Khilar, K. C. A review on experimental studies of surfactant adsorption at the hydrophilic solid–water interface. *Adv. Colloid Interface Sci.* **110,** 75-95 (2004).

184. Paria, S., Manohar, C. & Khilar, K. C. Adsorption of anionic and non-ionic surfactants on a cellulosic surface. *Colloids and Surfaces A: Physicochemical and Engineering Aspects* **252,** 221-229 (2005).

185. Alexandridis, P. & Hatton, T. A. Poly (ethylene oxide) • poly (propylene oxide) • poly (ethylene oxide) block copolymer surfactants in aqueous solutions and at interfaces: Thermodynamics, structure, dynamics, and modeling. *Colloids and Surfaces A: Physicochemical and Engineering Aspects* **96,** 1-46 (1995).

186. Chen, Y. *et al.* Aggregation behavior of x-shaped branched block copolymers at the air/water interface: Effect of block sequence and temperature. *Colloid. Polym. Sci.* **293,** 97-107 (2015).

187. Kataura, H. *et al.* Optical properties of single-wall carbon nanotubes. *Synth. Met.* **103,** 2555-2558 (1999).

188. Kamps, R., Personal communication. 2016.

189. Bailar, J. C. Chemistry of the coordination compounds. (1956).

190. Freedman, M. L. Polymerization of anions: The hydrolysis of sodium tungstate and of sodium chromate1. *JACS* **80,** 2072-2077 (1958).

191. Bettinger, D. J. & Tyree Jr, S. Y. Studies of the tungsten-containing species present in acidified sodium tungstate solutions1. *JACS* **79,** 3355-3358 (1957).

192. Freedman, M. L. The tungstic acids. *JACS* **81,** 3834-3839 (1959).

193. Plewinsky, B. & Kamps, R. Sodium metatungstate, a new medium for binary and ternary density gradient centrifugation. *Macromol. Chem. Phys.* **185,** 1429-1439 (1984).

194. Ifft, J. B., Voet, D. H. & Vinograd, J. The determination of density distributions and density gradients in binary solutions at equilibrium in the ultracentrifuge1. *The Journal of Physical Chemistry* **65,** 1138-1145 (1961).

195. Boyle, W. & Chow, A. Isolation of human lymphocytes by a ficoll barrier method. *Transfusion* **9,** 151-155 (1969).

196. Green, A. A. & Hersam, M. C. Colored semitransparent conductive coatings consisting of monodisperse metallic single-walled carbon nanotubes. *Nano Lett.* **8,** 1417-1422 (2008).

197. *Crc handbook of chemistry and physics* 83rd ed (Taylor & Francis, 2002)

198. Yongsheng Chen, Y. H., Kungang Li Temperature effect on the aggregation kinetics of ceo2 nanoparticles in monovalent and divalent electrolytes. *J Environ Anal Toxicol* **2,** 158 (2012).

199. Rajter, R. F., French, R. H., Ching, W., Podgornik, R. & Parsegian, V. A. Chirality-dependent properties of carbon nanotubes: Electronic structure, optical dispersion properties, hamaker coefficients and van der waals–london dispersion interactions. *RSC Advances* **3,** 823-842 (2013).

200. Liu, H., Nishide, D., Tanaka, T. & Kataura, H. Large-scale single-chirality separation of single-wall carbon nanotubes by simple gel chromatography. *Nat. Commun.* **2,** 309 (2011).

201. Journet, C. *et al.* Large-scale production of single-walled carbon nanotubes by the electric-arc technique. *Nature* **388,** (1997).

202. Fagan, J. A. *et al.* Analyzing surfactant structures on length and chirality resolved (6,5) single-wall carbon nanotubes by analytical ultracentrifugation. *ACS Nano* **7,** 3373-3387 (2013).

203. Lam, S., Zheng, M. & Fagan, J. A. Characterizing the effect of salt and surfactant concentration on the counterion atmosphere around surfactant stabilized swcnts using analytical ultracentrifugation. *Langmuir* **32,** 3926-3936 (2016).

204. Walter, J. *et al.* Multidimensional analysis of nanoparticles with highly disperse properties using multiwavelength analytical ultracentrifugation. *ACS Nano* (2014).

205. Schuck, P. On the analysis of protein self-association by sedimentation velocity analytical ultracentrifugation. *Anal. Biochem.* **320,** 104-124 (2003).

206. Vajtai, R. *Handbook of nanomaterials* (Springer Berlin Heidelberg, 2013)

207. Huang, L. *et al.* A generalized method for evaluating the metallic-to-semiconducting ratio of separated single-walled carbon nanotubes by uv−vis−nir characterization. *J. Phys. Chem. C* **114,** 12095-12098 (2010).

208. Saito, R. *et al.* Chirality-dependent g-band raman intensity of carbon nanotubes. *Physical Review B* **64,** 085312 (2001).

209. Gomulya, W. *et al.* Effect of temperature on the selection of semiconducting single walled carbon nanotubes using poly(3-dodecylthiophene-2,5-diyl). *Carbon* **84,** 66-73 (2015).

210. Shimizu, M., Fujii, S., Tanaka, T. & Kataura, H. Effects of surfactants on the electronic transport properties of thin-film transistors of single-wall carbon nanotubes. *J. Phys. Chem. C* **117,** 11744-11749 (2013).

211. Schießl, S. P. *et al.* Polymer-sorted semiconducting carbon nanotube networks for high-performance ambipolar field-effect transistors. *ACS Appl. Mater. Interfaces* **7,** 682-689 (2015).

212. Cao, Q. *et al.* Gate capacitance coupling of singled-walled carbon nanotube thin-film transistors. *Appl. Phys. Lett.* **90,** 023516-023516-3 (2007).

213. Cao, Q. *et al.* Origins and characteristics of the threshold voltage variability of quasiballistic single-walled carbon nanotube field-effect transistors. *ACS Nano* **9,** 1936-1944 (2015).

214. Franklin, A. D., Farmer, D. B. & Haensch, W. Defining and overcoming the contact resistance challenge in scaled carbon nanotube transistors. *ACS Nano* **8,** 7333-7339 (2014).

215. García, G., Atilhan, M. & Aparicio, S. Theoretical study of renewable ionic liquids in the pure state and with graphene and carbon nanotubes. *J. Phys. Chem. B* **119,** 12224-12237 (2015).

216. Kettner, M., Vladimirov, I., Strudwick, A. J., Schwab, M. G. & Weitz, R. T. Ionic gel as gate dielectric for the easy characterization of graphene and polymer field-effect transistors and electrochemical resistance modification of graphene. *J. Appl. Phys.* **118,** 025501 (2015).

217. Gomulya, W., Gao, J. & Loi, M. A. Conjugated polymer-wrapped carbon nanotubes: Physical properties and device applications. *EPJ B* **86,** 1-13 (2013).

218. Javey, A. *et al.* Carbon nanotube field-effect transistors with integrated ohmic contacts and high-κ gate dielectrics. *Nano Lett.* **4,** 447-450 (2004).

219. Derenskyi, V. *et al.* Carbon nanotube network ambipolar field-effect transistors with 10^8 on/off ratio. *Adv. Mater.* **26,** 5969-5975 (2014).

220. Brady, G. J. *et al.* Quasi-ballistic carbon nanotube array transistors with current density exceeding si and gaas. *Science Advances* **2,** (2016).

221. NanoIntergris. *Electronically enriched (semiconducting or metallic) hipco ®*. 2016 [cited 2016; Available from: http://www.nanointegris.com/hipco-enrich.

222. Yomogida, Y. *et al.* Industrial-scale separation of high-purity single-chirality single-wall carbon nanotubes for biological imaging. *Nat. Commun.* **7,** (2016).

223. Rice, N. A., Subrahmanyam, A. V., Laengert, S. E. & Adronov, A. The effect of molecular weight on the separation of semiconducting single-walled carbon nanotubes using poly(2,7-carbazole)s. *Journal of Polymer Science Part a-Polymer Chemistry* **53,** 2510-2516 (2015).

224. Brady, G. J. *et al.* Polyfluorene-sorted, carbon nanotube array field-effect transistors with increased current density and high on/off ratio. *ACS Nano* (2014).

225. Hennrich, F. *et al.* Length-sorted, large-diameter, polyfluorene-wrapped semiconducting single-walled carbon nanotubes for high-density, short-channel transistors. *ACS Nano* (2016).

226. Kane, A. A., Ford, A. C., Nissen, A., Krafcik, K. L. & Léonard, F. Etching of surfactant from solution-processed, type-separated carbon nanotubes and impact on device behavior. *ACS Nano* **8,** 2477-2485 (2014).

227. Nanot, S., Hároz, E. H., Kim, J.-H., Hauge, R. H. & Kono, J. Optoelectronic properties of single-wall carbon nanotubes. *Adv. Mater.* **24,** 4977-4994 (2012).

228. Tanaka, T. *et al.* Simple and scalable gel-based separation of metallic and semiconducting carbon nanotubes. *Nano Lett.* **9,** 1497-1500 (2009).